AWARD NUMBER: W81XWH-20-1-0288

TITLE: Targeting Ligand-Dependent BMP Signaling in Melanoma

PRINCIPAL INVESTIGATOR: Craig J. Ceol, Ph.D.

CONTRACTING ORGANIZATION: University of Massachusetts Medical School
Worcester, MA

REPORT DATE: JULY 2022

TYPE OF REPORT: Annual Report

PREPARED FOR: U.S. Army Medical Research and Development Command
Fort Detrick, Maryland 21702-5012

DISTRIBUTION STATEMENT: Approved for Public Release;
Distribution Unlimited

The views, opinions and/or findings contained in this report are those of the author(s) and should not be construed as an official Department of the Army position, policy or decision unless so designated by other documentation.

REPORT DOCUMENTATION PAGE

Form Approved
OMB No. 0704-0188

Public reporting burden for this collection of information is estimated to average 1 hour per response, including the time for reviewing instructions, searching existing data sources, gathering and maintaining the data needed, and completing and reviewing this collection of information. Send comments regarding this burden estimate or any other aspect of this collection of information, including suggestions for reducing this burden to Department of Defense, Washington Headquarters Services, Directorate for Information Operations and Reports (0704-0188), 1215 Jefferson Davis Highway, Suite 1204, Arlington, VA 22202-4302. Respondents should be aware that notwithstanding any other provision of law, no person shall be subject to any penalty for failing to comply with a collection of information if it does not display a currently valid OMB control number. **PLEASE DO NOT RETURN YOUR FORM TO THE ABOVE ADDRESS.**

1. REPORT DATE	2. REPORT TYPE	3. DATES COVERED
July 2022	Annual Report	01Jul2021-30Jun2022

4. TITLE AND SUBTITLE

Targeting Ligand-Dependent BMP Signaling in Melanoma

5a. CONTRACT NUMBER

5b. GRANT NUMBER
W81XWH-20-1-0288

5c. PROGRAM ELEMENT NUMBER

6. AUTHOR(S)
Craig J. Ceol, Ph.D.

E-Mail: craig.ceol@umassmed.edu

5d. PROJECT NUMBER

5e. TASK NUMBER

5f. WORK UNIT NUMBER

7. PERFORMING ORGANIZATION NAME(S) AND ADDRESS(ES)

University of Massachusetts Medical School

Worcester, MA

8. PERFORMING ORGANIZATION REPORT NUMBER
DUNS 603847393

9. SPONSORING / MONITORING AGENCY NAME(S) AND ADDRESS(ES)

U.S. Army Medical Research and Development Command
Fort Detrick, Maryland 21702-5012

10. SPONSOR/MONITOR'S ACRONYM(S)

11. SPONSOR/MONITOR'S REPORT NUMBER(S)

12. DISTRIBUTION / AVAILABILITY STATEMENT

Approved for Public Release; Distribution Unlimited

13. SUPPLEMENTARY NOTES

14. ABSTRACT

The studies in this project seek to understand the role of bone morphogenetic protein (BMP) signaling in melanoma and develop a treatment to target ligand-dependent BMP signaling. From previous studies we know that BMP signaling represses MITF expression and upregulates expression of neural crest genes, imparting a less-differentiated neural crest-like identity to melanoma cells. Inhibition of BMP signaling causes melanoma cells to express differentiation genes and die, preventing outgrowth of xenografted tumors. To target BMP signaling, we have created monoclonal antibodies that neutralize the BMP ligand GDF6. The GDF6 gene is copy number amplified in melanoma cells, and elevated expression of GDF6 is associated with a dependence of melanoma cells on BMP activity. Preliminary results suggest anti-GDF6 monoclonal antibodies effectively inhibit BMP signaling, blocking growth and causing death of melanoma cells. We will test if these antibodies shrink xenografted tumors and determine their effects on melanoma cells. We will also determine if the most effective of these antibodies complements existing melanoma therapies in shrinking melanoma xenografts. Additionally, the presence of BMP signaling in rare acral and mucosal melanoma subtypes will be determined, and, should BMP signaling be prevalent, the dependence of these subtypes on GDF6 will be tested in vitro and in xenograft studies. This combination of experiments will determine if the BMP activity that is evident in a majority of melanomas can be targeted as a monotherapy, in combination with existing therapies and as a treatment for rare acral and mucosal melanoma subtypes.

15. SUBJECT TERMS Acral melanoma, BMP, Bone Morphogenetic Protein, GDF6, Melanoma, Mucosal melanoma, Neural crest, Xenograft					
16. SECURITY CLASSIFICATION OF:			17. LIMITATION OF ABSTRACT	18. NUMBER OF PAGES	19a. NAME OF RESPONSIBLE PERSON USAMRDC
a. REPORT Unclassified	b. ABSTRACT Unclassified	c. THIS PAGE Unclassified	Unclassified	95	19b. TELEPHONE NUMBER *(include area code)*

Standard Form 298 (Rev. 8-98)
Prescribed by ANSI Std. Z39.18

TABLE OF CONTENTS

	Page
1. Introduction	1
2. Keywords	1
3. Accomplishments	1
4. Impact	3
5. Changes/Problems	3
6. Products	4
7. Participants & Other Collaborating Organizations	4
8. Special Reporting Requirements	5
9. Appendices	5

INTRODUCTION

The studies in this project seek to understand the role of bone morphogenetic protein (BMP) signaling in melanoma and develop a treatment to target ligand-dependent BMP signaling. From previous studies we know that BMP signaling represses MITF expression and upregulates expression of neural crest genes, imparting a less-differentiated neural crest-like identity to melanoma cells. Inhibition of BMP signaling causes melanoma cells to express differentiation genes and die, preventing outgrowth of xenografted tumors. To target BMP signaling, we have created monoclonal antibodies that neutralize the BMP ligand GDF6. The GDF6 gene is copy number amplified in melanoma cells, and elevated expression of GDF6 is associated with a dependence of melanoma cells on BMP activity. Preliminary results suggest anti-GDF6 monoclonal antibodies effectively inhibit BMP signaling, blocking growth and causing death of melanoma cells. We will test if these antibodies shrink xenografted tumors and determine their effects on melanoma cells. We will also determine if the most effective of these antibodies complements existing melanoma therapies in shrinking melanoma xenografts. Additionally, the presence of BMP signaling in rare acral and mucosal melanoma subtypes will be determined, and, should BMP signaling be prevalent, the dependence of these subtypes on GDF6 will be tested in vitro and in xenograft studies. This combination of experiments will determine if the BMP activity that is evident in a majority of melanomas can be targeted as a monotherapy, in combination with existing therapies and as a treatment for rare acral and mucosal melanoma subtypes.

KEYWORDS

Acral melanoma
BMP
Bone morphogenetic protein
GDF6
Melanoma
Mucosal melanoma
Neural crest
Xenograft

ACCOMPLISHMENTS

• Major goals of the project:

1) Test whether anti-GDF6 antibodies can cause melanoma regression in vivo
    a. ACURO review/approval of IACUC protocol (months 0-3; 100% complete)
    b. IRB approval, HRPO approval (months 0-3; 40% complete)
    c. Produce anti-GDF6 antibody for injection into xenografted mice (months 1-3; 100% complete)
    d. Inject anti-GDF6 antibody into xenografted mice (months 1-6; 50% complete)
    e. In harvested tumors quantify proliferation index, cell death, BMP activity (months 1-6; 50% complete)
2) Determine the ability of anti-GDF6 antibodies to complement existing melanoma therapies
    a. Produce anti-GDF6 antibody for injection into xenografted mice (months 1-6; 100% complete)
    b. Inject anti-GDF6 antibody into xenografted mice in combination with dabrafenib and trametinib (months 6-18; 0% complete)
    c. In harvested tumors quantify proliferation index, cell death, BMP activity (months 12-18; 0% complete)
    d. Inject anti-GDF6 antibody into xenografted mice in combination with anti-PD1 antibody (months 18-36; 0% complete)
    e. In harvested tumors quantify proliferation index, cell death, BMP activity (months 30-36; 0% complete)
3) Assess the extent of GDF6 expression and BMP activity in rare melanoma subtypes
    a. Staining of acral and mucosal melanoma samples with anti-GDF6 and anti-phospho-SMAD1/5/8 antibodies (months 1-18; 0% complete)
    b. Correlative analysis of GDF6 and phospho-SMAD1/5/8 staining with clinical outcome (months 12-18; 0% complete)

4) Determine the sensitivity of acral and mucosal melanomas to GDF6 inhibition
    a. In vitro knockdown of GFD6 in acral and mucosal melanoma cell lines and quantification of cell viability and cell death (months 12-24; 20% complete)
    b. Produce anti-GDF6 antibody for injection into xenografted mice (months 21-27; 50% complete)
    c. Knockdown of GDF6 in acral and mucosal melanomas and xenotransplant into immunocompromised mice (months 24-36; 0% complete)
    d. Inject anti-GDF6 antibody into mice xenografted with acral and mucosal melanomas (months 24-36; 0% complete)
    e. In harvested tumors quantify proliferation index, cell death, BMP activity (months 30-36; 0% complete)

• Progress toward these goals:

1) Test whether anti-GDF6 antibodies can cause melanoma regression in vivo
• In this reporting period, progress has been made in testing the impact of anti-GDF6 antibodies on the growth of tumors in vivo. Previously experiments were done to study anti-GDF6 in vitro. During this period we conducted a longer-term study of the effect of anti-GDF6 antibodies on established tumors. SK-MEL28 cells were injected into the flanks of nude mice and allowed to establish tumors. When tumors reached ~100mm3, animals were treated with anti-GDF6 antibody. Anti-GDF6 antibodies caused rapid regression of tumors, whereas treatment with a control antibody did not cause regression (Figure 1A). We also tested the effect of anti-GDF6 antibodies on the growth of tumors in NSG immunocompromised mice. In these mice we saw little effect of antibody treatment (Figure 1B). Nude and NSG mice differ in their complement of innate immune cells (e.g. natural killer cells are present in nude but not NSG mice), and we suspect that this difference accounts for the different results. Indeed, some therapeutic antibodies (e.g. trastuzumab for breast cancer) kill cells via antibody-dependent cellular cytotoxicity (ADCC), which is dependent on natural killer cells. We are currently preparing experiments that will determine whether anti-GDF6 antibodies act through ADCC. Answering this question is critical to determining the mechanism of action for anti-GDF6 antibodies and has a substantial impact on the design of future experiments investigating anti-GDF6 effects in vivo.

2) Determine the ability of anti-GDF6 antibodies to complement existing melanoma therapies
• We have not begun these studies yet. Given the finding above that we saw little effect of anti-GDF6 antibodies in NSG mice, we are currently determining the most suitable background for these studies.

3) Assess the extent of GDF6 expression and BMP activity in rare melanoma subtypes
• During this reporting period we have obtained IRB approval from the VA Maryland Health Care System for the proposed studies. These studies are meant to assess GDF6 and phosphorylated SMAD1/5/8 expression in acral and mucosal melanoma subtypes, using discarded and deidentified patient tissue from the VA collection accessible to our collaborator Dr. Thomas Hornyak. In addition to IRB approval, Dr. Hornyak's group has performed in silico searches of VA archived tissue and found samples that are suitable for our study. GDF6 is a BMP ligand that triggers BMP signaling pathway activity (Figure 2A), and the antibodies we have generated recognized GDF6 mature ligand and GDF6 proprotein (Figure 2B). We have conducted preliminary stainings of melanoma samples using in-house produced anti-GDF6 antibody (Figure 2C), which show tumor-specificity and strong signal. We have produced sufficient anti-GDF6 antibody to conduct these stainings. The phosphorylated SMAD1/5/8 antibody used is commercially available.

4) Determine the sensitivity of acral and mucosal melanomas to GDF6 inhibition
• We have received acral and mucosal cell lines and are currently optimizing conditions to be used for GDF6 inhibition experiments.

• Opportunities for training and professional development:
The experiments performed to date have afforded professional development opportunities for Revati Darp, a graduate student in the Ceol laboratory. She worked closely with Dr. Ceol to perform antibody dosing and tumor monitoring on xenografted animals.

• Dissemination of results to communities of interest:
Nothing to Report.

• Plan for next reporting period to accomplish these goals:

1) In the next reporting period, we plan to confirm that nude mice are the most the most suitable strain background to test the efficacy of anti-GDF6 antibody.

2) After confirming that the nude mouse background is most suitable, we will perform xenograft experiments to test the effects of anti-GDF6 antibody in combination with small molecule inhibitors of BRAF and MEK.

3) We have begun staining of acral and mucosal melanomas and expect in the next reporting period to complete this subaim. A large collection of acral and mucosal melanoma samples will be stained for GDF6 and phosphorylated SMAD1/5/8. Staining immunointensity and immunopositivity will be scored to obtain quantitative staining measurements. These quantitative measurments will be analyzed with patient outcome data to determine if there is a relationship between GDF6 and BMP pathway activity to various measures of patient outcome.

4) In the next reporting period we anticipate conducting in vitro studies in which GDF6 and BMP signaling are inhibited in acral and mucosal cell lines. Based on these results we expect to begin testing the effects of anti-GDF6 antibodies on the growth of acral and mucosal melanoma xenografted tumors.

IMPACT

• Impact on the development of the principal disciplines of the project:
The principal discipline of this project is cancer biology and, more specifically, targeting bone morphogenetic protein (BMP) signaling as melanoma therapy. The project is the first to explore targeting BMP signaling in melanoma and thus has the potential to have a substantial impact on the discipline. The targeting of BMP signaling is to be accomplished by creating monoclonal antibodies that are directed against the BMP simulators ligand GDF6. Such antibodies have been generated and tested against melanoma cells in culture, and these antibodies can effectively cause the death of cultured melanoma cells. The primary goals of this project are to determine whether these antibodies are effective in shrinking melanoma tumors, are effective in combination with existing melanoma therapies, and are effective against rare acral and mucosal subtypes of melanoma. Thus far our results show that we can produce these antibodies at a large enough scale for our pre-clinical studies and that these antibodies can effectively shrink melanoma tumors in animal models. These studies and additional ones in this project are necessary to show efficacy of these antibodies and provide pre-clinical data prior to testing in humans. Because of the trajectory toward human studies, this project has potential to impact melanoma therapy and patient outcomes.

• Impact on other disciplines:
Nothing to Report.

• Impact on technology transfer:
Nothing to Report.

• Impact on society beyond science and technology:
Nothing to Report.

CHANGES/PROBLEMS

• Changes in approach and reasons for change:
Nothing to Report.

• Actual or anticipated problems or delays and actions or plans to resolve them:
The project has met with delays over this most recent reporting period. Scientifically, our finding that NSG appears to be an unsuitable strain for studies has delayed the beginning of subaim 2. To resolve this delay, we

have conducted additional experiments to assess nude mice as a suitable background. We anticipate being able to use nude mice for our studies and should be able to begin subaim 2 shortly.

• Changes that had a significant impact on expenditures:
The delay in beginning subaim 2 has meant that expenditures anticipated for this subaim have not been spent. In the next reporting period we anticipated using funds to complete this subaim. Also, during this most recent reporting period, the technician in the Ceol laboratory who had been working on this project, Melissa Guerin, left the laboratory to join a private sector biotechnology company. A portion of her salary support has thus been unspent. Assigning new staff to the project will result in the expenditure of this salary support.

• Significant changes in use or care of human subjects, vertebrate animals, biohazards, or select agents:
Nothing to Report.

PRODUCTS

• Publications, conference papers, and presentations:

Publications:

• Frantz, W.T., Ceol, C.J. (2021). Research techniques made simple: zebrafish models for human dematologic disease. *Journal of Investigative Dermatology*, *142*, 499-506.

• Frantz, W.T., Ceol, C.J. (2021). Working together: heterotypic clusters and collective cell migration in melanoma metastasis. *Developmental Cell*, *56*, 2783-4.

• Wilcock, D.J., Badrock, A.P., Owen, R., Guerin, M., Southam, A., Johnston, H., Ogden, S., Fullwood, P., Watson, J., Ferguson, H., Haworth, J., Richardson, D., Dunn, W., Wellbrock, C., Lorigan, P., Ceol, C., Francavilla, C., Smith, M.P., Hurlstone, A. (2022). Oxidative stress from DGAT1 oncoprotein inhibition in melanoma suppresses tumor growth when ROS defenses are breached. *Cell Reports*, *39*, 110995.

• Vittoria, M.A., Kingston, N., Xia, E., Hong, R., Huang, L., McDonald, S., Tilston-Lunel, A., Darp, R., Campbell, J., Lang, D., Xu, X., Ceol, C**.**, Varelas, X. and Ganem, N.J. (2022). Inactivation of the Hippo tumor suppressor pathway promotes melanoma. *Nature Communications*, *13*, 3732.

• Darp, R., Vittoria, M.A., Ganem, N.J. and Ceol, C.J. (2022). Oncogenic BRAF induces whole-genome doubling through suppression of cytokinesis. *Nature Communications*, *13*, 4109.

Presentations:

• Hallmarks of Skin Cancer Conference (Keynote) 2021
German Cancer Research Center (DFKZ), Heidelberg, Germany

• UMass Chan Medical School Clinical and Translational Sciences Symposium 2022
UMass Chan Medical School, Worcester, Massachusetts

• Websites or Internet sites:
Nothing to Report.

• Technologies or techniques:
Nothing to report.

• Inventions, patent applications, or licenses:
Nothing to report.

• Other products:
Nothing to Report.

PARTICIPANTS AND OTHER COLLABORATING ORGANIZATIONS

• Individuals who have worked on this project:
Dr. Craig Ceol

Role: PI, University of Massachusetts Medical School
Researcher ORCID ID: 0000-0002-7188-7580
Months worked: 3
Contribution to project: Dr. Ceol has overseen all aspects of anti-GDF6 antibody testing.
Funding support: no change

Ms. Revati Darp
Role: Graduate Student, University of Massachusetts Medical School
Researcher ID: n/a
Months worked: 3
Contribution to project: Ms. Darp has conducted tests of antibody efficacy in vitro and assisted with in vivo testing of antibodies in xenografted mice.
Funding support: no change

Dr. Yang Wang
Role: co-PI, MassBiologics and University of Massachusetts Medical School
Researcher ID: n/a
Months worked: 0.24
Contribution to project: Dr. Wang has overseen production of anti-GDF6 antibodies.
Funding support: no change

Dr. Monir Ejemel
Role: Postdoctoral Fellow, MassBiologics and University of Massachusetts Medical School
Researcher ID: n/a
Months worked: 2.4
Contribution to project: Dr. Ejemel has conducted production and purification of anti-GDF6 antibodies.
Funding support: no change

• Change in active other support of the PD/PIs or senior/key personnel since last reporting period:
Nothing to Report.

• Other organizations involved as partners:
Collaborating organization Baltimore Research and Education Foundation has received funds to conduct planned studies on acral and mucosal melanomas.

SPECIAL REPORTING REQUIREMENTS
Nothing to Report.

APPENDICES
Please see Figures 1-2 appended in pages 6-7.

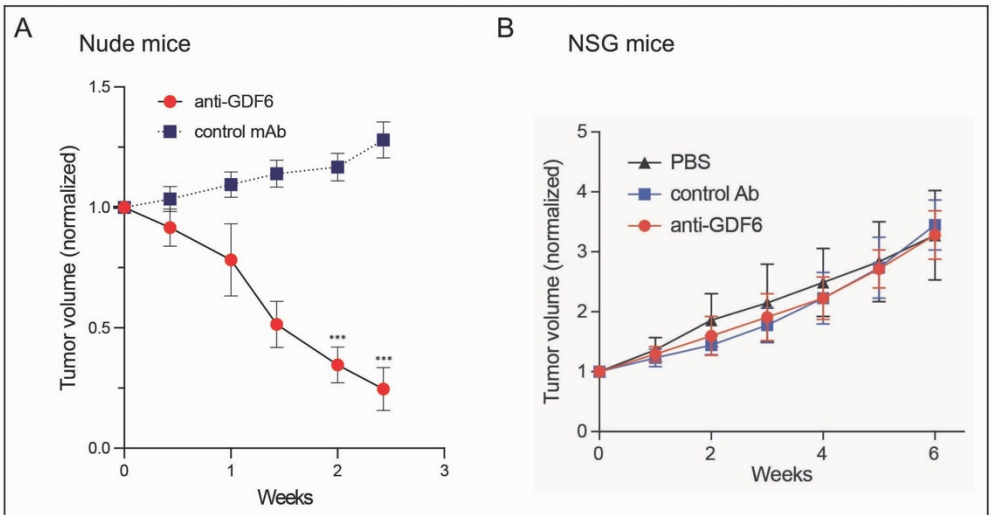


Figure 1: Effects of anti-GDF6 antibody treatment on xenografted tumors
A) Tumor volume measurement of nude mice xenografted with SKMEL28 cells and treated with anti-GDF6#1 or control antibody when tumors reached 100mm3. anti-GDF6#1 treatment caused rapid regression of xenografted tumors. B) Tumor volume measurement of NSG mice xenografted with SKMEL28 cells and treated with anti-GDF6#1 or control antibody or untreated (PBS) when tumors reached 100mm3. Tumor regression upon treatment with anti-GDF6#1 did not occur in the NSG strain background.

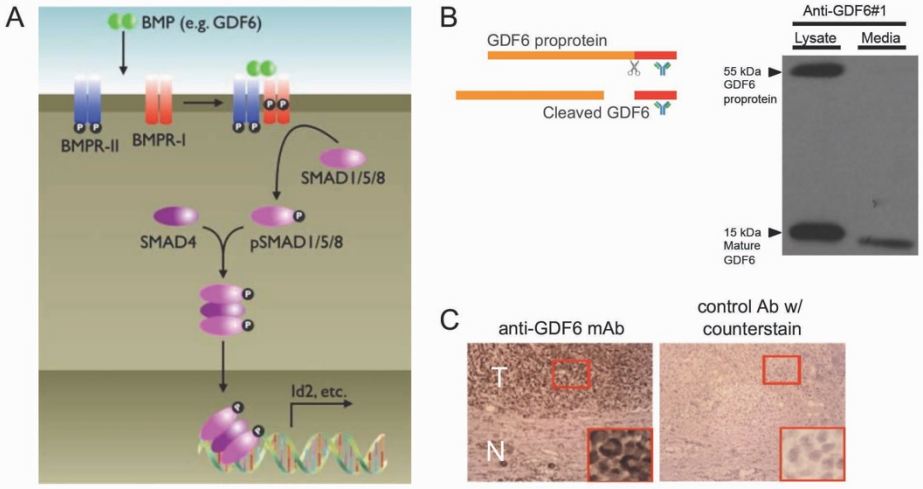


Figure 2: BMP signaling in melanomas.
A) Canonical BMP signaling: ligand binding induces receptor heterotetrameric assembly, leading to phosphorylation of type I receptors and subsequent phosphorylation of downstream SMAD1/5/8 effectors. Phosphorylated SMAD1/5/8 proteins enter and are retained in the nucleus. B) Left, schematic of the GDF6 proprotein and ligand showing the anti-GDF6 antibody recognition site. Right, western blot of A375 melanoma cell lysate and conditioned media using anti-GDF6#1. C) Staining of a primary melanoma with anti-GDF6#1 antibody. GDF6 is predominantly localized to the cytosol.

Research Techniques Made Simple: Zebrafish Models for Human Dermatologic Disease

William Tyler Frantz[1,2] and Craig J. Ceol[1,2]

Skin diseases affect nearly one third of the world's population. Disease types range from oncologic to inflammatory, and outcomes can be as severe as death and disfigurement. Although many skin diseases have been modeled in murine models, the advantages of zebrafish models have led to recent increasing use in modeling human disease. Their rapid development, comparable skin architecture, tractable genetics, unparalleled optical properties, and straightforward drug screens make them an excellent model to study skin disease. In this review, we discuss the attributes of the zebrafish model system as well as current zebrafish models for dermatologic diseases, including melanoma, squamous cell carcinoma, vitiligo, epidermal bullosa, psoriasis, and wounding.

Journal of Investigative Dermatology (2022) **142,** 499–506; doi:10.1016/j.jid.2021.10.016

Introduction

Originally used to study development, over the past two decades, zebrafish have become an important model organism for studying human skin disease. Zebrafish have highly homologous skin architecture (Li et al., 2011). Similar to that in mammals, the zebrafish skin is organized into two layers: an epidermis, made up of multiple layers of keratinocytes (KCs), and dermis, which contains admixed fibroblasts, KCs, pigment cells, and immune cells. These two layers are separated by a basement membrane. These structures develop rapidly, with KCs appearing as early as 1 day after fertilization and an epidermal/dermal boundary by day 6 after fertilization. At approximately 25 days after fertilization, basal *p63*-expressing zebrafish stem cells proliferate, forming a new layer of suprabasal transient amplifying cells (Guzman et al., 2013). Similar to that in human skin, a subset of zebrafish epidermal stem cells engage in asymmetric proliferation and change shape during epidermal thickening (Rangel-Huerta et al., 2021). In the adult zebrafish, this multilayered stratified squamous epithelium is separated from the dermis by the basement membrane zone (Sonawane et al., 2005).

Zebrafish melanocytes, similar to their mammalian counterparts, are neural crest–derived cells responsible for pigment production (Sauka-Spengler and Bronner-Fraser, 2008). In adult zebrafish, melanocytes can be found in two locations: in the epidermal layer found on top of the scales and in highly organized stripes found in the hypodermis (Hirata et al., 2003). Zebrafish have a few other differences in skin architecture. Zebrafish skin does not form a stratum corneum (Le Guellec et al., 2004). As aquatic animals, zebrafish have no need for the water-impermeable barrier functions of the mammalian stratum corneum. Zebrafish also lack hair follicles; instead, zebrafish are covered in rows of overlapping scales, with the base of each serving an analogous function to a hair follicle (Rakers et al., 2010). Sebaceous glands are also absent. Despite these differences, the overall architecture and cellularity of the zebrafish skin are similar to those of mammalian skin and are well-suited to investigating human skin disease.

Annotation of the first zebrafish reference genome revealed that 71.4% of all human protein-coding genes and 82% of disease-causing genes have clear zebrafish orthologs (Howe et al., 2013). These include orthologs for numerous skin genes implicated in human disease, including epidermal markers *BPAG1*, *PLEC1*, and keratin (K) gene *K1* and *K5* and numerous integrins and collagen encoding genes (Li et al., 2011). Immune cell markers are also well-persevered. For example, zebrafish macrophages express an ortholog of *MPEG1*, neutrophils express an ortholog of *LYZ*, and zebrafish T cells express orthologs of *CD4* or *CD8* (Kitaguchi et al., 2009; Martins et al., 2019; Moore et al., 2016). In addition to the conservation of skin cell–specific genes, signaling pathways critical to skin development and function, such as Shh, TP63-associated, and Notch pathways, are well-conserved (Rangel-Huerta et al., 2021).

Although zebrafish were classically used as a forward genetic system through ethylnitrosourea (ENU) mutagenesis, the development of genetic tools such as morpholinos and recent advances in efficient genetic engineering approaches such as CRISPR/Cas9 allow precise manipulation of disease-causing genes and rapid development of novel disease models (Haffter et al., 1996a; Hwang et al., 2013b; Nasevicius and Ekker, 2000). These tools, combined with well-conserved genetics, allow for the straightforward creation of new tissue-specific reporters and disease-modeling mutants.

In addition to their conserved skin architecture and tractable genetics, zebrafish also have desirable optical properties. Zebrafish embryos and larvae are transparent, enabling

[1]*Program in Molecular Medicine, University of Massachusetts Chan Medical School, Worcester, Massachusetts, USA; and* [2]*Department of Molecular, Cellular and Cancer Biology, University of Massachusetts Chan Medical School, Worcester, Massachusetts, USA*

Correspondence: Craig J. Ceol, Program in Molecular Medicine, University of Massachusetts Chan Medical School, 368 Plantation Street, ASC-1041, Worcester, Massachusetts 01605, USA. E-mail: craig.ceol@umassmed.edu

Abbreviations: BCC, basal cell carcinoma; EB, epidermolysis bullosa; ENU, ethylnitrosourea; H_2O_2, hydrogen peroxide; K, keratin; KC, keratinocyte; OSCC, oral squamous cell carcinoma; MMP, matrix metalloprotein; SCC, squamous cell carcinoma; WT, wild-type

© 2021 The Authors. Published by Elsevier, Inc. on behalf of the Society for Investigative Dermatology.

SUMMARY POINTS

Advantages

- Conserved disease-related genetics;
- Conserved epidermal/dermal junction;
- Rapid development and organogenesis;
- Easy breeding with large numbers of offspring;
- Unparalleled optical properties;
- Amenable to high-throughput drug screening

Limitations

- Lack of some properties of mammalian skin structure such as the hair follicle, sebaceous glands, and a stratum corneum;
- Lack of antibodies recognizing zebrafish proteins;
- Unclear cytokine orthologs;
- Multiple orthologs for many mammalian genes

unparalleled visualization of organ development. Although less transparent than embryos, adult zebrafish still exhibit desirable optical properties for visualizing external structures such as the skin. Furthermore, zebrafish's easy breeding and large numbers of embryos, rapid ex utero development, and water-borne drug administration permit high-throughput drug screening.

Current zebrafish disease models

In the last two decades, zebrafish have emerged as an invaluable model for studying human disease. Early forward genetic screens identified large classes of mutants that serve as models for hematopoietic, pigmentation, and other disease types (Haffter et al., 1996a, 1996b). Shortly after, the first cancer models emerged, including models for acute lymphoblastic leukemia and melanoma (Langenau et al., 2003; Patton et al., 2005). In the last 20 years, zebrafish have also been increasingly utilized to model nononcological skin diseases such as psoriasis, vitiligo, epidermal bullosa, and chronic wounding (Table 1).

Oncologic. Melanoma, a lethal malignancy of melanocytes, is responsible for most skin cancer deaths and kills nearly 60,000 patients worldwide each year (Sung et al., 2020). Whereas most cutaneous melanomas are diagnosed and excised at early stages, melanomas that progress to metastatic disease have poor outcomes. New small molecule and immunotherapies have improved patient outcomes, but a substantial fraction of patients still succumb to melanoma, underlining a need for greater insights into melanomagenesis (Larkin et al., 2019). To develop the first zebrafish model of human melanoma, Patton et al. (2005) expressed the human oncogene $BRAF^{V600E}$ in melanocytes in the tumor suppressor *p53* loss-of-function, *p53(lf)*, mutants. These *Tg(mitfa:*$BRAF^{V600E}$*);p53(lf)* zebrafish develop tumors that histopathologically mirror human melanomas. Since this landmark discovery, other human oncogenes, such as $NRAS^{Q61K}$, have been used to engineer zebrafish models for cutaneous melanoma (Dovey et al., 2009). Comparisons between genetic signatures in human melanomas and zebrafish melanoma models have also discovered critical melanoma-modifying genes important for disease progression (Ceol et al., 2011; Venkatesan et al., 2018). These studies and the expansive use of zebrafish to model human melanoma have been extensively reviewed (Frantz and Ceol, 2020; White et al., 2013).

In contrast to melanoma, which has been the subject of extensive zebrafish-modeling studies, there are currently no models of basal cell carcinoma (BCC) and no transgenic models of squamous cell carcinoma (SCC). However, BCCs and SCCs are still the most common malignancies, and zebrafish can contribute to understanding their pathogenesis and treatment. Original efforts to model epidermal neoplasms exposed zebrafish to the mutagenic alkylating agent ENU. Twelve months after exposure, 100% of ENU-treated adult fish developed epidermal papillomas, with histological features consistent with those of epidermal hyperplasia (Beckwith et al., 2000). More recently, zebrafish embryonic xenograft models have been used to dissect the role of metastasis-associated gene expression signatures, such as *AXL* expression, on SCC progression. In 2014, Cichoń et al. (2014) injected *AXL*-knockdown SCC cells into zebrafish embryos and monitored for in vivo tumor formation. Interestingly, cells with *AXL* knockdown failed to form tumors, showing a role for AXL-mediated SCC progression (Cichoń et al., 2014). Similarly, an embryo xenograft model has also been used to model oral SCC (OSCC). To determine whether the overexpression of matrix metalloprotein 9 (MMP9) seen in human OSCCs has mechanistic importance for disease spread, Wen et al. (2020) implanted OSCC cells with short hairpin RNA—mediated *MMP9* knockdown into zebrafish embryos and tracked migration distance. Cells with *MMP9* knockdown migrated less than wild-type (WT) controls, indicative of a role for cell-intrinsic *MMP9* expression in OSCC metastasis.

The embryonic xenograft model has also been used to investigate novel treatments of SCC. In human SCC, relapsed tumors express higher levels of the tyrosine kinase receptor *DDR2* than primary tumors, indicative of a potential role in disease progression. Von Mässenhausen et al. (2016), investigated the role of *DDR2* in SCC disease progression by transplanting DDR2-overexpressing SCC cell lines into zebrafish embryos and monitoring for migration. They observed enhanced migration in *DDR2*-overexpressing SCC lines compared with that in WT SCC cells, suggesting an increased metastatic potential. Interestingly, treatment with the Food and Drug Administration—approved RTK inhibitor dasatinib decreased migration in *DDR2*-overexpressing cells, indicating a potential therapeutic role in treating relapsed *DDR2*-expressing SCCs (von Mässenhausen et al., 2016).

Congenital skin disease. Zebrafish are also a practical platform for studying congenital skin diseases. Zebrafish are particularly well-suited to investigating inherited hypopigmentation and hyperpigmentation disorders. Hypopigmentation diseases, which include albinism, piebaldism, and Waardenburg syndrome, are caused by varying levels of impairment in genes governing melanocyte function. The mechanisms governing melanocyte development are well-conserved in zebrafish, and mutations in orthologs of

pigment production genes display hypopigmentation phenotypes. Waardenburg syndrome, an auditory pigment disorder, is caused by mutations in genes essential for neural crest formation and melanocyte development. In zebrafish, such as in humans, loss of *sox10* or *mitfa* results in pigmentation defects and melanocyte deficiency (Dutton et al., 2001; Lister et al., 1999). The receptor tyrosine kinase *c-KIT*, which is partially lost in piebaldism, is also conserved in zebrafish (Parichy et al., 1999). Loss of the ortholog *kita* results in defects of melanocyte survival and migration, the hypothesized causes of the patterning seen in human disease (Rawls and Johnson, 2003). Albinism, typified by hair and skin lacking pigmentation, is caused by mutations in pigment synthesis and trafficking genes such as *TYR* and the aptly named *OCA2* (Braasch et al., 2007; Haffter et al., 1996a). Mutations in zebrafish orthologs of these genes lead to depigmented zebrafish, mirroring the genetic/phenotypic relationship of human disease.

Zebrafish have also been used to model congenital hyperpigmentation diseases and elicit mechanisms underpinning their biology. In addition to the nevus-like hyperpigmentations seen in Patton et al. (2005) seminal work, numerous other studies have used zebrafish to study hyperpigmentation disorders. In 2016, Thomas et al. (2016) found that mosaic expression of ocular melanoma drivers *GNAQ* and *GNA11* drives the congenital pigmentation found in phakomatosis pigmentovascularis.

Zebrafish models have also contributed to understanding two other MAPK-signaling related diseases: the RASopathies Noonan syndrome and Noonan syndrome with multiple letingies (formerly LEOPARD syndrome). In 2011, Runtuwene et al. (2011) sequenced a patient with Noonan syndrome features and identified a novel potential activating mutation in *NRAS*. Expression of this mutant *NRAS* in zebrafish embryos led to craniofacial features phenocopying those found in Noonan syndrome, supporting the role of activating *NRAS* mutations in disease pathogenesis (Runtuwene et al., 2011). Similarly, Stewart et al. (2010) compared cohorts of patients with Noonan and LEOPARD syndrome and identified *PTPN11*, which encodes an SHP2 tyrosine phosphatase ortholog that acts upstream of *NRAS*, as being differentially activated, suggestive of a possible causative role in LEOPARD pathogenesis. When *ptpn11* was inhibited with morpholinos, zebrafish exhibited phenotypes supporting a role for SHP2 in regulating the numerous hyperpigmented café-au-lait spots seen on patients with LEOPARD syndrome (Stewart et al., 2010).

The advantages of these conserved genetics in modeling human disease extends beyond inherited pigment disorders and to other skin disorders. Epidermolysis bullosa (EB) is a group of rare inherited skin disorders characterized by fragile blistering skin. These blisters are caused by deficiencies in structural proteins that make up dermoepidermal complexes and govern epidermal adhesion. Owing to their conserved epidermal and dermal structures, zebrafish are an appropriate model for EB. The first zebrafish model for basal epidermal structural weaknesses was the *pen/lgl2* mutant (Sonawane et al., 2005). These loss-of-function mutants fail to form basal hemidesmosomes, resulting in skin detachment from the basement membrane and epidermal hyperproliferation, reminiscent of human EB (Sonawane et al., 2009, 2005). Although the epidermal hyperproliferation aspect of this mutant has been used to model psoriasis, the destruction of the epidermal/dermal adhesion makes this model most analogous to EB. Subsequent studies have utilized reverse genetics to target the genes implicated in human EB. In 2010, Kim et al. (2010) knocked down an ortholog for the gene encoding for the hemidesmosome protein type XVII collagen, *col17a1a*. The knockdown led to perturbations in the basement membrane zone and a blistering phenotype, both characteristics of human EB (Kim et al., 2010).

Many other hemidesmosome and basement membrane proteins implicated in EB are conserved and expressed in the zebrafish skin, such as the integrin *itga6*, yet the role of these proteins in EB has yet to be studied in zebrafish. With a firm beginning to model EB in zebrafish, future studies can combine new genetic knockout models with small-molecule epistatic experiments to elucidate the mechanisms of EB pathogenesis.

Immune-mediated and inflammatory disease. Zebrafish have also been used to model inflammatory diseases. Vitiligo, a disease characterized by autoimmune-mediated destruction of the epidermal melanocytes, has been the subject of recent modeling attempts in zebrafish. In 2018, Zhou et al. (2018) investigated the role of stress-induced *IL17* and *IL1β* expression in precipitating the melanocyte destruction that occurs in vitiligo. IL-17 treatment of developing zebrafish larvae resulted in mitochondrial dysfunction and inhibition of melanogenesis, presumptively through KC-derived *il1b* expression (Zhou et al., 2018). Another study developed a knockout for the gamma secretase complex subunit *nicastrin* (Hsu et al., 2020; Shah et al., 2005). It has been established that gamma secretase facilitates NOTCH signaling, and NOTCH signaling is required for proper pigmentation (Osawa and Fisher, 2008). Similar to that in human vitiligo, these *nicastrin*-deficient animals exhibit skin inflammation. However, unlike in vitiligo where the immune cells likely cause melanocyte death, in these mutants, *nicastrin* deficiency leads to necrotic melanocytes, which likely recruit immune cells (Hsu et al., 2020). Although these studies provide interesting insights into the role of KCs, cytokines, immune cells, and melanocytes in skin inflammation, a vitiligo model comparable with murine models remains elusive (Harris et al., 2012).

Similar to vitiligo, psoriasis is a complex immune-mediated disease. Instead of melanocyte destruction, psoriasis is characterized by an overproliferation of KCs. KC proliferation results in scaling erythematous plaques and occurs in roughly 3% of people worldwide (Lebwohl, 2003). In 2008, Webb et al. (2008) established one of the first zebrafish psoriasis models when they described *atp1b1a* mutants, which were obtained from an ethylmethanesulfonate screen. These mutants, with a loss of *atp1b1a* function, display widespread overproliferation of the epidermis and a defect in KC differentiation, resulting in aggregates of epidermal cells, all key hallmarks of human psoriasis (Hatzold et al., 2016; Webb et al., 2008). Other studies have sought to model the immunologic component to psoriatic disease. A series of studies have developed models where the loss of *spint1a*, also known as *hai1a*, results in neutrophil infiltration of the skin and loss of KC−KC contact (Carney et al., 2007; Mathias et al., 2007). The neutrophil infiltration causes chronic inflammation and

Table 1. Major Models of Human Dermatologic Disease in Zebrafish

Category	Disease	Model	Notable Features	Citation
Oncologic	Melanoma	*mitfa:BRAF^{V600E};p53(lf)*	Invasive melanomas	(Patton et al., 2005)
	Melanoma	*mitfa:NRAS^{Q61K};p53(lf)*	Invasive melanomas, rapid onset	(Dovey et al., 2009)
	Squamous cell carcinoma	ENU mutagenesis	Epidermal papillomas with hyperproliferation	(Beckwith et al., 2000)
Congenital	Albinism	*tyr(lf)* *oca2(lf)*	Pigmentless melanocytes	(Braasch et al., 2007; Haffter et al., 1996b)
	Waardenburg syndrome	*mitfa(lf)* *sox10(lf)*	No melanocytes	(Dutton et al., 2001; Lister et al., 1999)
	Piebaldism	*kita(lf)*	Impaired melanocyte function and number	(Parichy et al., 1999)
	Noonan syndrome	Mosaic NRAS^{I24N} NRAS^{G60E}	Developmental craniofacial defects	(Runtuwene et al., 2011)
	LEOPARD syndrome	Mosaic *shp2^{A663T}*	Hyperpigmentation	(Stewart et al., 2010)
	Phakomatosis pigmentovascularis	Mosaic *GNA11^{R183C}* *GNA11^{Q209L}*	Dermal melanocytosis	(Thomas et al., 2016)
	Epidermolysis bullosa	*penner/lgl2(lf)*	Hemidesmosome breakdown, blistering, and overproliferation	(Sonawane et al., 2005)
	Epidermolysis bullosa	*col17a1a* knockdown	Blistering	(Kim et al., 2010)
Inflammatory	Psoriasis	*m14*	Overproliferation of keratinocytes leading to aggregates	(Webb et al., 2008)
	Psoriasis	*spint1a(lf)*	Skin inflammation and overproliferation of keratinocytes	(Carney et al., 2007; Mathias et al., 2007)
	Vitiligo	*nicastrin(lf)*	Skin inflammation and hypopigmentation	(Hsu et al., 2020)
Wounding	Wounding and regeneration	HyPer	ROS detection after tail fin amputation	(Niethammer et al., 2009)
	Wounding and regeneration	Skinbow	Multicolor *CreER* labeling of keratinocytes	(Chen et al., 2016)
	Wounding and regeneration		Laser and mechanical destruction of zebrafish skin	(Richardson et al., 2016, 2013)

eventual KC proliferation, both characteristics of human psoriasis (Carney et al., 2007; Mathias et al., 2007). These studies establish the models for understanding and visualizing proinflammatory and proproliferative events in real time, which will be invaluable for a better understanding of the pathogenesis of human psoriasis.

Wound repair. Wound repair is critical to recovery from wounds induced by trauma, diabetes, infection, and numerous other diseases. Repair requires complex cell–cell signaling events to restore proper tissue function and homeostasis. A rapid cascade of injury detection, wound closure, acute scarring, and subacute wound healing occurs in a finely orchestrated fashion. These processes require coordination among KCs, fibroblasts, and resident immune cells. Zebrafish are a highly regenerative species, capable of regenerating their fins, melanocytes, skin, axons, and even hearts (Gemberling et al., 2013; Iyengar et al., 2015; Richardson et al., 2013). Owing to their regenerative capacity, optical transparency, and conserved skin architecture, zebrafish models have yielded unique insights into the mechanisms governing these processes.

The first zebrafish wounding models utilized caudal fin amputation, where the distal two third of the fin is clipped and regenerates over the following weeks. In 2009, Niethammer et al. (2009) utilized a genetically encoded radiometric sensor for hydrogen peroxide (H_2O_2) to visualize dynamic ROS gradients created after fin amputation. They found that a Nox/Duox-mediated burst of H_2O_2 production was required for leukocyte recruitment to the wound site (Niethammer et al., 2009). Additional studies confirmed that ROS production was critical for compensatory proliferation and proper fin regeneration (Gauron et al., 2013). Similar studies have elucidated the roles of another innate immune cell, the macrophage. In 2014, Petrie et al. (2014) found that macrophages are recruited to the wound site, and knockout of the macrophage lineage through inducible macrophage-specific cell killing resulted in impaired wound healing and tail fin regeneration. Tetracycline inducible tools (TetON) have also been adapted to study zebrafish tailfin regeneration. In 2014, Wehner et al. (2014) used a TetON system to show that WNT signaling is critical to regeneration.

Recent studies have also sought to expand the modeling of skin wounding and healing beyond the tail fin amputation

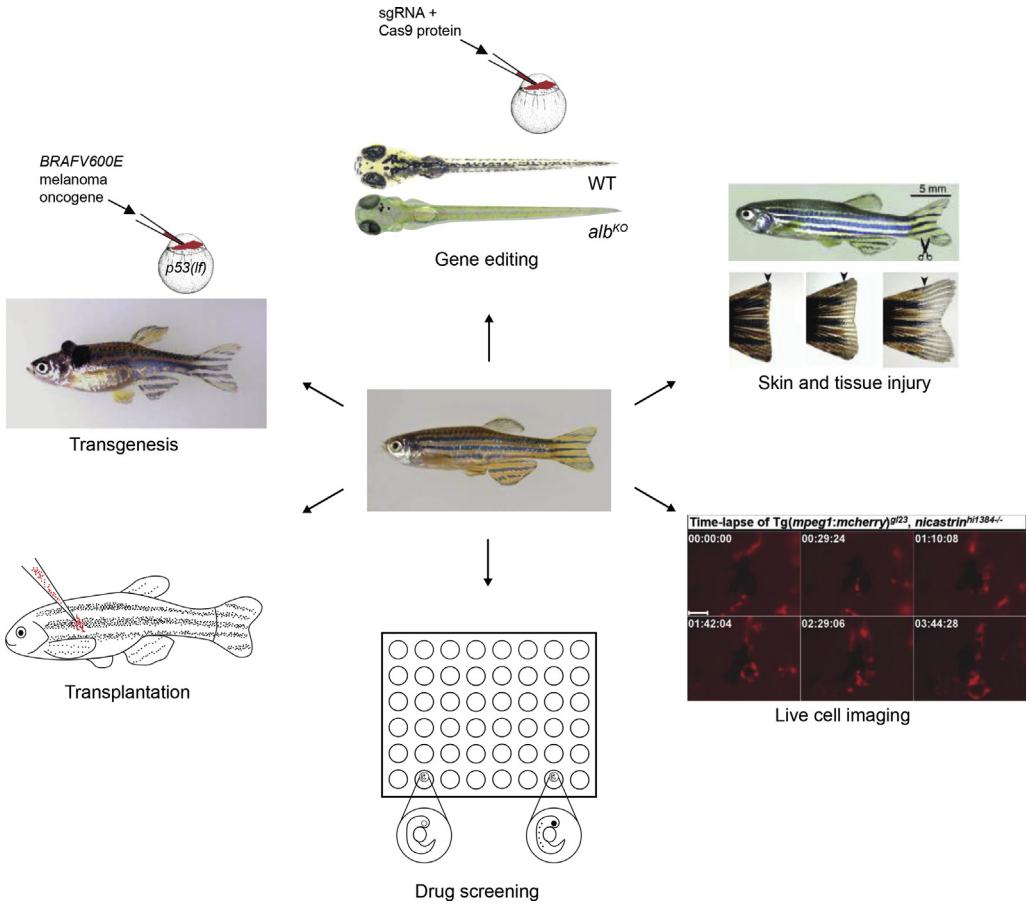


Figure 1. A selection of techniques used in zebrafish to investigate dermatologic processes and pathologies. Clockwise from top left. Transgenesis: Injection of *BRAFV600E* into a *p53(lf)*-mutant embryo causes melanoma (Patton et al., 2005). Gene editing: Knockout of the *albino* locus with CRISPR–Cas9 produces hypopigmented mutants (Irion et al., 2014). Skin and tissue injury: Zebrafish caudal fins regenerate after amputation, allowing insights into skin and tissue regeneration (Grotek et al., 2013). Live-cell imaging: Tracking of fluorescently labeled macrophages during melanocyte death in vivo allows for insight into inflammatory and immune processes (Hsu et al., 2020). Drug screening: Screening of zebrafish embryos developmental phenotypes for potential therapeutic small molecules (Peterson et al., 2000). Transplantation: Transplantation of fluorescently tagged melanoma cells into adult zebrafish to assay for metastasis (Yan et al., 2019). KO, knockout; sgRNA, single guide RNA; WT, wild-type.

model. In 2013, Richardson et al. (2013) developed the first dermal regeneration model when they created full-thickness wounds with a dermatology laser. They later expanded on this model by utilizing depilation of the zebrafish scales to induce partial-thickness wounds of the zebrafish skin (Richardson et al., 2016). In these studies, Richardson et al. (2013) found that zebrafish engage in re-epithelization of the wound without scar formation or a lag phase. Furthermore, the surrounding KCs stretch and migrate to seal the wound, before engaging in proliferation to reconstitute the epithelial sheet. Further investigation by Morris et al. (2018) developed a GFP-tagged collagen I fusion line to reveal the role of collagen deposition during wound healing. Chen et al. (2016) engineered a *CreER*-based multicolor-labeling Skinbow system to track individual epithelial cells during regeneration. This powerful system makes intravital imaging of individual migrating and proliferating KCs possible during regeneration, yielding unparalleled resolution to the skin wounding and regenerative process.

Inflammatory wound responses are also important to understanding the interplay between melanocytes, melanoma, and immune cells. In 2010, Feng et al. (2010) showed that H_2O_2 mediates leukocyte recruitment to transformed oncogenic cells. Further investigation of immune recruitment with transgenic collagen reporter zebrafish revealed that leukocytes migrate through the basement membrane to early melanomas (Van Den Berg et al., 2019). Immune cell–mediated inflammation is also capable of recruiting untransformed melanocytes to sites of tissue damage, resulting in hyperpigmentation of healing wounds, reinforcing the importance of inflammation in immune cell–melanocyte interactions (Lévesque et al., 2013).

Expanded models and improvements on the horizon

Further understanding of how the immune system functions in the skin will yield crucial insights into the pathogenesis and treatment of diverse types of skin disease. Much as in human skin, the zebrafish skin contains KCs, fibroblasts, resident immune cells, melanocytes, vasculature, and adipocytes. Human skin disease involves any number of these cells, and zebrafish offer an opportunity to utilize in vivo imaging to understand complex cell type–specific contributions to the pathogenesis and treatment of these diseases. In oncologic disease, inflammatory disease, and wound recovery, the immune system plays a critical role in disease progression, modulation, and recovery. Zebrafish have an innate immune system with macrophages, neutrophils, eosinophils, and mast cells. They also have an adaptive immune system with B cells, T cells, and regulatory T cells (Martins et al., 2019). However, it is not yet clear whether all of the immune cell types found in humans have clear orthologs in zebrafish and vice versa. Deeper knowledge of the similarities and differences between the human and zebrafish immune systems will enable apt comparisons and invaluable insights into the pathogenesis of human diseases.

Xenografts and drug screens. Zebrafish xenografts are a key tool in understanding skin cancer disease progression and treatment (Figure 1) (Cichoń et al., 2014; Haldi et al., 2006; Lee et al., 2005; Stoletov et al., 2007; Topczewska et al., 2006; von Mässenhausen et al., 2016). Their transparency, available transgenic reporters, and the absence of an adaptive immune system make zebrafish embryos a convenient system for performing xenografts (Lieschke and Trede, 2009). Furthermore, their small size, high fecundity, and high fertility facilitate high-throughput drug screening (Precazzini et al., 2020). In addition to their utility in xenograft drug screens, drug screens on zebrafish larvae (Figure 1) with cell-specific reporters have been used to discover novel functions for oncogenes such as *PRL3* or identify small-molecule regulators of the neural crest such as capheic acid phenethyl ester (Ciarlo et al., 2017; Johansson et al., 2020).

New adult zebrafish xenograft models have been developed to allow long-term engraftment and study of tumor biology in a stable adult milieu (Yan et al., 2019). These tools allow for creating new models for rare subtypes of melanoma and testing novel therapeutics in an expedited fashion. These screens can be integrated with murine studies to further elucidate the conserved mechanisms of disease and therapy (Patton et al., 2021). Together, these models present a comprehensive arsenal for using zebrafish to understand the mechanisms governing the initiation, progression, and treatment of skin cancer.

Efficient genetic tools for the generation of new models. Although zebrafish have been utilized as a powerful model for forward genetic screens, recent development of efficient genetic editing techniques in the zebrafish has enabled easier loss-of-function studies (Figure 1). The CRISPR–Cas9 system efficiently creates somatic and germline mutant zebrafish (Hwang et al., 2013a, 2013b). These tools have since been applied to create novel disease models. In 2015, Ablain et al. (2015) utilized CAS9 expressed behind a cell-specific promoter to show the ability to disrupt cell-specific gene expression in zebrafish using CRISPR–Cas9. These tools have recently been utilized to elucidate the novel roles for *HEXIM1* and *SPRED1* as modulators of melanoma (Ablain et al., 2018; Tan et al., 2016). Application of these new reverse genetic tools to generate models for other skin diseases such as SCC, EB, vitiligo, and psoriasis will create opportunities to better understand their pathogenesis.

Where do we go from here?

The recent expansion of sequencing capacity and adjunct modalities such as chromatin profiling and single-cell sequencing enables previously impractical dissection of tissue heterogeneity and signaling mechanisms during homeostasis, regeneration, and disease. Leveraging insights garnered using these technologies into the similarities and differences between zebrafish and human skin biology will enhance the utility of further zebrafish models for human skin disease. Much of the expansive technique toolbox for zebrafish has been built and tested in developmental and oncologic models, leaving great room for growth in other skin disease models. The application of these tools will lead to deeper understandings of cell–cell interactions and signaling pathways relevant to skin disease. In addition, efficient genetic engineering tools will undoubtedly be used to generate new disease models that will prove invaluable in understanding skin pathologies. Similarly, these biological insights and tools can be combined with zebrafish's high-throughput screening attributes to enable the discovery and evaluation of novel therapeutics for human skin disease.

MULTIPLE CHOICE QUESTIONS

1. **Zebrafish were classically used to model which of the following:**
   - A. Cancer progression
   - B. Inflammatory disorders
   - C. Inherited hypopigmentation disorders
   - D. Embryonic development
2. **Zebrafish are lacking a clear analog of which layer of the human skin**
   - A. Dermis
   - B. Basement membrane
   - C. Stratum corneum
   - D. Hypodermis
3. **Zebrafish have been used to model the following skin diseases EXCEPT for:**
   - A. Melanoma
   - B. Basal cell carcinoma
   - C. Epidermolysis bullosa
   - D. Psoriasis
4. **Which of the following is available for modeling cancer in zebrafish?**
   - A. Genetic mutations in tumor suppressor genes
   - B. Transgenic expression of human oncogenes
   - C. Xenografts of tumor cells
   - D. All of the above
5. **Regeneration studies in zebrafish have used the following tools to wound skin EXCEPT for:**
   - A. Chemical burns
   - B. Caudal fin amputation
   - C. Scale depilation
   - D. Dermatology lasers

Conclusion

Although in vitro experiments and murine models have produced critical insights into the pathogenesis of and development of treatments for skin diseases, there remain significant gaps in our understanding of many of these diseases. The use of zebrafish models for human skin disease has already yielded promising results, and the evolution of new genetic tools will increase the number and quality of available models, presenting greater opportunities to model human skin disease and develop future therapeutics.

ORCIDs

William Tyler Frantz: http://orcid.org/0000-0003-1207-9652
Craig J. Ceol: http://orcid.org/0000-0002-7188-7580

CONFLICT OF INTEREST

The authors state no conflict of interest.

ACKNOWLEDGMENTS

This work was supported by grants from the National Cancer Institute (T32 CA130807) to W.T.F. and US Department of Defense (W81XWH2010288) to C.J.C.

SUPPLEMENTARY MATERIAL

Supplementary material is linked to this paper. Teaching slides are available as supplementary material.

REFERENCES

Ablain J, Durand EM, Yang S, Zhou Y, Zon LI. A CRISPR/Cas9 vector system for tissue-specific gene disruption in zebrafish. Dev Cell 2015;32:756–64.

Ablain J, Xu M, Rothschild H, Jordan RC, Mito JK, Daniels BH, et al. Human tumor genomics and zebrafish modeling identify *SPRED1* loss as a driver of mucosal melanoma. Science 2018;362:1055–60.

Becerra J, Montes GS, Bexiga SR, Junqueira LC. Structure of the tail fin in teleosts. Cell Tissue Res 1983;230:127–37.

Beckwith LG, Moore JL, Tsao-Wu GS, Harshbarger JC, Cheng KC. Ethylnitrosourea induces neoplasia in zebrafish (Danio rerio). Lab Invest 2000;80:379–85.

Berghmans S, Murphey RD, Wienholds E, Neuberg D, Kutok JL, Fletcher CD, et al. tp53 mutant zebrafish develop malignant peripheral nerve sheath tumors. Proc Natl Acad Sci USA 2005;102:407–12.

Braasch I, Schartl M, Volff JN. Evolution of pigment synthesis pathways by gene and genome duplication in fish. BMC Evol Biol 2007;7:74.

Carney TJ, von der Hardt S, Sonntag C, Amsterdam A, Topczewski J, Hopkins N, et al. Inactivation of serine protease Matriptase1a by its inhibitor Hai1 is required for epithelial integrity of the zebrafish epidermis. Development 2007;134:3461–71.

Ceol CJ, Houvras Y, Jane-Valbuena J, Bilodeau S, Orlando DA, Battisti V, et al. The histone methyltransferase SETDB1 is recurrently amplified in melanoma and accelerates its onset. Nature 2011;471:513–7.

Chen CH, Puliafito A, Cox BD, Primo L, Fang Y, Di Talia S, et al. Multicolor cell barcoding technology for long-term surveillance of epithelial regeneration in zebrafish. Dev Cell 2016;36:668–80.

Ciarlo C, Kaufman CK, Kinikoglu B, Michael J, Yang S, D Amato C, et al. A chemical screen in zebrafish embryonic cells establishes that Akt activation is required for neural crest development. Elife 2017;6:e29145.

Cichoń MA, Szentpetery Z, Caley MP, Papadakis ES, Mackenzie IC, Brennan CH, et al. The receptor tyrosine kinase Axl regulates cell-cell adhesion and stemness in cutaneous squamous cell carcinoma. Oncogene 2014;33:4185–92.

Dovey M, White RM, Zon LI. Oncogenic NRAS cooperates with p53 loss to generate melanoma in zebrafish. Zebrafish 2009;6:397–404.

Dutton KA, Pauliny A, Lopes SS, Elworthy S, Carney TJ, Rauch J, et al. Zebrafish colourless encodes sox10 and specifies non-ectomesenchymal neural crest fates. Development 2001;128:4113–25.

Feng Y, Santoriello C, Mione M, Hurlstone A, Martin P. Live imaging of innate immune cell sensing of transformed cells in zebrafish larvae: parallels between tumor initiation and wound inflammation [published correction appears in PLoS Biol 2016;14:e1002377]. PLoS Biol 2010;8,e1000562.

Frantz WT, Ceol CJ. From tank to treatment: modeling melanoma in zebrafish. Cells 2020;9:1289.

Gauron C, Rampon C, Bouzaffour M, Ipendey E, Teillon J, Volovitch M, et al. Sustained production of ROS triggers compensatory proliferation and is required for regeneration to proceed. Sci Rep 2013;3:2084.

Gemberling M, Bailey TJ, Hyde DR, Poss KD. The zebrafish as a model for complex tissue regeneration. Trends Genet 2013;29:611–20.

Grotek B, Wehner D, Weidinger G. Notch signaling coordinates cellular proliferation with differentiation during zebrafish fin regeneration. Development 2013;140:1412–23.

Guzman A, Ramos-Balderas JL, Carrillo-Rosas S, Maldonado E. A stem cell proliferation burst forms new layers of P63 expressing suprabasal cells during zebrafish postembryonic epidermal development. Biol Open 2013;2:1179–86.

Haffter P, Granato M, Brand M, Mullins MC, Hammerschmidt M, Kane DA, et al. The identification of genes with unique and essential functions in the development of the zebrafish, Danio rerio. Development 1996a;123:1–36.

Haffter P, Odenthal J, Mullins MC, Lin S, Farrell MJ, Vogelsang E, et al. Mutations affecting pigmentation and shape of the adult zebrafish. Dev Genes Evol 1996b;206:260–76.

Haldi M, Ton C, Seng WL, McGrath P. Human melanoma cells transplanted into zebrafish proliferate, migrate, produce melanin, form masses and stimulate angiogenesis in zebrafish. Angiogenesis 2006;9:139–51.

Harris JE, Harris TH, Weninger W, Wherry EJ, Hunter CA, Turka LA. A mouse model of vitiligo with focused epidermal depigmentation requires IFN-γ for autoreactive $CD8^+$ T-cell accumulation in the skin. J Invest Dermatol 2012;132:1869–76.

Hatzold J, Beleggia F, Herzig H, Altmüller J, Nürnberg P, Bloch W, et al. Tumor suppression in basal keratinocytes via dual non-cell-autonomous functions of a Na,K-ATPase beta subunit. Elife 2016;5:e14277.

Hirata M, Nakamura K, Kanemaru T, Shibata Y, Kondo S. Pigment cell organization in the hypodermis of zebrafish. Dev Dyn 2003;227:497–503.

Howe K, Clark MD, Torroja CF, Torrance J, Berthelot C, Muffato M, et al. The zebrafish reference genome sequence and its relationship to the human genome [published correction appears in Nature 2014;505:248]. Nature 2013;496:498–503.

Hsu CH, Liou GG, Jiang YJ. Nicastrin deficiency induces tyrosinase-dependent depigmentation and skin inflammation. J Invest Dermatol 2020;140:404–414.e13.

Hwang WY, Fu Y, Reyon D, Maeder ML, Kaini P, Sander JD, et al. Heritable and precise zebrafish genome editing using a CRISPR-Cas system. PLoS One 2013a;8:e68708.

Hwang WY, Fu Y, Reyon D, Maeder ML, Tsai SQ, Sander JD, et al. Efficient genome editing in zebrafish using a CRISPR-Cas system. Nat Biotechnol 2013b;31:227–9.

Irion U, Krauss J, Nüsslein-Volhard C. Precise and efficient genome editing in zebrafish using the CRISPR/Cas9 system. Development 2014;141:4827–30.

Iyengar S, Kasheta M, Ceol CJ. Poised regeneration of zebrafish melanocytes involves direct differentiation and concurrent replenishment of tissue-resident progenitor cells. Dev Cell 2015;33:631–43.

Johansson JA, Marie KL, Lu Y, Brombin A, Santoriello C, Zeng Z, et al. PRL3-DDX21 transcriptional control of endolysosomal genes restricts melanocyte stem cell differentiation. Dev Cell 2020;54:317–332.e9.

Kim SH, Choi HY, So JH, Kim CH, Ho SY, Frank M, et al. Zebrafish type XVII collagen: gene structures, expression profiles, and morpholino "knockdown" phenotypes. Matrix Biol 2010;29:629–37.

Kitaguchi T, Kawakami K, Kawahara A. Transcriptional regulation of a myeloid-lineage specific gene lysozyme C during zebrafish myelopoiesis. Mech Dev 2009;126:314–23.

Langenau DM, Traver D, Ferrando AA, Kutok JL, Aster JC, Kanki JP, et al. Myc-induced T cell leukemia in transgenic zebrafish. Science 2003;299:887–90.

Larkin J, Chiarion-Sileni V, Gonzalez R, Grob JJ, Rutkowski P, Lao CD, et al. Five-year survival with combined nivolumab and ipilimumab in advanced melanoma. N Engl J Med 2019;381:1535–46.

Le Guellec D, Morvan-Dubois G, Sire JY. Skin development in bony fish with particular emphasis on collagen deposition in the dermis of the zebrafish (Danio rerio). Int J Dev Biol 2004;48:217–31.

Lebwohl M. Psoriasis. Lancet 2003;361:1197–204.

Lee LM, Seftor EA, Bonde G, Cornell RA, Hendrix MJ. The fate of human malignant melanoma cells transplanted into zebrafish embryos: assessment of migration and cell division in the absence of tumor formation. Dev Dyn 2005;233:1560–70.

Lévesque M, Feng Y, Jones RA, Martin P. Inflammation drives wound hyperpigmentation in zebrafish by recruiting pigment cells to sites of tissue damage. Dis Model Mech 2013;6:508–15.

Li Q, Frank M, Thisse CI, Thisse BV, Uitto J. Zebrafish: a model system to study heritable skin diseases. J Invest Dermatol 2011;131:565–71.

Lieschke GJ, Trede NS. Fish immunology. Curr Biol 2009;19:R678–82.

Lister JA, Robertson CP, Lepage T, Johnson SL, Raible DW. nacre encodes a zebrafish microphthalmia-related protein that regulates neural-crest-derived pigment cell fate. Development 1999;126:3757–67.

Martins RR, Ellis PS, MacDonald RB, Richardson RJ, Henriques CM. Resident immunity in tissue repair and maintenance: the zebrafish model coming of age. Front Cell Dev Biol 2019;7:12.

Mathias JR, Dodd ME, Walters KB, Rhodes J, Kanki JP, Look AT, et al. Live imaging of chronic inflammation caused by mutation of zebrafish Hai1. J Cell Sci 2007;120:3372–83.

Moore FE, Garcia EG, Lobbardi R, Jain E, Tang Q, Moore JC, et al. Single-cell transcriptional analysis of normal, aberrant, and malignant hematopoiesis in zebrafish. J Exp Med 2016;213:979–92.

Morris JL, Cross SJ, Lu Y, Kadler KE, Lu Y, Dallas SL, et al. Live imaging of collagen deposition during skin development and repair in a collagen I - GFP fusion transgenic zebrafish line. Dev Biol 2018;441:4–11.

Nasevicius A, Ekker SC. Effective targeted gene 'knockdown' in zebrafish. Nat Genet 2000;26:216–20.

Niethammer P, Grabher C, Look AT, Mitchison TJ. A tissue-scale gradient of hydrogen peroxide mediates rapid wound detection in zebrafish. Nature 2009;459:996–9.

Osawa M, Fisher DE. Notch and melanocytes: diverse outcomes from a single signal. J Invest Dermatol 2008;128:2571–4.

Parichy DM, Rawls JF, Pratt SJ, Whitfield TT, Johnson SL. Zebrafish sparse corresponds to an orthologue of c-kit and is required for the morphogenesis of a subpopulation of melanocytes, but is not essential for hematopoiesis or primordial germ cell development. Development 1999;126:3425–36.

Patton EE, Mueller KL, Adams DJ, Anandasabapathy N, Aplin AE, Bertolotto C, et al. Melanoma models for the next generation of therapies. Cancer Cell 2021;39:610–31.

Patton EE, Widlund HR, Kutok JL, Kopani KR, Amatruda JF, Murphey RD, et al. BRAF mutations are sufficient to promote nevi formation and cooperate with p53 in the genesis of melanoma. Curr Biol 2005;15:249–54.

Peterson RT, Link BA, Dowling JE, Schreiber SL. Small molecule developmental screens reveal the logic and timing of vertebrate development. Proc Natl Acad Sci USA 2000;97:12965–9.

Petrie TA, Strand NS, Yang CT, Rabinowitz JS, Moon RT. Macrophages modulate adult zebrafish tail fin regeneration [published correction appears in Development 2015;142:406]. Development 2014;141:2581–91.

Precazzini F, Pancher M, Gatto P, Tushe A, Adami V, Anelli V, et al. Automated in vivo screen in zebrafish identifies clotrimazole as targeting a metabolic vulnerability in a melanoma model. Dev Biol 2020;457:215–25.

Rakers S, Gebert M, Uppalapati S, Meyer W, Maderson P, Sell AF, et al. 'Fish matters': the relevance of fish skin biology to investigative dermatology. Exp Dermatol 2010;19:313–24.

Rangel-Huerta E, Guzman A, Maldonado E. The dynamics of epidermal stratification during post-larval development in zebrafish. Dev Dyn 2021;250:175–90.

Rawls J, Johnson SL. Temporal and molecular separation of the kit receptor tyrosine kinase's roles in zebrafish melanocyte migration and survival. Dev Biol 2003;262:152–61.

Richardson R, Metzger M, Knyphausen P, Ramezani T, Slanchev K, Kraus C, et al. Re-epithelialization of cutaneous wounds in adult zebrafish combines mechanisms of wound closure in embryonic and adult mammals. Development 2016;143:2077–88.

Richardson R, Slanchev K, Kraus C, Knyphausen P, Eming S, Hammerschmidt M. Adult zebrafish as a model system for cutaneous wound-healing research. J Invest Dermatol 2013;133:1655–65.

Runtuwene V, Van Eekelen M, Overvoorde J, Rehmann H, Yntema HG, Nillesen WM, et al. Noonan syndrome gain-of-function mutations in NRAS cause zebrafish gastrulation defects. Dis Model Mech 2011;4:393–9.

Sauka-Spengler T, Bronner-Fraser M. A gene regulatory network orchestrates neural crest formation. Nat Rev Mol Cell Biol 2008;9:557–68.

Shah S, Lee SF, Tabuchi K, Hao YH, Yu C, LaPlant Q, et al. Nicastrin functions as a gamma-secretase-substrate receptor. Cell 2005;122:435–47.

Sonawane M, Carpio Y, Geisler R, Schwarz H, Maischein HM, Nuesslein-Volhard C. Zebrafish penner/lethal giant larvae 2 functions in hemidesmosome formation, maintenance of cellular morphology and growth regulation in the developing basal epidermis. Development 2005;132:3255–65.

Sonawane M, Martin-Maischein H, Schwarz H, Nüsslein-Volhard C. Lgl2 and E-cadherin act antagonistically to regulate hemidesmosome formation during epidermal development in zebrafish. Development 2009;136:1231–40.

Stewart RA, Sanda T, Widlund HR, Zhu S, Swanson KD, Hurley AD, et al. Phosphatase-dependent and -independent functions of Shp2 in neural crest cells underlie Leopard syndrome pathogenesis. Dev Cell 2010;18:750–62.

Stoletov K, Montel V, Lester RD, Gonias SL, Klemke R. High-resolution imaging of the dynamic tumor cell vascular interface in transparent zebrafish. Proc Natl Acad Sci USA 2007;104:17406–11.

Sung H, Ferlay J, Siegel RL, Laversanne M, Soerjomataram I, Jemal A, et al. Global cancer statistics 2020: GLOBOCAN estimates of incidence and mortality worldwide for 36 cancers in 185 countries. CA Cancer J Clin 2020;71:209–49.

Tan JL, Fogley RD, Flynn RA, Ablain J, Yang S, Saint-André V, et al. Stress from nucleotide depletion activates the transcriptional regulator HEXIM1 to suppress melanoma. Mol Cell 2016;62:34–46.

Thomas AC, Zeng Z, Rivière JB, O'Shaughnessy R, Al-Olabi L, St-Onge J, et al. Mosaic activating mutations in GNA11 and GNAQ are associated with phakomatosis pigmentovascularis and extensive dermal melanocytosis. J Invest Dermatol 2016;136:770–8.

Topczewska JM, Postovit LM, Margaryan NV, Sam A, Hess AR, Wheaton WW, et al. Embryonic and tumorigenic pathways converge via nodal signaling: role in melanoma aggressiveness. Nat Med 2006;12:925–32.

Van Den Berg MCW, Maccarthy-Morrogh L, Carter D, Morris J, Ribeiro Bravo I, Feng Y, et al. Proteolytic and opportunistic breaching of the basement membrane zone by immune cells during tumor initiation. Cell Rep 2019;27:2837–2846.e4.

Venkatesan AM, Vyas R, Gramann AK, Dresser K, Gujja S, Bhatnagar S, et al. Ligand-activated BMP signaling inhibits cell differentiation and death to promote melanoma. J Clin Invest 2018;128:294–308.

von Mässenhausen A, Sanders C, Brägelmann J, Konantz M, Queisser A, Vogel W, et al. Targeting DDR2 in head and neck squamous cell carcinoma with dasatinib. Int J Cancer 2016;139:2359–69.

Webb AE, Driever W, Kimelman D. psoriasis regulates epidermal development in zebrafish. Dev Dyn 2008;237:1153–64.

Wehner D, Cizelsky W, Vasudevaro MD, Ozhan G, Haase C, Kagermeier-Schenk B, et al. Wnt/β-catenin signaling defines organizing centers that orchestrate growth and differentiation of the regenerating zebrafish caudal fin [published correction appears in Cell Rep 2014;6:777–8]. Cell Rep 2014;6:467–81.

Wen J, Yin P, Li L, Kang G, Ning G, Cao Y, et al. Knockdown of matrix metallopeptidase 9 inhibits metastasis of oral squamous cell carcinoma cells in a zebrafish xenograft model. BioMed Res Int 2020;2020:4350783.

White R, Rose K, Zon L. Zebrafish cancer: the state of the art and the path forward. Nat Rev Cancer 2013;13:624–36.

Yan C, Brunson DC, Tang Q, Do D, Iftimia NA, Moore JC, et al. Visualizing engrafted human cancer and therapy responses in immunodeficient zebrafish. Cell 2019;177:1903–1914.e14.

Zhou J, An X, Dong J, Wang Y, Zhong H, Duan L, et al. IL-17 induces cellular stress microenvironment of melanocytes to promote autophagic cell apoptosis in vitiligo. FASEB J 2018;32:4899–916.

DETAILED ANSWERS

1. **Zebrafish were classically used to model which of the following:**

CORRECT ANSWER: D. Embryonic development.

Zebrafish were first utilized for investigating development owing to their transparent structures and rapid ex utero development. Many of the first disease models were created with forward genetic screens, which were published in a special issue of Development in 1996 (Haffter et al., 1996a).

2. **Zebrafish are lacking a clear analog of which layer of the human skin**

CORRECT ANSWER: C. Stratum corneum.

As aquatic animals, zebrafish never developed the water-impermeable stratum corneum found in most land animals (Li et al., 2011).

3. **Zebrafish have been used to model the following skin diseases EXCEPT for:**

CORRECT ANSWER: B. Basal cell carcinoma.

Zebrafish have been used to model melanoma (Patton et al., 2005), epidermolysis bullosa (Sonawane et al., 2005), and psoriasis (Carney et al., 2007; Mathias et al., 2007; Webb et al., 2008) but have not yet been used to model basal cell carcinoma, possibly owing to low morbidity and readily available disease treatments.

4. **Which of the following is available for modeling cancer in zebrafish?**

CORRECT ANSWER: D. All of the above.

Zebrafish have an expansive genetic toolbox that includes genetic mutations in tumor suppressor genes such as *tp53* (Berghmans et al., 2005), transgenic expression of human oncogenes (Patton et al., 2005), and xenografts of tumor cells (Lee et al., 2005).

5. **Regeneration studies in zebrafish have used the following tools to wound skin EXCEPT for:**

CORRECT ANSWER: A. Chemical burns.

Investigators of regenerative mechanisms have used caudal fin amputation (Becerra et al., 1983), scale depilation (Richardson et al., 2016), and dermatology lasers (Richardson et al., 2013) to induce wounds and study regeneration involving skin tissue in zebrafish. However, there are currently no works using chemical agents to wound the zebrafish dermis.

Developmental Cell

CellPress

Previews

Working together: Heterotypic clusters and collective cell migration in melanoma metastasis

William T. Frantz[1] and Craig J. Ceol[1,*]
[1]Program in Molecular Medicine and Department of Cancer Biology, University of Massachusetts Chan Medical School, 368 Plantation Street, Worcester, MA 01605, USA
*Correspondence: craig.ceol@umassmed.edu
https://doi.org/10.1016/j.devcel.2021.10.003

In this issue of *Developmental Cell*, Campbell et al. (2021) show that melanoma cells with distinct invasive or proliferative gene signatures can form heterotypic clusters that extravasate collectively and readily seed the growth of metastatic lesions. These findings highlight interactions between heterogenous tumor cells as being critical for metastasis.

Solid tumors are typically composed of cells that exhibit marked heterogeneity as determined by extensive pathological, immunohistochemical, differential cell isolation and now single-cell analyses. Functional studies of tumor cell heterogeneity have focused on several important properties, including the abilities of tumor cell subpopulations to initiate new tumors or enable drug resistance. In general, these studies have found that subpopulations differ in their functional capabilities and that certain subpopulations are better able to execute functions necessary for oncogenesis and tumor maintenance. However, because many studies have justifiably studied tumor cell subpopulations in isolation, it is less understood how such subpopulations interact when juxtaposed as they are in a native tumor environment. There are indications that interactions occur and could be productive. Receptor/ligand expression profiles suggest signaling between subpopulations, and circulating tumor cell clusters composed of mixed cell subpopulations suggest their involvement in metastasis. In this issue of *Developmental Cell*, Campbell et al. (2021) examine whether melanoma cell subpopulations have different metastatic potentials and how interactions between such subpopulations facilitate metastasis (Campbell et al., 2021).

Transcriptomic studies of melanomas have revealed subpopulations that are characterized by different levels of expression of the *MITF* melanocyte regulatory transcription factor. As described in the *MITF* "rheostat" model originally proposed by Goding and colleagues (Carreira et al., 2006), low *MITF* levels are associated with stem cell-like properties and invasiveness, higher levels with proliferative capacity, and very high levels with terminal melanocytic differentiation. Single-cell analyses have demonstrated that most melanomas, both primary and metastatic, are composed of a heterogenous mixture of cells that express different *MITF* levels (Tirosh et al., 2016), and melanoma cells along this *MITF* expression continuum have phenotypic states corresponding to those defined in melanocytes. Other factors have been useful in further classifying melanoma cell subpopulations; for example, subpopulations with high levels of the *AXL* or *EGFR* receptor tyrosine kinases exhibit profound resistance to MAPK-pathway inhibitor therapies (Dugo et al., 2015; Konieczkowski et al., 2014). Additional studies (Rambow et al., 2018; Roesch et al., 2013) have indicated that drug-resistant disease can arise not only from drug-induced positive selection of rare drug-resistant cells in a tumor but also from the ability of drug-sensitive cells to undergo "phenotype switching," i.e., dynamically switch into cells with a drug-resistant phenotype. However, very little is known about how different subpopulations contribute to metastatic spread. Important gaps in our understanding have included the nature of subpopulations that are involved in metastasis, whether these subpopulations exhibit plasticity in their phenotypic states, and, importantly, whether subpopulations can act in a coordinated fashion to seed metastatic disease.

Campbell et al. began to explore these gaps by establishing, from zebrafish melanomas, stable invasive (INV) and proliferative (PRO) cell cultures. Using an *in vivo* metastasis assay, INV cells injected into the circulatory system were better able to invade tissue and seed tumors as compared to PRO cells. While these results helped to establish the system, additional analyses gave counterintuitive results. INV cells, with their increased motility and metastatic propensity, were expected to be less adhesive. However, INV cells were enriched for genes involved in cell-cell adhesion and formed large cell clusters when grown in low-adherent plates. In mixing experiments, co-cultures of INV and PRO cells formed heterotypic clusters, with a core of INV cells surrounded by a shell of PRO cells. Interestingly, in a zebrafish extravasation assay, nearly half of the extravasation events from an injected mixture of INV and PRO cells were heterotypic, suggesting that the adhesion observed *in vitro* can take place *in vivo* during an important part of the metastatic process. In a separate zebrafish metastasis assay, mixing of INV and PRO cells did not change the presence of INV cells in metastases, but the presence of PRO cells in metastases was markedly increased. The increased metastatic propensity that PRO cells derived from admixture with INV cells suggested some degree of cooperativity,

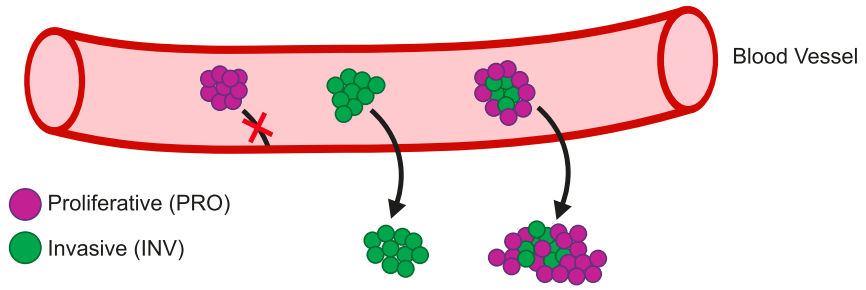


Figure 1. Model for heterotypic cell clusters in metastatic outgrowth
Melanoma cells with a proliferative (PRO) gene signature are poor at extravasation, and those with an invasive (INV) signature are able to extravasate but grow slowly in target tissues. Heterotypic clusters of PRO and INV cells are able to both extravasate efficiently and grow rapidly to form metastases.

with the potential tumorigenic benefit being the deposition in nascent metastases of proliferative cells that would otherwise not be able to get there.

To identify regulators of cluster formation, transcription factors driving gene expression differences between INV and PRO cells were investigated. Targets of TFAP2, a family of transcription factors with roles in neural crest and melanocyte development, were among the most differentially regulated genes with upregulation in PRO cells and downregulation in INV cells. Functional studies validated roles for *TFAP* members in maintaining the PRO cell state. Importantly, in blood from human melanoma patients, TFAP2A-positive PRO cells were found in heterotypic INV/PRO cell clusters. Thus, heterotypic clusters provide a means for INV and PRO cells to cooperatively promote metastasis, are regulated by TFAP2, and can be found in a clinical setting most relevant to metastasis.

Collective cell migration has roles in normal processes such as developmental tissue remodeling and wound healing, and its importance in metastasis is being increasingly recognized (Vilchez Mercedes et al., 2021). In the study by Campbell et al., heterotypic cluster formation and collective cell migration are proposed to act in concert to facilitate metastasis. A model emerging from this study indicates that PRO cells alone are poor at reaching sites amenable to metastatic growth and that INV cells alone can reach these sites but grow slowly, but that INV/PRO clusters can both reach these sites and grow rapidly (Figure 1). The enrichment of adhesion gene expression in INV cells suggests a role for cell-cell adhesion in promoting cluster formation, although it is unclear whether adhesion contacts are unbiased toward homotypic and heterotypic clusters or specifically promote heterotypic cluster formation. The finding of heterotypic circulating tumor cell clusters in melanoma patients is particularly exciting, as it leads to questions of whether these patients are at increased risk of metastasis and whether such clusters can serve as predictive biomarkers of metastasis.

Relating this model to prior work on INV and PRO states also raises interesting questions. These cell states have predominantly been defined by their expression level of *MITF*. However, in this study, levels of the zebrafish *MITF* ortholog *mitfa* were not noted to drive INV and PRO states. Rather, *TFAP* gene knockout affected INV state maintenance without altering *mitfa* expression, suggesting that critical aspects of these cell states, and heterotypic clustering in particular, are maintained independently of *MITF*. The extent to which phenotype switching between INV and PRO states influences heterotypic clustering, collective cell migration, and growth of metastases is unclear. Longitudinal tracking of zebrafish INV and PRO cells suggested these cell states are relatively stable, although some shift of INV cells toward a mixed INV/PRO state was observed in zebrafish metastatic lesions. However, as noted above, growth of metastatic lesions seeded only by INV cells was slower than that of lesions seeded by mixed INV and PRO cells. Overall, this suggests there is a benefit to mixed INV and PRO cell metastatic seeding over INV-only seeding that is accompanied by phenotype switching. It will be interesting to determine if micrometastases in animal models and potentially even humans show evidence of heterotypic cell origins.

REFERENCES

Campbell, N.R., Rao, A., Hunter, M.V., Sznurkowska, M.K., Briker, L., Zhang, M., Baron, M., Heilmann, S., Deforet, M., Kenny, C., et al. (2021). Cooperation between melanoma cell states promotes metastasis through heterotypic cluster formation. Dev. Cell *56*, 2808–2825.

Carreira, S., Goodall, J., Denat, L., Rodriguez, M., Nuciforo, P., Hoek, K.S., Testori, A., Larue, L., and Goding, C.R. (2006). Mitf regulation of Dia1 controls melanoma proliferation and invasiveness. Genes Dev. *20*, 3426–3439.

Dugo, M., Nicolini, G., Tragni, G., Bersani, I., Tomassetti, A., Colonna, V., Del Vecchio, M., De Braud, F., Canevari, S., Anichini, A., and Sensi, M. (2015). A melanoma subtype with intrinsic resistance to BRAF inhibition identified by receptor tyrosine kinases gene-driven classification. Oncotarget *6*, 5118–5133.

Konieczkowski, D.J., Johannessen, C.M., Abudayyeh, O., Kim, J.W., Cooper, Z.A., Piris, A., Frederick, D.T., Barzily-Rokni, M., Straussman, R., Haq, R., et al. (2014). A melanoma cell state distinction influences sensitivity to MAPK pathway inhibitors. Cancer Discov. *4*, 816–827.

Rambow, F., Rogiers, A., Marin-Bejar, O., Aibar, S., Femel, J., Dewaele, M., Karras, P., Brown, D., Chang, Y.H., Debiec-Rychter, M., et al. (2018). Toward minimal residual disease-directed therapy in melanoma. Cell *174*, 843–855.

Roesch, A., Vultur, A., Bogeski, I., Wang, H., Zimmermann, K.M., Speicher, D., Körbel, C., Laschke, M.W., Gimotty, P.A., Philipp, S.E., et al. (2013). Overcoming intrinsic multidrug resistance in melanoma by blocking the mitochondrial respiratory chain of slow-cycling JARID1B(high) cells. Cancer Cell *23*, 811–825.

Tirosh, I., Izar, B., Prakadan, S.M., Wadsworth, M.H., 2nd, Treacy, D., Trombetta, J.J., Rotem, A., Rodman, C., Lian, C., Murphy, G., et al. (2016). Dissecting the multicellular ecosystem of metastatic melanoma by single-cell RNA-seq. Science *352*, 189–196.

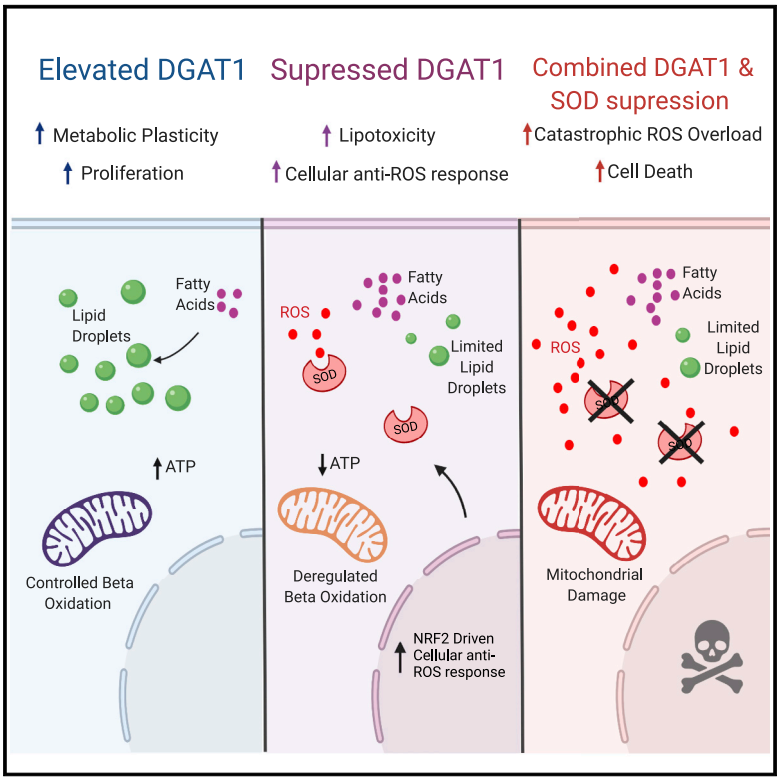
Vilchez Mercedes, S.A., Bocci, F., Levine, H., Onuchic, J.N., Jolly, M.K., and Wong, P.K. (2021). Decoding leader cells in collective cancer invasion. Nat. Rev. Cancer *21*, 592–604.

Cell Reports

Article

Oxidative stress from DGAT1 oncoprotein inhibition in melanoma suppresses tumor growth when ROS defenses are also breached

Graphical abstract



Highlights

- DGAT1 is up-regulated in melanoma cells and is an oncoprotein
- DGAT1 induced lipid droplet formation creates a reservoir for excess fatty acid
- DGAT1 inhibition causes excess fatty acid oxidation, ROS generation, and NRF2 activation
- Suppression of tumor growth requires inhibiting both DGAT1 and the NRF2 target SOD1

Authors

Daniel J. Wilcock, Andrew P. Badrock, Chun W. Wong, ..., Chiara Francavilla, Michael P. Smith, Adam F.L. Hurlstone

Correspondence

michael.smith-8@manchester.ac.uk (M.P.S.), adam.hurlstone@manchester.ac.uk (A.F.L.H.)

In brief

Wilcock et al. find that DGAT1, which stimulates triglyceride and lipid droplet formation, is a melanoma oncoprotein. Lipid droplets are a fatty acid reservoir, controlling fatty acid oxidation. With DGAT1 inhibited, deregulated fatty acid oxidation results in ROS accumulation that proves lethal when the NRF2 target SOD1 is also inhibited.

Wilcock et al., 2022, Cell Reports *39*, 110995
June 21, 2022 © 2022 The Authors.
https://doi.org/10.1016/j.celrep.2022.110995

CellPress

Cell Reports

CellPress
OPEN ACCESS

Article

Oxidative stress from DGAT1 oncoprotein inhibition in melanoma suppresses tumor growth when ROS defenses are also breached

Daniel J. Wilcock,[1,10] Andrew P. Badrock,[2,10,11] Chun W. Wong,[3] Rhys Owen,[1] Melissa Guerin,[4] Andrew D. Southam,[5,6] Hannah Johnston,[1] Brian A. Telfer,[1] Paul Fullwood,[2] Joanne Watson,[2] Harriet Ferguson,[2] Jennifer Ferguson,[2] Gavin R. Lloyd,[5,6] Andris Jankevics,[5,6] Warwick B. Dunn,[5,6,7] Claudia Wellbrock,[1] Paul Lorigan,[1,8] Craig Ceol,[4] Chiara Francavilla,[2,11] Michael P. Smith,[2,*] and Adam F.L. Hurlstone[3,9,12,*]

[1]Division of Cancer Studies, School of Medical Sciences, Faculty of Biology, Medicine and Health, The University of Manchester, Manchester M13 9PT, UK

[2]Division of Molecular and Cellular Function, School of Biological Sciences, Faculty of Biology, Medicine and Health, The University of Manchester, Dover Street, Manchester M13 9PT, UK

[3]Division of Infection Immunity and Respiratory Medicine, School of Biological Sciences, Faculty of Biology, Medicine and Health, The University of Manchester, Dover Street, Manchester M13 9PT, UK

[4]Program in Molecular Medicine, Department of Molecular, Cell and Cancer Biology, University of Massachusetts Medical School, Worcester, MA 01605, USA

[5]School of Biosciences, Edgbaston, University of Birmingham, Birmingham B15 2TT, UK

[6]Phenome Centre Birmingham, University of Birmingham, Edgbaston, Birmingham B15 2TT, UK

[7]Institute of Metabolism and Systems Research, University of Birmingham, Edgbaston, Birmingham B15 2TT, UK

[8]Department of Medical Oncology, The Christie NHS Foundation Trust, Wilmslow Road, Withington, Manchester M20 4BX, UK

[9]Lydia Becker Institute of Immunology, The University of Manchester, Dover Street, Manchester M13 9PT, UK

[10]These authors contributed equally

[11]Senior author

[12]Lead contact

*Correspondence: michael.smith-8@manchester.ac.uk (M.P.S.), adam.hurlstone@manchester.ac.uk (A.F.L.H.)

https://doi.org/10.1016/j.celrep.2022.110995

SUMMARY

Dysregulated cellular metabolism is a cancer hallmark for which few druggable oncoprotein targets have been identified. Increased fatty acid (FA) acquisition allows cancer cells to meet their heightened membrane biogenesis, bioenergy, and signaling needs. Excess FAs are toxic to non-transformed cells but surprisingly not to cancer cells. Molecules underlying this cancer adaptation may provide alternative drug targets. Here, we demonstrate that diacylglycerol *O*-acyltransferase 1 (DGAT1), an enzyme integral to triacylglyceride synthesis and lipid droplet formation, is frequently up-regulated in melanoma, allowing melanoma cells to tolerate excess FA. DGAT1 over-expression alone transforms p53-mutant zebrafish melanocytes and co-operates with oncogenic BRAF or NRAS for more rapid melanoma formation. Antagonism of DGAT1 induces oxidative stress in melanoma cells, which adapt by up-regulating cellular reactive oxygen species defenses. We show that inhibiting both DGAT1 and superoxide dismutase 1 profoundly suppress tumor growth through eliciting intolerable oxidative stress.

INTRODUCTION

The growth and survival of cancer cells is underpinned by dysregulated cellular metabolism (DeBerardinis and Chandel, 2016), which further promotes cancer progression by reprogramming stromal cells, mediating evasion of immune responses, and promoting metastasis (Andrejeva and Rathmell, 2017; Lee et al., 2018; Lyssiotis and Kimmelman, 2017). A central facet of cancer cell metabolism is a shift in glucose usage away from oxidative phosphorylation toward biosynthetic reactions. Without compensation by fatty acid oxidation (FAO) and glutaminolysis, this shift would result in deficiencies in citric acid cycle intermediates needed for ATP production (DeBerardinis and Chandel, 2016).

Although catabolism of fatty acids (FA) maintains ATP production, increased lipogenesis (lipid generation) is simultaneously required for cell membrane synthesis, for which FA are principal building blocks (Koundouros and Poulogiannis, 2020). Furthermore, lipid signaling molecules such as phosphatidylinositides, diacylglycerides (DAG), lysophosphatidic acid, and prostaglandins, implicated in multiple cancer hallmarks (Chen and Huang, 2019), are also derived from FA. To satisfy these competing demands, cancer cells increase FA supply. This can be achieved by initiating *de novo* FA synthesis, normally a function of adipocytes

This is an open access article under the CC BY license (http://creativecommons.org/licenses/by/4.0/).

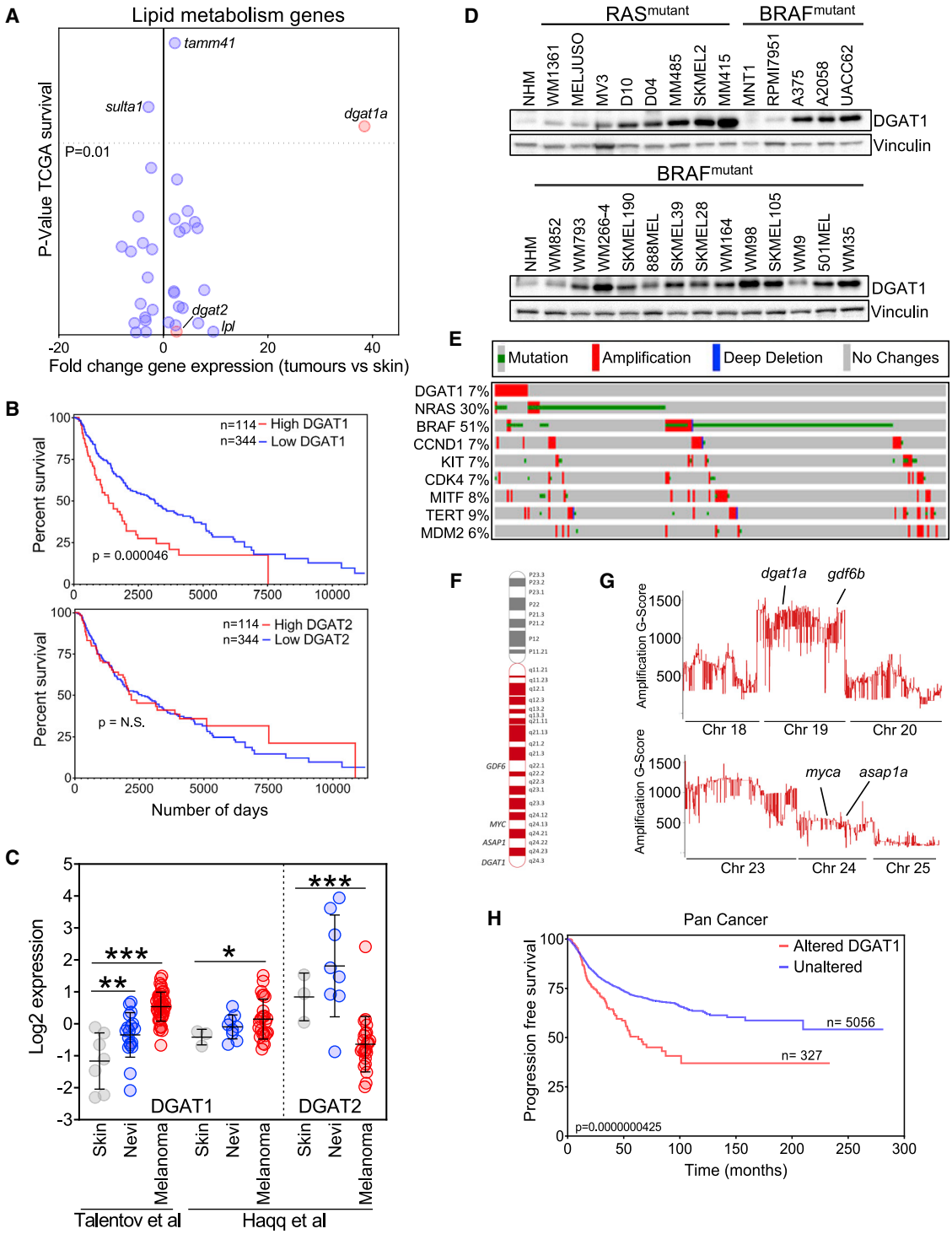


Figure 1. DGAT1 amplification and up-regulation is associated with poor prognosis in melanoma

(A) Patient survival from TCGA melanoma cohort (25% top versus 75% bottom by mRNA abundance, y axis) versus fold change in mRNA expression of lipid metabolism genes in zebrafish tumors (x axis).

(B) Kaplan-Meier survival plot comparing melanoma patients based on expression of *DGAT1* or *DGAT2* (top 25% versus bottom 75%, TCGA dataset).

(C) *DGAT1* and *DGAT2* relative gene expression in skin, nevi, and melanoma tumors from indicated studies. Mean ± SD, n > 3. *p < 0.05, **p < 0.01, and ***p < 0.001.

(legend continued on next page)

and hepatocytes but an acquired characteristic of cancer cells driven by elevated FA synthase (FASN) expression (Koundouros and Poulogiannis, 2020). Alternatively, FA can be acquired from the diet, directly from the circulation or indirectly from adipose tissue. Cancer cells utilize secreted lipases like lipoprotein lipase (LPL) to hydrolyze FA from triglycerides, and FA transporter proteins (FATP) like CD36 and SLC27 family members and FA-binding proteins (FABP) to facilitate uptake (Lengyel et al., 2018). Enhanced FA uptake by cancer cells promotes tumor growth and dissemination (Nieman et al., 2011; Pascual et al., 2017; Watt et al., 2019). Intracellular lipases also liberate FA from intracellular lipid stores (Maan et al., 2018). One such lipase, monoacylglycerol lipase (MAGL or MGLL), is upregulated in aggressive cancers, wherein its suppression impedes tumor growth and metastasis (Nomura et al., 2010).

Whereas adipocytes are adapted to store FA, non-adipose, non-transformed cells that become overloaded with FA suffer from lipotoxicity, characterized by reduced insulin signaling (insulin resistance) and increased cell death (Brookheart et al., 2009). Multiple processes underlie lipotoxicity, including increased ceramide synthesis, dysregulation of phospholipid production compromising mitochondrial and ER membrane integrity, impaired ATP generation, and induction of reactive oxygen species (ROS) (Brookheart et al., 2009). How dysregulated metabolism favoring FA acquisition is tolerated by cancer cells and how the toxic by-products of rampant FAO (principally ROS, including lipid peroxides) are suppressed or neutralized, are incompletely understood. Targeting the ability of cancer cells to manage potentially cytotoxic metabolites that arise from the rewiring of metabolic pathways is an intriguing therapeutic avenue warranting further exploration.

Diacylglycerol *O*-acyltransferase 1 (DGAT1) is an ER-resident enzyme that catalyzes the final step in triacylglyceride (TAG) synthesis from DAG and FA. DGAT1 is required for lipid droplets (LD), cytosolic organelles comprising a core of neutral lipids (mainly triglycerides and sterol esters) delimited by a monolayer of phospholipids (Wilfling et al., 2013). The signficance of DGAT1 up-regulation and subsequent formation of LD to cancer has recently been demonstrated in glioblastoma models, in which DGAT1 inhibition led to tumor cell death through induction of lipotoxicity and oxidative stress (Cheng et al., 2020). Here, we demonstrate the oncogenic ability of DGAT1 in melanoma using zebrafish and find that DGAT1 again exerts this effect primarily through shielding melanoma cells from lipotoxicity. Consequently, DGAT1 inhibition results in oxidative stress in melanoma cells but this is countered by adaptive up-regulation of ROS-neutralizing enzymes such as superoxide dismutase 1 (SOD1). However, simultaneous DGAT1 and SOD1 inhibition leads to catastrophic levels of ROS accumulating in tumor cells, triggering their death.

RESULTS

DGAT1 amplification and up-regulation associates with poor prognosis in melanoma

Few oncoproteins directly dysregulating cellular metabolism have been identified. Point mutations in the isocitrate dehydrogenases IDH1 and IDH2 have been confirmed as oncogenic drivers in only 0.9%–3% of all cancers (Molenaar et al., 2018) (Figure S1A). The gene encoding FASN is frequently amplified in cancer (Koundouros and Poulogiannis, 2020) (Figure S1A); however, FASN inhibitors have failed to gain clinical approval (Flavin et al., 2010). LPL, CD36, FATP1 (SLC27A1), and FATP2 (SLC27A2), implicated in increased FA uptake into melanoma cells (Alicea et al., 2020; Henderson et al., 2019; Pascual et al., 2017; Zhang et al., 2018), are unaffected by point mutation in cancer and display gene amplification in 2%–8% of cases (Figure S1A).

Given this dearth of therapeutic targets but also the significance of lipid metabolism for melanoma development (Fischer et al., 2018), we interrogated genes that we previously identified as accompanying progression of oncogenic RAS-driven melanoma in zebrafish (Henderson et al., 2019). Plotting expression fold change against association with patient survival, *dgat1a*/*DGAT1* emerged as an outlier, being both highly up-regulated in zebrafish melanoma and significantly associated with reduced patient survival (Figures 1A and 1B). In contrast, expression of the gene encoding the functionally related, although structurally distinct, *Dgat2*/DGAT2 did not change significantly, nor was it associated with patient survival (Figures 1A and 1B). Furthermore, we confirmed elevated expression of human *DGAT1* but not *DGAT2* mRNA in melanoma tumors relative to both skin and nevi (Figure 1C) and elevated DGAT1 protein in human melanoma cell lines relative to primary melanocytes irrespective of NRAS or BRAF mutational status (Figure 1D).

We next considered what might underlie DGAT1 up-regulation in melanoma. Visualization of structural alterations of the *DGAT1* gene in the Cancer Genome Atlas firehose legacy cutaneous melanoma dataset using cBioPortal revealed significant focal amplification (as defined by the stringent GISTIC 2.0 algorithm) in up to 7% of melanoma cases with available copy number variation (CNV) data (Figure 1E), comparable to other recognized melanoma oncogenes (namely *CCND1*, *KIT*, *CDK4*, *MITF*, *TERT*, and *MDM2*). An extra copy of chromosome 8q, containing the *DGAT1* locus but also other putative melanoma oncogenes *ASAP1*/*DDEF*, *MYC*, and *GDF6* (Ehlers et al., 2005; Schlagbauer-Wadl et al., 1999; Venkatesan et al., 2018) (Figure 1F), has been observed in approximately 30% of melanoma cases (Bastian et al., 1998). Consistently, *DGAT1*, *ASAP1*, *MYC*, and *GDF6* are co-amplified in melanoma and other cancers (Figures S1B and S1C). However, of these four, *DGAT1* mRNA expression displayed the strongest association with reduced patient survival

(D) Protein expression of DGAT1 and vinculin (loading control). NHM, normal human melanocytes.
(E) Genetic alterations in the TCGA firehose legacy melanoma dataset (counting only samples with CNV data) obtained from cBioPortal.
(F) Schematic depicting human chromosome 8, the amplified arm (red), and known/putative melanoma oncogenes within this region.
(G) G-score of amplified regions of zebrafish chromosomes found in $BRAF^{V600E}$-positive; *tp53* mutant tumors indicating the position of presumed melanoma oncogene homologs.
(H) Kaplan-Meier progression free-survival plot comparing patients across multiple cancer types based on *DGAT1* amplification.

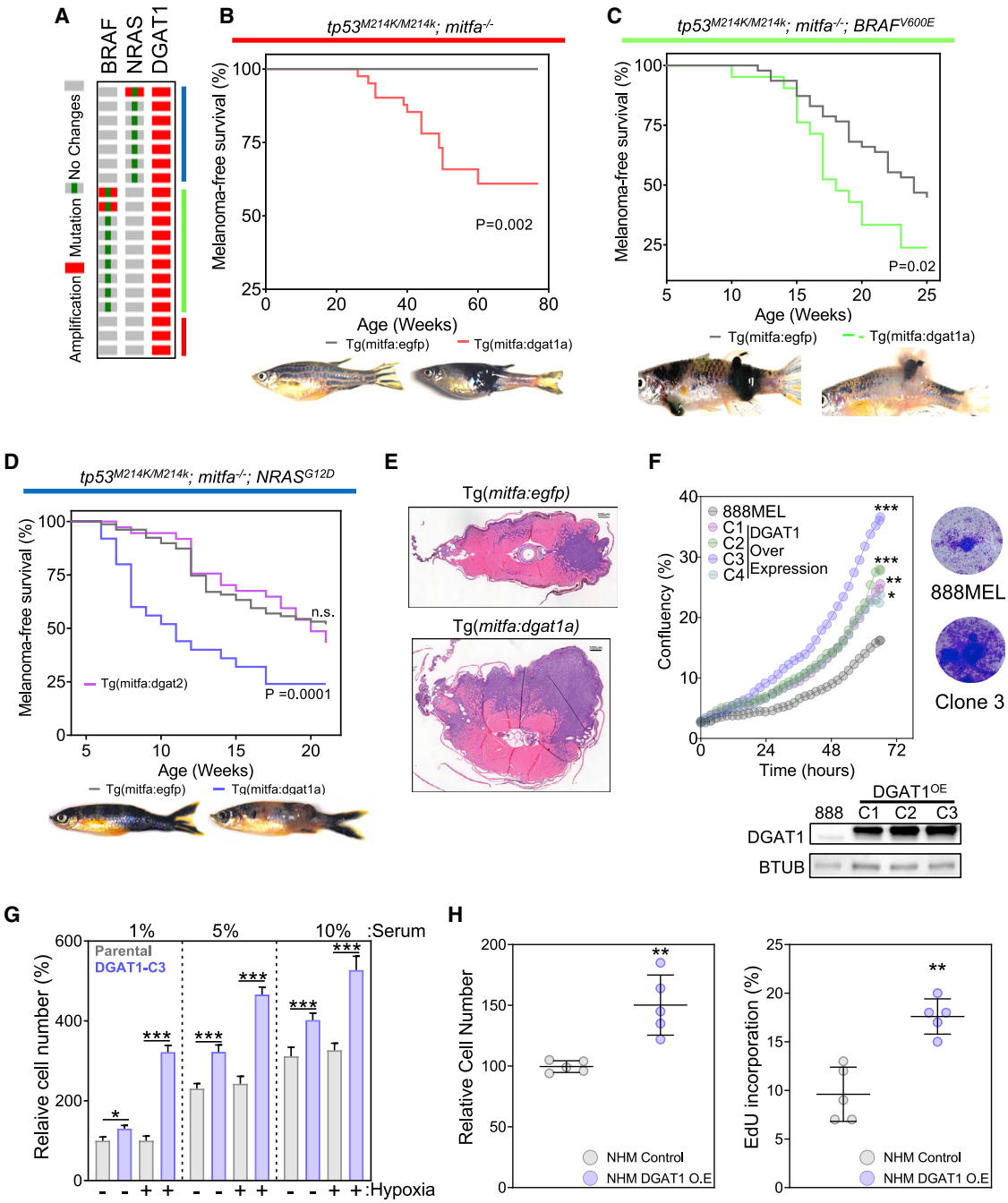


Figure 2. DGAT1 functions as an oncoprotein in zebrafish and human melanocytes

(A) *DGAT1* amplification distribution in TCGA melanoma samples.

(B) Kaplan-Meier plot of melanoma tumor nodule incidence in EGFP control or Dgat1a over-expressing animals on the *tp53* mutant;*nacre* genetic background. Representative images shown for EGFP- and Dgat1a-positive animals at 54 and 76 weeks post-fertilization, respectively (mitfa:egfp n = 20; mitfa:dgat1a n = 20).

(C) As for (B) but on the transgenic *mitfa:BRAF*^{V600E};*tp53* mutant;*nacre* genetic background. Representative images are shown at 12 weeks post-fertilization (mitfa:egfp n = 46; mitfa:dgat1a n = 21).

(D) As for (C) but on the transgenic *mitfa:NRAS*^{G12D};*tp53* mutant;*nacre* genetic background, also shown the effect of Dgat2 over-expression (mitfa:egfp n = 120; mitfa:dgat1a n = 69; mitfa:dgat2 n = 35).

(E) Hematoxylin and eosin-stained transverse sections of EGFP-expressing or Dgat1a-over-expressing melanoma on the transgenic *mitfa:NRAS*^{G12D};*tp53* mutant;*nacre* genetic background. Scale bars, 200 μm

(F) Confluence of parental 888MEL cells and cells following lentiviral transduction with a DGAT1 over-expression vector and clonal selection (mean, n = 3, top left). Corresponding crystal violet staining after 72-h growth (top right). Corresponding protein expression of DGAT1 (bottom).

(legend continued on next page)

(Figures 1B and S1D). Furthermore, our previous comparative oncogenomic analysis (Venkatesan et al., 2018) uncovered amplification of *dgat1a* together with *gdf6b* (both on chromosome 19) in oncogenic-BRAF-driven zebrafish melanoma, concomitant with up-regulation of *dgat1a* and *gdf6b* mRNA (Figure 1G and Table S1). In contrast, neither *dgat1b* nor *gdf6a* on chromosome 16, nor any *myc* or *asap1* paralogs (on chromosomes 2 and 24) were amplified or up-regulated (Figures 1G and S1E, and Table S1). Finally, we found *DGAT1* to be frequently amplified in other human cancers, a feature of many well-characterized oncogenes, most notably in up to 26% of cases of ovarian cancer (Figures S1A and S1F). Strikingly, *DGAT1* amplification was associated with significantly poorer progression-free survival across multiple cancer types (Figure 1H). Thus, from a cancer genomics perspective, *DGAT1* exhibits the hallmarks of an oncogene.

DGAT1 functions as an oncoprotein in zebrafish and human melanocytes

In human melanoma, *DGAT1* amplification was observed to co-occur with *BRAF* and *NRAS* mutation but also independently of either (Figure 2A). To elucidate further the oncogenic potential of *DGAT1*, we utilized a melanocyte rescue and lineage-restricted expression system as described previously (Ceol et al., 2011; Venkatesan et al., 2018). Remarkably, we found that forcing Dgat1a expression in zebrafish melanocytes lacking functional p53 was sufficient to induce melanoma (Figure 2B). Moreover, Dgat1a cooperated with both oncogenic BRAF and NRAS to accelerate the development of nodular tumors (Figures 2C–2E). Thus, in zebrafish, Dgat1 behaves as a melanoma oncoprotein. Significantly, effects of forcing Dgat2 expression were indistinguishable from the non-oncogenic EGFP control (Figure 2D), indicating that Dgat1 stimulation of tumorigenesis cannot be replicated by the functionally related Dgat2.

In human melanoma models, *DGAT1* also exhibited oncogenic characteristics. Forced expression of *DGAT1* in the DGAT1^{Low} melanoma cell line 888MEL led to an increase in cellular proliferation in all four clones tested (Figures 2F and S2A). Cancer cells can sustain their growth despite transient or limited nutrient availability in the tumor microenvironment (Ackerman and Simon, 2014). We therefore investigated the role of DGAT1 over-expression in allowing melanoma cells to tolerate nutrient and oxygen deprivation in culture. DGAT1-overexpressing melanoma cells exhibited a 100%–200% increase in cell number compared with parental DGAT1^{Low} cells under conditions of greatest stress: 1% serum and hypoxia (1% O_2) (Figures 2G, S2B, and S2C). A growth advantage conferred by DGAT1 over-expression was also observed in normal human melanocytes (NHM) (Figures 2H and S2D). Our zebrafish and human models demonstrate that in melanocytes DGAT1 has the hallmarks of an oncoprotein, conferring a growth advantage especially under stress conditions likely encountered in the tumor microenvironment.

DGAT1 antagonism decreases melanoma cell proliferation and survival

Having uncovered DGAT1 as an oncoprotein, we next assessed the impact of DGAT1 antagonism in human melanoma cell lines. DGAT1 depletion using siRNA reduced cell proliferation and decreased the fractions of cells in S-phase (Figures 3A and S3A), in contrast to the increased proliferation and cell cycle progression observed with stable DGAT1 over-expression (Figures 2F and S2A). As DGAT1 has been mooted as a clinical target for combating obesity, several potent and selective small-molecule inhibitors are already available for repurposing (DeVita and Pinto, 2013). To determine whether DGAT1 depletion effects were due to the enzymatic function of DGAT1, we utilized four selective DGAT1 inhibitors (AZD3988, AZD7687, A922500, or T863). Similarly to siRNA-mediated depletion, pharmacological antagonism of DGAT1 suppressed growth of DGAT1^{High} (A375, MM485, and SKMEL105) and DGAT1^{Amplified} (LOXIMVI and SKMEL5) melanoma cells over 96 h (Figures 3B and S3B), accompanied by decreased cell cycle progression (Figure 3B). In contrast, no changes in cell growth or cell cycle progression were observed following DGAT2 depletion or inhibition (Figures S3C–S3E).

Given that DGAT1 over-expression exhibited the largest relative effect on cell growth under conditions of cellular stress, we hypothesized that, conversely, the impact of DGAT1 inhibition would be exacerbated when cells were exposed to nutrient and hypoxic stress. Indeed, we found that DGAT1 antagonism significantly impaired proliferation when external lipid sources were restricted, with the greatest reduction in cell number observed at the lowest levels of serum (Figure 3C). Moreover, exposing cells to hypoxic conditions (1% O_2) led to a further decrease in cell number upon DGAT1 inhibition (Figure 3D). Further highlighting the key role of DGAT1 up-regulation in melanoma cells, even under standard tissue culture conditions, siRNA knockdown or pharmacological inhibition of DGAT1 led to apoptosis, quantified through an increase in cleaved caspase-3 (Figures 3E and 3F). The significant impact of DGAT1 antagonism on melanoma cell proliferation and survival, exacerbated under conditions mimicking tumor microenvironmental stresses, highlights DGAT1 as a possible therapeutic target in melanoma.

DGAT1 is essential for LD formation and acts as a caretaker of mitochondrial health

To address the effect of DGAT1 on melanoma lipid metabolism, we performed ultra-high-performance liquid chromatography-mass spectrometry (UHPLC-MS) to identify and contrast lipid species extracted from NRAS^{G12D} Dgat1a-over-expressing or

(G) Relative cell numberof parental 888MEL cells and cells following lentiviral transduction with a DGAT1 over-expression vector, determined using crystal violet staining following 48-h culture in indicated serum levels under hypoxic (1% O_2) or normoxic conditions (mean ± SEM, n > 3).
(H) Relative cell number of NHM and NHM following lentiviral transduction with a DGAT1 over-expression vector determined using crystal violet staining (left). Percentage of NHM and NHM following lentiviral transduction with a DGAT1 over-expression vector in S-phase by using EdU incorporation (right) (mean ± SEM, n = 5). (F–H) For significance: *p < 0.05, **p < 0.01, and ***p < 0.001.

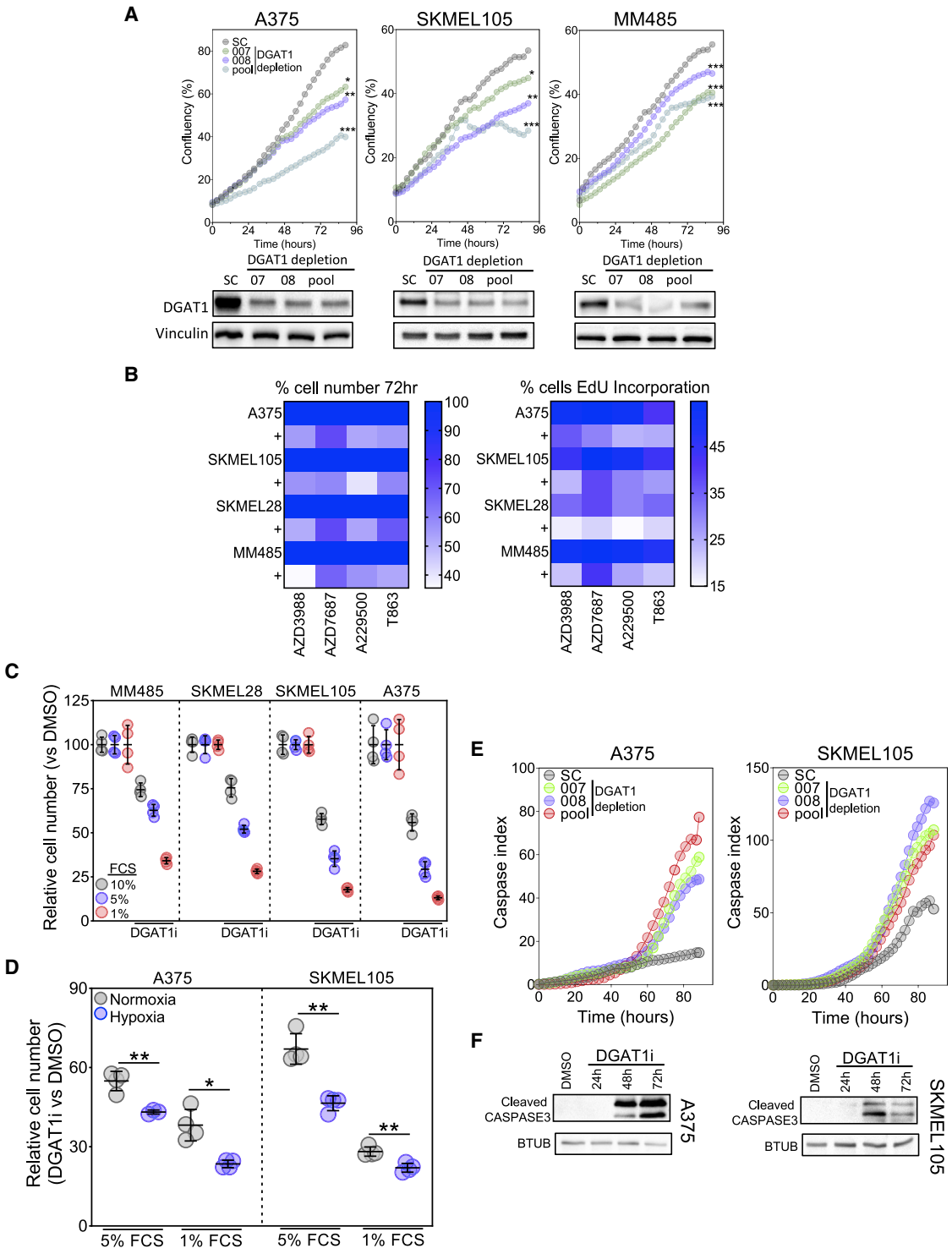


Figure 3. DGAT1 antagonism decreases melanoma cell proliferation and survival

(A) Confluence of cell lines transfected with DGAT1 targeting (007, 008, pool) or scrambled (sc) siRNAs (mean, n = 3, top). Corresponding protein expression of DGAT1 (bottom).

(B) Left: relative cell number (mean, n > 3) in indicated cell lines determined by crystal violet following 72-h DGAT1 inhibitor treatment (50 μM AZD3988, 30 μM A922500, 50 μM AZD7687, or 70 μM T863). Right: percentage of cells in S-phase by using EdU incorporation following 24-h DGAT1 inhibitor treatment (mean, n > 3).

(legend continued on next page)

$NRAS^{G12D}$ EGFP-expressing zebrafish tumors. This analysis revealed increased concentrations of almost all TAG species detected in tumors with forced Dgat1a expression, with longer polyunsaturated FA (PUFA) chains showing the greatest increases (Figures 4A and S4A and Table S2), although changes in individual species were not deemed statistically significant after correction for multiple testing. Several factors confounded the detection of lipid species changes in Dgat1a-over-expressing tumors. First, EGFP-expressing tumors also over-express Dgat1a and have ample LD (Henderson et al., 2019). Second, lipids originating from associated stromal cells dilute the lipids derived from tumor cells.

In order to overcome the complexity of whole-tumor analysis, we turned to melanoma cell lines. Over-expression of DGAT1 in human melanoma cells resulted in a striking increase in LD (Figure 4B), consistent with cells adopting an engorged morphology (Figure 4B). Moreover, this was also observed in NHM upon DGAT1 over-expression (Figure S4B). In parallel, UHPLC-MS lipidomic analysis revealed an increase in almost all TAG species (Figure 4B and Tables S3 and S4), corroborating the trend in TAG seen in zebrafish tumors over-expressing Dgat1a (Figure 4A). Conversely, antagonism or depletion of DGAT1 in melanoma cell lines over-expressing endogenous DGAT1 led to a reduction in the amount of LD beginning between 12 and 24 h and continuing until 72 h (Figures 4C and S4C), as previously reported for glioblastoma cells (Cheng et al., 2020) and other cell types (Nguyen et al., 2017). In contrast, LD were not affected by DGAT2 depletion (Figure S4D). As expected, UHPLC-MS lipidomic analysis revealed a reduction of multiple TAG species already at 24 h that was maintained until 72 h, (Figures 4D and S4E and Tables S5 and S6), with TAG-containing PUFA particularly affected (Figure S4A).

Alongside the anticipated changes in TAG levels following manipulation of DGAT1 activity, we also observed a decrease in several acylcarnitine (AcCa) species upon DGAT1 over-expression (Figure 4B and Tables S3 and S4) and a reciprocal increase in AcCa species following DGAT1 inhibition (Figures 4D, 4E, and S4E and Tables S5 and S6). AcCa, formed by esterification of FA (typically long chain) to L-carnitine, are transported into mitochondria to be processed into acetyl-CoA through β-oxidation. The production of AcCa determines the rate of FAO (Falomir-Lockhart et al., 2019). Moreover, excessive FAO can result in mitochondrial dysfunction (Koves et al., 2008). Indeed, we observed impaired ATP production following DGAT1 inhibition, implied by the increased phosphorylation of both AMPK and RAPTOR (Figure 4F). Furthermore, we observed reduced oxygen consumption in DGAT1-inhibited cells after 48 h (Figure 4G), implying decreased mitochondrial respiratory function despite levels of AcCa remaining elevated (Figures 4D and S5E). Additionally, post-24-h DGAT1 inhibition, we observed loss of mitochondrial membrane potential, decreased PINK1 cleavage, and increased levels of mitophagy factor PARKIN (Figure 4H). Moreover, by blocking AcCa synthesis using etomoxir (a carnitine palmitoyltransferase inhibitor), we could partially restore mitochondrial membrane potential and cell proliferation (Figures S4F and S4G). Taking these results together, we conclude that DGAT1 maintains mitochondrial function in melanoma cells by regulating the availability of FA for FAO.

DGAT1 promotes survival of melanoma cells through suppressing ROS generation

To better understand the effects of DGAT1 inhibition on cellular signaling and metabolism, we performed MS-based whole-proteome analysis in SILAC-labeled A375 cells. Analysis of differentially expressed proteins highlighted three key areas: (1) FAO (consistent with increased AcCa availability), (2) peroxisome proliferator-activated receptor (PPAR) signaling, presumably indicating the increased availability of lipid regulators of PPAR transcription factors, and (3) nuclear regulatory factor 2 (NRF2) signaling, which is a well-established response to ROS production that dampens ROS-mediated cellular damage (Sajadimajd and Khazaei, 2018) (Figures 5A, S5A, and S5B). Quantitative gene expression analysis further corroborated the effects of DGAT1 inhibition on these three key biological processes (Figure 5B).

To measure the impact of DGAT1 suppression on ROS generation, we stained cells with fluorescent probes whose emission is changed by ROS. We observed increasing ROS production over time upon DGAT1 inhibition in multiple melanoma cell lines (Figures 5C and S5C). We also observed an increase specifically in mitochondrial ROS upon both DGAT1 inhibition and depletion (Figures S5D and S5E), a predicted consequence of excessive FAO (Koves et al., 2008). Through a chain reaction, oxygen-centered ROS can yield highly reactive and cytotoxic lipid peroxides responsible for ferroptosis (Conrad and Pratt, 2019), a form of programmed cell death. Accordingly, DGAT1 inhibition led to an increase in lipid peroxidation from 24 h, with further increases by 48 h both in the cytoplasm (Figure 5D) and in the mitochondria specifically (Figure 5E). Additionally, depletion of DGAT1 resulted in increased protein conjugation with 4-hydroxynonenal (4HNE) (Figure 5F), a lipid peroxidation by-product (Dalleau et al., 2013). Conversely, we observed decreased 4HNE protein conjugation in DGAT1-over-expressing melanoma cells (Figure 5G) and in zebrafish tumors over-expressing Dgat1a (Figure 5H), indicating that lipid peroxidation and its suppression by DGAT1 occurs not only in cell lines but also within tumors.

We next investigated whether ROS induction upon DGAT1 suppression affected melanoma cell survival. Introduction of the ROS-scavenging agents Tempol and Ebselen partially

(C) Relative cell number determined by crystal violet staining following 72-h A922500 treatment with cells grown in varying concentrations of fetal calf serum (FCS; mean ± SD, n > 3).
(D) Relative cell number determined by crystal violet staining following 48-h A922500 treatment under normoxic or hypoxic conditions (1% O_2) with cells grown in varying concentrations of FCS (relative to DMSO control for each condition; mean ± SD, n > 3).
(E) Cleaved caspase index in indicated cell lines following transfection with either a DGAT1-targeting siRNA (007, 008, pool) or a sc control (mean, n = 3).
(F) Protein expression of cleaved caspase-3 following treatment with/without A922500 for 24–72 h.
(A) and (D) For significance: *p < 0.05, **p < 0.01, and ***p < 0.001.

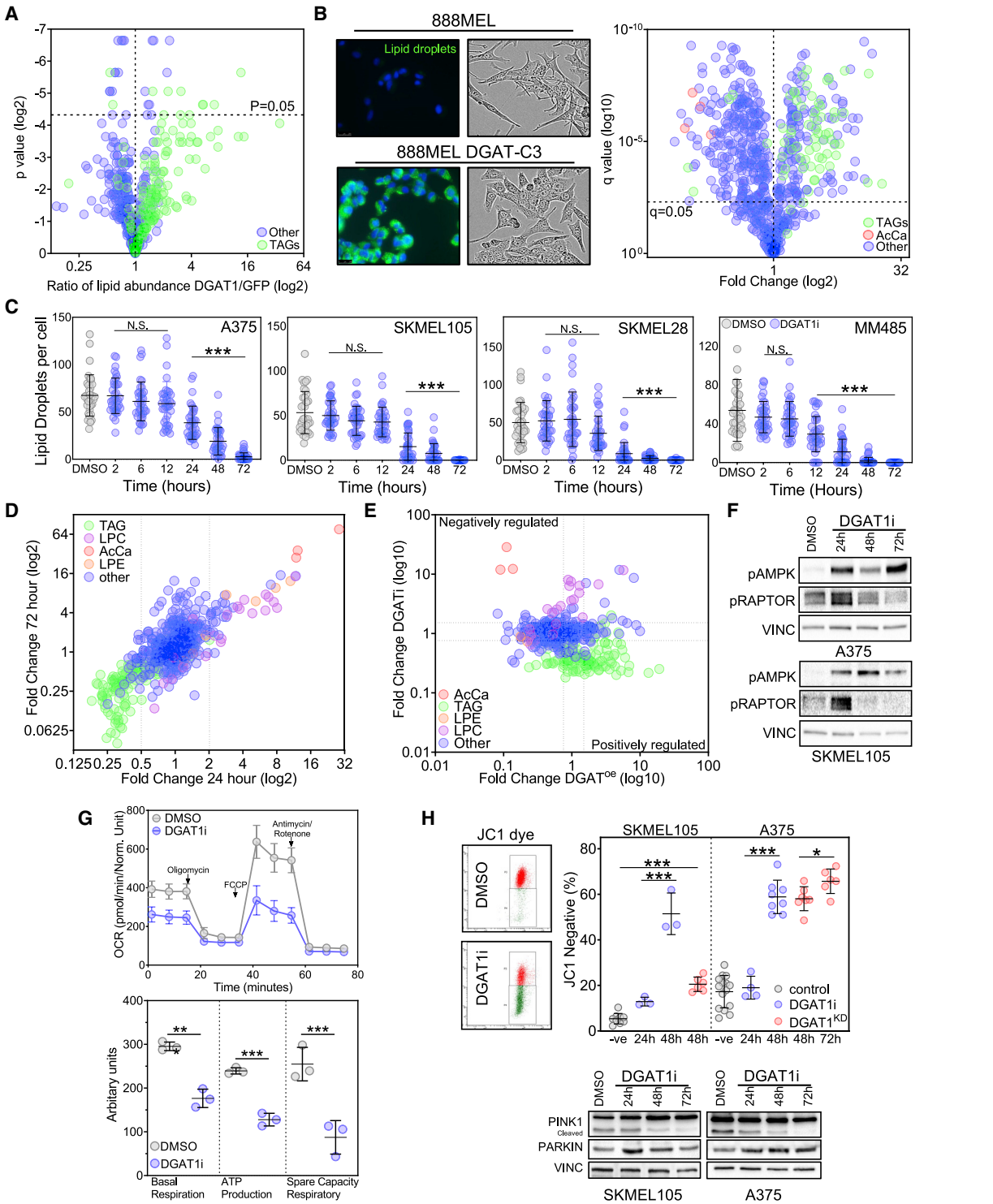


Figure 4. DGAT1-formed lipid droplets act as caretakers of mitochondrial health

(A) Lipidomic profiling using UHPLC-MS of NRASG12D-positive EGFP-expressing (n = 6) and NRASG12D-positive Dgat1a-over-expressing (n = 6) tumors showing the ratio of individual lipid species annotated by MS/MS.

(B) Representative images of 888MEL and Clone 3 cells stained with BODIPY (left; scale bar, 10 μm). Brightfield images of 888MEL parental cells and Clone 3 DGAT1-over-expressing cells (middle). UHPLC-lipidomic analysis of 888MEL parental and Clone 3 DGAT1-over-expressing cells. Fold change relative to 888MEL parental cells (right) (all conditions n = 3). TAG, triacylglycerides; AcCa, acylcarnitine.

(C) Number of lipid droplets per cell visualized using BODIPY staining following AZD3988 (DGAT1i) treatment (mean ± SD, n > 30).

(legend continued on next page)

suppressed apoptosis induced by DGAT1 depletion (Figure 5I). Conversely, stable over-expression of DGAT1 was protective against ROS-mediated cell death triggered by chemical ROS inducers (Figure S5F). Moreover, ferrostatin-1, a potent ferroptosis inhibitor (Skouta et al., 2014), rescued the reduction in cell number observed upon DGAT1 inhibition, an effect also observed with Tempol and Ebselen. Combining ferrostatin-1 with either Tempol or Ebselen led to the greatest rescue of cell number and further suppressed apoptosis driven by DGAT1 inhibition (Figure S5G). Thus, DGAT1 promotes the survival of melanoma cells by suppressing the ROS production and lipid peroxidation that would otherwise occur as a result of their increased FA acquisition.

Combined DGAT1 and SOD1 inhibition halts tumor growth

There are few pan-cancer-druggable metabolic oncoproteins whose suppression is well tolerated. We wished to establish whether pharmacological inhibition of DGAT1 would be a viable strategy to halt tumor growth in mice. We implanted DGAT1^{High} A375 melanoma cells in mouse flanks and commenced daily oral treatment with the DGAT1 inhibitor A922500 (90 mg/kg/day) when tumors reached approximately 100 mm^3. Surprisingly, A922500 treatment had no significant impact upon tumor growth *in vivo* (Figure 6A) despite an increase in tumor ROS levels revealed by increased 4HNE conjugation to protein (Figure S6A). We hypothesized that this might be due to more effective ROS neutralization *in vivo*, which would need to be antagonized in order to suppress tumor growth. We therefore investigated expression of the ROS-detoxifying enzymes SOD1 and -2, two known NRF2 target genes (Dreger et al., 2010; Ma et al., 2021; Park and Rho, 2002; Taylor et al., 2008). Indeed, inhibition of DGAT1 in melanoma cell lines led to increased SOD1 and -2 as well as SESTRIN2 (SESN2) (Figure S6B), a NRF2 activator induced upon mitochondrial respiratory malfunction (Bae et al., 2013; Garaeva et al., 2016), in agreement with our earlier MS-based whole-proteome and quantitative PCR analyses demonstrating activation of NRF2 signaling following DGAT1 inhibition (Figures 5A and 5B). To confirm the role of SESN2/NRF2 signaling in inducing SOD expression following DGAT1 inhibition, we depleted SESN2 using siRNA and in parallel treated cells with NRF2 inhibitor ML385 (Singh et al., 2016). These treatments prevented the induction of SOD1, SOD2 and an additional established NRF2 target, HMOX1, by DGAT1 inhibition (Figures S6C–S6F), consistent with SOD induction being driven through a SESN2/NRF2-signaling axis. Moreover, further analysis of the A375 tumors treated with A922500 revealed increased SESN2, SOD1, and SOD2 expression (Figure S6A), concomitant with increased lipid peroxidation, confirming that our A922500 administration had been effective in inducing ROS and NRF2 signaling in tumor cells *in vivo*.

Assuming that ROS-neutralizing factors such as SOD enzymes were limiting the tumor inhibitory effects of DGAT1 antagonism, we next examined whether blocking the induction of SOD1 would augment the impact of DGAT1 inhibition on melanoma cell growth and survival. Indeed, we found that combining DGAT1 inhibition with SOD1 knockdown led to increased ROS generation concomitant with a dramatic reduction in cell number when compared with inhibition of DGAT1 alone (Figures S6G–S6I). In the clinic, tetrathiomolybdate (TTM) anions are used to chelate cupric cations and have been shown to potently inhibit SOD1, which uses cupric cations as a co-factor, leading to clinical trials of TTM as anti-cancer agents (Juarez et al., 2006; Lowndes et al., 2008; Redman et al., 2003). Again, compared with DGAT1 inhibitor treatment alone, the combination of DGAT1 inhibitor and TTM led to a significant increase in ROS generation and 4HNE protein conjugates (Figures 6B and S6J), concomitant with a marked decrease in cell growth and induction of apoptosis (Figures 6B and S6K). We next assessed the impact of combining inhibition of DGAT1 and SOD1 on tumor growth by using not only the BRAF^{V600E}-mutant A375 xenograft model but also an NRAS^{Q61R}-mutant MM485 xenograft model. In both models, similarly to DGAT1 inhibition alone, SOD1 inhibitor treatment alone had no significant impact on tumor growth (Figures 6C and 6D). Strikingly, combined DGAT1 and SOD1 inhibition led to a profound reduction in tumor growth, with most animals demonstrating tumor regression in the MM485 xenograft model (Figures 6C and 6D). Western blotting of protein extracts from tumors revealed the expected increase in 4HNE protein conjugates in tumors treated with DGAT1 inhibitor or SOD1 inhibitor alone, and elevated SOD1 expression following treatment with DGAT1 inhibitor alone. Significantly, 4HNE protein conjugates were most elevated in tumors treated with a combination of the DGAT1 and SOD1 inhibitors (Figures 6E and 6F). Thus, combinatorial DGAT1 and SOD1 inhibition synergized to create a toxic overload of ROS in tumors, severely retarding the growth of melanoma cells *in vivo*.

DISCUSSION

The role of dysregulated lipid metabolism, encompassing more than just *de novo* FA synthesis, in promoting neoplasia is increasingly apparent (Guri et al., 2017; Nomura et al., 2010; Watt et al., 2019). Previously, we demonstrated that enhanced FA uptake accompanies neoplastic progression in melanocytes (Henderson et al., 2019), and this was shown to be a metabolic

(D) UHPLC-lipidomic analysis of SKMEL105 cells following A922500 treatment. Fold change relative to DMSO (all conditions n = 3). TAG, triacylglycerides; LPC, lysophosphatidycholine; LPE, lysophosphatidylethanolamine.
(E) Lipid species fold changes in SKMEL105 following 72-h A922500 treatment plotted versus lipid species fold changes observed in Clone 3 cells.
(F) Protein expression of phospho-AMPK and phospho-RAPTOR following A922500 (DGAT1i) treatment.
(G) Oxygen consumption rate in A375 cells following 48-h A922500 treatment (top). Basal respiration, ATP production, and spare respiratory capacity were calculated (bottom) (mean ± SD, n = 3).
(H) Staining with JC-1 dye following A922500 treatment or following transfection with DGAT1 targeting siRNA. The percentage of cells that lost red aggregates was calculated by using 1 μM CCP as a positive control and comparing this with untreated cells to create two populations of cells for flow cytometry analysis (top; mean ± SD, n > 3). Protein expression of PINK1 and PARKIN following A922500 treatment (bottom).
(C, G, and H) For significance: *p < 0.05, **p < 0.01, and ***p < 0.001.

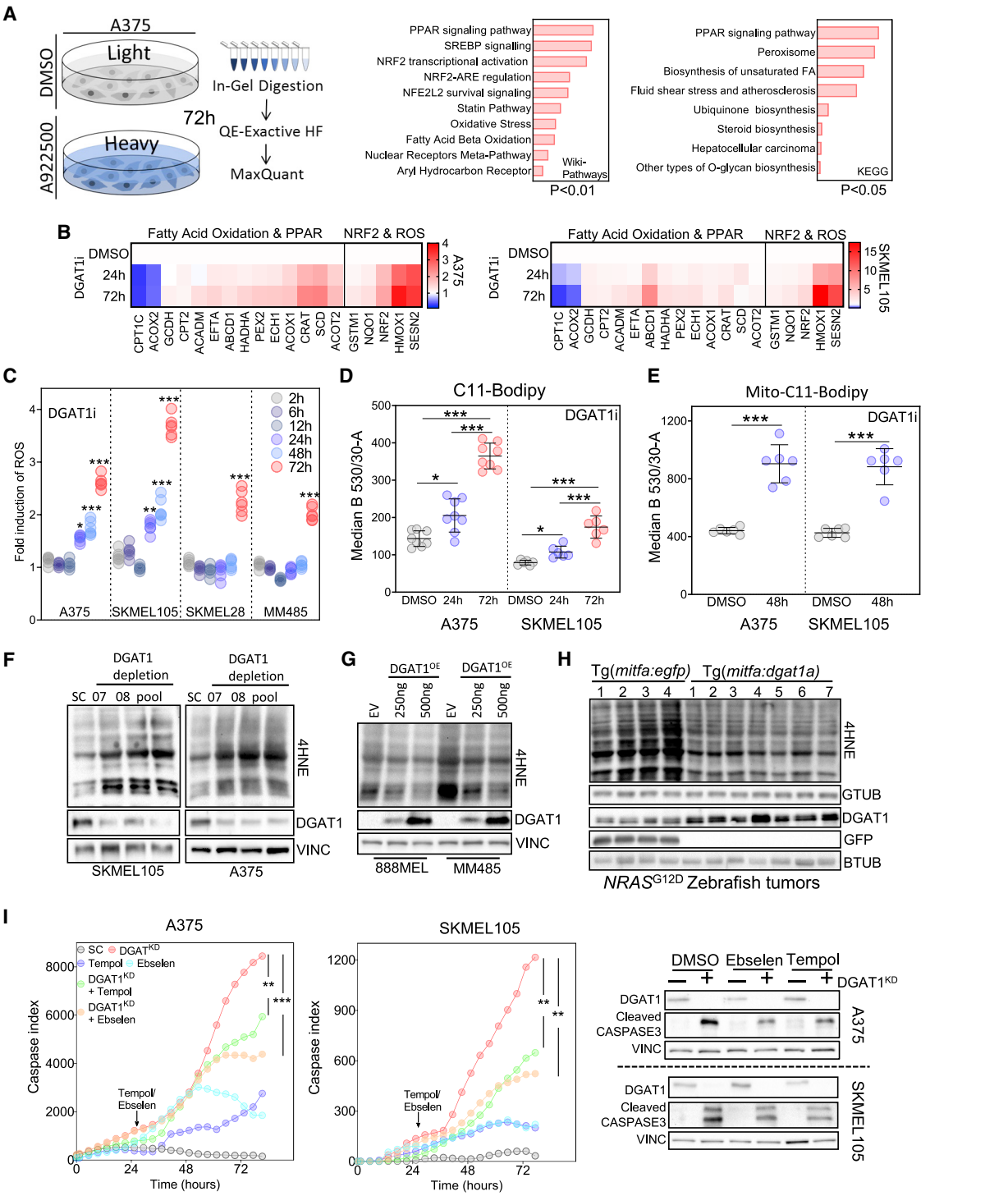


Figure 5. DGAT1 promotes survival of melanoma cells through suppressing ROS generation

(A) Total proteomics workflow (left). GEO of up-regulated proteins (114) ranked by combined score (wikipathways) or log-adjusted p values (metascape, right). (DMSO n = 3, A922500 n = 3).

(B) RT-qPCR analysis following A922500 treatment. Fold change relative to DMSO (mean, n = 3).

(C) ROS levels quantified using dihydroethidium (DHE) fluorescence following A922500 (DGAT1i) treatment. Fold change relative to DMSO (n > 4).

(D) C11-Bodipy staining following A922500 treatment. Mean fluorescence determined using FACS (mean ± SD, n > 6).

(E) Mito-C11-Bodipy staining following A922500 treatment. Mean fluorescence determined using FACS (mean ± SD, n > 6).

(legend continued on next page)

feature of tumor-initiating cells in particular (Pascual et al., 2017) and to drive melanoma tumor development, dissemination, and resistance to targeted therapy (Alicea et al., 2020; Zhang et al., 2018). However, the adaptations allowing melanoma cells to tolerate exposure to excess FA had been overlooked. We now demonstrate that DGAT1 is a *bona fide* metabolism oncoprotein that stimulates melanoma tumorigenesis by conferring protection against ROS, including lipid peroxidation, through inducing LD formation (see model; Figure 7).

DGAT2, a functionally related albeit structurally distinct enzyme, appeared less important than DGAT1 for melanoma LD formation, cell growth, and survival, as was shown previously to be the case for glioblastoma cells (Cheng et al., 2020). This distinction in oncopotency may reflect the distinct roles performed by DGAT1 and DGAT2 in LD formation and adipocyte biology: DGAT1 is exclusively ER resident and responsible for initiating LD formation (Wilfling et al., 2013) and for protecting ER membranes in adipocytes against lipotoxicity (Chitraju et al., 2019); DGAT2 can relocate to LD from the ER and is responsible for further enlarging LD when FA are abundant (Wilfling et al., 2013). Moreover, whereas *Dgat1*-null mice are viable, *Dgat2*-null mice die at birth lacking >90% of TAG (Stone et al., 2004).

We uncovered frequent *DGAT1* amplification and up-regulation in melanoma but also in many other cancers, notably ovarian, breast, uterine, esophageal, liver, pancreatic, head and neck, prostate, stomach, and lung cancers. Abundant LD have been observed in a range of cancers, consistent with widespread up-regulation of DGAT1 (Cheng et al., 2020; Cruz et al., 2020; Petan et al., 2018), indicating that DGAT1 is likely to perform an oncogenic role in these other cancers too. The co-occurrence of *DGAT1* amplification with *FASN*, *CD36*, or *MAGL* amplification in human cancers was significant, arguing for these co-aberrations being synergistic, in keeping with DGAT1 facilitating safe accumulation of FA in cancer cells.

We propose that FA sequestration as TAG in LD allows melanoma cells to accumulate and utilize FA safely, thereby avoiding cell death. As previously described in non-transformed embryonic fibroblasts (Nguyen et al., 2017) and glioblastoma cells (Cheng et al., 2020), we observed that DGAT1 suppression resulted in overloading of mitochondria with AcCa, driving excessive FAO and ROS production. Thus, the pathophysiological role of DGAT1 is to regulate the supply of FA to mitochondria within tolerable limits. Evidently, cancer cells, having elevated FA, require more DGAT1 to achieve this. Lipid peroxides are especially cytotoxic and are generated by the action of oxygen-centered radicals on PUFA preferentially (Gaschler and Stockwell, 2017). As PUFA are concentrated in LD, where they are shielded from peroxidation (Jarc et al., 2018), enhanced LD levels mediated by DGAT1 up-regulation confer dual protection from cell death, both by moderating FAO-triggered ROS production and by simultaneously suppressing PUFA peroxidation.

LD are known to protect non-transformed and transformed cells against a range of cellular stresses typically encountered in the tumor microenvironment, including nutrient deprivation and hypoxia (Cruz et al., 2020; Petan et al., 2018). Indeed, these conditions induce LD formation downstream of autophagy (Nguyen et al., 2017). Additionally, low pH up-regulates DGAT1 and consequently increases LD formation. In turn, LD are required for acidosis-induced metastasis (Corbet et al., 2020). Nutrient deprivation and hypoxia compromise *de novo* FA synthesis and desaturation. Unsaturated FA are essential for membrane fluidity and cell viability, and in the absence of desaturation reactions or the ability to scavenge unsaturated FA from the circulation, cancer cells must draw on LD for unsaturated FA in order to survive (Ackerman et al., 2018). The above roles for LD are consistent with our observation that the effect of DGAT1 suppression on cell growth was exacerbated by serum withdrawal and hypoxia and explains why conversely DGAT1 over-expression conferred its greatest growth advantage under these conditions.

The ability of DGAT1 inhibitor alone to suppress tumor growth was recently shown in a glioblastoma xenograft model (Cheng et al., 2020). However, we did not observe efficacy of DGAT1 inhibition alone in our mouse melanoma xenograft models, most likely due to a striking upregulation of the anti-ROS response. In order to antagonize this adaptation, we employed TTM, a clinically relevant SOD1 inhibitor. Combinatorial DGAT1 and SOD1 inhibition led to a profound impairment of melanoma growth *in vivo*. DGAT1 is pan-cancer amplified, and it remains to be determined to what extent other cancers can mount the anti-ROS responses we observed in our melanoma xenograft models. Thus, future studies should focus on evaluating the efficacy of DGAT1 inhibition alone, or in combination with inhibition of anti-ROS mechanisms, to induce the most well-tolerated and beneficial outcomes for cancer patients.

Limitations of the study

Our study relied on established human melanoma cell lines to explore DGAT1 function, and these may have adapted to *ex vivo* culture in ways that make them less representative than primary cells. To antagonize DGAT1 in cell cultures, we mostly used 30 μM A922500 to ensure complete inhibition over the 24–72 h required to fully deplete LD and to suppress cell viability. Although in excess of doses required to inhibit transiently DGAT1 catalytic activity, this concentration is still beneath that required

(F) 4-Hydroxynonenal (4HNE) protein conjugate abundance and protein expression of DGAT1 following transfection with either DGAT1-targeting siRNA or a scrambled control for 48 h.

(G) 4HNE protein conjugate abundance and protein expression of DGAT1 following transfection with either DGAT1 over-expression vector or an empty vector control for 48 h.

(H) 4HNE protein conjugate abundance and protein expression of Dgat1 and GFP in $NRAS^{G12D}$-positive EGFP-expressing (n = 4) and $NRAS^{G12D}$-positive Dgat1a-over-expressing (n = 7) tumors.

(I) Cleaved-caspase index following transfection of a DGAT1-targeting or scrambled siRNA. At 24 h, cells were treated with/without Tempol or Ebselen (mean, n = 3, outer). Corresponding protein expression of DGAT1 and cleaved caspase-3 (inner).

(C–E and I) For significance: *p < 0.05, **p < 0.01, and ***p < 0.001.

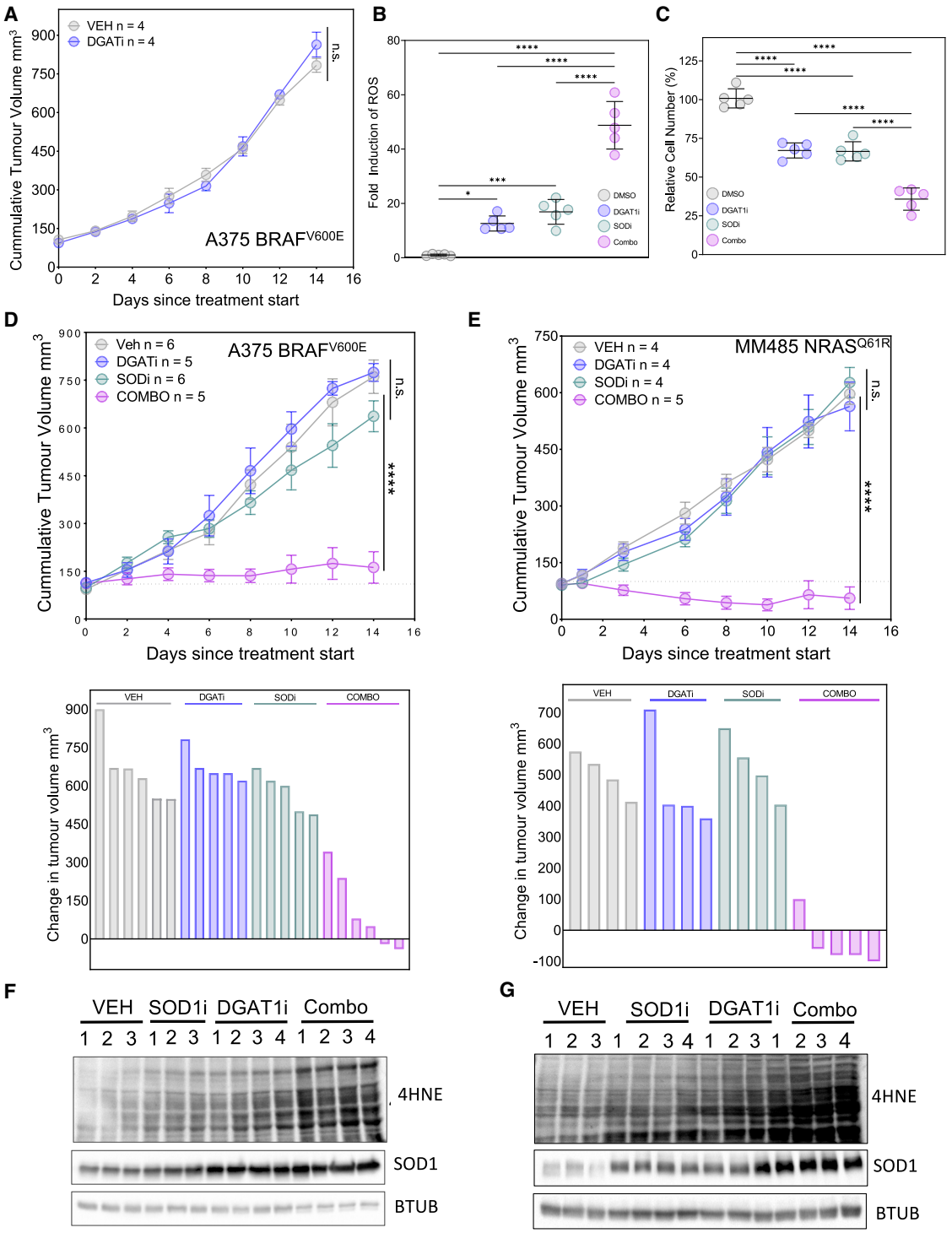


Figure 6. Combined DGAT1 and SOD1 inhibition halts tumor growth

(A) Nude mice bearing A375 tumors were treated (*n* = number of mice per group) with vehicle or A922500 (DGAT1i; 90 mg/kg/day) for 14 days. Data are presented as mean tumor volumes ±SD.

(B) Quantification of ROS levels by DHE fluorescence in A375 cells following treatment with either A922500 or ATN-224 (SOD1i) alone or in combination (combo). Fold change relative to DMSO (mean ± SD, n = 5).

(C) Relative number of A375 cells following treatment with either A922500 or ATN-224 alone or in combination. Fold change relative to DMSO (mean ± SD, n = 5).

(legend continued on next page)

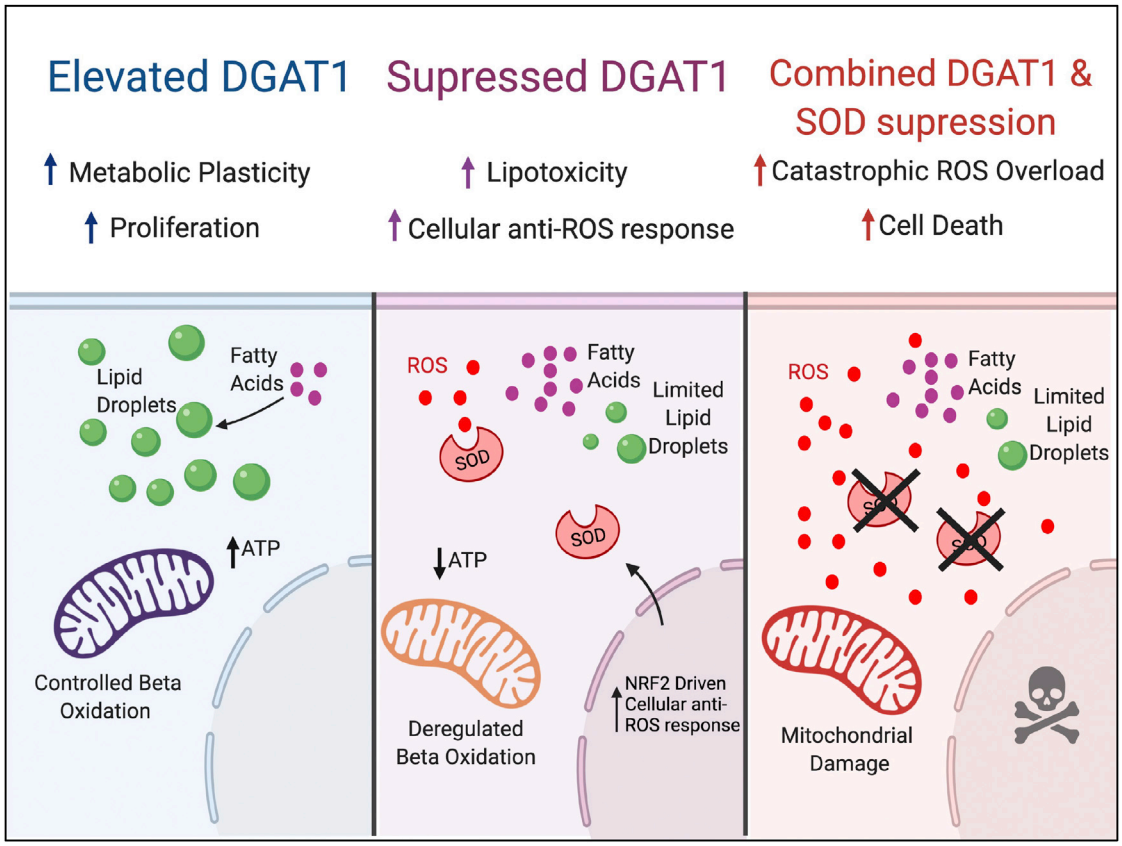


Figure 7. Model

Elevation of DGAT1 allows sequestration of fatty acids as triacylglycerides in lipid droplets and a controlled rate of fatty acid oxidation in mitochondria. If DGAT1 is suppressed, then fatty acids are oxidized, and cytotoxic reactive oxygen species are generated. However, these are neutralized through elevation of SOD1. However, if SOD1 is also suppressed, then the build-up of ROS is intolerable, and cells die.

to suppress the activity of related acyltransferases including DGAT2 (King et al., 2009). Moreover, an even higher dose of A922500 (47 μM) was unable to suppress LD dependent on DGAT2 or to markedly suppress viability in glioblastoma cells over-expressing DGAT2 (Cheng et al., 2020), consistent with A922500 being a selective DGAT1 inhibitor at this concentration. That we can reproduce the effects of A922500 on LD depletion and cell viability with other DGAT1 inhibitors and with siRNA targeting DGAT1 and observe the converse upon over-expressing DGAT1 further corroborate that the effects of A922500 are DGAT1 dependent. To demonstrate the interaction between DGAT1 and SOD1 on tumor growth *in vivo*, we have again relied on pharmacological agents that may have generated off-target effects that contributed to tumor growth inhibition. Additionally, durability of tumor growth suppression was not established in our study, nor host tolerance to chronic drug treatment, albeit that treatment was well tolerated by mice over the time course it was evaluated. As a further limitation, xenograft models do not fully recapitulate features of spontaneous tumors in notably developing in the absence of adaptive immunity. Potentially, PDX models, autochthonous genetically engineered mouse melanoma models, or *ex vivo* tumor explant culture might have allowed us to maintain more features of melanoma in which to assess the impact of DGAT1 depletion or antagonism.

STAR★METHODS

Detailed methods are provided in the online version of this paper and include the following:

- KEY RESOURCE TABLE
- RESOURCE AVAILABILITY
  - Lead contact
  - Materials availability

(D and E) Nude mice bearing A375 tumors (D) or MM485 tumors (E) were treated (*n* = number of mice per group) with vehicle, A922500 (90 mg/kg/day) or TTM (SODi; 5 mg/kg/day) alone or in combination for 14 days. Data are presented as mean tumor volumes ±SD (top) or change in individual tumor volume (bottom).
(F and G) 4HNE protein conjugate abundance and protein expression of SOD1 in A375 tumors (F) or MM485 tumors (G) treated with vehicle, A922500, or TTM alone or in combination.
(B–E) For significance: *p < 0.05, ***p < 0.001, and ****p < 0.0001.

- Data and code availability
- EXPERIMENTAL MODEL AND SUBJECT DETAILS
  - Zebrafish models
  - Mouse xenograft assays
  - Cell lines
- METHOD DETAILS
  - Compounds and antibodies
  - Plasmid cloning and transfection & siRNA transfection
  - Viral transduction
  - Protein lysate preparation and western blotting
  - Lipid droplet staining and image analysis
  - RNA isolation and real-time PCR analysis
  - Flow cytometry
  - Proliferation assays
  - Dihydroethidium assay
  - Cancer bioinformatics
- QUANTIFICATION AND STATISTICAL ANALYSIS
  - Proteomics
  - Lipidomics

SUPPLEMENTAL INFORMATION

Supplemental information can be found online at https://doi.org/10.1016/j.celrep.2022.110995.

ACKNOWLEDGMENTS

We thank staff of the Biological Mass Spectrometry facility, Bio-imaging facility, Biological Services facility, and Flow facility (all FBMH, UoM) for experimental support. We thank Olivia Sloss and Angeliki Malliri for critically reading the manuscript. A.H. was funded by grant ERC-2011-StG-282059 from the ERC, grant 610262 from the Melanoma Research Alliance, and a PhD studentship A23251 from Cancer Research UK to support D.J.W. C.F. was supported by the Wellcome Trust (Sir Henry Dale fellowship grant number 107636/Z/15/Z) and Biotechnology and Biological Sciences Research Council (grant number BB/R015864/1). The Medical Research Council (MRC) funded the Phenome Centre Birmingham (MR/M009157/1).

AUTHOR CONTRIBUTIONS

Cell-line-based experimentation: D.J.W., M.P.S., R.O., and J.H. Zebrafish models: A.P.B., D.J.W., H.J., M.G., and C.C. Mouse experiments: D.J.W., C.W.W., and B.A.T. Proteomics: M.P.S., D.J.W., P.F., and C.F. Lipidomics: D.J.W., M.P.S., A.D.S., A.J., G.R.L., and W.B.D. Bio-informatics analysis: D.J.W., J.W., H.F., C.F., and M.P.S. Experimental design: D.J.W., A.P.B., C.F., M.P.S, and A.H. Sample acquisition and cell lines: P.L., C.W., M.P.S., and A.H. Conceptualization: A.P.B., M.P.S., and A.H. Drafting of manuscript: D.J.W., A.P.B., M.P.S., and A.H. Revisions by all authors. Acquisition of funds: C.W., C.F., and A.H. Study supervision: M.P.S. and A.H.

DECLARATION OF INTERESTS

The authors declare no competing interests.

Received: September 19, 2021
Revised: March 30, 2022
Accepted: June 1, 2022
Published: June 21, 2022

REFERENCES

Ackerman, D., and Simon, M.C. (2014). Hypoxia, lipids, and cancer: surviving the harsh tumor microenvironment. Trends Cell Biol. *24*, 472–478. https://doi.org/10.1016/j.tcb.2014.06.001.

Ackerman, D., Tumanov, S., Qiu, B., Michalopoulou, E., Spata, M., Azzam, A., Xie, H., Simon, M.C., and Kamphorst, J.J. (2018). Triglycerides promote lipid homeostasis during hypoxic stress by balancing fatty acid saturation. Cell Rep. *24*, 2596–2605.e5. https://doi.org/10.1016/j.celrep.2018.08.015.

Alicea, G.M., Rebecca, V.W., Goldman, A.R., Fane, M.E., Douglass, S.M., Behera, R., Webster, M.R., Kugel, C.H., 3rd, Ecker, B.L., Caino, M.C., et al. (2020). Changes in aged fibroblast lipid metabolism induce age-dependent melanoma cell resistance to targeted therapy via the fatty acid transporter FATP2. Cancer Discov. *10*, 1282–1295. https://doi.org/10.1158/2159-8290.Cd-20-0329.

Anaya, J. (2016). OncoLnc: linking TCGA survival data to mRNAs, miRNAs, and lncRNAs. Peerj Comput. Sci. *2*, e67. https://doi.org/10.7717/peerj-cs.67.

Andrejeva, G., and Rathmell, J.C. (2017). Similarities and distinctions of cancer and immune metabolism in inflammation and tumors. Cell Metabol. *26*, 49–70. https://doi.org/10.1016/j.cmet.2017.06.004.

Bae, S.H., Sung, S.H., Oh, S.Y., Lim, J.M., Lee, S.K., Park, Y.N., Lee, H.E., Kang, D., and Rhee, S.G. (2013). Sestrins activate Nrf2 by promoting p62-dependent autophagic degradation of Keap1 and prevent oxidative liver damage. Cell Metabol. *17*, 73–84. https://doi.org/10.1016/j.cmet.2012.12.002.

Bastian, B.C., LeBoit, P.E., Hamm, H., Bröcker, E.B., and Pinkel, D. (1998). Chromosomal gains and losses in primary cutaneous melanomas detected by comparative genomic hybridization. Cancer Res. *58*, 2170–2175.

Brookheart, R.T., Michel, C.I., and Schaffer, J.E. (2009). As a matter of fat. Cell Metabol. *10*, 9–12. https://doi.org/10.1016/j.cmet.2009.03.011.

Casar, B., Badrock, A.P., Jiménez, I., Arozarena, I., Colón-Bolea, P., Lorenzo-Martín, L.F., Barinaga-Rementería, I., Barriuso, J., Cappitelli, V., Donoghue, D.J., et al. (2018). RAS at the Golgi antagonizes malignant transformation through PTPRκ-mediated inhibition of ERK activation. Nat. Commun. *9*, 3595. https://doi.org/10.1038/s41467-018-05941-8.

Ceol, C.J., Houvras, Y., Jane-Valbuena, J., Bilodeau, S., Orlando, D.A., Battisti, V., Fritsch, L., Lin, W.M., Hollmann, T.J., Ferré, F., et al. (2011). The histone methyltransferase SETDB1 is recurrently amplified in melanoma and accelerates its onset. Nature *471*, 513–517. https://doi.org/10.1038/nature09806.

Chambers, M.C., Maclean, B., Burke, R., Amodei, D., Ruderman, D.L., Neumann, S., Gatto, L., Fischer, B., Pratt, B., Egertson, J., et al. (2012). A cross-platform toolkit for mass spectrometry and proteomics. Nat. Biotechnol. *30*, 918–920. https://doi.org/10.1038/nbt.2377.

Chen, E.Y., Tan, C.M., Kou, Y., Duan, Q., Wang, Z., Meirelles, G.V., Clark, N.R., and Ma'ayan, A. (2013). Enrichr: interactive and collaborative HTML5 gene list enrichment analysis tool. BMC Bioinf. *14*, 128. https://doi.org/10.1186/1471-2105-14-128.

Chen, M., and Huang, J. (2019). The expanded role of fatty acid metabolism in cancer: new aspects and targets. Precis. Clin. Med. *2*, 183–191. https://doi.org/10.1093/pcmedi/pbz017.

Cheng, X., Geng, F., Pan, M., Wu, X., Zhong, Y., Wang, C., Tian, Z., Cheng, C., Zhang, R., Puduvalli, V., et al. (2020). Targeting DGAT1 ameliorates glioblastoma by increasing fat catabolism and oxidative stress. Cell Metabol. *32*, 229–242.e8. https://doi.org/10.1016/j.cmet.2020.06.002.

Chitraju, C., Walther, T.C., and Farese, R.V., Jr. (2019). The triglyceride synthesis enzymes DGAT1 and DGAT2 have distinct and overlapping functions in adipocytes. J. Lipid Res. *60*, 1112–1120. https://doi.org/10.1194/jlr.M093112.

Conrad, M., and Pratt, D.A. (2019). The chemical basis of ferroptosis. Nat. Chem. Biol. *15*, 1137–1147. https://doi.org/10.1038/s41589-019-0408-1.

Corbet, C., Bastien, E., Santiago de Jesus, J.P., Dierge, E., Martherus, R., Vander Linden, C., Doix, B., Degavre, C., Guilbaud, C., Petit, L., et al. (2020). TGFβ2-induced formation of lipid droplets supports acidosis-driven EMT and the metastatic spreading of cancer cells. Nat. Commun. *11*, 454. https://doi.org/10.1038/s41467-019-14262-3.

Cox, J., Neuhauser, N., Michalski, A., Scheltema, R.A., Olsen, J.V., and Mann, M. (2011). Andromeda: a peptide search engine integrated into the MaxQuant environment. J. Proteome Res. *10*, 1794–1805. https://doi.org/10.1021/pr101065j.

Cruz, A.L.S., Barreto, E.d.A., Fazolini, N.P.B., Viola, J.P.B., and Bozza, P.T. (2020). Lipid droplets: platforms with multiple functions in cancer hallmarks. Cell Death Dis. *11*, 105. https://doi.org/10.1038/s41419-020-2297-3.

Dalleau, S., Baradat, M., Guéraud, F., and Huc, L. (2013). Cell death and diseases related to oxidative stress: 4-hydroxynonenal (HNE) in the balance. Cell Death Differ. *20*, 1615–1630. https://doi.org/10.1038/cdd.2013.138.

DeBerardinis, R.J., and Chandel, N.S. (2016). Fundamentals of cancer metabolism. Sci. Adv. *2*, e1600200. https://doi.org/10.1126/sciadv.1600200.

DeVita, R.J., and Pinto, S. (2013). Current status of the Research and development of diacylglycerol O-acyltransferase 1 (DGAT1) inhibitors. J. Med. Chem. *56*, 9820–9825. https://doi.org/10.1021/jm4007033.

Dieterle, F., Ross, A., Schlotterbeck, G., and Senn, H. (2006). Probabilistic quotient normalization as robust method to account for dilution of complex biological mixtures. Application in 1H NMR metabonomics. Anal. Chem. *78*, 4281–4290. https://doi.org/10.1021/ac051632c.

Dreger, H., Westphal, K., Wilck, N., Baumann, G., Stangl, V., Stangl, K., and Meiners, S. (2010). Protection of vascular cells from oxidative stress by proteasome inhibition depends on Nrf2. Cardiovasc. Res. *85*, 395–403. https://doi.org/10.1093/cvr/cvp279.

Ehlers, J.P., Worley, L., Onken, M.D., and Harbour, J.W. (2005). DDEF1 is located in an amplified region of chromosome 8q and is overexpressed in uveal melanoma. Clin. Cancer Res. *11*, 3609–3613. https://doi.org/10.1158/1078-0432.CCR-04-1941.

Falomir-Lockhart, L.J., Cavazzutti, G.F., Giménez, E., and Toscani, A.M. (2019). Fatty acid signaling mechanisms in neural cells: fatty acid receptors. Front. Cell. Neurosci. *13*, 162. https://doi.org/10.3389/fncel.2019.00162.

Fischer, G.M., Vashisht Gopal, Y.N., McQuade, J.L., Peng, W., DeBerardinis, R.J., and Davies, M.A. (2018). Metabolic strategies of melanoma cells: mechanisms, interactions with the tumor microenvironment, and therapeutic implications. Pigment Cell Melanoma Res. *31*, 11–30. https://doi.org/10.1111/pcmr.12661.

Flavin, R., Peluso, S., Nguyen, P.L., and Loda, M. (2010). Fatty acid synthase as a potential therapeutic target in cancer. Future Oncol. *6*, 551–562. https://doi.org/10.2217/fon.10.11.

Francavilla, C., Papetti, M., Rigbolt, K.T.G., Pedersen, A.K., Sigurdsson, J.O., Cazzamali, G., Karemore, G., Blagoev, B., and Olsen, J.V. (2016). Multilayered proteomics reveals molecular switches dictating ligand-dependent EGFR trafficking. Nat. Struct. Mol. Biol. *23*, 608–618. https://doi.org/10.1038/nsmb.3218.

Gao, J., Aksoy, B.A., Dogrusoz, U., Dresdner, G., Gross, B., Sumer, S.O., Sun, Y., Jacobsen, A., Sinha, R., Larsson, E., et al. (2013). Integrative analysis of complex cancer genomics and clinical profiles using the cBioPortal. Sci. Signal. *6*, pl1. https://doi.org/10.1126/scisignal.2004088.

Garaeva, A.A., Kovaleva, I.E., Chumakov, P.M., and Evstafieva, A.G. (2016). Mitochondrial dysfunction induces SESN2 gene expression through activating transcription factor 4. Cell Cycle *15*, 64–71. https://doi.org/10.1080/15384101.2015.1120929.

Gaschler, M.M., and Stockwell, B.R. (2017). Lipid peroxidation in cell death. Biochem. Biophys. Res. Commun. *482*, 419–425. https://doi.org/10.1016/j.bbrc.2016.10.086.

Guri, Y., Colombi, M., Dazert, E., Hindupur, S.K., Roszik, J., Moes, S., Jenoe, P., Heim, M.H., Riezman, I., Riezman, H., and Hall, M.N. (2017). mTORC2 promotes tumorigenesis via lipid synthesis. Cancer Cell *32*, 807–823.e12. https://doi.org/10.1016/j.ccell.2017.11.011.

Henderson, F., Johnston, H.R., Badrock, A.P., Jones, E.A., Forster, D., Nagaraju, R.T., Evangelou, C., Kamarashev, J., Green, M., Fairclough, M., et al. (2019). Enhanced fatty acid scavenging and glycerophospholipid metabolism accompany melanocyte neoplasia progression in zebrafish. Cancer Res. *79*, 2136–2151. https://doi.org/10.1158/0008-5472.CAN-18-2409.

Jarc, E., Kump, A., Malavašič, P., Eichmann, T.O., Zimmermann, R., and Petan, T. (2018). Lipid droplets induced by secreted phospholipase A2 and unsaturated fatty acids protect breast cancer cells from nutrient and lipotoxic stress. Biochim. Biophys. Acta Mol. Cell Biol. Lipids *1863*, 247–265. https://doi.org/10.1016/j.bbalip.2017.12.006.

Juarez, J.C., Betancourt, O., Pirie-Shepherd, S.R., Guan, X., Price, M.L., Shaw, D.E., Mazar, A.P., and Doñate, F. (2006). Copper binding by tetrathiomolybdate attenuates angiogenesis and tumor cell proliferation through the inhibition of superoxide dismutase 1. Clin. Cancer Res. *12*, 4974–4982. https://doi.org/10.1158/1078-0432.CCR-06-0171.

King, A.J., Segreti, J.A., Larson, K.J., Souers, A.J., Kym, P.R., Reilly, R.M., Zhao, G., Mittelstadt, S.W., and Cox, B.F. (2009). Diacylglycerol acyltransferase 1 inhibition lowers serum triglycerides in the Zucker fatty rat and the hyperlipidemic hamster. J. Pharmacol. Exp. Ther. *330*, 526–531. https://doi.org/10.1124/jpet.109.154047.

Koundouros, N., and Poulogiannis, G. (2020). Reprogramming of fatty acid metabolism in cancer. Br. J. Cancer *122*, 4–22. https://doi.org/10.1038/s41416-019-0650-z.

Koves, T.R., Ussher, J.R., Noland, R.C., Slentz, D., Mosedale, M., Ilkayeva, O., Bain, J., Stevens, R., Dyck, J.R.B., Newgard, C.B., et al. (2008). Mitochondrial overload and incomplete fatty acid oxidation contribute to skeletal muscle insulin resistance. Cell Metabol. *7*, 45–56. https://doi.org/10.1016/j.cmet.2007.10.013.

Lee, S.Y., Ju, M.K., Jeon, H.M., Lee, Y.J., Kim, C.H., Park, H.G., Han, S.I., and Kang, H.S. (2018). Oncogenic metabolism acts as a prerequisite step for induction of cancer metastasis and cancer stem cell phenotype. Oxid. Med. Cell. Longev. *2018*, 1027453. https://doi.org/10.1155/2018/1027453.

Lengyel, E., Makowski, L., DiGiovanni, J., and Kolonin, M.G. (2018). Cancer as a matter of fat: the crosstalk between adipose tissue and tumors. Trends Cancer *4*, 374–384. https://doi.org/10.1016/j.trecan.2018.03.004.

Liao, Y., Smyth, G.K., and Shi, W. (2014). featureCounts: an efficient general purpose program for assigning sequence reads to genomic features. Bioinformatics *30*, 923–930. https://doi.org/10.1093/bioinformatics/btt656.

Libiseller, G., Dvorzak, M., Kleb, U., Gander, E., Eisenberg, T., Madeo, F., Neumann, S., Trausinger, G., Sinner, F., Pieber, T., and Magnes, C. (2015). IPO: a tool for automated optimization of XCMS parameters. BMC Bioinf. *16*, 118. https://doi.org/10.1186/s12859-015-0562-8.

Lowndes, S.A., Adams, A., Timms, A., Fisher, N., Smythe, J., Watt, S.M., Joel, S., Donate, F., Hayward, C., Reich, S., et al. (2008). Phase I study of copper-binding agent ATN-224 in patients with advanced solid tumors. Clin. Cancer Res. *14*, 7526–7534. https://doi.org/10.1158/1078-0432.CCR-08-0315.

Lyssiotis, C.A., and Kimmelman, A.C. (2017). Metabolic interactions in the tumor microenvironment. Trends Cell Biol. *27*, 863–875. https://doi.org/10.1016/j.tcb.2017.06.003.

Ma, C.-s., Lv, Q.-m., Zhang, K.-r., Tang, Y.-b., Zhang, Y.-f., Shen, Y., Lei, H.-m., and Zhu, L. (2021). NRF2-GPX4/SOD2 axis imparts resistance to EGFR-tyrosine kinase inhibitors in non-small-cell lung cancer cells. Acta Pharmacol. Sin. *42*, 613–623. https://doi.org/10.1038/s41401-020-0443-1.

Maan, M., Peters, J.M., Dutta, M., and Patterson, A.D. (2018). Lipid metabolism and lipophagy in cancer. Biochem. Biophys. Res. Commun. *504*, 582–589. https://doi.org/10.1016/j.bbrc.2018.02.097.

Mermel, C.H., Schumacher, S.E., Hill, B., Meyerson, M.L., Beroukhim, R., and Getz, G. (2011). GISTIC2.0 facilitates sensitive and confident localization of the targets of focal somatic copy-number alteration in human cancers. Genome Biol. *12*, R41. https://doi.org/10.1186/gb-2011-12-4-r41.

Molenaar, R.J., Maciejewski, J.P., Wilmink, J.W., and van Noorden, C.J.F. (2018). Wild-type and mutated IDH1/2 enzymes and therapy responses. Oncogene *37*, 1949–1960. https://doi.org/10.1038/s41388-017-0077-z.

Nguyen, T.B., Louie, S.M., Daniele, J.R., Tran, Q., Dillin, A., Zoncu, R., Nomura, D.K., and Olzmann, J.A. (2017). DGAT1-Dependent lipid droplet biogenesis protects mitochondrial function during starvation-induced autophagy. Dev. Cell *42*, 9–21.e5. https://doi.org/10.1016/j.devcel.2017.06.003.

Nieman, K.M., Kenny, H.A., Penicka, C.V., Ladanyi, A., Buell-Gutbrod, R., Zillhardt, M.R., Romero, I.L., Carey, M.S., Mills, G.B., Hotamisligil, G.S., et al. (2011). Adipocytes promote ovarian cancer metastasis and provide energy

for rapid tumor growth. Nat. Med. *17*, 1498–1503. https://doi.org/10.1038/nm.2492.

Nomura, D.K., Long, J.Z., Niessen, S., Hoover, H.S., Ng, S.-W., and Cravatt, B.F. (2010). Monoacylglycerol lipase regulates a fatty acid network that promotes cancer pathogenesis. Cell *140*, 49–61. https://doi.org/10.1016/j.cell.2009.11.027.

Olsen, J.V., Blagoev, B., Gnad, F., Macek, B., Kumar, C., Mortensen, P., and Mann, M. (2006). Global, in vivo, and site-specific phosphorylation dynamics in signaling networks. Cell *127*, 635–648. https://doi.org/10.1016/j.cell.2006.09.026.

Park, E.Y., and Rho, H.M. (2002). The transcriptional activation of the human copper/zinc superoxide dismutase gene by 2, 3, 7, 8-tetrachlorodibenzo-p-dioxin through two different regulator sites, the antioxidant responsive element and xenobiotic responsive element. Mol. Cell. Biochem. *240*, 47–55. https://doi.org/10.1023/a:1020600509965.

Parsons, H.M., Ludwig, C., Günther, U.L., and Viant, M.R. (2007). Improved classification accuracy in 1- and 2-dimensional NMR metabolomics data using the variance stabilising generalised logarithm transformation. BMC Bioinf. *8*, 234. https://doi.org/10.1186/1471-2105-8-234.

Pascual, G., Avgustinova, A., Mejetta, S., Martín, M., Castellanos, A., Attolini, C.S.O., Berenguer, A., Prats, N., Toll, A., Hueto, J.A., et al. (2017). Targeting metastasis-initiating cells through the fatty acid receptor CD36. Nature *541*, 41–45. https://doi.org/10.1038/nature20791.

Petan, T., Jarc, E., and Jusović, M. (2018). Lipid droplets in cancer: guardians of fat in a stressful world. Molecules *23*, 1941. https://doi.org/10.3390/molecules23081941.

Redman, B.G., Esper, P., Pan, Q., Dunn, R.L., Hussain, H.K., Chenevert, T., Brewer, G.J., and Merajver, S.D. (2003). Phase II trial of tetrathiomolybdate in patients with advanced kidney cancer. Clin. Cancer Res. *9*, 1666–1672.

Rhodes, D.R., Yu, J., Shanker, K., Deshpande, N., Varambally, R., Ghosh, D., Barrette, T., Pander, A., and Chinnaiyan, A.M. (2004). ONCOMINE: a cancer microarray database and integrated data-mining platform. Neoplasia *6*, 1–6. https://doi.org/10.1016/s1476-5586(04)80047-2.

Sajadimajd, S., and Khazaei, M. (2018). Oxidative stress and cancer: the role of Nrf2. Curr. Cancer Drug Targets *18*, 538–557. https://doi.org/10.2174/1568009617666171002144228.

Schindelin, J., Arganda-Carreras, I., Frise, E., Kaynig, V., Longair, M., Pietzsch, T., Preibisch, S., Rueden, C., Saalfeld, S., Schmid, B., et al. (2012). Fiji: an open-source platform for biological-image analysis. Nat. Methods *9*, 676–682. https://doi.org/10.1038/nmeth.2019.

Schlagbauer-Wadl, H., Griffioen, M., van Elsas, A., Schrier, P.I., Pustelnik, T., Eichler, H.G., Wolff, K., Pehamberger, H., and Jansen, B. (1999). Influence of increased c-Myc expression on the growth characteristics of human melanoma. J. Invest. Dermatol. *112*, 332–336. https://doi.org/10.1046/j.1523-1747.1999.00506.x.

Singh, A., Venkannagari, S., Oh, K.H., Zhang, Y.Q., Rohde, J.M., Liu, L., Nimmagadda, S., Sudini, K., Brimacombe, K.R., Gajghate, S., et al. (2016). Small molecule inhibitor of NRF2 selectively intervenes therapeutic resistance in KEAP1-deficient NSCLC tumors. ACS Chem. Biol. *11*, 3214–3225. https://doi.org/10.1021/acschembio.6b00651.

Skouta, R., Dixon, S.J., Wang, J., Dunn, D.E., Orman, M., Shimada, K., Rosenberg, P.A., Lo, D.C., Weinberg, J.M., Linkermann, A., and Stockwell, B.R. (2014). Ferrostatins inhibit oxidative lipid damage and cell death in diverse disease models. J. Am. Chem. Soc. *136*, 4551–4556. https://doi.org/10.1021/ja411006a.

Smith, C.A., Want, E.J., O'Maille, G., Abagyan, R., and Siuzdak, G. (2006). XCMS: processing mass spectrometry data for metabolite profiling using nonlinear peak alignment, matching, and identification. Anal. Chem. *78*, 779–787. https://doi.org/10.1021/ac051437y.

Stone, S.J., Myers, H.M., Watkins, S.M., Brown, B.E., Feingold, K.R., Elias, P.M., and Farese, R.V., Jr. (2004). Lipopenia and skin barrier abnormalities in DGAT2-deficient mice. J. Biol. Chem. *279*, 11767–11776. https://doi.org/10.1074/jbc.M311000200.

Sumner, L.W., Amberg, A., Barrett, D., Beale, M.H., Beger, R., Daykin, C.A., Fan, T.W.M., Fiehn, O., Goodacre, R., Griffin, J.L., et al. (2007). Proposed minimum reporting standards for chemical analysis chemical analysis working group (CAWG) metabolomics standards initiative (MSI). Metabolomics *3*, 211–221. https://doi.org/10.1007/s11306-007-0082-2.

Taylor, R.C., Acquaah-Mensah, G., Singhal, M., Malhotra, D., and Biswal, S. (2008). Network inference algorithms elucidate Nrf2 regulation of mouse lung oxidative stress. PLoS Comput. Biol. *4*, e1000166. https://doi.org/10.1371/journal.pcbi.1000166.

Venkatesan, A.M., Vyas, R., Gramann, A.K., Dresser, K., Gujja, S., Bhatnagar, S., Chhangawala, S., Gomes, C.B.F., Xi, H.S., Lian, C.G., et al. (2018). Ligand-activated BMP signaling inhibits cell differentiation and death to promote melanoma. J. Clin. Invest. *128*, 294–308. https://doi.org/10.1172/JCI92513.

Watt, M.J., Clark, A.K., Selth, L.A., Haynes, V.R., Lister, N., Rebello, R., Porter, L.H., Niranjan, B., Whitby, S.T., Lo, J., et al. (2019). Suppressing fatty acid uptake has therapeutic effects in preclinical models of prostate cancer. Sci. Transl. Med. *11*, eaau5758. https://doi.org/10.1126/scitranslmed.aau5758.

Wilfling, F., Wang, H., Haas, J.T., Krahmer, N., Gould, T.J., Uchida, A., Cheng, J.X., Graham, M., Christiano, R., Fröhlich, F., et al. (2013). Triacylglycerol synthesis enzymes mediate lipid droplet growth by relocalizing from the ER to lipid droplets. Dev. Cell *24*, 384–399. https://doi.org/10.1016/j.devcel.2013.01.013.

Zhang, M., Di Martino, J.S., Bowman, R.L., Campbell, N.R., Baksh, S.C., Simon-Vermot, T., Kim, I.S., Haldeman, P., Mondal, C., Yong-Gonzales, V., et al. (2018). Adipocyte-derived lipids mediate melanoma progression via FATP proteins. Cancer Discov. *8*, 1006–1025. https://doi.org/10.1158/2159-8290.CD-17-1371.

Zhou, Y., Zhou, B., Pache, L., Chang, M., Khodabakhshi, A.H., Tanaseichuk, O., Benner, C., and Chanda, S.K. (2019). Metascape provides a biologist-oriented resource for the analysis of systems-level datasets. Nat. Commun. *10*, 1523. https://doi.org/10.1038/s41467-019-09234-6.

STAR★METHODS

KEY RESOURCE TABLE

REAGENT or RESOURCE	SOURCE	IDENTIFIER
Antibodies		
Rabbit monoclonal anti-DGAT1	Abcam	RRID: ab181180
Mouse monoclonal anti-Vinculin	Proteintech	RRID: 66305-1-Ig
Rabbit monoclonal anti- GFP (D5.1) XP	Cell Signaling	RRID: Cat# 2956
Rabbit polyclonal anti-Beta Tubulin	Proteintech	RRID: 10094-1-AP
Rabbit polyclonal anti-Phospho-AMPKα (Thr172)	Cell Signaling	RRID: Cat# 50081
Rabbit polyclonal anti-Phospho-Raptor (Ser792)	Cell Signaling	RRID: Cat# 2083
Rabbit polyclonal anti-PINK1	Proteintech	RRID: 23274-1-AP
Rabbit polyclonal anti-Parkin	Proteintech	RRID: 14060-1-AP
Rabbit polyclonal anti-Caspase-3	Cell Signaling	RRID: Cat# 9662
Rabbit polyclonal anti-SOD1	Proteintech	RRID: 10269-1-AP
Rabbit polyclonal anti-SOD2	Proteintech	RRID: 24127-1-AP
Mouse monoclonal anti-GAPDH	Proteintech	RRID: 60004-1-Ig
Rabbit monoclonal anti-Phospho-Akt (Ser473)	Cell Signaling	RRID: Cat# 4060
Mouse monoclonal anti-ERK 1/2	Santa Cruz Biotechnology	RRID: sc-135900
Rabbit monoclonal phospho-ERK 1/2 (Thr202/Tyr204)	Cell Signaling	RRID: Cat# 4370
Rabbit polyclonal anti-4 Hydroxynonenal	Abcam	RRID: ab46545
Rabbit Sestrin 2 Polyclonal antibody	Proteintech	RRID: 10795-1-AP
Mouse monoclonal anti-γ-Tubulin	Sigma-Aldrich	RRID: T5326
Bacterial and virus strains		
NEB® 10-beta Competent E. coli (High Efficiency)	New England Biolabs	Cat. No: C3019H
Chemicals, peptides, and recombinant proteins		
Trypsin porcine pancreas (proteomics grade)	Sigma-Aldrich	T6567
Lysyl Endopeptidase	FUJIFILM Wako Chemicals	129-02541
Pre-cast gradient gel: Nu-PAGE 4–12% Bis-Tris Gel 1.0 mm 10 well	Invitrogen	NP0321BOX
Sep-Pak Classic C18 cartridges	Waters	WAT051910
Solid Phase Extraction Disk "Empore" C18 (Octadecyl) 3M	Agilent Technologies	2215
Solid Phase Extraction Disk "Empore" C8 (Octyl) 3M	Agilent Technologies	2214
L-ARGININE:HCL	Cambridge Isotope Laboratories	CLM-2265-H-0.25
L-ARGININE:HCL	Cambridge Isotope Laboratories	CNLM-539-H-0.5
L-ARGININE:HCL	Sigma-Aldrich	A6969
L-LYSINE:2HCL	Cambridge Isotope Laboratories	DLM-2640-0.5
L-LYSINE:2HCL	Cambridge Isotope Laboratories	CNLM-291-H-0.5
L-LYSINE:2HCL	Sigma-Aldrich	L8662
2,5-Dihydroxybenzoic acid	Sigma-Aldrich	85707
RPMI 1640 Medium for SILAC	ThermoFisher Scientific	88365

(*Continued on next page*)

Continued

REAGENT or RESOURCE	SOURCE	IDENTIFIER
TRIzol™ Reagent	ThermoFisher Scientific	Cat. No. 15596026
T863- DGAT1 Inhibitor	Sigma-Aldrich	SML0539-5MG
A922500- DGAT1 Inhibitor	Stratech Scientific Ltd	A4382-APE-50mg
AZD3988- DGAT1 Inhibitor	Tocris Bioscience	Cat. No. 4837
AZD7687- DGAT1 Inhibitor	Stratech Scientific Ltd	A3215-APE-5mg
PF 4708671	Generon	A11755-25
Polybrene Transfection Reagent	Millipore UK Limited	R-1003-G
PARAQUAT DICHLORIDE X-HYDRATE PESTANAL	Sigma-Aldrich	36541-100MG
Menadione	Fluorochem Limited	049845-25G
Oligomycin A	Sigma-Aldrich	75351
FCCP	Cambridge Bioscience Limited	2398-5
Oligomycin Complex	Stratech Scientific Ltd	C3007-APE-5mg
Rotenone, PESTANAL, analytical standard	Scientific Laboratory Supplies Ltd	45656-250MG
Antimycin A from Streptomyces sp.	Sigma-Aldrich	A8674
PF-06424439- DGAT2 Inhibitor	Sigma-Aldrich	PZ0233
Ebselen	Sigma-Aldrich	E3520-25MG
Tempol	Stratech Scientific Ltd	S2910-SEL-100mg
Etomoxir	Stratech Scientific Ltd	A3404-APE-10mg
Ferrostatin-1	Stratech Scientific Ltd	S7243
ML385	Selleckchem	S8790
ATN-224	Cayman Chemical	23553
Ammonium tetrathiomolybdate	Sigma-Aldrich	323446
BODIPY 581/591 C11 (Lipid Peroxidation Sensor)	ThermoFisher Scientific	D3861
MitoPerOx, fluorescent mitochondria-targeted lipid peroxidation probe	Abcam	ab146820
BODIPY™ 493/503 (4,4-Difluoro-1,3,5,7,8-Pentamethyl-4-Bora-3a,4a-Diaza-s-Indacene)	Life Technologies	D3922
HCS LipidTOX™ Green Neutral Lipid Stain	ThermoFisher Scientific	H34475
Molecular Probes MitoSOX Red Mitochondrial Superoxide Indicator	ThermoFisher Scientific	11579096
DIHYDROETHIDIUM	Cambridge Bioscience	12013-5mg-CAY
H2DCFDA	Tocris Bioscience	5935/100
Hoechst 33342	New England Biolabs	4082S
Lipofectamine RNAiMAX Transfection Reagent	ThermoFisher Scientific	10601435
Lipofectamine Transfection Reagent	Life Technologies	18324020
FuGENE HD Transfection Reagent	Promega UK	E2311
Seahorse XFe96 FluxPak mini	Agilent Technologies	102601-100
Seahorse XF DMEM medium, pH 7.4, 500 mL.	Agilent Technologies	103575-100
qPCRBIO SyGreen Mix Separate-ROX	PCR Biosystems	PB20.14
Crystal violet solution	Sigma-Aldrich	V5265-250ML
Critical commercial assays		
Click-iT EdU Alexa Fluor 488 Imaging Kit-1 kit	Life Technologies	C10337
MitoProbe JC-1 Assay Kit	Life Technologies	M34152
CellEvent Caspase-3/7 Green Detection Reagent	Life Technologies	C10423

(*Continued on next page*)

Continued

REAGENT or RESOURCE	SOURCE	IDENTIFIER
ProtoScript; II First Strand cDNA Synthesis Kit	New England Biolabs	E6560L
RNeasy RNA Extraction Kit	Qiagen	74136
Deposited data		
Proteome data	ProteomeXchange Consortium	PRIDE: PXD017487
Experimental models: Cell lines		
normal human melanocytes	Cascade Biologics	C0245C
888MEL	Gift from Claudia Wellbrock	CVCL 4632
Lenti-X™ 293T Cell Line	Takara bio	632180
888MEL Clone 1–3 DGAT Overexpression	This study	N/A
SKMEL28	ATCC	HTB-72
SKMEL105	Memorial Sloan Kettering Cancer Center	N/A
A375	ATCC	CRL- 1619
MM485	Gift from Claudia Wellbrock	CVCL_2610
WM266-4	Gift from Claudia Wellbrock	CVCL_2765
LOX-IMVI	Sigma-Aldrich	SCC201
SKMEL5	ATCC	HTB-70
Experimental models: Organisms/strains		
tp53m214K/m214k; mitfa−/−	Leonard Zon	N/A
tp53m214K/m214k; mitfa−/−; braf V600E	Craig Ceol	N/A
tp53m214K/m214k; mitfa−/−; nras G12D	This study	N/A
Recombinant DNA		
pMDLg/pRRE	Gift from Angeliki Malliri	Addgene #12251
pRSV-Rev	Gift from Angeliki Malliri	Addgene #12253
pMD2.G	Gift from Angeliki Malliri	Addgene #12259
pCDH-EF1α-MCS*-T2A-GFP	Gift from Andrew Gilmore	Systems Bioscience CD526A-1
pCDH-EF1α-MCS*-T2A-mApple	This study	N/A
pCDH-EF1α-DGAT1-T2A-mApple	This study	N/A
pDONR221	ThermoFisher Scientific	12536017
pDest-mitfa:dgat1a-pA	This study	N/A
pDest-mitfa:dgat2-pA	This study	N/A
pCS2-TP	Gift from Koichi Kawakami	N/A
pRK7-HA-S6K1-WT	Addgene	#8984
pRK7-HA-S6K1- F5A-E389-deltaCT	Addgene	#8990
pcDNA3.1-mMaroon1	Addgene	# 83840
pcDNA3.1-DGAT1	This study	N/A
Software and algorithms		
Fiji- Image J	(Schindelin et al., 2012)	https://imagej.net/Fiji
GraphPad Prism version 8.0.0	GraphPad Software	www.graphpad.com
Enrichr	(Chen et al., 2013)	https://amp.pharm.mssm.edu/Enrichr/
WebGestalt	(Liao et al., 2014)	http://www.webgestalt.org/#
Metascape	(Zhou et al., 2019))	https://metascape.org/gp/index.html#/main/step1
MaxQuant	(Cox et al., 2011)	https://www.maxquant.org
Lipidomics analysis scripts	This study	https://github.com/computational-metabolomics
Proteome analysis scripts	This study	https://github.com/JoWatson2011/DGAT_2019
FlowJo	www.flowjo.com	N/A

RESOURCE AVAILABILITY

Lead contact

Further information and requests for resources and reagents should be directed to and will be fulfilled by the lead contact, Adam Hurlstone (adam.hurlstone@manchester.ac.uk).

Materials availability

- Plasmids and cell lines generated in this study can be requested from the lead contact.

Data and code availability

- The mass spectrometry proteomics data have been deposited with the ProteomeXchange Consortium PRIDE: PXD017487. Extended Lipidomics Data for zebrafish tumors and human melanoma cell lines can be found in Tables S2–S6.
- Code for lipidomics analysis can be found at https://github.com/computational-metabolomics and proteomics analysis at https://github.com/JoWatson2011/DGAT_2019.

EXPERIMENTAL MODEL AND SUBJECT DETAILS

Zebrafish models

Regulated procedures involving zebrafish were ethically approved by The University of Manchester Animal Welfare and Ethical Review Body (AWERB), or by the UMMS Institution Animal Care and Use Committee (A-2016, A-2171), and carried out under a license issued by the appropriate national regulatory authority. Zebrafish were housed at ~28°C under a 14 h light/10 h dark cycle. Transgenic zebrafish expressing *BRAF*^{V600E} or *NRAS*^{G12D} have been previously described (Casar et al., 2018; Ceol et al., 2011) and were crossed onto a *mitfa*$^{w2/w2}$ (*mitfa*$^{-/-}$) background to suppress melanocyte development and further onto a *tp53*$^{M214K/M214K}$ background to promote tumorigenesis. Melanocyte restoration and simultaneous over-expression of Dgat1a, Dgat2 or EGFP was then achieved by injection of embryos with a mitfa-minigene containing plasmid as previously described (Ceol et al., 2011). Briefly, zebrafish *dgat1a* and *dgat2* were amplified from cDNA of wild-type 48 h post-fertilization zebrafish embryos, and subcloned into the pDONR221 vector (see Table S7 for oligonucleotide sequences). The pDest-mitfa:dgat1a-pA and pDest-mitfa:dgat2-pA destination vectors were created using an LR clonase reaction consisting of p5E-mitfap, pME-dgat1a or pME-dgat2, p3E-pA and an empty destination vector. Expression plasmid was injected into zebrafish zygotes along with Tol2 mRNA. pCS2-TP plasmid for Tol2 mRNA generation was a kind gift from Dr Koichi Kawakami (National Institute of Genetics). Sufficient embryos for all experimental arms were generated simultaneously, pooled and then randomly assigned to a construct, although formal randomization techniques were not used. Zebrafish were group-housed according to the construct. Only zebrafish embryos with near complete melanocyte rescue at 5 days were retained for further analysis. Analysis of tumor formation was not performed blinded to the construct identity. Sample sizes were not predetermined based on statistical power calculations but were based on our experience with these assays. To assess the statistical significance of differences in overall survival, we used Mantel–Cox's log-rank tests.

Mouse xenograft assays

Mice were housed in the University of Manchester Biological Safety Unit. CD1® nude mice (female, 8 weeks of age) were injected subcutaneously into the left flank with 4×10^6 A375 cells or MM485 cells (in PBS). When animals had developed melanoma nodules of ~100 mm^3, animals were allocated randomly to a treatment group and drug administration was initiated (4–6 mice per group). Treatment was by oral gavage once daily with vehicle (1% Tween80 in PBS), DGAT1 inhibitor A922500 (90 mg/kg) or SOD1 inhibitor ammonium tetrathiomolybdate (5 mg/kg). After the indicated number of days, tumors were isolated and analyzed as described.

Cell lines

Human melanoma cell lines were cultured in High Glucose DMEM with 10% FBS, and penicillin–streptomycin (Sigma) at 37°C and 5% CO_2. Normal human melanocytes were purchased from Cascade Biologics and cultured according to the manufacturer's guidelines. Lenti-X cells were cultured in High Glucose DMEM with 10 %v/v FBS, and penicillin–streptomycin (Sigma) at 37°C and 5% CO_2. All cells tested negative for mycoplasma and cell lines were authenticated using STR profiling (See Table S8 for DGAT1 characteristics of cell lines used in this study.).

METHOD DETAILS

Compounds and antibodies

Compounds were used at the following concentrations unless otherwise noted: 50 μM AZD3988 (Tocris), 30 μM A922500 (Stratech), 50 μM AZD7687 (Stratech), 70 μM T863 (Sigma), 1 μM Oligomycin (Sigma), 0.5 μM FCCP (Sigma), 1 μM Antimycin-A (Sigma), 1 μM Rotenone (Sigma), 50 μM PF-06424439 (Sigma), 5 μM Ebselen (Tocris), 1 mM Tempol, 200 μM Paraquat (Sigma), Menadione (Sigma), 100 μM Etomoxir (Sigma), 2 μM Ferrostatin-1 (Sigma), 5 μM ML385 (Selleckchem), and 1 μM ATN-224 (Cayman Chemical).

Antibodies against DGAT1 (ab54037) and 4-Hydroxynonenal (ab46545) were purchased from abcam. Antibodies against Vinculin (66305-1-Ig), Beta-Tubulin (10094-1-AP), PINK1 (23274-1-AP), Parkin (14060-1-AP), SOD1 (10269-1-AP), SOD2 (24127-1-AP), SESN2 (10795-1-AP) and GAPDH (60004-1-Ig) were purchased from Proteintech. Antibodies against phospho-AMPK (50081), phospho-RAPTOR (2083), Caspase-3 (9662), phospho-ERK (4370) and GFP (2956) were purchased from Cell Signalling. The antibody against gamma-tubulin (T5326) was purchased from Sigma. The antibody against ERK2 (C-14) was from Santa Cruz Biotechnology.

Plasmid cloning and transfection & siRNA transfection

The following plasmid used was purchased from Addgene: pcDNA3.1-mMaroon1 (83840). The GFP and WPRE elements were excised from pCDH-MCS-T2A-copGFP (a kind gift from Andrew Gilmore, The University of Manchester) using BspEI and KpnI. mApple (BspEI and XhoI adapters) and WPRE (XhoI-KpnI adapters) were PCR amplified, digested and subcloned to create the pCDH-MCS-T2A-mApple vector. DGAT1 was further subcloned into the both the pCDNA3.1 vector and pCDH-MCS-T2A-mApple using the MCS. All plasmids were transfected using Lipofectamine (Invitrogen) following standard protocols. All siRNA was transfected using Lipofectamine RNAi Max (Invitrogen) following standard protocols.

Viral transduction

Briefly, Lenti-X^{TM} HEK293 cells (Takara Bio) were transfected with pMDLg/pRRE, pMD2.G, pRSV-Rev plasmids (all kind gifts from Angeliki Malliri, Cancer Research UK Manchester Institute) and pCDH-EF1α-DGAT1-T2A-mApple viral vectors using Fugene (Promega) following standard protocols. The viral containing supernatant was filtered using a 0.45 μm filter and frozen at -80°C prior to transduction of target cells. The supernatant containing the viral particles was added to target cells along with 10 ng/mL Polybrene (Millipore) for 24 h. Target cells were then grown and selected from single cell colonies.

Protein lysate preparation and western blotting

Cells were washed with PBS and lysed with sample buffer (62.5 mM TRIS pH 6.8, 2 %w/v Sodium dodecyl sulfate (SDS), 10 %v/v glycerol, 0.01%w/v bromophenol blue, 3 %v/v 2-mercaptoethanol). Lysates were then sonicated and heated to 95°C for 10 minutes prior to being evenly loaded onto SDS-polyacrylamide gels using the Mini Trans-Bot electrophoresis system (Biorad), followed by transfer to PVDF using standard western blotting procedures.

Lipid droplet staining and image analysis

BODIPY 493/503

Indicated cells were stained with 2 μM BODIPY 493/503 (ThermoFisher Scientific) and 5 ng/mL Hoecsht 3342 (Cell Signalling) for 30 minutes prior to fixing in 4 %w/v paraformaldehyde and imaging using a Leica microscope system. Images were processing using Fiji.

Lipidtox

Indicated cells were fixed in 4 %w/v paraformaldehyde and stained with LipidTox Green (ThermoFisher Scientific) according to manufacturer's instructions, and 5 ng/mL Hoecsht 3342 (Cell Signalling) for 15 minutes prior to imaging using a Leica microscope system. Images were processing using Fiji.

RNA isolation and real-time PCR analysis

RNA from cell lines was isolated with TRIZOL® (Invitrogen). After chloroform extraction and centrifugation, 5 μg RNA was DNase treated using RNase-Free DNase Set (Qiagen). 1 μg of DNase treated RNA was then taken for cDNA synthesis using the Protoscript I first strand cDNA synthesis kit (New England Biolabs). Selected genes were amplified by quantitative real time PCR (RT-qPCR) using Sygreen (PCR Biosystems). Relative expression was calculated using the delta-delta CT methodology and beta-actin was used as reference housekeeping gene. Sequences for primers used can be found in the Table S7.

Flow cytometry

Mitochondrial membrane potential

Indicated cell lines were trypzinized and pelleted by centrifugation at 500 g for 5 min, washed with PBS. For mitochondrial membrane potential cells were stained with 2 μM JC-1 (Life Technologies) for 30 minutes at 37°C. For positive control samples 0.5μM FCCP was added simultaneously with JC-1. Data was acquired by the BD BIOsciences Foretessa and quantified using the Flowjo software. A minimum of 10,000 cells were analyzed per condition.

Lipid peroxidation

Indicated cell lines were trypzinized and pelleted by centrifugation at 500 g for 5 min, followed by a PBS wash. For lipid peroxidation cells were stained with either 5 μM BODIPY^{TM} 581/591 C11 (ThermoFisher Scientific) or MitoPerOx (Abcam) for 30 minutes at 37°C. Data was acquired by the BD BIOsciences Foretessa and quantified using the Flowjo software. A minimum of 10,000 cells were analyzed per condition.

Mitochondrial ROS

Indicated cell lines were trypzinized and pelleted by centrifugation at 500 g for 5 min, followed by a PBS wash. For mitochondrial specific ROS detection, cells were stained with 2.5 μM Mitosox (ThermoFisher Scientific) for 30 minutes at 37°C. Data was acquired by the BD BIOsciences Foretessa and quantified using the Flowjo software. A minimum of 10,000 cells were analyzed per condition.

Proliferation assays

Crystal violet

Indicated cells were stained and fixed with 0.5 %w/v crystal violet (Sigma) in 4 %w/v paraformaldehyde/PBS for 30 minutes. Fixed cells were then solubilized in 2 %w/v SDS/PBS and absorbance measured at 595 nm using Synergy H1 microplate reader (BioTek).

EdU incorporation

Indicated cells were labelled with 20 μM 5-ethynyl-2′-deoxyuridine (EdU) for 4 h and processed following the manufacturer's protocol (Click-iT® EdU Alexa Fluor® 488 Imaging Kit, Thermo Fisher). Prior to imaging cells were then stained with 5 ng/mL Hoecsht 3342 for 15 minutes. Stained cells were analyzed using a using a Leica microscope system. Images were processing using Fiji.

Incucyte cell-proliferation assay and apoptosis assay

Indicated cell lines were seeded into 24-well plates at a density of 15,000–20,000 cells per well, depending on growth rate and the design of the experiment. After 24 h drugs or siRNA were added, and cells were imaged every hour using the Incucyte ZOOM (Essen Bioscience) Phase-contrast images were analyzed to detect cell proliferation based on cell confluence. For cell apoptosis, caspase-3 and caspase-7 green apoptosis-assay reagent (Life Technologies) was added to the culture medium following manufacturer's instructions. Cell apoptosis was analyzed based on green fluorescent staining of apoptotic cells.

Dihydroethidium assay

Cells were stained with 5 μM Dihydroethidium for 20 minutes in the dark at 37°C. Fluorescence was measured at excitation 480 nm emission 570 nm using Synergy H1 micro plate reader (BioTek). Fluorescence values were normalized to cell number by staining the cells with crystal violet after fluorescence read.

Cancer bioinformatics

We evaluated both point mutations and CNV in the TCGA SKCM firehose legacy, TCGA pan-cancer and Cancer Cell Line Encyclopedia datasets using the cBioPortal platform (Gao et al., 2013). The GISTIC2.0 algorithm was used to identify focal amplifications (Mermel et al., 2011). Gene Ontology analysis was carried out using both enrichR (Chen et al., 2013) and metascape software (Zhou et al., 2019). Association between mRNA expression in TCGA datasets and survival was evaluated using OncoLnc (Anaya, 2016). mRNA levels determined by microarray were accessed through the Oncomine platform (Rhodes et al., 2004).

QUANTIFICATION AND STATISTICAL ANALYSIS

Data was tested for normality using the Shapiro-Wilk test. Data was considered to be normally distributed if $p > 0.05$. Differences in the number of lipid droplets per cell, relative cell number and percentage EdU incorporation between DMSO and drug treated cells were assessed using an unpaired two-sided *t*-test, or Mann-Whitney test if data were not normally distributed. In comparing the differences in these same characteristics between cells transfected with either non-target or one of several siRNA oligonucleotides, a one-way ANOVA with Tukey's multiple comparisons test (or Friedman with Dunn's multiple comparisons test if data were not normally distributed) was used to measure significance. Differences were considered significant if $p < 0.05$. All data obtained were analyzed using Graphpad Prism 8.1.

Proteomics

SILAC labelling

For quantitative mass spectrometry, A375 cells were labelled in SILAC DMEM supplemented with 10 %v/v dialyzed fetal bovine serum (Sigma), 2 mM glutamine, 100 U/mL penicillin and 100 μg/mL streptomycin for 15 days to ensure complete incorporation of amino acids. Two cell populations were obtained: one labelled with natural variants of the amino acids (light label; Lys0, Arg0) and a second one with heavy variants of the amino acids (L-[13C6,15N4]Arg (+10) and L- [13C6,15N2]Lys (+8)) (Lys8,Arg10). The light amino acids were from Sigma, while their heavy variants were from Cambridge Isotope Labs.

Sample preparation for mass spectrometry analysis

Cells from the two SILAC conditions treated as indicated were lysed at 4°C in ice cold modified RIPA buffer (50 mM Tris, pH 7.5, 150 mM NaCl, 1 %v/v NP-40, 0.1 %w/v sodium deoxycholate, 1 mM EDTA, 5 mM β-glycerolphosphate, 5 mM sodium fluoride, 1 mM sodium orthovanadate, 1 complete inhibitor cocktail Tablet per 50 mL). Proteins were precipitated for two hours at −20°C in four-fold excess of ice-cold acetone. The acetone-precipitated proteins were solubilized in denaturation buffer (10 mM HEPES, pH 8.0, 6 M urea, 2 M thiourea) and the SILAC-labelled lysates were mixed 1:1 based on protein concentrations. Proteins were reduced with 1 mM dithiothreitol (DTT) for 60 min, alkylated with 5.5 mM chloroacetamide (CAA) for 60 min and digested first with endoproteinase Lys-C (Wako, Osaka, Japan) and then, after a five-fold dilution with 50 mM ammonium bicarbonate (ABC), with trypsin (modified sequencing grade, Sigma). The peptide mixture was desalted and concentrated on a C18-SepPak cartridge (Waters, USA) and eluted with 50 %v/v acetonitrile. Equal amounts of SILAC lysates were then mixed 1:1, reduced with DTT, and alkylated with CAA before being resolved on SDS-PAGE (8–12 %w/v, Invitrogen). Separated proteins were fixed in the gel and visualized with colloidal Coomassie staining (Invitrogen). Each gel lane was excised and separated into eight segments that were sliced, destained with 50 %v/v EtOH in 25 mM ABC and dehydrated with 100 %v/v EtOH. Proteins were digested with sequence-grade trypsin (Sigma) overnight. Trypsin activity was quenched by acidification with trifluoroacetic acid (TFA) and peptides were extracted

from the gel sections with increasing concentrations of acetonitrile. Organic solvent was evaporated in a vacuum centrifuge, as described (Francavilla et al., 2016).

Mass spectrometry analysis

Enriched in-gel digested peptides were desalted and concentrated on STAGE-tips with two C18 filters and eluted using 40 %v/v acetonitrile, dried and reconstituted in 5 %v/v acetonitrile in 0.1 %v/v formic acid prior to analysis by LC-MS/MS using an UltiMate 3000 Rapid Separation LC (RSLC, Dionex Corporation, Sunnyvale, CA) coupled to a QE HF (Thermo Fisher Scientific, Waltham, MA) mass spectrometer. Mobile phase A was 0.1 %v/v formic acid in water and mobile phase B was 0.1 %v/v formic acid in acetonitrile and the analytical column utilized was a 75 mm × 250 μm inner diameter 1.7 μm CSH C18 (Waters). Samples were transferred to a 5 μL loop before loading on to the column at a flow of 300 nL/min for 5 minutes at 5 %v/v B. The loop was subsequently taken out of line and the peptides separated using a gradient that went from 5 %v/v to 7 %v/v B and from 300 nL/min to 200 nL/min in 1 min followed by a shallow gradient from 7 %v/v to 18 %v/v B in 64 min, then from 18 %v/v to 27 %v/v B in 8 min and finally from 27 %v/v B to 60 %v/v B in 1 min. The column was washed at 60 %v/v B for 3 min before re-equilibration to 5 %v/v B in 1 min. At 85 min, the flow was increased to 300 nL/min until the end of the run at 90 min. Mass spectrometry data was acquired in a data dependent manner for 90 min in positive mode. Peptides were selected for fragmentation automatically by data dependent analysis on a basis of the top 8 (phospho-proteome) or top 12 (proteome) peptides with m/z between 300 to 1750 Th and a charge state of 2, 3 or 4 with a dynamic exclusion set at 15 sec. The MS Resolution was set at 120,000 with an AGC target of 3e6 and a maximum fill time set at 20 ms. The MS2 Resolution was set to 30,000, with an AGC target of 2e5, a maximum fill time of 45 ms, isolation window of 1.3 Th and a collision energy of 28.

Data analysis of quantitative MS data

Raw data were analyzed with the MaxQuant software suite, version 1.5.6.5, with the integrated Andromeda search engine (Cox et al., 2011). Proteins were identified by searching the HCD-MS/MS peak lists against a target/decoy version of the human Uniprot database, which consisted of the complete proteome sets and isoforms (2016 release) supplemented with commonly observed contaminants such as porcine trypsin and bovine serum proteins. Tandem mass spectra were initially matched with a mass tolerance of 7 ppm on precursor masses and 0.02 Da or 20 ppm for fragment ions. Cysteine carbamidomethylation was searched as a fixed modification. Protein N-acetylation, oxidized methionine and either deamidation of asparagine and glutamine (proteome analysis) were searched as variable modifications. Labelled lysine and arginine were specified as fixed or variable modification, depending on prior knowledge about the parent ion (MaxQuant SILAC identification). False discovery rate was set to 0.01 for peptides, proteins and modification sites. Minimal peptide length was six amino acids. Only peptides with Andromeda score >40 were included. Potential contaminants, reverse sequenced peptides and phosphorylation sites with a localization probability of less than 0.75 (class I) (Olsen et al., 2006) were filtered from the dataset. The remaining data were filtered to remove sites or peptides without quantification in at least two of the three replicates for each time point. The median of the replicates was taken. Sites or peptides with a SILAC ratio of greater than 1.5 were considered up-regulated whilst those with a ratio less than 0.75 were considered down-regulated. Gene network visualization was performed using enrichR (Chen et al., 2013). For the proteome analysis a minimum of three to seven peptide identifications with at least two being uniquely assigned to the particular protein were required. Sequence coverage of the identified proteins was at least 5%. Gene Ontology analysis was carried out using enrichR (Chen et al., 2013) and metascape (Zhou et al., 2019).

Lipidomics

UHPLC-MS

The samples were maintained at 4°C and analyzed applying two Ultra-High-Performance Liquid Chromatography-Mass Spectrometry (UHPLC-MS) methods using a Dionex UltiMate 3000 Rapid Separation LC system (Thermo Fisher Scientific, MA, USA) coupled with a heated electrospray Q Exactive Focus mass spectrometer (Thermo Fisher Scientific, MA, USA). Lipid extracts were analyzed on a Hypersil GOLD column (100 × 2.1 mm, 1.9 μm; Thermo Fisher Scientific, MA, USA). Mobile phase A consisted of 10 mM ammonium formate and 0.1 %v/v formic acid in 60 %v/v acetonitrile/water and mobile phase B consisted of 10 mM ammonium formate and 0.1 %v/v formic acid in 90 %v/v propan-2-ol/water. Flow rate was set for 0.40 mL.min-1 with the following gradient: t = 0.0, 20 % v/v B; t = 0.5, 20 %v/v B, t = 8.5, 100 %v/v B; t = 9.5, 100 %v/v B; t = 11.5, 20 %v/v B; t = 14.0, 20 %v/v B, all changes were linear with curve = 5. The column temperature was set to 55°C and the injection volume was 2 μL. Data were acquired in positive and negative ionization mode separately within the mass range of 150–2000 m/z at resolution 70,000 (FWHM at m/z 200). Ion source parameters were set as follows: Sheath gas = 48 arbitrary units, Aux gas = 15 arbitrary units, Sweep gas = 0 arbitrary units, Spray Voltage = 3.2 kV (positive ion)/2.7 kV (negative ion), Capillary temp. = 380°C, Aux gas heater temp. = 450°C. Data dependent MS2 in 'Discovery mode' was used for the MS/MS spectra acquisition using following settings: resolution = 17,500 (FWHM at m/z 200); Isolation width = 3.0 m/z; stepped collision energies (stepped CE) = 20, 40, 100 [positive ion mode]/40, 60, 130 [negative ion mode]. Spectra were acquired in five different mass ranges: 150–510 m/z; 500–710 m/z; 700–860 m/z; 850–1010 m/z; 1000–2000 m/z. A Thermo ExactiveTune 2.8 SP1 build 2806 was used as instrument control software in both cases and data were acquired in profile mode. Quality control (QC) samples were analyzed as the first ten injections and then every seventh injection with two QC samples at the end of the analytical batch. Two blank samples were analyzed, the first as the sixth injection and then the second at the end of each batch.

Mass spectrometry raw metabolomics data processing

Raw data acquired in each analytical batch were converted from the instrument-specific format to the mzML file format applying the open access ProteoWizard (version 3.0.11417) msconvert tool (Chambers et al., 2012). During this procedure, peak picking and

centroiding, were achieved using vendor algorithms. Isotopologue Parameter Optimization (IPO - version 1.0.0, using XCMS - version 1.46.0) (Libiseller et al., 2015) was used to perform automatic optimization of XCMS (Smith et al., 2006) peak picking parameters. For centWave peak picking algorithm following parameters and ranges were used: min_peakwidth (from 2 to 10); max_peakwidth (from 20 to 60); ppm (from 5 to 15); mzdiff (−0.001 to 0.01); snthresh (10); noise (10,000); prefilter (3); value_of_prefilter (100); mzCenterFun (wMean); integrate (1); fitgauss (FALSE); verbose.columns (FALSE). Optimised XCMS parameters for raw data files deconvolution were: min_peakwidth (6); max_peakwidth (30); ppm (14); mzdiff (0.001); snthresh (10); noise (100); prefilter (3); value_of_prefilter (100); mzCenterFun (wMean); integrate (1); fitgauss (FALSE); verbose.columns (FALSE). For feature grouping method *density* was used with following: minfrac (0.5); minsamp (1); bw (0.25); mzwid (0.01); max (50); sleep (0). A data matrix of metabolite features (*m/z*-retention time pairs) versus samples was constructed with peak areas provided where the metabolite feature was detected for each sample.

Peak matrix processing

The data for pooled QC samples were applied to perform QC filtering. The first five QCs for each batch were used to equilibrate the analytical system and therefore subsequently removed from the data before the data was processed and analyzed. The data from the pooled QC samples were used to apply QC filtering. For each metabolite feature detected QC samples 1–8 were removed (i.e. leaving a blank and 2 QCs at the start of each batch) and the relative standard deviation and percentage detection rate were calculated using the remaining QC samples. Blank samples at the start and end of a run were used to remove features from non-biological origins. Any feature with an average QC intensity less than 20 times the average intensity of the blanks was removed. Any samples with >50% missing values were excluded from further analysis. Metabolite features with a RSD > 30% and present in less than 90% of the QC samples were deleted from the dataset. Features with a <50% detection rate over all samples were also removed. Prior to statistical analysis, the data was normalized using probabilistic quotient normalization (PQN) (Dieterle et al., 2006). For multivariate analysis missing values were replaced by applying *k* nearest neighbor (kNN) missing value imputation (k = 5) followed by log transformation (Parsons et al., 2007).

Lipid annotation

LipidSearch (version 4.2, Thermo Fisher Scientific) was used to annotate peaks based on their MS/MS fragmentation patterns. For lipid annotation, all experimental LC-MS/MS spectra data were searched against a MS/MS lipid library in the LipidSearch software database using the following potential ion forms: positive ion = $[M+H]^+$, $[M+NH_4]^+$, $[M+Na]^+$, $[M+K]^+$, $[M+2H]^{2+}$; negative ion = $[M-H]^-$, $[M+HCOO]^-$, $[M+CH_3COO]^-$, $[M+Cl]^-$, $[M-2H]^{2-}$. The quality of the annotation was graded as A-D. This is defined as: Grade A = all fatty acyl chains and class were completely identified; Grade B = some fatty acyl chains and the class were identified; Grade C = either the lipid class or some fatty acyls were identified; Grade D = identification of less specific fragment ions. Only peaks with an MS/MS identification were discussed in this manuscript. All lipid annotations are reported at a confidence of level 3 according to the Metabolomics Standards Initiative (Sumner et al., 2007).

Univariate statistics

For univariate statistics the normalized data was used to avoid including imputed values in the calculations. Fold changes were computed between all pairs of groups. For 2-group comparisons a t-test was applied to determine features showing a significant different between groups. For comparisons exploring two factors a 2-way ANOVA with an interaction term was applied to determine features showing a significant difference between factor levels. For features found to be significant, Tukey's Honest Significant Difference (HSD) was applied to determine between which levels the difference was significant ($p < 0.05$). A False Discovery Rate (FDR) correction (Benjamini-Hochburg) was applied to adjust for multiple testing and control the number of false positives ($q < 0.05$) for both t-test and ANOVA.

Software

All peak matrix processing, univariate and multivariate analyses were performed in the R environment using STRUCT (STatistics in R Using Class Templates) and STRUCTToolbox packages, which make use of PMP and SBCMS packages. These packages are maintained by Phenome Centre Birmingham and available on GitHub (https://github.com/computational-metabolomics).

Cell Reports, Volume *39*

Supplemental information

Oxidative stress from DGAT1 oncoprotein inhibition in melanoma suppresses tumor growth when ROS defenses are also breached

Daniel J. Wilcock, Andrew P. Badrock, Chun W. Wong, Rhys Owen, Melissa Guerin, Andrew D. Southam, Hannah Johnston, Brian A. Telfer, Paul Fullwood, Joanne Watson, Harriet Ferguson, Jennifer Ferguson, Gavin R. Lloyd, Andris Jankevics, Warwick B. Dunn, Claudia Wellbrock, Paul Lorigan, Craig Ceol, Chiara Francavilla, Michael P. Smith, and Adam F.L. Hurlstone

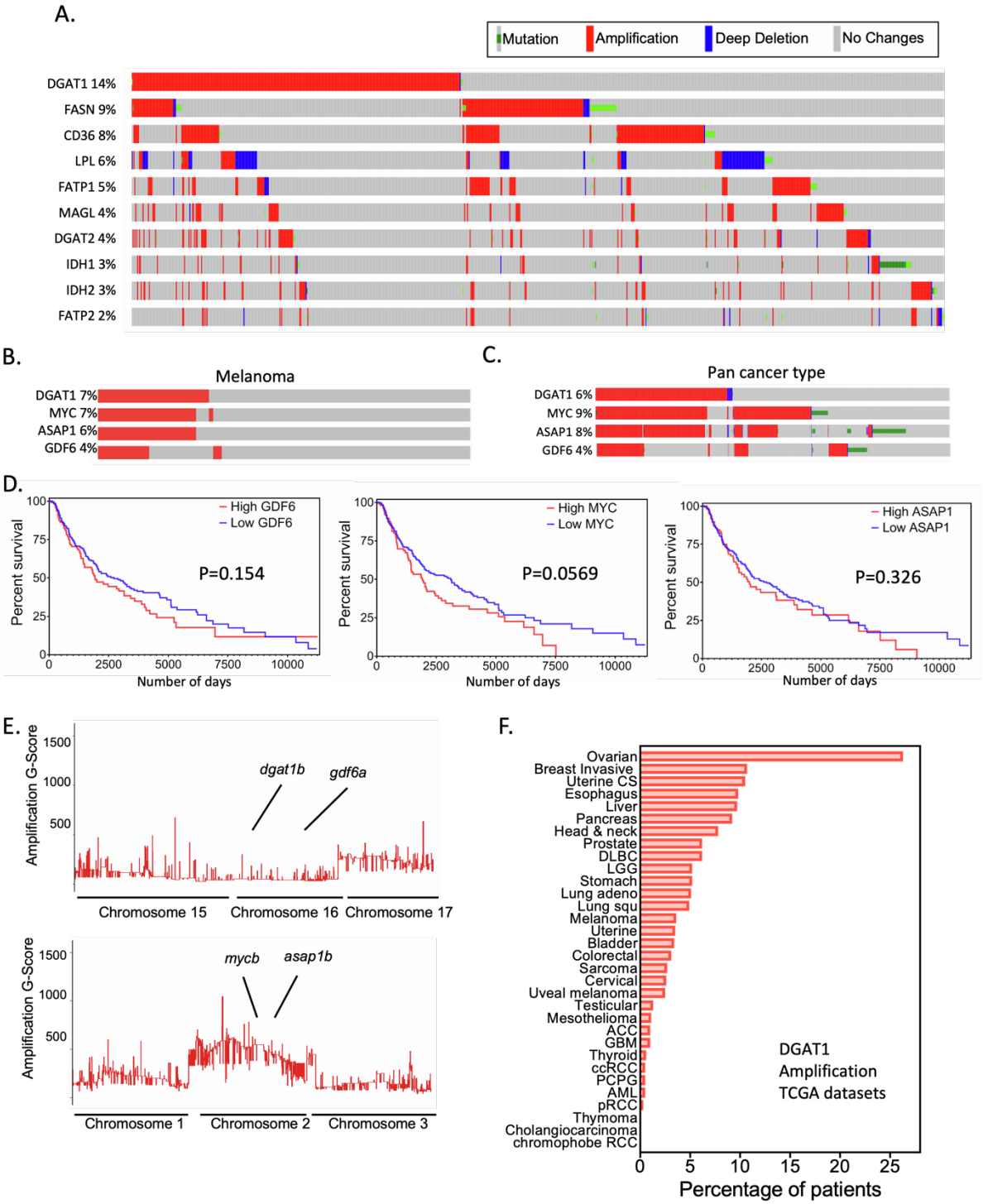

A.
Mutation
Amplification
Deep Deletion
No Changes
DGAT1 14%
FASN 9%
CD36 8%
LPL 6%
FATP1 5%
MAGL 4%
DGAT2 4%
IDH1 3%
IDH2 3%
FATP2 2%
B.
Melanoma
DGAT1 7%
MYC 7%
ASAP1 6%
GDF6 4%
C.
Pan cancer type
DGAT1 6%
MYC 9%
ASAP1 8%
GDF6 4%
D.
Percent survival
High GDF6
Low GDF6
P=0.154
Number of days
High MYC
Low MYC
P=0.0569
High ASAP1
Low ASAP1
P=0.326
E.
Amplification G-Score
dgat1b
gdf6a
Chromosome 15
Chromosome 16
Chromosome 17
mycb
asap1b
Chromosome 1
Chromosome 2
Chromosome 3
F.
Ovarian
Breast Invasive
Uterine CS
Esophagus
Liver
Pancreas
Head & neck
Prostate
DLBC
LGG
Stomach
Lung adeno
Lung squ
Melanoma
Uterine
Bladder
Colorectal
Sarcoma
Cervical
Uveal melanoma
Testicular
Mesothelioma
ACC
GBM
Thyroid
ccRCC
PCPG
AML
pRCC
Thymoma
Cholangiocarcinoma
chromophobe RCC
DGAT1
Amplification
TCGA datasets
Percentage of patients

Figure S1. *DGAT1* amplification and up-regulation associates with poor prognosis in melanoma (related to Figure 1)

(A) Alterations in indicated genes in the TGCA pan-cancer data set accessed via cBioPortal.

(B) Alterations in indicated genes in the TCGA firehose legacy melanoma data set accessed via cBioPortal.

(C) TGCA pan-cancer data set accessed via cBioPortal quantifying alterations in indicated genes.

(D) Kaplan-Meier survival plots for co-amplified genes found on chromosome 8 in melanoma (top 25% *vs* bottom 75%, TCGA database).

(E) G-Score of amplified regions of zebrafish chromosomes found in *BRAF*^{V600E}-positive; *tp53* mutant tumors, locations of human chromosome 8 zebrafish paralogues identified.

(F) TGCA pan-cancer data set accessed via cBioPortal quantifying amplification of *DGAT1* per cancer type.

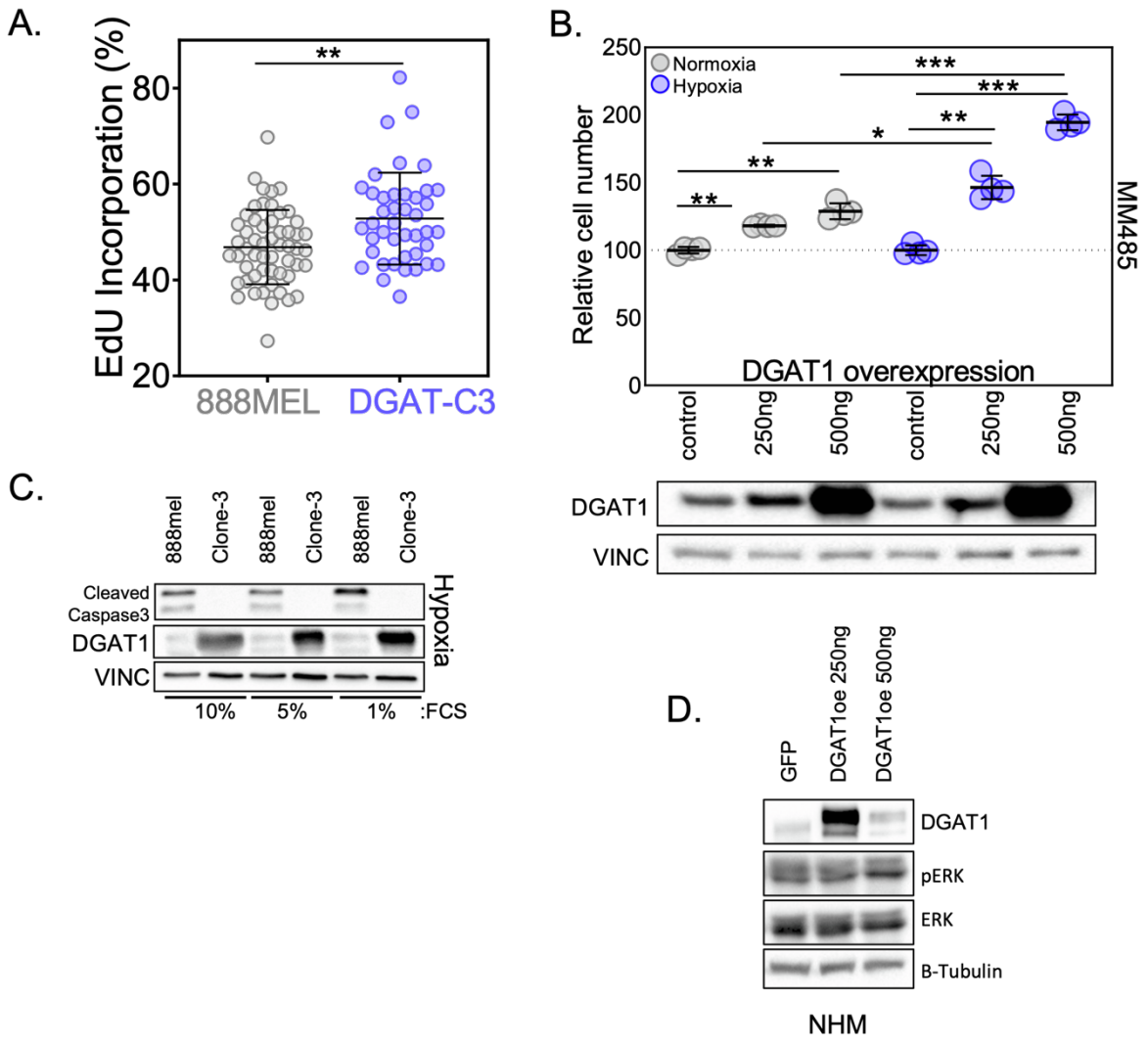


Figure S2. DGAT1 functions as an oncoprotein in zebrafish and human melanocytes (related to Figure 2)

(A) Quantification of the percentage of 888MEL parental cells or Clone 3 DGAT1 over-expressing cells in S-phase following EdU incorporation (Mean ± SD, n>40).

(B) Relative cell number determined by crystal violet following transfection with DGAT1 overexpression vector or an empty vector control under normoxic or hypoxic conditions for 48 h. (1 % O_2) (upper) (Mean, n>3). Corresponding protein expression of DGAT1 (lower).

(C) Protein expression in 888mel parental or Clone 3 DGAT1 overexpressing cells of DGAT1 and cleaved caspase 3 in indicated FCS serum levels under hypoxic (1% O2) conditions.

(D) Protein expression of DGAT1, phospho-ERK and ERK in NHM following overexpression of DGAT1 or GFP.

(A and B) For significance: ∗p < 0.05, ∗∗p < 0.01, and ∗∗∗p < 0.001

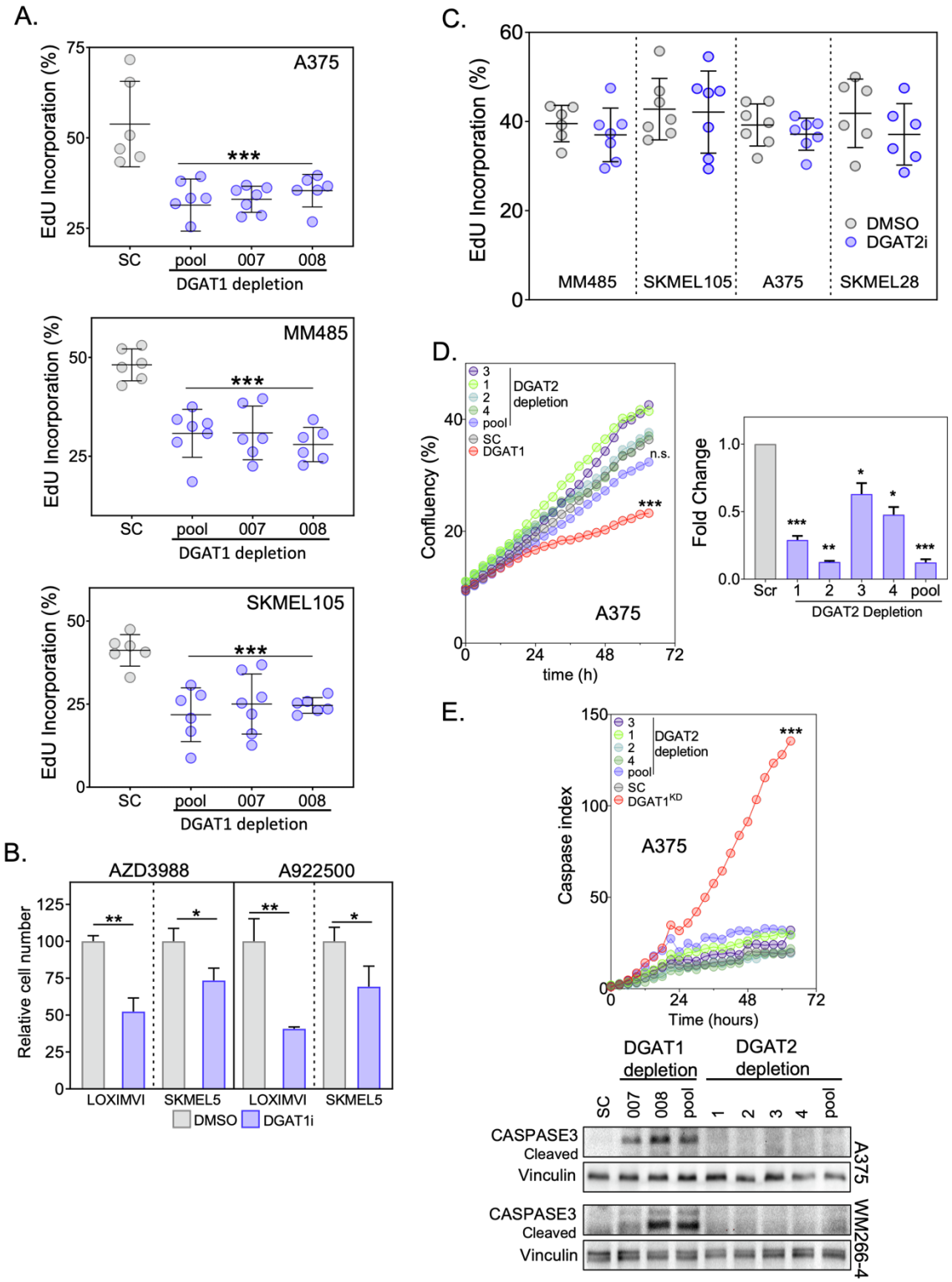

A.
A375
EdU Incorporation (%)
75
50
25
***
SC
pool
007
008
DGAT1 depletion
MM485
EdU Incorporation (%)
50
25
***
SC
pool
007
008
DGAT1 depletion
SKMEL105
EdU Incorporation (%)
50
25
0
***
SC
pool
007
008
DGAT1 depletion
B.
AZD3988
A922500
Relative cell number
125
100
75
50
25
0
**
*
**
*
LOXIMVI
SKMEL5
LOXIMVI
SKMEL5
DMSO
DGAT1i
C.
EdU Incorporation (%)
60
40
20
0
MM485
SKMEL105
A375
SKMEL28
DMSO
DGAT2i
D.
3
1
2
4
pool
DGAT2 depletion
SC
DGAT1
Confluency (%)
40
20
0
n.s.
***
A375
0
24
48
72
time (h)
Fold Change
1.0
0.5
0.0
***
**
*
*
***
Scr
1
2
3
4
pool
DGAT2 Depletion
E.
3
1
2
4
pool
DGAT2 depletion
SC
DGAT1KD
Caspase index
150
100
50
0
***
A375
0
24
48
72
Time (hours)
DGAT1 depletion
DGAT2 depletion
SC
007
008
pool
1
2
3
4
pool
CASPASE3 Cleaved
Vinculin
A375
CASPASE3 Cleaved
Vinculin
WM266-4

Figure S3. DGAT1 antagonism decreases melanoma cell proliferation and survival (related to Figure 3)

(A) Quantification of the population of cells in S-phase using EdU incorporation following transfection with DGAT1 targeting siRNA (007, 008, pool) or scrambled control for 48 h (Mean ± SD, n>5).

(B) Relative cell number determined by crystal violet staining following 72 h treatment with/without AZD3988 or A922500 (Mean ± SD, n>3).

(C) Quantification of the percentage of cells in S-phase using EdU incorporation following 24 h treatment with/without DGAT2 inhibitor (Mean ± SD, n>5).

(D) Confluency curves determined by time-lapse microscopy in A375 cells following transfection with DGAT2 (001, 002, 003, 004, pool) or DGAT1 targeting scrambled siRNA using an Incucyte zoom system (Mean, n>3) (left). RT-qPCR analysis of DGAT2 gene expression in A375 cells following transfection with DGAT2 targeting siRNA (001, 002, 003, 004, pool) or scrambled control for 48 h (Mean ± SD, n=3) (right).

(E) Cleaved caspase index in A375 cells following transfection with either a DGAT2 targeting (001, 002, 003, 004, pool), DGAT1 targeting or a scrambled siRNA determined by time-lapse microscopy using an Incucyte zoom system (Mean, n=3) (upper). Corresponding protein expression of cleaved caspase3 following transfection with either a DGAT2 targeting siRNA (001, 002, 003, 004, pool), DGAT1 targeting siRNA (007, 008, pool) or a scrambled control (lower).

For significance: $*p < 0.05$, $**p < 0.01$, and $***p < 0.001$

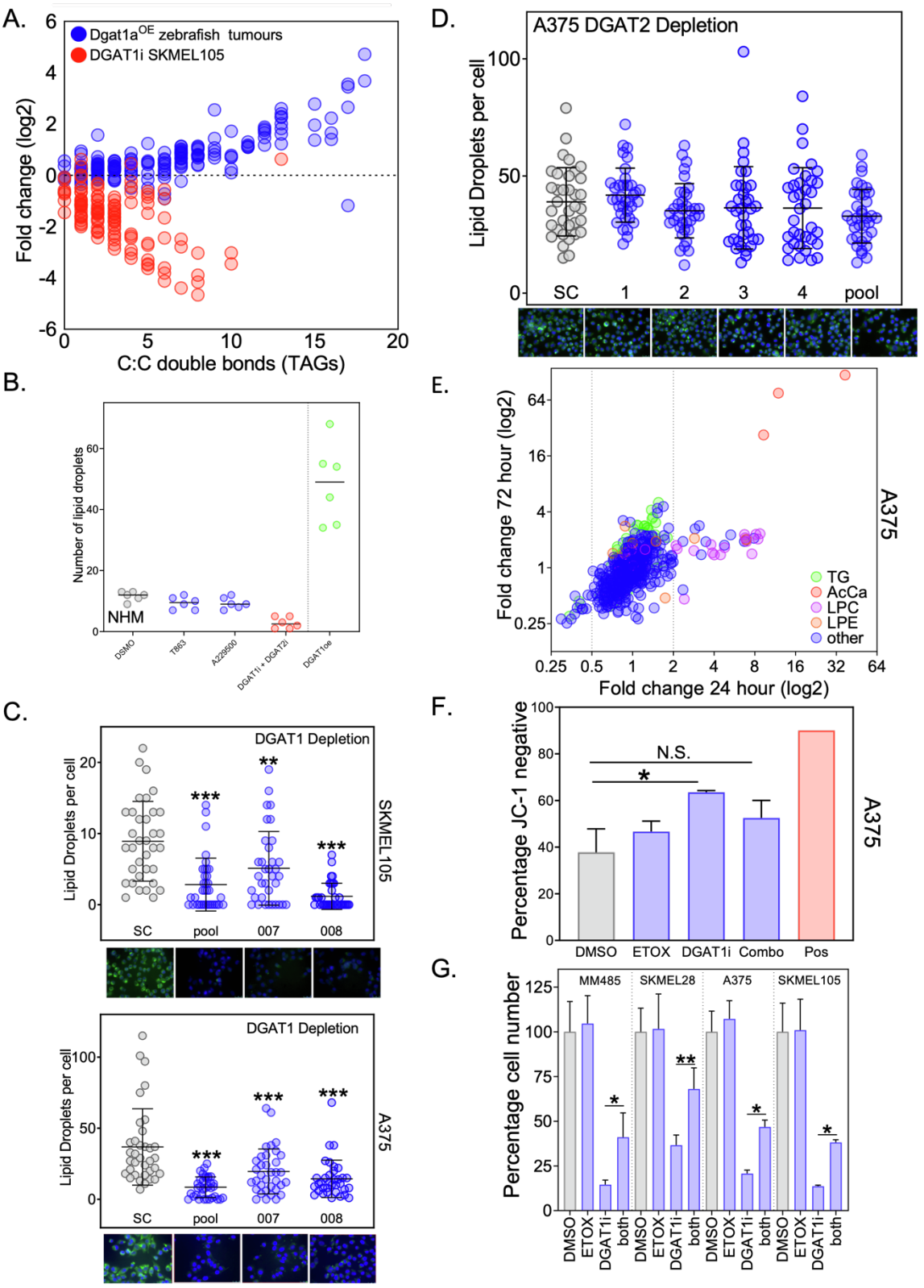

A.
Dgat1a^OE zebrafish tumours
DGAT1i SKMEL105
Fold change (log2)
C:C double bonds (TAGs)
B.
Number of lipid droplets
NHM
DSMO
T863
A939500
DGAT1i + DGAT2i
DGAT1oe
C.
DGAT1 Depletion
Lipid Droplets per cell
SKMEL105
SC
pool
007
008
DGAT1 Depletion
Lipid Droplets per cell
A375
SC
pool
007
008
D.
A375 DGAT2 Depletion
Lipid Droplets per cell
SC
1
2
3
4
pool
E.
Fold change 72 hour (log2)
Fold change 24 hour (log2)
A375
TG
AcCa
LPC
LPE
other
F.
Percentage JC-1 negative
N.S.
A375
DMSO
ETOX
DGAT1i
Combo
Pos
G.
Percentage cell number
MM485
SKMEL28
A375
SKMEL105
DMSO
ETOX
DGAT1i
both

Figure S4. DGAT1-formed lipid droplets act as caretakers of mitochondrial health (related to Figure 4)

(A) UHPLC- lipidomic analysis of NRASG12D-positive Dgat1a-over-expressing (n=6) tumors and SKMEL105 cells following treatment with A922500 for 72 h and showing the number of carbon-carbon double bonds in TAG species compared to the fold increase relative to control samples.

(B) Number of lipid droplets per cell in NHM treated with DGAT1 inhibitors alone or combined with DGAT2 inhibitor or in NHM overexpressing DGAT1 quantified using BODIPY staining (Mean ± SD, n = 6 replicates).

(C) Representative images and quantification of the number of lipid droplets per cell following BODIPY staining. Indicated cell lines were transfected with either DGAT1 targeting siRNA (007, 008, pool) or scrambled control for 48 h (Mean ± SD, n>30).

(D) Representative images and quantification of the number of lipid droplets per cell following BODIPY staining. A375 cells were transfected with either DGAT2 targeting siRNA (001, 002, 003, 004, pool) or a scrambled control for 48 h (Mean ± SD, n>30).

(E) UHPLC- lipidomic analysis of A375 cells following treatment with/without A922500 for 24 or 72 h (showing lipid species that were annotated using MS/MS). Fold-change calculated relative to DMSO treated control (All conditions n=3).

(F) A375 cells were stained with JC-1 dye following treatment with/without A922500 for 48 h and with/without Etomoxir for 4 h. The percentage of cells that lost red J-aggregates was calculated by using 1 μM CCP as a positive control for loss of mitochondrial membrane potential and comparing this to untreated cells to create two populations of cells in the flow cytometry analysis (Mean± SD, n>3).

(G) Relative cell number as determined by crystal violet staining, indicted cell 24 lines were treated with/without A922500 for 48 h and with/without Etomoxir for 24 h (Mean± SD, n=3).

(C, F and G) For significance: $*p < 0.05$, $**p < 0.01$, and $***p < 0.001$

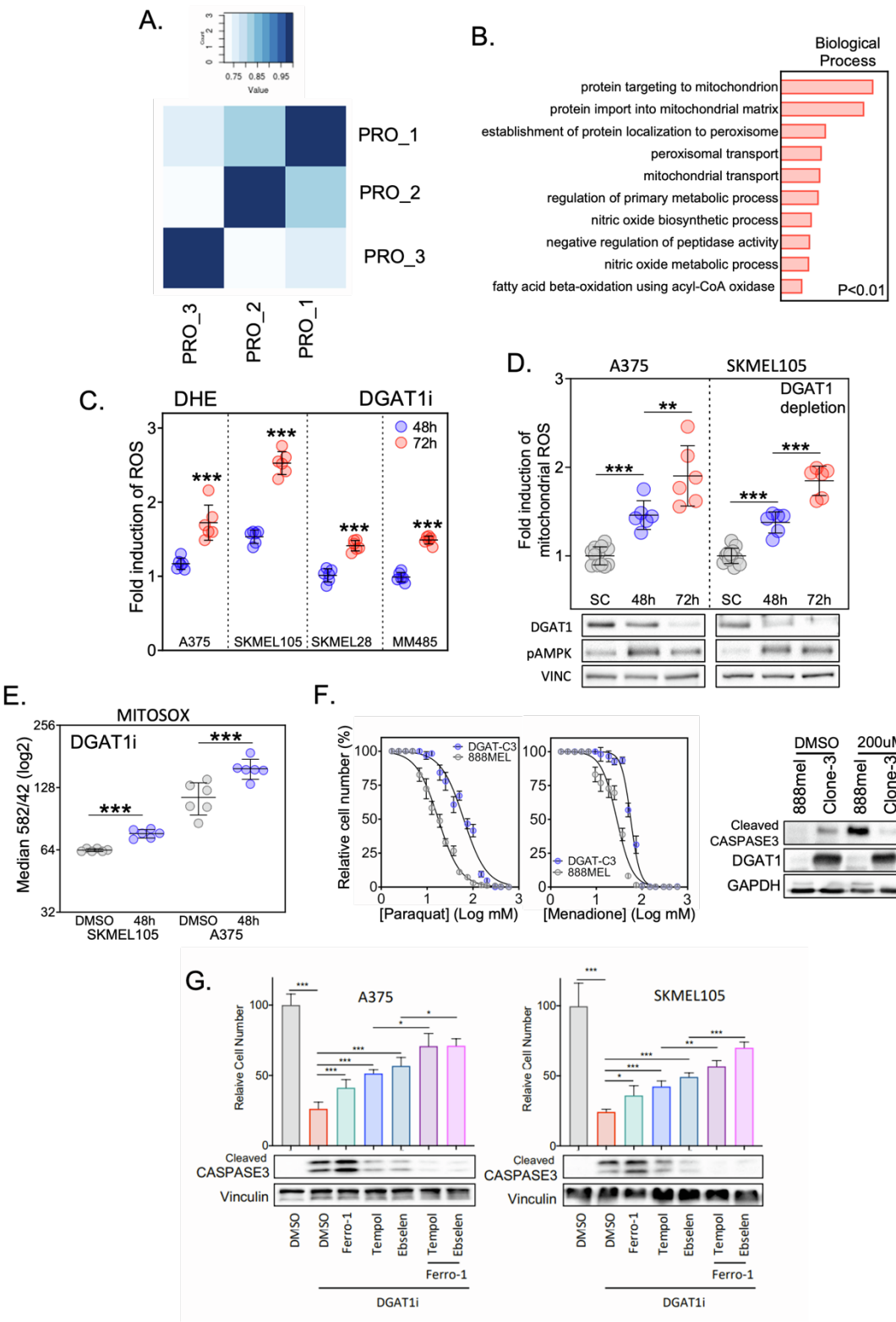

A.
PRO_1
PRO_2
PRO_3
B.
Biological Process
protein targeting to mitochondrion
protein import into mitochondrial matrix
establishment of protein localization to peroxisome
peroxisomal transport
mitochondrial transport
regulation of primary metabolic process
nitric oxide biosynthetic process
negative regulation of peptidase activity
nitric oxide metabolic process
fatty acid beta-oxidation using acyl-CoA oxidase
P<0.01
C.
DHE
DGAT1i
48h
72h
Fold induction of ROS
A375
SKMEL105
SKMEL28
MM485
D.
A375
SKMEL105
DGAT1 depletion
Fold induction of mitochondrial ROS
SC
48h
72h
DGAT1
pAMPK
VINC
E.
MITOSOX
DGAT1i
Median 582/42 (log2)
DMSO
48h
SKMEL105
A375
F.
DGAT-C3
888MEL
Relative cell number (%)
[Paraquat] (Log mM)
[Menadione] (Log mM)
DMSO
200uM
400uM
888mel
Clone-3
Cleaved CASPASE3
DGAT1
GAPDH
G.
A375
SKMEL105
Relaive Cell Number
Cleaved CASPASE3
Vinculin
DMSO
Ferro-1
Tempol
Ebselen
DGAT1i

Figure S5. DGAT1 promotes survival of melanoma cells through suppressing ROS generation (related to Figure 5)

(A) Pearson correlation between total proteome samples following treatment of A375 cells with/without A922500 for 72 h (n=3).

(B) Gene Ontology analysis of up-regulated genes (114) in A375 cells following treatment with A922500 for 72 h compared to DMSO treated control. Gene Ontology analysis was carried out using biological processes (enrichR) ranked by combined score.

(C) ROS levels quantified using dihydroethidium (DHE) fluorescence following treatment with/without A922500 for 48-72 h. Fold change calculated relative to DMSO treated control (Mean, n>4).

(D) ROS levels quantified using mitosox fluorescence following transfection with either DGAT1 targeting siRNA or a scrambled control for 48-72 h. Fold-change calculated relative to scrambled control (Mean ± SD, n=3) (upper). Corresponding protein expression of DGAT1 and phospho-AMPK (lower).

(E) ROS levels quantified using mitosox fluorescence following treatment with A922500 for 48 h (Mean ± SD, n=6).

(F) Drug-dose response curve after 72 h treatment with ROS inducers (left) (Mean ± SD, n=3). Protein expression of cleaved-caspase3 and DGAT1 following 72 h paraquat treatment (right).

(G) Relative cell number following crystal violet staining, indicated cells were either with/without A922500, Ferrsostatin-1 (Ferro-1), Ebselen and Tempol (Mean ± SD, n=3) (Upper). Corresponding protein expression of cleaved caspase-3 in indicated cell lines.

For significance: $*p < 0.05$, $**p < 0.01$, and $***p < 0.001$

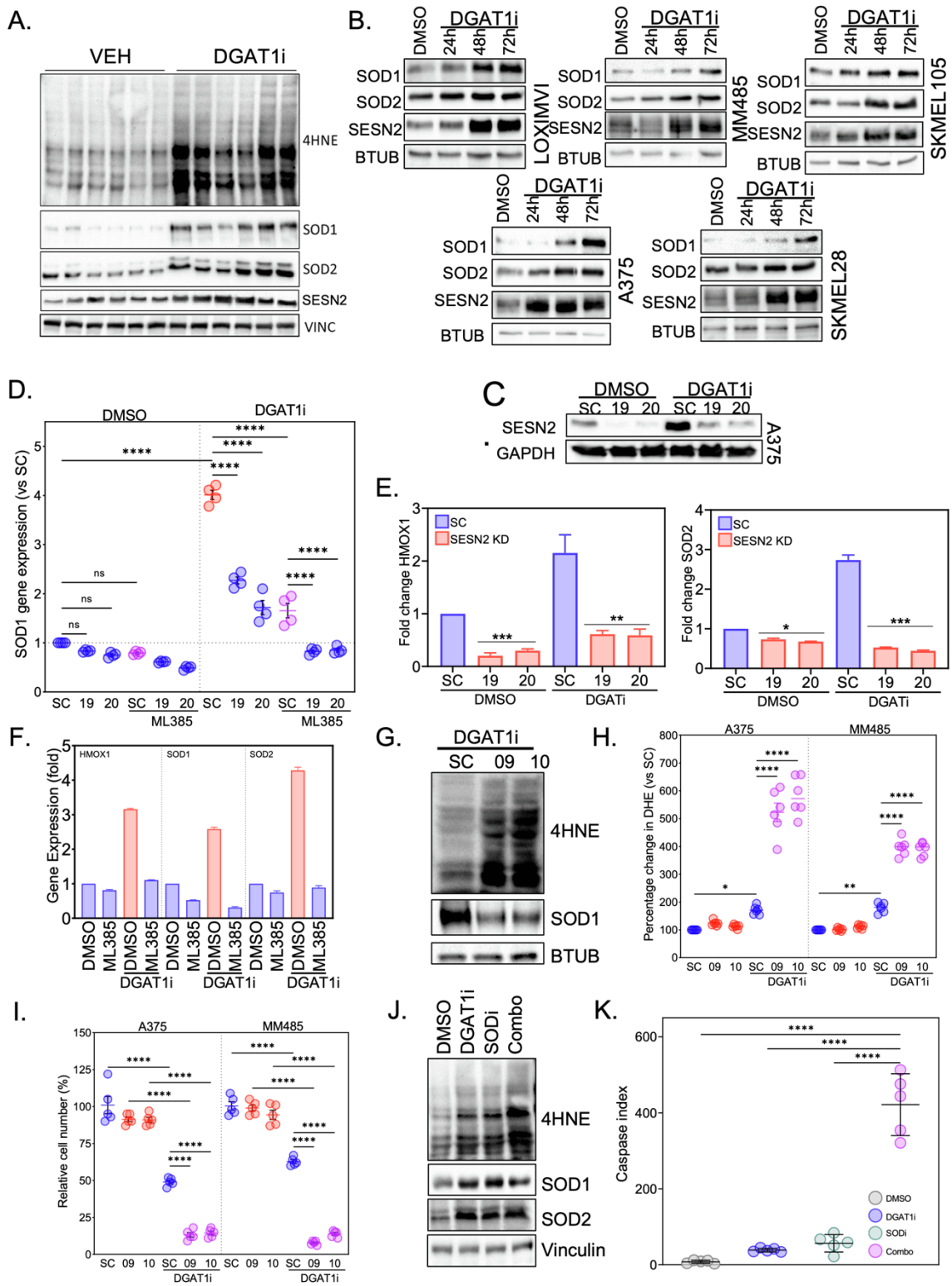

A.
VEH
DGAT1i
4HNE
SOD1
SOD2
SESN2
VINC
B.
DMSO
DGAT1i
24h
48h
72h
SOD1
SOD2
SESN2
BTUB
LOXIMVI
MM485
SKMEL105
A375
SKMEL28
C
DMSO
DGAT1i
SC 19 20 SC 19 20
SESN2
GAPDH
A375
D.
DMSO
DGAT1i
SOD1 gene expression (vs SC)
ns
****
SC 19 20 SC 19 20 SC 19 20 SC 19 20
ML385
ML385
E.
SC
SESN2 KD
Fold change HMOX1
Fold change SOD2
***
**
*
DMSO
DGATi
F.
HMOX1
SOD1
SOD2
Gene Expression (fold)
DMSO
ML385
DGAT1i
G.
DGAT1i
SC 09 10
4HNE
SOD1
BTUB
H.
A375
MM485
Percentage change in DHE (vs SC)
SC 09 10 SC 09 10 SC 09 10 SC 09 10
DGAT1i
I.
A375
MM485
Relative cell number (%)
SC 09 10 SC 09 10 SC 09 10 SC 09 10
DGAT1i
J.
DMSO
DGAT1i
SODi
Combo
4HNE
SOD1
SOD2
Vinculin
K.
Caspase index
DMSO
DGAT1i
SODi
Combo

Figure S6 Combined DGAT1 and SOD1 inhibition halts tumor growth (related to Figure 6)

(A) 4-Hydroxynonenal (4HNE) protein conjugate abundance and protein expression of SOD1, SOD2 and SESN2 in A375 tumors treated with either vehicle or A922500 (DGAT1i).

(B) Protein expression of SOD1, SOD2 and SESN2 following A922500 treatment for 24-72 hours in a panel of melanoma cell lines.

(C) Protein expression of SESN2 in A375 cells following treatment with/without A922500 and with either scrambled control (SC) or SESN2 targeting siRNA (19 or 20) for 48 hours.

(D) SOD1 gene expression in A375 cells following treatment with/without A922500 and ML385 and treatment with either scrambled control (SC) or SESN2 targeting siRNA (19 or 20) for 48 hours. (Mean ± SD, n=3)

(E) HMOX (left) & SOD2 (right) gene expression in A375 cells following treatment with/without A922500 and with either scrambled control (SC) or SESN2 targeting siRNA (19 or 20) for 48 hours. (Mean ± SD, n=3)

(F) HMOX, SOD1 & SOD2 gene expression in A375 cells following treatment with/without A922500 and with/without ML385 for 48 hours. (Mean ± SD, n=3)

(G) 4HNE protein conjugate abundance and protein expression of SESN2 in A375 cells following treatment with A922500 and with either scrambled control (SC) or SOD1 targeting siRNA (09 or 10) for 48 hours.

(H) Quantification of ROS levels using dihydroethidium (DHE) fluorescence in A375 cells following treatment with/without A922500 and with either scrambled control (SC) or SOD1 targeting siRNA (09 or 10) for 48 hours. (Mean ± SD, n=6)

(I) Relative cell number following crystal violet staining in A375 cells following treatment with/without A922500 and with either scrambled control (SC) or SOD1 targeting siRNA (09 or 10) for 48 hours. (Mean ± SD, n=5)

(J) 4HNE protein conjugate abundance and protein expression of SOD1 and SOD2 in A375 cells following treatment with either A922500 or ATN-224 (SODi) alone or in combination.

(K) Cleaved-caspase index in A375 cells following treatment with either A922500 or ATN-224 alone or in combination (combo). Fold-change relative to DMSO (Mean ± SD, n=5). For significance: $*p < 0.05$, $**p < 0.01$, and $***p < 0.001$

Cell line	Genetic drivers	DGAT1 status
888MEL	$BRAF^{V600E}$	DGAT1 low
SKMEL28	$BRAF^{V600E}$	DGAT1 medium
SKMEL2	$NRAS^{Q61R}$	DGAT1 over expressed
MM485	$NRAS^{Q61R}$	DGAT1 over expressed
A375	$BRAF^{V600E}$	DGAT1 over expressed
SKMEL105	$BRAF^{V600E}$	DGAT1 over expressed
LOXIMVI	$BRAF^{V600E}$	DGAT1 amplified
SKMEL5	$BRAF^{V600E}$	DGAT1 amplified

Supplementary Table 8 DGAT1 status of cell lines used in this study (related to STAR Methods)

nature COMMUNICATIONS

ARTICLE

https://doi.org/10.1038/s41467-022-31399-w OPEN

Inactivation of the Hippo tumor suppressor pathway promotes melanoma

Marc A. Vittoria[1], Nathan Kingston[2], Kristyna Kotynkova[1], Eric Xia[1], Rui Hong[3], Lee Huang[4], Shayna McDonald[1], Andrew Tilston-Lunel[2], Revati Darp[5], Joshua D. Campbell[3], Deborah Lang[4], Xiaowei Xu[6], Craig J. Ceol[5], Xaralabos Varelas[2] & Neil J. Ganem[1,3]✉

Melanoma is commonly driven by activating mutations in the MAP kinase BRAF; however, oncogenic BRAF alone is insufficient to promote melanomagenesis. Instead, its expression induces a transient proliferative burst that ultimately ceases with the development of benign nevi comprised of growth-arrested melanocytes. The tumor suppressive mechanisms that restrain nevus melanocyte proliferation remain poorly understood. Here we utilize cell and murine models to demonstrate that oncogenic BRAF leads to activation of the Hippo tumor suppressor pathway, both in melanocytes in vitro and nevus melanocytes in vivo. Mechanistically, we show that oncogenic BRAF promotes both ERK-dependent alterations in the actin cytoskeleton and whole-genome doubling events, which independently reduce RhoA activity to promote Hippo activation. We also demonstrate that functional impairment of the Hippo pathway enables oncogenic *BRAF*-expressing melanocytes to bypass nevus formation and rapidly form melanomas. Our data reveal that the Hippo pathway enforces the stable arrest of nevus melanocytes and represents a critical barrier to melanoma development.

[1] Department of Pharmacology & Experimental Therapeutics, Boston University School of Medicine, Boston, MA 02118, USA. [2] Department of Biochemistry, Boston University School of Medicine, Boston, MA 02118, USA. [3] Department of Medicine, Boston University School of Medicine, Boston, MA 02118, USA. [4] Department of Dermatology, Boston University School of Medicine, Boston, MA 02118, USA. [5] Program in Molecular Medicine, University of Massachusetts Medical School, Worcester, MA 01605, USA. [6] Department of Pathology and Laboratory Medicine, University of Pennsylvania Perelman School of Medicine, Philadelphia, PA 19104, USA. ✉email: nganem@bu.edu

Cutaneous melanoma arises from the malignant transformation of melanocytes, which are neural crest-derived cells mainly localized to the basal layer of the epidermis. When locally resected, melanoma is highly curable; however, melanoma is the most aggressive of all skin cancers and distant-stage disease is associated with significant mortality[1]. Unraveling the molecular features underlying the pathogenesis of cutaneous melanoma is essential for the development of preventative and therapeutic treatment strategies.

The vast majority of melanocytic neoplasms are initiated by oncogenic mutations in the mitogen-activated protein kinase (MAPK) pathway, with activating mutations in *BRAF* and *NRAS* occurring in ~50% and ~20% of cutaneous melanomas, respectively[2]. Within *BRAF*-mutant melanomas, the most common activating mutation results from a single amino acid substitution from a valine to a glutamic acid generating the constitutively active mutant $BRAF^{V600E}$[3,4]. Despite strongly inducing proliferative signaling, melanocyte-specific expression of $BRAF^{V600E}$ is insufficient to induce melanoma in multiple animal models; instead, $BRAF^{V600E}$ expression leads to the development of benign nevi (moles) comprised of growth-arrested melanocytes[5–10]. This is corroborated by clinical evidence as melanocytes within benign human nevi also frequently contain $BRAF^{V600E}$ mutations[11,12] and these melanocytic nevi rarely transform into melanoma (annual rate <0.0005%)[13]. Similarly, mutations within *NRAS* are commonly detected in congenital nevi and oncogenic *NRAS* expression in melanocytes in vivo does not rapidly yield melanoma[14–16]. Although the risk of any single melanocytic nevus transforming into melanoma is minimal, understanding how such transformations occur is paramount as roughly one-third of all melanomas co-exist with or arise from nevi[17].

These observations indicate that tumor suppression mechanisms restrain melanoma development following the acquisition of activating MAPK pathway mutations in melanocytes. A longstanding view is that strong oncogenic signals driven by mutations in MAPK pathway components lead to oncogene-induced cellular senescence (OIS), which safeguards against tumorigenesis[18–20]. Supporting this view, it has been demonstrated that expression of $BRAF^{V600E}$ in primary melanocytes in vitro induces an immediate cell cycle arrest and that these arrested melanocytes exhibit all of the hallmarks of oncogene-induced senescence: they become large, flat, vacuolar, express $p16^{INK4A}$, display senescence-associated β-galactosidase (SA-β-gal) activity, and have increased heterochromatic foci and DNA damage[18,21].

However, while it is clear that oncogene-induced senescence occurs in vitro, the extent to which this mechanism operates to ward off tumorigenesis in vivo remains unclear[22–24]. Several pieces of evidence argue against OIS as being the predominant mechanism restraining the proliferation of melanocytes harboring oncogenic mutations in vivo (extensively reviewed in ref. [16]). Most notably, oncogene expression (e.g., $BRAF^{V600E}$) in melanocytes does not induce an immediate proliferative block in vivo. Rather, these oncogenes initially induce proliferation, as evidenced by the clonal outgrowth of melanocytes that ultimately form a nevus, which requires many rounds of cell division. Furthermore, melanocytes lacking proteins known to enforce senescence, such as p16 and p53, retain the capacity to enter a growth-arrested state, as melanocytes in $Braf^{V600E}/Cdkn2a^{-/-}$ and $Braf^{V600E}/Trp53^{-/-}$ mouse models still primarily form nevi, with only a rare few melanocytes stochastically transforming into melanoma[7].

Collectively, these data suggest that additional tumor suppressive mechanisms have the capacity to restrain the proliferation of $Braf^{V600E}$-positive mouse melanocytes, independent of inducing senescence. Recent modeling studies have led to the postulation that the growth arrest of nevus melanocytes is not solely due to oncogene activation and OIS in individual cells, but rather due to cells sensing and responding to their collective overgrowth, similar to what occurs in normal tissues[25]. This cell growth arrest is reminiscent of the arrest induced by activation of the Hippo tumor suppressor pathway, which is an evolutionarily conserved pathway known to regulate organ size. When the Hippo pathway is activated, the Hippo kinases LATS1/2 phosphorylate the transcriptional co-activators YAP (*YAP1*) and TAZ (*WWTR1*), resulting in their inactivation by nuclear exclusion and subsequent degradation[26,27]. In contrast, when the Hippo pathway is inactivated, YAP and TAZ are active and form DNA-binding complexes with the TEAD family of transcription factors, which act synergistically with AP-1 complexes to stimulate the expression of genes mediating entry into the S-phase and cell proliferation[28,29].

It is not known if Hippo pathway activation contributes to the growth arrest of nevus melanocytes. Moreover, while Hippo pathway inactivation has been suggested to promote cutaneous melanoma growth and invasion[30–32], it remains unknown whether Hippo inactivation is sufficient to induce cutaneous melanoma initiation and/or progression. Here, we use a combination of in vitro and in vivo model systems to examine the role of the Hippo tumor-suppressor pathway in restraining melanoma development.

Results

$BRAF^{V600E}$ expression activates the Hippo tumor-suppressor pathway in vitro. We sought to examine if the expression of $BRAF^{V600E}$ is sufficient to induce activation of the Hippo tumor-suppressor pathway in cultured melanocytes. Previous studies using primary melanocytes have demonstrated that exogenous expression of oncogenic $BRAF^{V600E}$ leads to an immediate p53-dependent growth arrest[9,33]. We, therefore, developed a system in which $BRAF^{V600E}$ expression could be induced without an immediate cell cycle arrest in an attempt to explore Hippo pathway activation over multiple cell cycles. To do so, we generated a doxycycline-inducible system to permit controlled $BRAF^{V600E}$ expression in non-transformed Simian Virus 40 (SV-40) immortalized melanocytes (Mel-ST cells)[34]. Expression of the SV-40 early region, which encodes the small and large T viral antigens, imparts immortality to primary melanocytes via multiple mechanisms including impairment of the p53/Rb pathways[34]. Induction of $BRAF^{V600E}$ expression in Mel-ST cells increased the phosphorylation levels of the downstream kinases ERK and RSK, indicating that the cell model successfully hyperactivates MAPK signaling upon the addition of doxycycline (dox) (Fig. 1a).

To determine if $BRAF^{V600E}$ activates the Hippo tumor-suppressor pathway in vitro, we induced $BRAF^{V600E}$ expression and examined the relative levels of active, phosphorylated LATS1/2 at the hydrophobic motif (T1079)[27]. We found a significant increase in LATS phosphorylation following expression of oncogenic $BRAF^{V600E}$ (Fig. 1b). We then assessed total YAP phosphorylation (p-YAP) via phos-tag gel electrophoresis. We observed that $BRAF^{V600E}$ induction promoted phosphorylation of YAP at multiple sites (Fig. 1c). Consequently, expression of $BRAF^{V600E}$ led to nuclear exclusion of YAP and a corresponding decrease in the expression of the YAP target genes *CYR61* and *AMOTL2* (Fig. 1d, e and Supplementary Fig. S1A). The observed effects on LATS and YAP activity were due to $BRAF^{V600E}$, as overexpression of wild-type *BRAF* had no effect on LATS or YAP phosphorylation (Supplementary Fig. S1B–E). We further confirmed these results in multiple cell lines, including

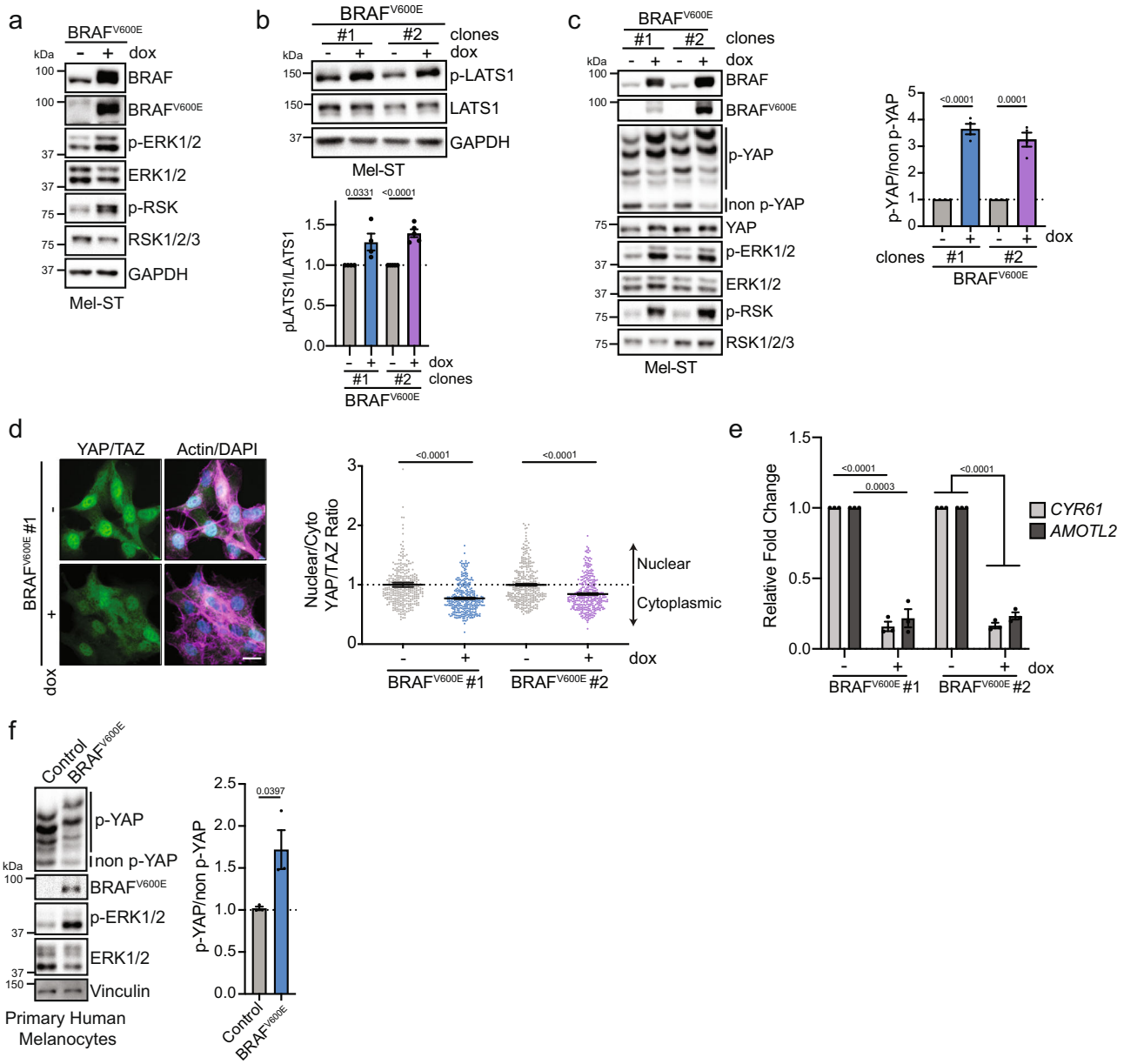


Fig. 1 *BRAF*^{V600E} activates the Hippo tumor-suppressor pathway. a Representative immunoblot (IB) of dox-inducible *BRAF*^{V600E} Mel-ST cells cultured ± dox for 24 h. **b** IB of two different dox-inducible *BRAF*^{V600E} Mel-ST clones cultured ± dox for 24 h ($n \geq 4$ independent experiments, graph shows mean relative intensity ± SEM, two-tailed unpaired *t* test). **c** Left, IB of two dox-inducible *BRAF*^{V600E} Mel-ST clones cultured ± dox for 24 h; Right, intensity quantification of YAP phosphorylation from phos-tag gel ($n = 4$ independent experiments, graph shows mean relative intensity ± SEM, two-tailed unpaired *t* test). **d** Left, representative immunofluorescence staining of YAP/TAZ (green) alone or merged with DNA (DAPI, blue) and actin (Phalloidin, magenta) in indicated *BRAF*^{V600E} Mel-ST clone; right, quantification of nuclear to cytoplasmic ratio of mean YAP/TAZ fluorescence ($n > 300$ cells from three independent experiments, graph shows mean ± SEM, scale bar = 20 µm, two-tailed Mann–Whitney test). **e** Relative expression of indicated genes from RT-PCR in *BRAF*^{V600E} Mel-ST clones cultured ± dox for 24 h ($n = 3$ independent experiments, graph shows mean ± SEM, two-tailed unpaired *t* test). **f** Left, IB of primary human melanocytes infected with lentivirus that express control vector (H2B-GFP) or BRAF^{V600E}; right, intensity quantification of YAP phos-tag ($n = 3$ independent experiments, graph shows mean ± SEM, two-tailed unpaired *t* test). Source Data are provided as a Source Data file.

non-immortalized primary adult human melanocytes with an intact p53 pathway (Fig. 1f and Supplementary Fig. S1F). Importantly, the observed effects of Hippo pathway activation were not limited to the expression of *BRAF*^{V600E} alone, as we also found that inducible expression of oncogenic *NRAS*^{Q61R} similarly activates the Hippo pathway (Supplementary Fig. S1G). Collectively, these data demonstrate that hyperstimulation of the MAPK signaling pathway through the expression of oncogenic *BRAF*^{V600E} or *NRAS*^{Q61R} leads to activation of the Hippo tumor-suppressor pathway in vitro.

Growth-arrested melanocytes in benign nevi show evidence of Hippo pathway activation. It is well established that melanocyte-specific expression of *Braf*^{V600E} in animal models gives rise to benign nevi that harbor non-proliferating melanocytes[5,25]. We hypothesized that these *Braf*^{V600E}-positive melanocytes may also demonstrate evidence of Hippo pathway activation, similar to our in vitro results. To test this possibility, we analyzed a single-cell RNA sequencing dataset of whole-skin extracts collected at postnatal days 30 (P30) and 50 (P50) from wild-type control mice and tamoxifen-painted

Tyr::CreER^{T2}/Braf^{CA} mice expressing active *Braf^{V600E}*[25]. We interrogated this dataset to examine if YAP/TAZ-dependent gene transcription was repressed in melanocytes expressing oncogenic *Braf^{V600E}*. Following dimensionality reduction and initial clustering, we identified the cluster representing melanocytes based on the expression of the melanocyte-lineage marker *Dct* as previously reported (Fig. 2a)[25]. As expected, this cluster was found to have high expression of other melanocyte-lineage markers, notably *Mlana* and *Mitf* (Supplementary Fig. S2A). We then employed the variance-adjusted Mahalanobis (VAM) method, a scRNA-seq optimized approach to obtain accurate signaling pathway scores, to examine if YAP/TAZ-mediated gene expression was decreased in *Braf^{V600E}*-expressing mouse melanocytes relative to wild-type melanocytes utilizing previously published YAP/TAZ gene expression profiles[35–37]. The most basic analysis, where all single cells were binned by genotype, demonstrated that YAP/TAZ gene expression targets were significantly reduced in *Braf^{V600E}*-positive melanocytes compared to wild-type (Fig. 2b).

We then performed unsupervised clustering, which generated five melanocyte subdivisions, to clarify which unique populations of oncogenic *Braf^{V600E}*-expressing melanocytes exhibited the least YAP/TAZ activity (Fig. 2c). We theorized that clusters containing nevus melanocytes would be exclusively populated by cells isolated from *Braf^{V600E}* mice, and be the primary melanocytic subtype isolated from 50-day-old mice. Based on these criteria, we identified clusters 0 and 1 as *Braf^{V600E}*-expressing melanocytes isolated from nevi (Fig. 2c and Supplementary Fig. S2B, S2C). In support of this prediction, expression of *Cdkn2a*, which is upregulated in nevus melanocytes, was found to be the highest in clusters 0 and 1, although *Cdkn2a* read-depth was limited throughout all clusters (Supplementary Fig. S2D). Compared to all other melanocytes, nevus melanocytes (clusters 0 and 1) exhibited the lowest YAP/TAZ activity scores of any cluster, demonstrating that YAP/TAZ-mediated gene expression is reduced following oncogenic *Braf* expression in mouse nevus melanocytes (Fig. 2d–f). Importantly, expression of Hippo pathway components remained unchanged regardless of genotype or cluster, suggesting decreased YAP/TAZ signaling was due to Hippo pathway activation, not altered expression of YAP/TAZ regulators (Supplementary Fig. S2E, F).

Not all melanocytes captured from *Braf^{V600E}* mice exhibited low YAP/TAZ activity scores. Clusters 2 and 4, which contain an appreciable portion of melanocytes from both *Braf$^{+/+}$* and *Braf^{V600E}* mice, demonstrated much higher YAP/TAZ activity relative to nevus melanocytes (Supplementary Fig. S2G). However, within these clusters, YAP/TAZ activity was still decreased in *Braf^{V600E}* melanocytes compared to wild-type cells. This suggests that cell-intrinsic mechanisms following *Braf^{V600E}* expression are only partially leading to decreased YAP/TAZ activity and that other mechanisms, possibly cell-extrinsic cues, may play additional roles in vivo. We suspect cluster 3, the only cluster that did not exhibit this trend, may be comprised of proliferating, follicular melanocytes as this cluster mainly contains melanocytes isolated at P30 when most murine hair follicles are in anagen[25]. Taken together, these data reveal *Braf^{V600E}*-expressing mouse melanocytes largely exhibit decreased YAP/TAZ activity, with the most significant decreases found within nevus melanocytes, strongly implying the Hippo pathway becomes activated in response to *Braf^{V600E}* expression and nevus formation in vivo. In support of these conclusions, immunofluorescence staining of three human benign nevi revealed YAP localization to be predominantly cytoplasmic and thus presumably inactivated in human nevus melanocytes, consistent with a previous study using a validated YAP antibody (Fig. 2g)[38].

***BRAF^{V600E}*-induced Hippo activation restrains oncogenic melanocyte proliferation**. We next investigated whether Hippo tumor-suppressor activation following *BRAF^{V600E}* expression leads to reduced melanocyte proliferation in vitro. Population doubling assays demonstrated that expression of *BRAF^{V600E}* reduced Mel-ST cell number ~30–40% relative to uninduced controls over a 4-day period, despite the fact these melanocytes were SV-40 immortalized (Fig. 3a). Live-cell imaging and proliferation assays revealed this was predominantly due to a proliferative arrest, rather than increased cell death (Supplementary Figs. S3A, B and 4A). To test whether the observed Hippo pathway activation induced by *BRAF^{V600E}* expression was responsible for this proliferative defect, we used RNAi to knock down the LATS1/2 kinases in the context of *BRAF^{V600E}* expression. We found that loss of LATS1/2 prevented YAP phosphorylation following induction of *BRAF^{V600E}* and fully rescued cell growth and viability (Fig. 3b, c). We further found that inhibition of LATS1/2 with a potent small-molecule inhibitor also rescued cell growth (Fig. 3d)[39]. We then validated these findings using soft-agar growth assays. While parental Mel-ST cells and Mel-ST cells expressing *BRAF^{V600E}* failed to efficiently grow under anchorage-independent conditions, Mel-ST cells expressing *BRAF^{V600E}* together with a constitutively active YAP mutant (YAP-5SA) demonstrated significant colony formation (Fig. 3e and data not shown). These data reveal that functional inactivation of the Hippo pathway, through either LATS1/2 depletion/inhibition, or constitutive YAP activation, is sufficient to restore proliferation to *BRAF^{V600E}*-expressing immortalized melanocytes in vitro.

We sought to determine to what extent human melanoma cells inactivate the Hippo pathway. We first interrogated the The Cancer Genome Atlas (TCGA), where we found that co-heterozygous loss of *LATS1/2* is observed in ~15% of human melanomas (Fig. 3f and Supplementary Fig. S3C, D). We then stained a panel of human melanoma samples for YAP localization utilizing SOX10 as a marker for melanoma cells and, in agreement with previous studies, found that multiple melanoma tumors exhibited strong nuclear YAP localization, suggesting Hippo pathway inactivation (Fig. 3g and Supplementary Fig. S3E)[31,38]. Collectively, these data reveal that a subset of oncogenic melanocytes during melanomagenesis will overcome or bypass Hippo pathway activation to regain proliferative capacity.

***BRAF^{V600E}*-induced Hippo activation is ERK-dependent and partially mediated by changes in the actin cytoskeleton**. We sought to understand the mechanisms through which *BRAF^{V600E}* directly or indirectly activates the Hippo tumor-suppressor pathway. Oncogenic MAPK signaling has previously been shown to impair mitosis, and complete mitotic failure can lead to the generation of tetraploid cells that activate the Hippo pathway[40–43]. We speculated that the expression of *BRAF^{V600E}* may lead to Hippo pathway activation by disrupting the normal completion of mitosis. To test this possibility, we performed live-cell imaging of doxycycline-inducible *BRAF^{V600E}* Mel-ST cells stably expressing the chromosome marker histone 2B-GFP (H2B-GFP). We observed that upon entering mitosis, cells expressing *BRAF^{V600E}* often exhibited widely oscillating chromosomes and were unable to maintain a tightly aligned metaphase plate relative to uninduced controls (Fig. 4a). These chromosome alignment defects impaired the ability of many cells to satisfy the spindle assembly checkpoint, and consequently a portion of the *BRAF^{V600E}*-expressing cells endured a significantly prolonged mitosis (Fig. 4a, b and Supplementary Fig. S4A, B). Cells that cannot satisfy the spindle assembly checkpoint either undergo mitotic cell death, or exit from mitosis without undergoing cell

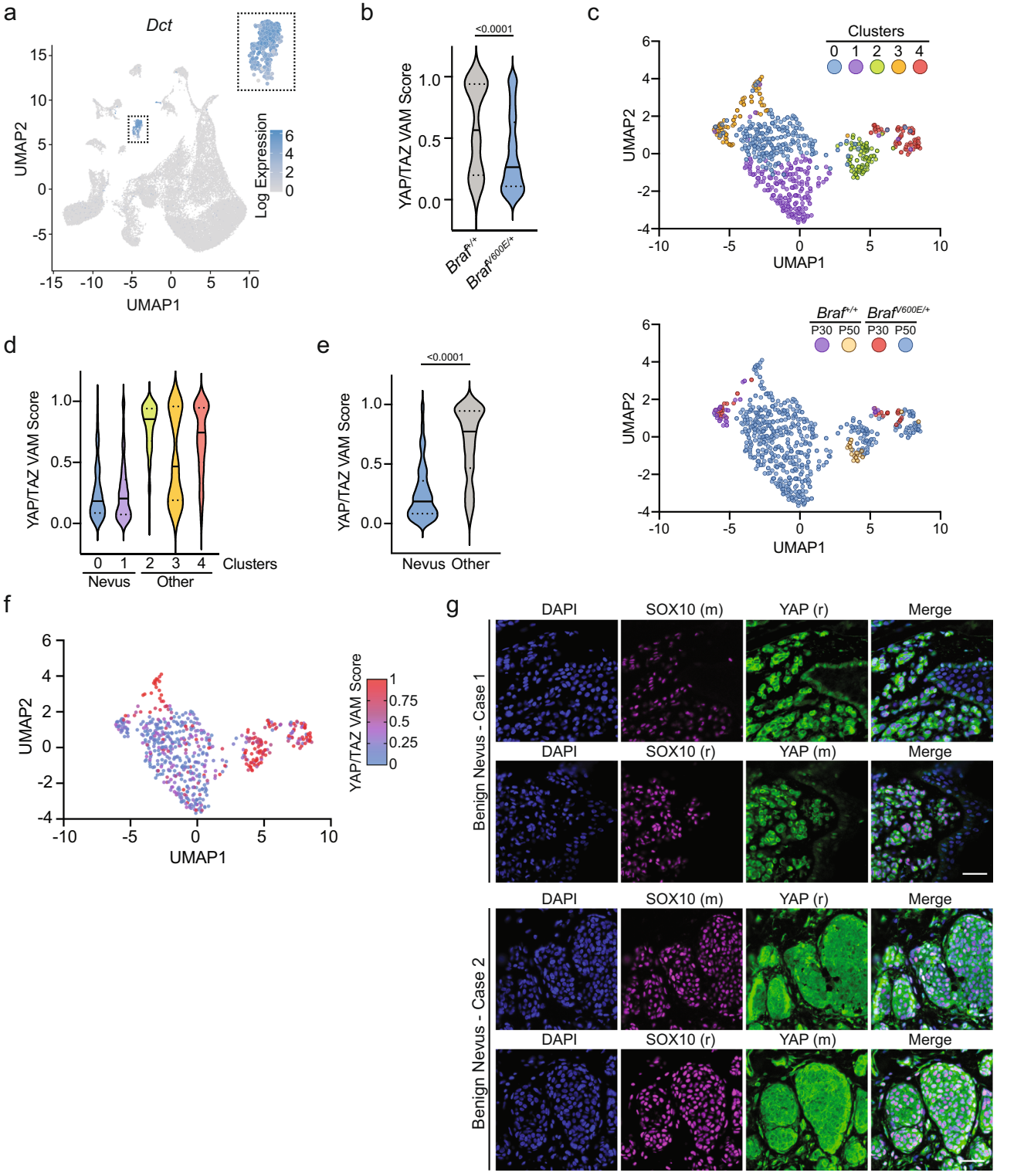


Fig. 2 *Braf*^{V600E}-expressing nevus melanocytes display decreased YAP/TAZ signaling. a UMAP of relative *Dct* expression of all single cells from nevus containing murine skin identifying a cluster of cells representing melanocytes from GSE154679. **b** YAP/TAZ VAM scores for melanocytes from indicated genotypes ($n = 46$ for *Braf*$^{+/+}$, $n = 543$ for *Braf*$^{V600E/+}$, two-tailed Mann–Whitney test). **c** Top, UMAP of melanocytes colored by subcluster; Bottom, UMAP of melanocytes colored by genotype and animal age ($n = 589$). **d** YAP/TAZ VAM score plotted by melanocyte subcluster. **e** YAP/TAZ VAM score comparing nevus (clusters 0, 1) and other melanocytes (clusters 2, 3, 4) (nevus $n = 408$, other $n = 181$, two-tailed Mann–Whitney test). **f** UMAP of melanocytes colored by gradient indicating YAP/TAZ VAM score. **g** Representative immunofluorescence staining of indicated proteins in two benign nevi cases with two different sets of antibodies, (r) = rabbit, (m) = mouse, DAPI (blue), YAP (green), SOX10 (magenta), scale bar = 50 μm. Source Data are provided as a Source Data file.

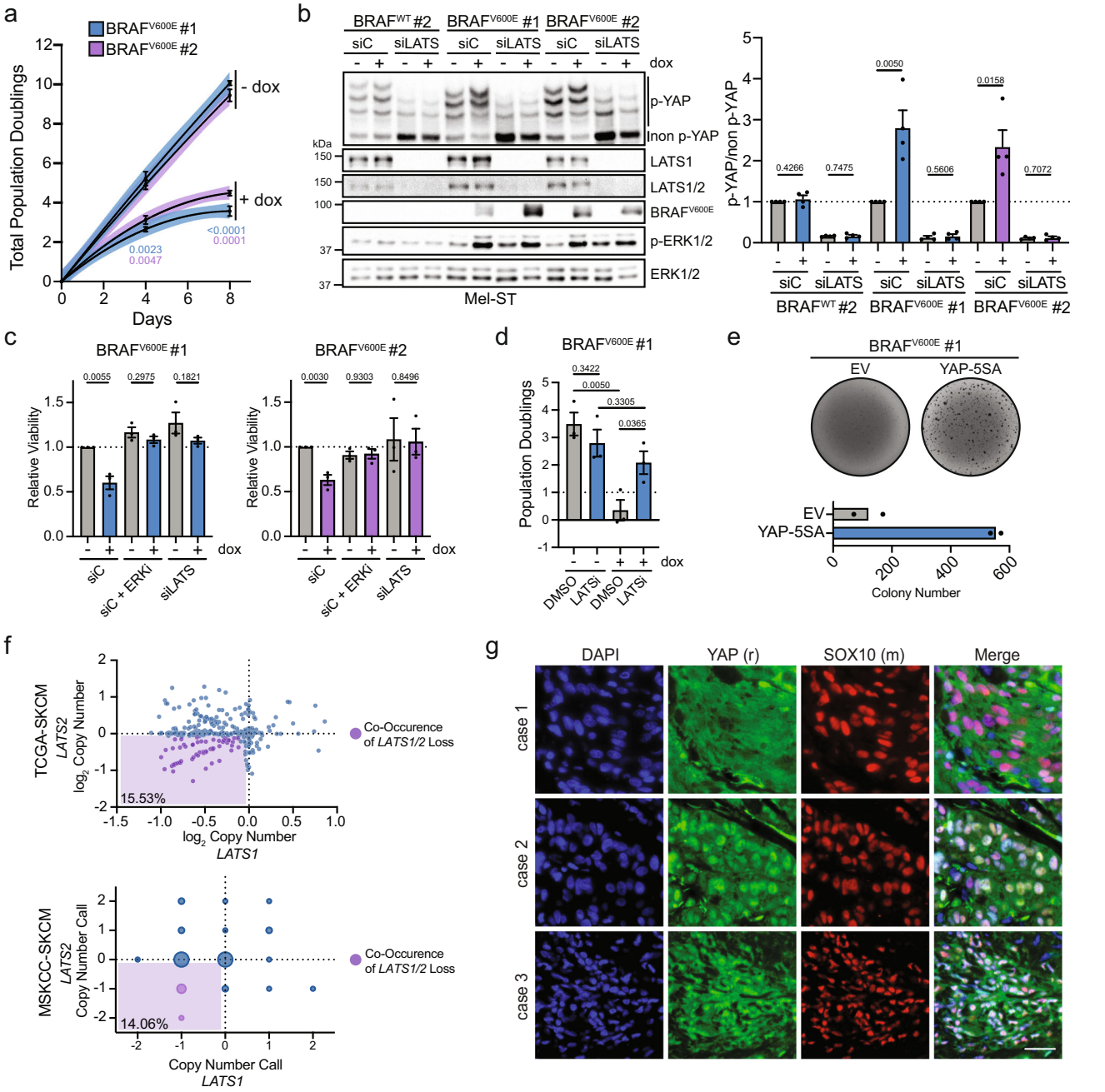


Fig. 3 Oncogenic BRAF-induced Hippo pathway activation restrains melanocyte growth. a Population doubling assay of two dox-inducible *BRAF*^{V600E} Mel-ST clones ± dox ($n = 3$ independent experiments, lines represent second-order polynomial non-linear fit, line color represents 95% confidence interval (dots show mean ± SEM, two-tailed unpaired *t* test). **b** Left, representative IB of two dox-inducible Mel-ST clones treated with control siRNA (siC) or LATS1 and LATS2 siRNAs (siLATS) ± dox for 24 h; right, intensity quantification of YAP phos-tag ($n = 4$ independent experiments, graph shows mean ± SEM, two-tailed unpaired *t* test). **c** Relative viability of Mel-ST cell lines treated with indicated siRNA or drugs for a 4-day period ($n = 3$ independent experiments in technical quintuplicate, graphs show mean ± SEM, two-tailed unpaired *t* test). **d** Number of population doublings of indicated dox-inducible Mel-ST clone over 4 days treated with either DMSO or a LATS1/2 inhibitor (LATSi), ± dox ($n = 3$ independent experiments, graph shows mean ± SEM, two-tailed unpaired *t* test). **e** Representative crystal violet stain of dox-inducible *BRAF*^{V600E} Mel-ST cell line expressing indicated genes grown in dox-containing soft agar with quantification below ($n = 2$ independent experiments in technical triplicate, graph shows mean). **f** Plot of $\log_2$ copy-number values from TCGA-SKCM or GISTIC 2.0 calls from MSKCC-SKCM databases for the genes *LATS1* and *LATS2*; bottom left percent is the frequency of *LATS1/2* co-heterozygous loss. **g** Representative immunofluorescence staining of indicated proteins in three human melanoma cases, scale bar = 25 µm). Source Data are provided as a Source Data file.

division, a phenomenon termed mitotic slippage[44]. Cells that undergo mitotic slippage often generate multinucleated tetraploid cells, and multinucleated melanocytes have been observed in human nevi[42,44,45]. We observed that upon induction of *BRAF*^{V600E} the number of mitoses producing tetraploid cells increased significantly (control: 2.47%, induced: 24.75%) and was mainly driven by an increase in mitotic slippage (control: ~1%, induced: ~20%) (Fig. 4b and Supplementary Fig. S4B). These data demonstrate that *BRAF*^{V600E} can impair mitosis leading to mitotic slippage and the formation of multinucleated tetraploid

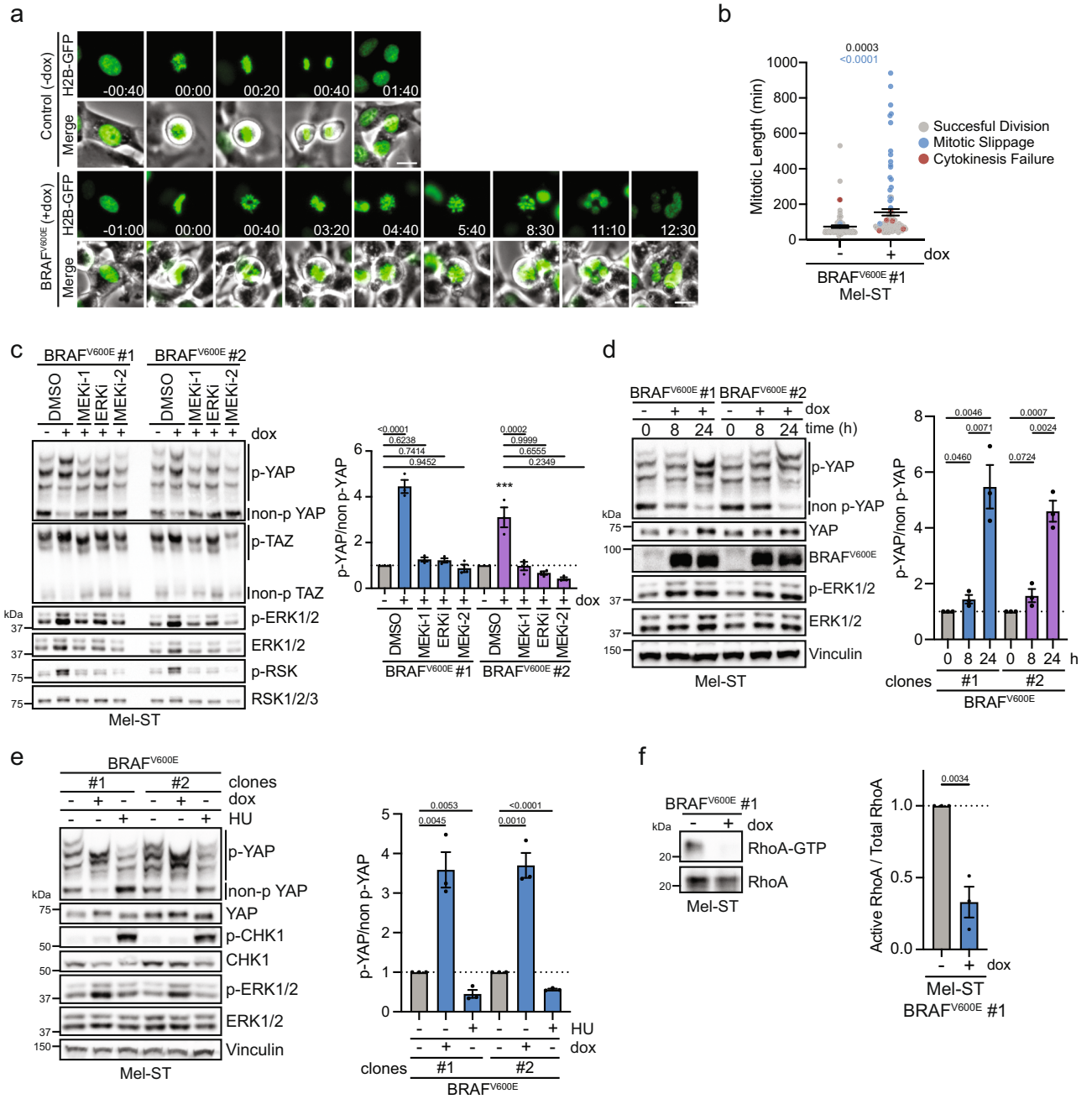


Fig. 4 Prolonged MAPK activation leads to cytoskeletal defects and Hippo activation. a Representative fluorescence and phase-contrast images from a live-cell video of dox-inducible *BRAF*^{V600E} Mel-ST cells expressing the chromosome marker H2B-GFP (green) cultured ± dox (scale bar = 25 µm, hh:mm). **b** Plot of mitotic duration and fate of individually tracked mitoses from (**a**) ($n > 80$ mitoses per condition from two independent experiments, graph shows mean ± SEM, dots represent individually tracked mitoses, black *P* value represent mitotic duration significance, two-tailed unpaired *t* test, blue *P* value represent significance for difference in frequency of whole-genome doubling events, two-sided Fisher's exact test). **c** Left, IB of indicated dox-inducible *BRAF*^{V600E} Mel-ST cell lines cultured ± dox for 24 h along with indicated drugs at the following doses: ERKi (20 nM), MEKi-1 (10 µM), MEKi-2 (20 nM); right, intensity quantification of YAP phos-tag ($n = 3$ independent experiments, graph shows mean ± SEM, one-way ANOVA with multiple comparisons). **d** Left, IB of dox-inducible *BRAF*^{V600E} Mel-ST cell lines cultured ± dox for indicated time; right, intensity quantification of YAP phos-tag ($n = 3$ independent experiments, graph shows mean ± SEM, two-tailed unpaired *t* test). **e** Left, representative IB of dox-inducible *BRAF*^{V600E} Mel-ST cell lines treated ± dox for 24 h or with 1 mM hydroxyurea for 6 h; right, intensity quantification of YAP phos-tag ($n = 3$ independent experiments, graph shows mean ± SEM, two-tailed unpaired *t* test). **f** Representative IB of RhoA-GTP pulldown in indicated dox-inducible *BRAF*^{V600E} Mel-ST cell line ± dox; right, intensity quantification of RhoA-GTP to total RhoA ($n = 3$ independent experiments, graph shows mean ± SEM, two-tailed unpaired *t* test). Source Data are provided as a Source Data file.

melanocytes in vitro. However, two lines of evidence suggested that mitotic errors leading to tetraploidization were not the major underlying driver of Hippo pathway activation in $BRAF^{V600E}$-expressing melanocytes. First, $BRAF^{V600E}$-expressing Mel-ST cells arrested in G_1 (via thymidine) or G_2 (via RO-3306-mediated CDK1 inhibition) still experienced Hippo activation despite their inability to become tetraploid (Supplementary Fig. S4C). Second, immunofluorescence experiments revealed that mononucleated diploid cells also exhibited decreased nuclear YAP/TAZ, demonstrating tetraploidization was not necessary to observe Hippo pathway activation (Fig. 1d).

We next investigated whether $BRAF^{V600E}$ specifically, or rather hyperactivation of the MAPK pathway generally, is responsible for Hippo pathway activation. We found that dampening of MAPK signaling via inhibition of the downstream kinases MEK1/2 or ERK1/2 fully prevented Hippo pathway activation, as measured by YAP/TAZ phosphorylation status, in $BRAF^{V600E}$-inducible cell lines (Fig. 4c and Supplementary Fig. S5A). These data demonstrated that Hippo pathway activation is entirely mediated by general hyperactivation of MAPK signaling and requires factors downstream of ERK. These data also discounted the possibility that oncogenic $BRAF^{V600E}$ activates Hippo signaling via direct phosphorylation of key Hippo pathway components.

We noted that phosphorylation of YAP following $BRAF^{V600E}$ expression required sustained MAPK stimulation over a period of at least 12–16 h, as transient MAPK activation only minimally affected YAP phosphorylation (Fig. 4d and Supplementary Fig. S5B). We speculated that mounting oncogene-induced replication stress may be promoting Hippo pathway activation; however, induction of replication stress by hydroxyurea treatment alone was not sufficient to activate the Hippo pathway (Fig. 4e). Alternatively, it has been demonstrated that oncogenic activation of the MAPK pathway dramatically alters actomyosin cytoskeletal contractility and reduces RhoA activity in an ERK1/2-dependent manner[46–48]. Reductions in active RhoA are well known to promote Hippo pathway activation and, furthermore, ERK1/2-dependent cytoskeletal changes have previously been shown to modulate YAP/TAZ activity in melanoma cell lines[40,49,50]. We, therefore, posited that the reduction of RhoA activity may represent a mechanism by which $BRAF^{V600E}$-expressing cells activate the Hippo pathway in vitro. Indeed, we observed that there was a significant reduction in the number of actin stress fibers in cells following activation of $BRAF^{V600E}$, indicating reduced RhoA activity (Supplementary Fig. S5C, D). We then directly measured RhoA activity via pull-down assay, which revealed significantly decreased levels of active RhoA in Mel-ST cells expressing $BRAF^{V600E}$ relative to controls (Fig. 4f). These data suggest that $BRAF^{V600E}$-induced Hippo pathway activation is at least partially mediated by prolonged MAPK hyperstimulation leading to ERK1/2-dependent cytoskeletal dysregulation. Supporting this view, endogenous $Braf^{V600E}$ expression in mouse embryonic fibroblasts has been shown to drastically reduce actin stress fibers, and a recent study has also demonstrated that expression of $BRAF^{V600E}$ in RPE-1 cells leads to decreased RhoA activity in vitro and cytokinesis failure in zebrafish (Darp et al. unpublished)[51].

***Lats1/2*$^{-/-}$ deletion promotes melanomagenesis**. Our data suggested that functional inactivation of the Hippo tumor-suppressor pathway may enable $BRAF^{V600E}$-expressing melanocytes to evade growth arrest and facilitate melanoma development. To test this, we generated mice carrying floxed alleles of both *Lats1* and *Lats2*[52] with *Tyr::CreER*^{T2} to allow for inducible, melanocyte-specific inactivation of the Hippo pathway (*Tyr::CreER*^{T2}/*Lats1*$^{f/f}$/*Lats2*$^{f/f}$). Deletion of *LATS1/2* is well established to completely abrogate the Hippo pathway, and co-heterozygous loss of *LATS1/2* is observed in ~15% of human melanomas, making deletion of *Lats1/2* clinically relevant (Fig. 3f and Supplementary Fig. S3C, D)[2,53]. We also crossed *Tyr::CreER*^{T2}/*Lats1*$^{f/f}$/*Lats2*$^{f/f}$ (*Lats1/2*$^{-/-}$) mice with mice expressing the Cre-activatable oncogenic *Braf* allele (*Braf*$^{CA/+}$), generating *Tyr::CreER*^{T2}/*Braf*^{CA}/*Lats1*$^{f/f}$/*Lats2*$^{f/f}$ (*Braf*^{V600E}/*Lats1/2*$^{-/-}$) mice (Fig. 5a and Supplementary Fig. S6A). We confirmed the melanocytic specificity of our *Tyr::CreER*^{T2} expressing mice via incorporation of a fluorescent lineage trace (*YFP*^{LSL}), whose expression was only observed in cells that co-stained for melanocyte markers (Supplementary Fig. S6B).

We observed that *Braf*^{V600E}/*Lats1/2*$^{-/-}$ mice were highly prone to developing spontaneous dermal tumors within weeks after birth, even without topical 4-hydroxytamoxifen (4-HT) administration. A similar melanoma mouse model, *Tyr::CreER*^{T2}/*Braf*^{CA}/*Pten*$^{f/f}$ (*Braf*^{V600E}/*Pten*$^{-/-}$), has also been shown to be prone to spontaneous melanoma formation in the absence of topical 4-HT, due to leakiness of the inducible Cre recombinase[54,55]. This suggests that deletion of *Lats1/2* plays a major role in promoting melanoma development, as *Braf*^{V600E} expression alone in murine melanocytes does not generate tumors[5,25] (Supplementary Fig. S6A). In the few mice where spontaneous tumorigenesis was absent or delayed, 4-HT administration to *Braf*^{V600E}/*Lats1/2*$^{-/-}$ flanks resulted in the potent form of tumors which appeared histologically similar to the spontaneously arising neoplasms (Fig. 5b, c and Supplementary Fig. S6C). These tumors exhibited strong nuclear YAP/TAZ staining, indicating Hippo inactivation, and positively stained for the melanocytic markers SOX10 and S100 (Fig. 5d). SOX10 staining was nuclear and homogenous whereas S100 staining was weakly heterogeneous. Subsequent histopathologic analysis by a dermatopathologist confirmed these infiltrative, spindle cell tumors to be mouse melanoma. Unlike other *Braf*^{V600E}-driven mouse melanoma models (e.g., *Braf*^{V600E}/*Cdkn2a*$^{-/-}$, *Braf*^{V600E}/*Trp53*$^{-/-}$), which still mainly induce nevus formation, we were unable to appreciate any obvious nevogenesis in *Braf*^{V600E}/*Lats1/2*$^{-/-}$ mice. These data imply oncogenic *Braf*^{V600E}-positive melanocytes may be incapable of entering an enduring growth arrest without a functional Hippo tumor-suppressor pathway.

We also investigated the consequences of *Lats1/2* loss in melanocytes in the absence of oncogenic *Braf*. We found that following melanocyte-specific deletion of *Lats1/2*, mice exhibited no obvious hyperpigmentation, yet still rapidly developed cutaneous tumors with 100% penetrance after 4–5 weeks (Fig. 5e–g and Supplementary Fig. S6C–E). Co-heterozygous deletion of *Lats1/2* also promoted cutaneous tumorigenesis, albeit at prolonged time scales (Supplementary Fig. S6F). Analysis of *Lats1/2*$^{-/-}$ tumor sections revealed non-pigmented neoplasms which were remarkably similar to invasive *Braf*^{V600E}/*Lats1/2*$^{-/-}$ mouse tumors, exhibited a comparable staining profile, and were subsequently diagnosed as mouse melanoma (Fig. 5h). Previous studies have identified TEAD and AP-1 transcription factors as major regulators of the melanoma invasive state, which is marked by dedifferentiation and loss of pigmentation signatures[56,57]. We hypothesized that YAP/TAZ-TEAD activation, driven by *Lats1/2* deletion, may enable melanocytes to directly access this invasive gene program explaining our observed lack of pigmentation. In support of this hypothesis, both *Braf*^{V600E}/*Lats1/2*$^{-/-}$ and *Lats1/2*$^{-/-}$ mouse melanomas exhibited markedly low staining for mature, differentiated melanocyte markers (Supplementary Fig. S6G).

Given *Lats1/2*$^{-/-}$ tumors did not exhibit overt signs of pigmentation, we sought to generate additional data to validate that these neoplasms were melanocytic in origin. It has recently been demonstrated that initiation of the hair follicle cycle, via depilation, strongly promotes melanocyte transformation in

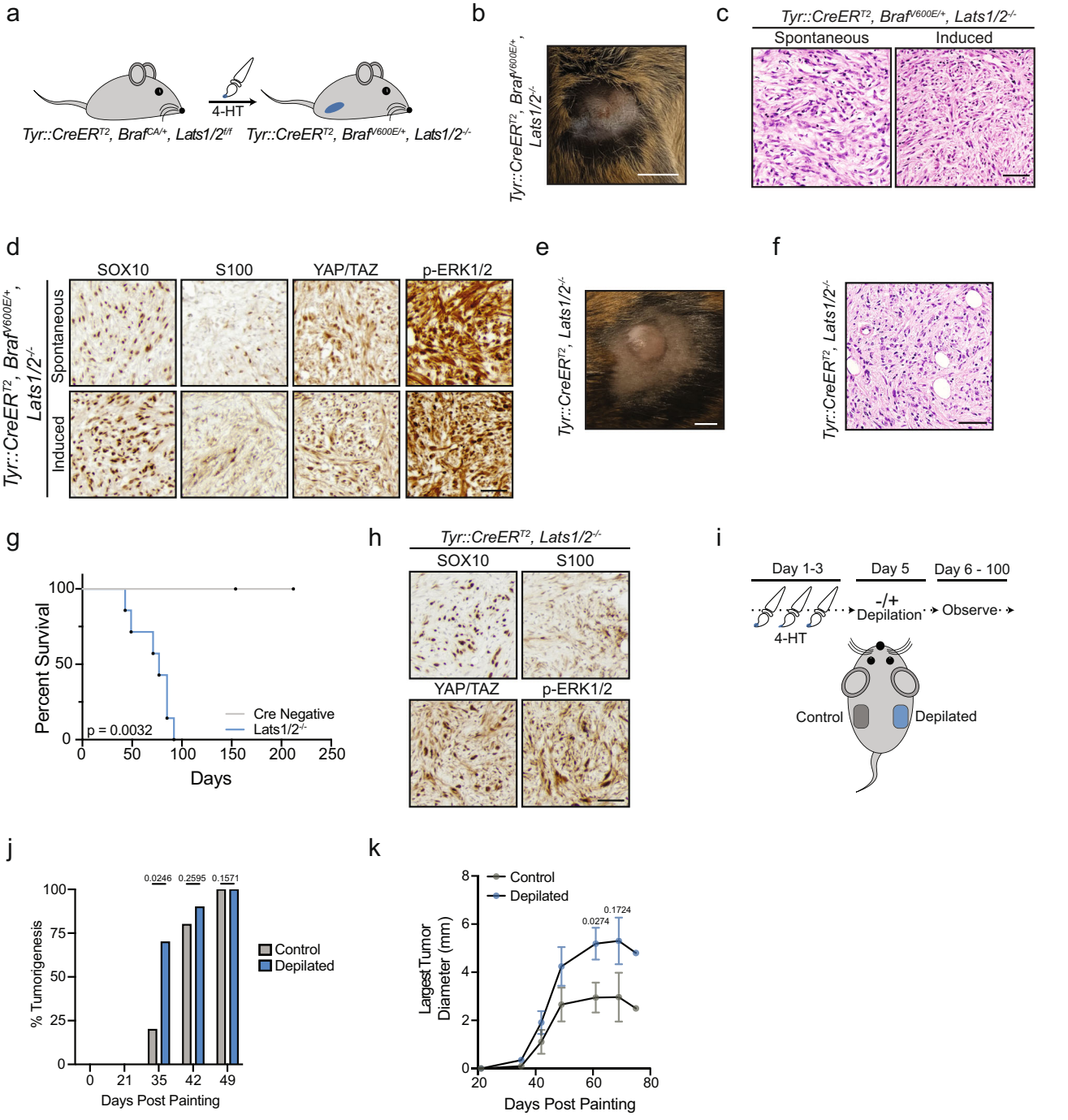


Fig. 5 *Lats1/2* deletion promotes melanoma formation. a Cartoon depicting 4-HT painting experiment. **b** Representative image of induced $Braf^{V600E}/Lats1/2^{-/-}$ mouse tumor, scale bar = 0.5 cm. **c** Representative hematoxylin and eosin staining of spontaneous or induced tumors from $Braf^{V600E}/Lats1/2^{-/-}$ mice, scale bar = 50 μm ($n > 3$ spontaneous tumors, $n = 2$ induced tumors from $Braf^{V600E}/Lats1/2^{-/-}$ mice). **d** Representative IHC of indicated proteins, scale bar = 40 μm ($n > 3$ spontaneous tumors, $n = 2$ induced tumors from $Braf^{V600E}/Lats1/2^{-/-}$ mice). **e** Representative image of induced $Lats1/2^{-/-}$ mouse tumor, scale bar = 0.5 cm. **f** Representative hematoxylin and eosin staining of induced flank tumor from $Lats1/2^{-/-}$ mouse, scale bar = 50 μm ($n > 6$ independent mice with similar results). **g** Survival plot from painting to study endpoint of $Lats1/2^{-/-}$ mice with 4-HT painted on flanks (Cre negative $n = 4$, $Lats1/2^{-/-}$ $n = 7$, log-rank test). **h** Representative IHC of indicated proteins, scale bar = 40 μm ($n \geq 3$ $Lats1/2^{-/-}$ mice). **i** Cartoon depicting depilation experiment in $Lats1/2^{-/-}$ mice. **j** Percent palpable tumorigenesis in $Lats1/2^{-/-}$ mice at indicated time points ($n = 10$ mice, two-tailed unpaired *t* test). **k** Diameter of largest tumor on each animal measured at indicated time points ($n \geq 3$ tumors measured at each timepoint with error bars ± SEM, ten mice total, two-tailed unpaired t test). Source Data are provided as a Source Data file.

$Braf^{V600E}/Pten^{-/-}$ mice[58,59]. We leveraged this unique characteristic of mouse melanomagenesis to test if $Lats1/2^{-/-}$ tumor formation was also promoted by depilation, suggesting a melanocytic origin. We induced loss of *Lats1/2* on opposing mouse flanks and then depilated only one flank so as to compare the tumorigenic rate from depilated and non-depilated regions (Fig. 5i). We observed that skin regions depilated following 4-HT treatment demonstrated significantly faster tumorigenesis, with palpable tumors observed in 70% of depilated areas compared to 20% of non-depilated areas about one month following treatment

(Fig. 5j). Not only did tumors appear faster in depilated areas, but these tumors also grew significantly larger (Fig. 5k). Collectively, our data demonstrate that melanocyte-specific loss of *Lats1/2* alone, or in conjunction with oncogenic *Braf* expression, promotes mouse melanocyte transformation and the formation of mouse melanoma.

We then investigated whether Hippo pathway inactivation was also occurring in other mouse models of melanoma. We performed gene set enrichment analyses (GSEA) using gene expression data collected from benign and transformed melanocytes from $Braf^{V600E}/Cdkn2a^{-/-}$ and $Braf^{V600E}/Cdkn2a^{-/-}/Lkb1^{-/-}$ mice[7]. GSEA revealed that YAP/TAZ gene sets were significantly enriched in murine melanoma cells as compared to both arrested nevus melanocytes and proliferating non-tumorigenic melanocytes (Fig. 6a and Supplementary Fig. S7A–D). These data reveal that the Hippo tumor-suppressor pathway becomes attenuated as these murine melanocytes transform into melanoma.

Active YAP drives melanoma development. We aimed to further define how deletion of *Lats1/2* promotes melanoma development in vivo. While it is well-described that *Lats1/2* loss functionally inactivates the Hippo pathway and leads to the activation of YAP and TAZ, LATS1/2 can also impinge upon additional signaling pathways that promote tumor development. For example, recent research has revealed inactivation of the Hippo pathway can promote mTOR signaling via multiple routes including YAP-driven expression of a micro-RNA, miR-29, which targets PTEN mRNA for silencing[60–62]. However, we detected no observable changes in PTEN protein level following either RNAi-mediated knockdown of LATS1/2 or expression of constitutively active YAP (YAP-5SA) or TAZ (TAZ-4SA) in Mel-ST cells (Fig. 6b, c). We also could not appreciate any significant change in phosphorylated S6 levels following *LATS1/2* silencing (Fig. 6b). Furthermore, examination of $Lats1/2^{-/-}$ tumors revealed PTEN remained strongly expressed in vivo (Fig. 6d). These data reveal that loss of *Lats1/2* is not driving melanomagenesis by activating mTOR via miRNA-mediated depletion of PTEN. It has also been demonstrated that active LATS2 can bind and inhibit MDM2 leading to increased p53 protein levels[63], raising the possibility that deletion of *Lats1/2* leads to decreases in p53, which may facilitate $Braf^{V600E}$-driven murine melanomagenesis[64]. Discounting this, we found that p53 still accumulates in $Lats1/2^{-/-}$ tumors (Fig. 6d). Previous studies have also demonstrated that *Lats1/2* knockout can induce cytokinesis failure and whole-genome doubling (WGD) in MEFs. Since WGD is well known to facilitate tumorigenesis, and a significant fraction of human melanomas are WGD, we speculated that *Lats1/2* loss may drive tumorigenesis in vivo through an initial WGD event. To test this possibility, we performed copy-number analysis using ultra-low pass whole-genome sequencing (ULP-WGS) to examine if genomic alterations, such as WGD events, were enriched in $Braf^{V600E}/Lats1/2^{-/-}$ tumors relative to $Braf^{V600E}/Pten^{-/-}$ tumors. However, sequencing revealed that all tumors from these models were diploid, excluding the possibility that *Lats1/2* deletion was primarily inducing melanoma through a WGD intermediate (Supplementary Fig. S8A).

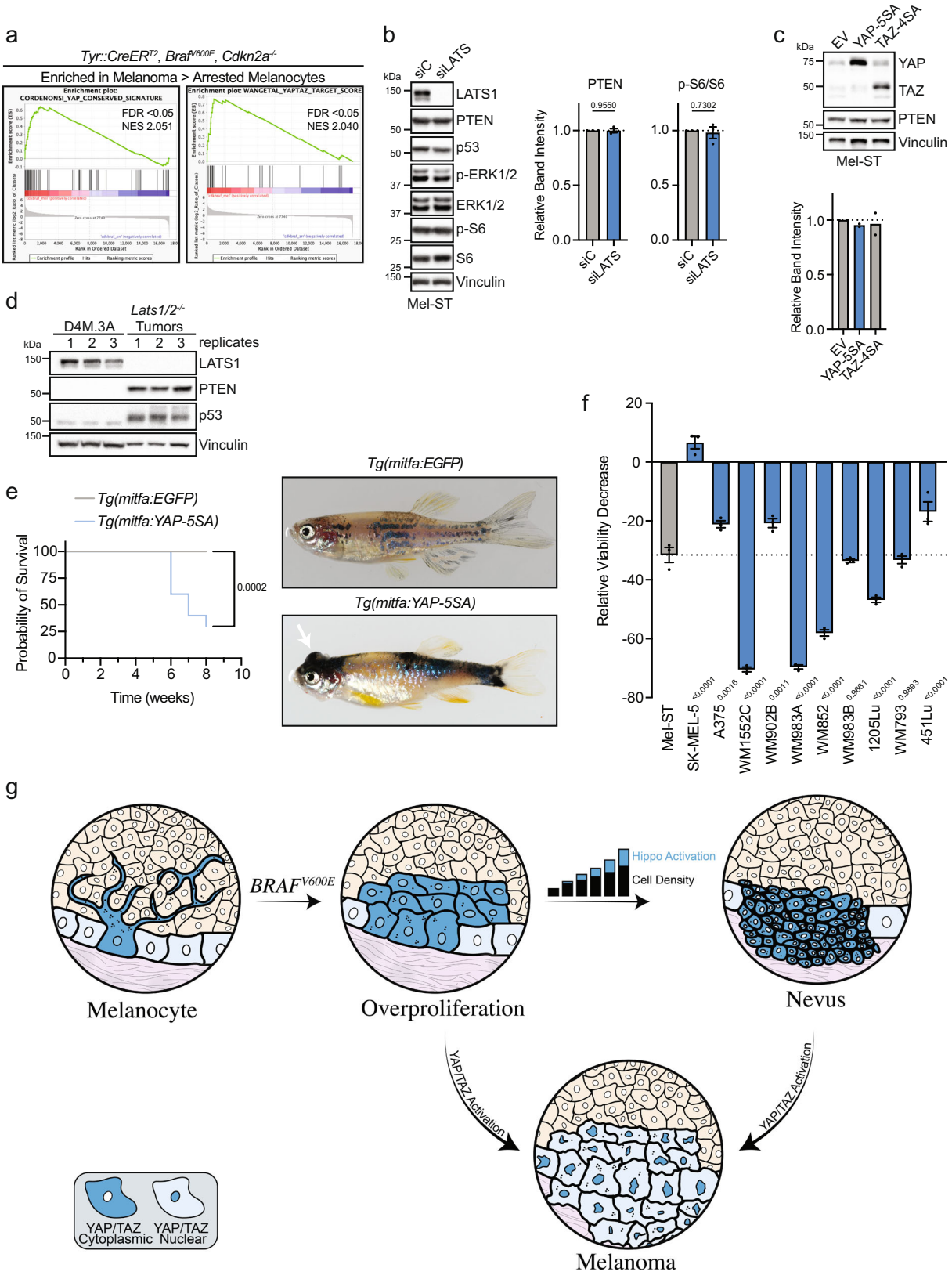
We then assessed whether YAP activation alone was sufficient to promote melanoma development. To do so, we generated a transgenic zebrafish model that expresses constitutively active YAP (YAP-5SA) in zebrafish melanocytes utilizing the mini-CoopR system[65]. These *Tg(mitfa:YAP-5SA)* zebrafish rapidly developed pigmented fish melanoma (Fig. 6e), demonstrating that constitutively active YAP is sufficient to induce melanoma development in a zebrafish model.

As activation of YAP/TAZ signaling was observed to promote melanomagenesis, we investigated whether depletion of YAP/TAZ could inhibit melanoma cell growth. RNAi-mediated knockdown of YAP/TAZ in the $Braf^{V600E}/Pten^{-/-}$ mouse melanoma cell line (D4M.3A) resulted in significantly decreased viability as compared to immortalized melanocytes (Supplementary Fig. S7E). We further explored YAP/TAZ dependency in a panel of human melanoma cell lines utilizing the pan-TEAD inhibitor MGH-CP1 and found that a number of melanoma cell lines were strikingly sensitive to inhibition of YAP/TAZ activity (Fig. 6f and Supplementary Fig. S7F)[66]. While *YAP1* is not commonly mutated in human melanoma, *YAP1* amplifications and mutations have been observed, and YAP staining in primary melanoma has been shown to significantly correlate with reduced patient survival[31,38,67]. Together, these data implicate YAP as a cutaneous melanoma oncogene and novel therapeutic target to further explore in the treatment of human melanoma.

Discussion

Discerning the molecular pathways that govern the growth arrest of nevus melanocytes, and how melanocytes ultimately overcome these barriers, is critical to fully understanding the mechanisms of melanomagenesis. A considerable body of work supports a role for OIS in preventing tumorigenic growth of melanocytes in vitro and in vivo; however, expanding lines of evidence demonstrate melanocytes within nevi retain proliferative capacity, in conflict with the absolute growth arrest implied by OIS[16]. Indeed, up to 30% of melanomas are predicted to arise from pre-cursor nevi[17]. These observations highlight nevi as being the product of "stable clonal expansion" rather than senescence[16]. Several genetic alterations that have the capacity to overcome the stable growth arrest of melanocytes expressing oncogenic MAPK mutations have been identified, including *CDKN2A, PTEN*, and *TP53*[3,5–7,64]. While deletion of *Cdkn2a* and *Trp53* with $Braf^{V600E}$ expression induces murine melanomagenesis, the vast majority of melanocytes still enter a stable growth arrest to form nevi[7]. Further, recent murine single-cell sequencing analyses reveal $Braf^{V600E}$-positive nevus melanocytes do not exhibit expression of senescence signatures[25]. Together, these discoveries suggest additional unidentified tumor suppressive mechanisms exist to enforce the arrest of nevus melanocytes.

We discovered that expression of $BRAF^{V600E}$ promotes activation of the Hippo tumor-suppressor pathway across multiple cell lines and that $Braf^{V600E}$-positive murine nevus melanocytes display significantly decreased YAP/TAZ signaling in vivo. Our data demonstrate that oncogenic *BRAF* expression induces Hippo pathway activation and cell cycle arrest in vitro by way of a cell-intrinsic mechanism, in which hyperactive MAPK signaling alters the cytoskeleton in part through decreased RhoA signaling and thus indirectly leads to Hippo pathway activation. However, our data also suggest that cell-extrinsic cues, perhaps secondary to the nevus microenvironment, may also be impinging upon YAP/TAZ signaling in vivo. Our single-cell sequencing analysis of mouse melanocytes indicated that while $Braf^{V600E}$-expression leads to a general repression of YAP/TAZ signaling in most melanocytes, the effect is strongest in nevus melanocytes (Fig. 2d). A recent modeling study has proposed that the growth arrest of nevus melanocytes may be due to cells sensing and responding to their collective overgrowth, rather than cell-autonomous mechanisms[25]. This growth arrest model is highly analogous to the collective cell processes mediating contact inhibition and organ growth, which are governed by the Hippo pathway. It is therefore tempting to speculate that melanocyte overgrowth induced by oncogene expression significantly increases melanocyte density over multiple rounds of division, ultimately promoting mounting activation of the Hippo tumor-suppressor pathway, eventual growth arrest, and nevus formation (Fig. 6g). If



true, one would predict Hippo pathway activation would only engage after a nevus passes a critical size threshold and that nevus melanocyte growth should be restored by reducing local melanocyte density. Intriguingly, nevi that are partially resected have been observed to regain proliferative capacity and the majority of these recurrent nevi did not grow beyond the limits of the original surgical scar, suggesting these nevus melanocytes arrest once they attain a similar size[68,69]. While growth arrest of oncogene-expressing melanocytes is conspicuous due the formation of pigmented nevi, it is also possible that oncogene-induced growth arrest of cells from other tissues is similarly mediated by activation of the Hippo pathway.

Fig. 6 YAP activation promotes melanomagenesis. a GSEA performed on GSE61750 comparing enrichment of YAP/TAZ signatures in melanoma to arrested melanocytes in indicated genotype (see Supplementary Fig. S7A, S7D). **b** Left, representative IB of Mel-ST parental cell line treated with control siRNA (siC) or LATS1 and LATS2 siRNAs (siLATS); right, quantification of PTEN and p-S6 proteins compared to loading control or total protein ($n = 3$ independent experiments, graphs show mean ± SEM, two-tailed unpaired *t* test). **c** Top, representative IB of Mel-ST parental cell line expressing indicated plasmids, EV: empty vector; bottom, quantification of PTEN compared to loading control ($n = 2$ independent experiments, graph shows mean). **d** IB comparing D4M.3 A cells and *Lats1/2*$^{-/-}$ tumor lysates where numbers represent replicates or different tumors, respectively ($n = 3$ independent experiments or mice). **e** Left, survival curve of zebrafish with indicated genotypes; right, representative images of zebrafish with indicated genotype ($n = 14$ independent EGFP fish, $n = 10$ independent YAP-5SA fish, log-rank test). **f** Graph shows relative viability decrease (%) in indicated cell lines treated with 10 μM MGH-CP1 for 4 days ($n = 3$ independent experiments in ≥technical quintuplicate, graph shows mean ± SEM, one-way ANOVA with Dunnett's multiple comparisons test). **g** Schematic model in which we propose overproliferation of melanocytes following acquisition of oncogenic *BRAF*^{V600E} leads to increases in local melanocyte density, which subsequently promotes Hippo pathway activation and contributes to growth arrest and nevus formation. Functional impairment of the Hippo pathway, leading to YAP/TAZ activation, enables melanocytes expressing *BRAF*^{V600E} to evade stable growth arrest and promote the development of melanoma. Source Data are provided as a Source Data file.

We also demonstrated that functional impairment of the Hippo pathway in melanocytes in vivo, either through deletion of *Lats1/2* in mice or expression of constitutively active *YAP1* in zebrafish, promotes cutaneous melanomagenesis. This finding has clinical relevance as co-heterozygous loss of *LATS1/2* and amplification of *YAP1* are observed in primary and metastatic human melanoma[31,32,38]. However, it should be noted that functional impairment of the Hippo pathway alone is not observed in human melanoma, and thus our model only partially replicates features of human tumors. Moving forward, it will be important to define additional mechanisms by which human melanoma cells circumvent the Hippo pathway to activate YAP[38,70,71]. For example, >80% of uveal melanomas and ~6% of cutaneous melanomas have mutations in GNAQ/GNA1 proteins, which stimulate RhoA activity and activate YAP/TAZ independent of any alterations in *LATS1/2*[72–74].

Our live-cell imaging also revealed that induction of oncogenic *BRAF* promotes chromosome alignment defects, prolonged mitosis, and mitotic or cytokinetic failures that lead to whole-genome doubling (WGD). Cells that have experienced a WGD (WGD$^+$ cells) are genomically unstable and tumorigenic, and their contribution to human cancer is significant[75–77]. Oncogenic *BRAF* may therefore facilitate tumorigenesis not only by activating MAPK signaling, but also by increasing the baseline level of oncogenic WGD$^+$ cells. However, while ~30–40% of all human melanomas, and the vast majority of human metastatic melanomas, demonstrate evidence of WGD[78], our mouse melanoma models failed to exhibit this genomic feature (Supplementary Fig. S8). This is likely because the mouse models are already potently tumorigenic without the need for the additional oncogenic effects imparted by a WGD; nevertheless, the lack of any appreciable WGD in murine melanomas illustrates that these models have limitations in recapitulating the human disease[45,76–78].

It is believed that activating MAPK mutations are critical for human melanocyte transformation; however, we found that murine melanocytes lacking *Lats1/2* rapidly developed into melanomas without the initial presence of any other genetic alterations that stimulate the MAPK pathway. Questions therefore remain as to how Hippo pathway inactivation alone can so strongly promote melanoma development in mice. We observed that melanomas generated from *Lats1/2*$^{-/-}$ mice exhibited strong p-ERK staining. This suggests that the *Lats1/2*$^{-/-}$ melanocytes likely evolved to hyperactivate the MAPK pathway during their transformation, either through the acquisition of additional genetic alterations or, potentially, by stimulating or emulating MAPK activity through YAP/TAZ-dependent transcriptomic changes[73]. Indeed, it has been observed that one common resistance mechanism to Vemurafenib, a BRAF^{V600E}-specific inhibitor, is the amplification and/or activation of YAP[49,70,79]. This suggests that YAP activity can compensate for loss of *BRAF*^{V600E} signaling. Given MAPK inhibitor resistance remains a significant component of treatment failure, our data suggests that co-targeting MAPK and YAP-TEAD signaling could simultaneously prevent resistance[70] and decrease melanoma cell viability[32,80].

In summary, we demonstrate that activation of the Hippo tumor-suppressor pathway promotes melanocyte growth arrest in response to the expression of oncogenic *BRAF*^{V600E}. Functional impairment of the Hippo pathway potently induces melanocyte growth in vitro and tumor development in vivo in multiple model organisms of melanomagenesis. Collectively, our data implicate the Hippo pathway as an important melanoma tumor suppressor and highlight YAP/TAZ as promising therapeutic targets to investigate for the treatment of human melanoma.

Methods

Cell culture. Immortalized melanocyte (Mel-ST) cells were a gift from the lab of Dr. Robert Weinberg. Mel-ST cells, and all derivative cell lines generated in this study, were grown in DMEM media containing 5% fetal bovine serum (FBS), 100 IU/mL penicillin, and 100 μg/mL streptomycin. Human Embryonic Kidney 293 (HEK293A) cells, and all derivative cell lines, were grown in DMEM media containing 10% FBS, 100 IU/mL penicillin, and 100 μg/mL streptomycin. hTERT-BJ fibroblasts, and all derivative cell lines, were grown in DMEM:F12 media containing 10% FBS, 100 IU/mL penicillin, and 100 μg/mL streptomycin. *Braf*^{V600E}/*Pten*$^{-/-}$ mouse tumor cells (D4M.3 A) were a generous gift of Dr. Constance Brinckerhoff. D4M.3 A mouse tumor cells were maintained in DMEM:F12 media containing 5% FBS. Primary adult epidermal melanocytes were purchased from ATCC (PCS-200-013) and maintained in Dermal Cell Basal Medium (ATCC PCS-200-030) supplemented with an Adult Melanocyte Growth Kit (ATCC PCS-200-042). All FBS used in these studies was confirmed to either be naturally absent of tetracyclines or below 20 ng/mL by the manufacturer. All cells were maintained at 37 °C with 5% CO_2 atmosphere and maintained at sub-confluent levels for passaging and all experiments. Cultures were regularly checked for mycoplasma contamination utilizing a PCR detection kit (G238, ABM) or Hoechst staining. Bright-field images of tissue culture cells were captured on an Echo Revolve Hybrid Microscopy system at ×10 or ×20 (Echo Laboratories).

Cell-line generation. To generate the *BRAF*^{V600E} doxycycline-inducible system Mel-ST, HEK293A, or hTERT-BJ fibroblasts were first infected with lentivirus generated from pLenti CMV TetR Blast (Tet Repressor) and selected. Following selection, cells were infected with lentivirus generated from pLenti CMV/TO BRAF^{V600E} Neo or pLenti CMV/TO BRAF Neo, selected, and single-cell cloned to establish cell lines which demonstrated no basal expression at baseline and strong induction after doxycycline addition. The expression of *BRAF*^{V600E} was confirmed using two different mutant-specific antibodies (VE1 and RM8 clones). To generate stably expressing H2B-GFP lines, cells were infected with lentivirus generated from pLenti H2B-GFP Blast. Mel-ST cells stably expressing empty vector (pLVX Puro), YAP-5SA (pBABE YAP-5SA Puro), and TAZ-4SA (pLVX Flag TAZ-4SA Puro) were generated via viral infection followed by selection. Tetraploid cells were generated by treating asynchronous cells with 4 μM DCB for 16 h, followed by gentle washing to remove drug (5 × 5 min); completion of cytokinesis was confirmed by phase-contrast imaging.

Viral infections and transfections. Mel-ST, HEK293A, or BJ Fibroblasts were infected for 12–16 h with virus-carrying genes of interest in the presence of 10 μg/mL polybrene, washed, and allowed to recover for 24 h before selection or single-cell cloning. Short-term viral infection of primary melanocytes was carried out

similarly, but with 2 μg/mL of polybrene. All RNAi transfections were performed using 25–50 nM siRNA with Lipofectamine RNAi MAX according to the manufacturer's instructions. Briefly, cells were seeded in 6 or 12-well plates either by addition of reverse transfection mixture overnight for 18 h, which was then washed with PBS and replaced with fresh media, or forward transfection mixture for 4 h, which was then replaced with fresh media. Cells were then incubated for 48–72 h prior to lysis at sub-confluent levels.

Plasmid generation. Plasmids encoding the Tetracycline Repressor, pLenti CMV TetR Blast (716-1), was a gift from Eric Campeau & Paul Kaufman (Addgene Plasmid #17492). To create pLenti CMV/TO BRAF Neo and pLenti CMV/TO BRAF^{V600E} Neo, we performed Gateway cloning using Gateway LR Clonase II (Invitrogen) according to manufacturer instructions to insert BRAF or BRAF^{V600E} into pLenti CMV/TO Neo DEST (685-3) using pENTR BRAF or pENTR BRAF^{V600E}. pENTR BRAF and pENTR BRAF^{V600E} were gifts from Craig Ceol and pLenti CMV/TO Neo DEST (685-3) was a gift from Eric Campeau & Paul Kaufman (Addgene plasmid #17292). To generate pLenti CMV/TO NRAS^{Q61R} Neo we performed Gateway cloning to insert NRAS^{Q61R} from the donor vector pDONR223 NRAS^{Q61R} into the destination vector pLenti CMV/TO Neo Dest. pDONR223 NRAS^{Q61R} was a gift from Jesse Boehm, William Hahn, and David Root (Addgene plasmid #81652).

Immunofluorescence and confocal microscopy. Cells were plated on glass coverslips, treated as indicated, washed in 1× phosphate-buffered saline (PBS) (Boston Bioproducts), and fixed in 4% paraformaldehyde for 10 min. Cells were then washed in PBS-0.01% Triton X-100, extracted in PBS-0.2% Triton X-100 for 10 min, blocked in Tris-buffered saline (TBS)-bovine serum albumin (BSA) (10 mM Tris, pH 7.5, 150 mM NaCl, 5% bovine serum antigen, 0.2% sodium azide) for 1 h, and incubated with primary antibodies diluted in TBS-BSA for 1 h at RT or overnight at 4 °C in a humidified chamber. Primary antibodies were visualized using species-specific fluorescent secondary antibodies (Molecular Probes, Alexa Fluor secondaries, 488 nm, 568 nm, 1:500) and DNA was detected with 2.5 μg/mL Hoechst. F-actin was visualized using rhodamine-conjugated phalloidin (1:2000, Molecular Probes, R415). Immunofluorescence images for analysis were collected on a Nikon Ti-E inverted microscope equipped with a Zyla 4.2 PLUS (Andor) and X-Cite 120 LED light source at the same exposure. Confocal immunofluorescence images were collected on a Nikon Ti-E inverted microscope equipped with a C2 + laser scanning confocal head with 405 nm, 488 nm, 561 nm, 640 nm laser lines. *Z*-stacks were acquired with a series of 0.5–1 μm optical slices which were then converted into a single, max-intensity projected image. Images were analyzed using NIS-Elements Advanced Research (AR) and ImageJ (Version 1.51). To assess YAP localization, two small square regions of interest were drawn at random in individual cells with one in the nucleus, and one in the cytoplasm. The background-corrected, mean fluorescence intensity of YAP was subsequently measured in these regions of interest and a nuclear to cytoplasmic ratio was determined. To assess stress fiber quantity, images were background-corrected, contrast normalized, and then fibers obvious to the naked eye were counted.

Live-cell imaging. Cells stably expressing H2B-GFP were grown on glass-bottom 12-well tissue culture-treated dishes (Cellvis) and treated with drugs of interest. Immediately post-treatment imaging was performed on a Nikon Ti-E inverted microscope equipped with the Nikon Perfect Focus system. The microscope stage was enclosed within a temperature and atmosphere-controlled environment at 37 °C and 5% humidified CO_2. Fluorescent or bright-field images were captured every 5–10 min with an ×10 or 20×0.5 NA Plan Fluor objective at multiple locations for 72–96 h. All captured images were analyzed using NIS-Elements AR software. The mitotic length was calculated by counting the duration from nuclear envelope breakdown to anaphase onset.

Tissue staining. At the experimental endpoint mice were euthanized and mouse tumors or skin samples were dissected and immediately fixed in 4% paraformaldehyde (PFA) in PBS for 16 h at 4 °C. Tissues were then paraffin-embedded for sectioning and mounting. PFA-fixed paraffin-embedded tissue sections were cut at 5 μm and mounted onto positively charged coverslips (Colorfrost Plus, Thermo). Mounted tissue samples were deparaffinized using xylenes and rehydrated via an ethanol:water gradient. For hematoxylin and eosin staining (H&E), the tissues were incubated in hematoxylin (#14166, Cell Signaling Technology), rinsed in water, differentiated with 1% acid ethanol, blued with 0.1% sodium bicarbonate solution, rinsed in water, dehydrated, cleared, and mounted with Cytoseal XYL (Thermo Scientific). For immunohistochemistry (IHC) or immunofluorescence (IF), antigen unmasking was performed on rehydrated tissue sections using either a citric-acid retrieval buffer (Vector Labs) or Tris-EDTA retrieval buffer (10 mM Tris, 1 mM EDTA, 0.05% Tween-20). Heat-mediated antigen retrieval was performed using either a standard microwave (95 °C, 20 min) or Decloaking Chamber NxGen (Biocare Medical) (110 °C, 12 min), followed by cooling to room temperature (~30–60 min). Citric-acid retrieval was used for most antibodies; Tris-EDTA retrieval was used for MelanA antibodies. For IHC, tissue sections were washed, endogenous peroxidase activity was quenched using 3% hydrogen peroxide in PBS for 10 min, and then blocked for 1 h in 10% goat serum in TBS (Sigma-Aldrich). For IF, tissue sections were blocked for 1 h in 10% goat serum in TBS. Following serum block, if necessary, tissue was incubated with Rodent Block M (Biocare Medical) for 30 min to block endogenous mouse IgG prior to murine primary antibody addition. Primary antibodies were diluted in 10% goat serum in TBS and incubated overnight at 4 °C in a humidified chamber. Following primary addition for IHC, slides were washed with TBS-0.01% Tween-20, incubated with anti-rabbit or mouse SignalStain Boost IHC detection reagent (Cell Signaling Technology) for 30 min and then developed with SignalStain DAB substrate kit (Cell Signaling Technology) according to manufacturer's instructions. Counterstaining was performed using hematoxylin, followed by dehydration, clearing, and mounting with Cytoseal XYL (Thermo Fisher). Images were captured at randomly selected points using a Nikon Ti-E inverted microscope equipped with a DS-Ri2 (Nikon). For IF, slides were incubated with species-specific fluorescent secondary antibodies (Molecular Probes) and 2.5 μg/mL Hoechst for 1 h at room temperature in a dark humidified chamber. Auto-fluorescence was quenched using Vector TrueVIEW according to the manufacturer's instructions, and slides were mounted using Prolong Gold Antifade (Invitrogen). Images were captured at randomly selected points using a Nikon Ti-E inverted microscope equipped with a Zyla 4.2 PLUS (Andor) and X-Cite 120 LED light source. For all staining experiments, tissue-specific secondary controls were included in each staining experiment to ensure specificity and control for endogenous tissue pigmentation levels.

Protein extraction and immunoblotting. Cells were gently washed twice in ice-cold 1X PBS and lysed using ice-cold cell lysis buffer (50 mM Tris-HCl, 2% w/v SDS, 10% glycerol) containing 1X HALT (dual-phosphatase and protease inhibitor, Thermo Fisher). Lysates were sonicated at 20% amplitude for 20 s, diluted in 4X Sample Buffer (Boston BioProducts), and resolved using SDS gel electrophoresis. For mouse tumor samples, 10 mg of tumor tissue was dissected and placed into RIPA lysis buffer (Boston BioProducts) supplemented with one Pierce protease inhibitor tablet and 1X HALT (Thermo Fisher). Tissue was mechanically dissociated initially using a 7-cm pestle (Kimble) followed by further homogenization with a 20-guage needle and brief sonication for 20 s at 20 kHz. Tissue lysate was then centrifuged at 4 °C and >15,000×*g* for 10 min. The supernatant was collected, diluted in 4× sample buffer to 2×, and resolved using SDS gel electrophoresis. For phos-tag immunoblots, a phos-tag gel was prepared with diluted Phos-Tag™ Acrylamide reagent (Wako Chemicals, AAL-107) according to the manufacturer's instructions utilizing manganese as the divalent cation. Proteins were then transferred onto PVDF membranes using a wet-tank transfer system (Bio-Rad), blocked for 1 h with TBS-0.1% Tween-20 containing 5% skim milk powder and then probed overnight at 4 °C with primary antibodies diluted in TBS-0.1% Tween-20 containing 1% skim milk powder. Bound antibodies were detected by incubating membranes with horseradish peroxidase-linked, species-specific, secondary antibodies (1:5000, Cell Signaling Technology) for 1 h, followed by 3 × 10 min washing in TBS-0.1% Tween-20, and then the addition of Clarity or Clarity Max ECL blotting substrate (Bio-Rad). Chemiluminescence acquisition was carried out using the Bio-Rad ChemiDox XRS + system and quantitative densitometry was measured using Image Lab (Bio-Rad).

Human nevi and melanoma samples. Human skin tissues with melanocytic nevi and melanoma were retrieved from archived material in the pathology laboratory at UMass Medical Center in compliance with all relevant ethical regulations and were determined to be exempt by the Institutional Review Board at UMass Medical Center (IRB H00007200). The tissue blocks were deidentified before tissue sections (10 μm) were obtained by the authors for IHC. These studies were reviewed in compliance with all relevant ethical regulations and were determined to be exempt by the Boston University School of Medicine Institutional Review Board (IRB H-37967).

RNA isolation and qRT-PCR. Total RNA from cultured cells was isolated using a Quick-RNA kit (Zymo Research). cDNA libraries were generated from RNA using the Superscript III kit and random hexamer primers (Invitrogen). Quantitative real-time PCR was performed using SYBR Green reagents in a StepOnePlus system (Applied Biosystems) according to manufacturer protocol. For each individual experiment, a technical triplicate was run which was then averaged to generate a single biological replicate. Primer sequences were as follows:

CYR61: forward, AGCCTCGCATCCTATACAACC; reverse, TTCTTTCACAA GGCGGCACTC

AMOTL2: forward, TTGGAATCTGCAAATCGCC; reverse, TGCTGTTCGTA GCTCTGAG

GAPDH: forward, GAGTCAACGGATTTGGTCG; reverse, CATTGATGGCA ACAATATCCAC

Antibodies. The antibodies used herein categorized by technique and company.

Immunofluorescence (cells): Santa Cruz Biotechnology: YAP 63.7, 1:250 (detects both YAP/TAZ, sc-101199).

Immunofluorescence (tissue): Cell Signaling Technologies: YAP (1A12) #12395, 1:100; YAP/TAZ (D24E4) #8418, 1:100; YAP (D8H1X) #14074, 1:100. Abcam: gp100 (ab137078), 1:250; SOX10 (Rabbit, ab180862), 1:250; SOX10 (Mouse, ab216020), 1:250.

Immunohistochemistry: Cell Signaling Technologies: YAP/TAZ (D24E4) #8418, 1:100; YAP (D8H1X) #14074, 1:100; GFP (D5.1, cross reacts with YFP) #2956, 1:100; phospho-p44/42 ERK1/2 (Thr202/Tyr204) #9101, 1:100; Abcam: gp100 (ab137078), 1:250; SOX10 (Rabbit, ab180862), 1:250; SOX10 (Mouse, ab216020), 1:250; MelanA (ab210546), 1:500. Dako: S100 (IS504), pre-diluted by the manufacturer.

Immunoblotting: Cell Signaling Technologies: B-Raf (D9T6S), 1:1000; phospho-p44/42 ERK1/2 (Thr202/Tyr204) #9101, 1:1000; p44/42 MAPK (ERK1/2) #9102, 1:1000; RSK1/RSK2/RSK3 (3D27) #9355, 1:1000; phospho-p90RSK (Ser380) (D3H11) #11989, 1:1000; GAPDH (14C10) #2118, 1:1000; YAP (D8H1X) #14074, 1:1000; LATS1 (C66B5) #3477, 1:1000; phospho-LATS1 (Thr1079) (D57D3) #8654, 1:1000; TAZ (E8E9G) #83669, 1:1000; TAZ (V386) #4883, 1:1000; phospho-S6 (Ser235/236) (D57.2.2E) XP #4858, 1:1000; PTEN (138G6) #9559, 1:1000; p53 (1C12) #2524, 1:1000; phospho-Chk1 (Ser345) #2341, 1:500. Abcam: Vinculin (ab18058), 1:4000. Invitrogen: $BRAF^{V600E}$ (RM8 Clone) #MA5-24661, 1:1000-2000. Bethyl Laboratories: LATS1/LATS2 (A300-479A), 1:1000. Santa Cruz Biotechnology: Chk1 (G-4) sc-8408, 1:500; S6 (C-8) sc-74459, 1:1000; N-Ras (F155) sc-31, 1:1000. Spring Biosciences: $BRAF^{V600E}$ (VE1 Clone) # E19290, 1:1000. Cytoskeleton: RhoA (ARH05), 1:500.

Soft-agar assays. In six-well dishes, sterile 2% noble agar stock solution in water was dissolved by heating to ~40–45 °C, mixed with warm media, plated at a final concentration of 0.6%, and allowed to cool and solidify at 4 °C. Following solidification, gels were warmed back to 37 °C. Next, cells were trypsinized, counted, 1×10^4 cells were plated in 0.3% noble agar and allowed to solidify at room temperature or briefly at 4 °C. Plates were maintained in a cell culture incubator for 2–4 weeks with feedings of 1.5 mL of 0.3% agarose solution weekly. All drugs were maintained at 2× concentration in underlays and independent experiments were done in technical triplicate. Total colonies per well were counted using phase-contrast imaging on an Echo Revolve Hybrid Microscopy system at ×10 (Echo Laboratories). For imaging, gels were stained for 20 min with 0.1% Crystal Violet, gently washed multiple times overnight, and imaged on a Chemi-Doc XRS + system under Fast Blast with 0.015-0.1 sec exposure.

EdU assays. Mel-ST cells were seeded on coverslips a day before each collection at a density of 4.5×10^4 cells/well in a 12-well culture dish. Cells were treated with DMSO as a negative control or doxycycline to induce expression of $BRAF^{V600E}$. EdU was added for a 30-min pulse at a final concentration of 10 μM and cells were then fixed with 4% PFA at different timepoints since the addition of doxycycline. Incorporated EdU was visualized using the Click-iT EdU kit from Invitrogen according to the manufacturer's protocol (C10337), imaged via fluorescence microscopy on a Nikon Ti-E inverted microscope equipped with a Zyla 4.2 PLUS (Andor) and X-Cite 120 LED light source at the same exposure, and analyzed in ImageJ (version 1.51).

RhoA pull-down activation assay. Active, GTP-bound RhoA was assessed using the RhoA activation assay, bead pull-down format, from Cytoskeleton, Inc (BK036) according to manufacturer instructions. Briefly, dox-inducible $BRAF^{V600E}$ expressing Mel-ST cells were plated at 3×10^4 cells in six-well dishes and allowed to grow for 2–3 days. Prior to reaching 70% confluence, cells were serum-starved and treated ± doxycycline for 24 h, then stimulated with complete media for 6 h prior to ice-cold lysis. Following lysis, input was isolated from total lysate prior to flash freezing with liquid nitrogen and storage at −80 °C. Active RhoA pulldown was performed according to manufacturer instructions utilizing GST-tagged Rhotekin-RBD protein on agarose beads. Samples were then analyzed using immunoblot according to manufacturer protocols.

Drug treatments. The concentrations used for the MAPK pathway inhibitors (MEKi-1/2 and ERKi) were determined experimentally to be the doses at which phosphorylation of ERK1/2 and RSK1/2/3 returned to baseline despite the presence of oncogenic *BRAF* expression. The reagents used in these studies are as follows: MEKi-1: U0126 (Selleck Chemicals), 10 μM; MEKi-2: Trametinib (GSK1120212), 20 nM (Selleck Chemicals); ERKi: SCH772984, 20 nM (Selleck Chemicals); Hydroxyurea, 1 mM (Selleck Chemicals); doxycycline, 1 μg/mL (Sigma-Aldrich D9891); thymidine, 2.5 mM (Sigma-Aldrich T1895); RO-3306, 7 μM (Sigma-Aldrich SML0569)

Population doubling and viability assays. For population doubling assays, initially 1×10^5 cells ($c_{initial}$) were plated in 10-cm dishes. After 4 days of growth cells were trypsinized, counted, and 1×10^5 cells were plated again. Cells were trypsinized and counted again after 4 more days. The number of population doublings (pd) were calculated by inputting the counted number of cells (c_{final}) into the following equation: $pd = \log_2(\frac{c_{final}}{c_{initial}})$. For viability assays, 4×10^3 cells per well were plated into a white-bottom 96-well dish in technical duplicate to quintuplicate, dependent upon the experiment. Cells were then treated with indicated siRNA and/or drugs for 4 days. The 96-well plate was then allowed to equilibrate at room temperature for 30 min followed by the addition of Cell Titer Glo (Promega) to each well according to the manufacturer's instructions. Viability was then assessed via luminescence using a BMG microplate reader and analyzed using BMG Labtech Optima v2.0R2 software. All technical replicates were averaged to generate a single biologic replicate.

Copy-number analysis. Log_2 copy-number values and/or putative copy-number GISTIC 2.0 values for *LATS1* and *LATS2* were downloaded from cBioPortal for the TCGA skin cutaneous melanoma (SKCM) subset of the PanCancer Atlas and Memorial Sloan Kettering Cancer Center (MSKCC), NEJM 2014 datasets. SKCM abbreviation represents skin cutaneous melanoma. Mutational status for *BRAF* and *NRAS* from the TCGA-SKCM dataset was also obtained from cBioPortal. Graphs were created in Prism 9.

Copy-number analysis by ultra-low-pass whole-genome sequencing. At the experimental endpoint, mice were euthanized and mouse tumors or skin samples were dissected, aliquoted, and immediately flash-frozen in liquid nitrogen and stored at −80 °C. For genomic DNA isolation, a Monarch Genomic DNA purification kit was utilized following the manufacturer's instructions. In brief, tumor or skin samples on ice were mixed with lysis buffer and proteinase K, vortexed, then incubated at 56 °C in a thermal mixer set to 1400 rpm agitation for 60 minutes. Lysed samples were then centrifuged for 3 min at >12,000×*g*. The supernatant was then mixed with RNase A, incubated for 5 minutes at 56 °C with full-speed agitation and then bound to the gDNA purification according to manufacturer instructions. gDNA was then eluted and stored at −20 °C until delivery to the Molecular Biology Core Facilities (MBCF) at Dana-Farber Cancer Institute (DFCI).

Library preparation and sequencing. gDNA was fragmented to 200 bp on a Covaris M220 instrument according to the manufacturer's protocol. Libraries were prepared using Swift S2 Acel reagents on a Beckman Coulter Biomek i7 liquid handling platform from approximately 200 ng of DNA according to the manufacturer's protocol with 14 cycles of PCR amplification. Finished libraries were quantified by Qubit fluorometer and fragment size distribution was evaluated by Agilent TapeStation 2200. Library pools were further evaluated for quality and balance with shallow sequencing on an Illumina MiSeq. Subsequently, libraries were sequenced targeting a depth of ~1X genome coverage on an Illumina NovaSeq6000 with paired-end 150 bp reads by the Molecular Biology Core Facilities at Dana-Farber Cancer Institute.

Copy-number analysis. Raw sequencing data (FASTQ files) were aligned to human and mouse reference genomes, GRCh37 and MM10 respectively, using BWA MEM (v.0.7.12). Both human and mouse alignment files were sorted by read names using Samtools (version 1.9). Software package Disambiguate (v. 1.0) was applied to sorted alignment files to infer the most likely source of each sequenced read (human or mouse genomes). Disambiguate output (BAM files) that comprised deconvoluted or "cleaned" human reads was used for further analysis. Precomputed bin annotations for human genome (GRCh37) and bin sizes of 100 Kb, 500 Kb, and 1 Mb were obtained with QDNASeq package (v. 1.28.0), along with GC-content and mappability profiles required for data normalization and bias correction. Normalized copy-ratios were estimated for each deconvoluted alignment file using QDNASeq capabilities. CBS algorithm as implemented in DNAcopy package was used to produce genome segmentation profiles. CNVKit package was used to generate ideogram representations of per-chromosome copy-number profiles.

Gene expression analysis. Publicly available microarray dataset GSE61750 was obtained from the Gene Expression Omnibus (GEO) (https://www.ncbi.nlm.nih.gov/geo/query/acc.cgi?acc=gse61750). For GSEA, indicated groups were normalized via meandiv, probes collapsed to max probe, and a weighted enrichment metric (log_2 Ratio of Classes) was utilized with 1000 permutations to determine enrichment in indicated gene sets. The YAP/TAZ target score gene set for VAM and GSEA was derived from ref. [36] and ref. [37]. Gene set can be found in Supplementary Table 1. The Hippo component gene set was derived from Reactome with additional genes added and can be found in Supplementary Table 2.

Single-cell RNAseq analysis. Count matrix of GSE154679 was downloaded from the GEO repository (https://www.ncbi.nlm.nih.gov/geo/query/acc.cgi?acc=GSE154679)[25]. Cells that had less than 200 expressed genes, more than 4000 expressed genes or >17% of mitochondrial gene were removed from analysis. A total of 35,214 cells were retained for downstream analysis. Normalization, dimensionality reduction, cell clustering and data visualization were analyzed with Seurat package[81]. PCA dimension reduction was performed using top 2000 highest variance genes. The top 15 principal components were utilized to calculate the k-nearest neighbors of each cell. Cell clusters were determined using Louvain algorithm at a resolution = 0.5, which was high enough to obtain clusters associated with cell lineage identity. We used UMAP to visualize and confirm cell clustering. Melanocyte cell population was identified based on the expression of canonical gene markers. To identify subclusters within melanocyte cell populations, we re-analyzed cells within melanocyte cell clusters using the same analysis pipeline described above. To quantify gene sets activity in each cell, gene set testing of scRNA-seq data was performed following VAM pipeline[35]. Data Normalization

and highest variable genes were analyzed using pipeline described above. VAM method was executed using vamForSeurat() function on the melanocyte cell population for each gene set. Graphs were created in Seurat or data was imported into Prism 9 for graph creation.

Murine studies. All animal experiments were conducted according to protocols approved by the Institutional Animal Care and Use Committee (IACUC) at Boston University (Protocol # PROTO201800236). Per Boston University IACUC protocol the maximum allowable mouse tumor size is 20 mm in diameter which was not exceeded. For mouse studies, a mix of male and female mice of the C57BL/6 strain were utilized under standard housing conditions (temperature: 68–79 °F, humidity: 30–70%, light cycles: 12 h on, 12 h off). All other mouse strains were sourced from Jackson Laboratory: *Tyr::CreER^{T2}* (Jax # 012328), *Lats1$^{f/f}$* (Jax # 024941), *Lats2$^{f/f}$* (Jax # 025428), *BRAF^{V600E}* (Jax # 017837), *R26-YFP^{LSL}* (Jax # 006148) and were crossed in-house. 4-hydroxytamoxifen (4-HT [Sigma, H7904]) was dissolved in methanol to a concentration of 5 mg/ml. To induce knockout in *Lats1/2$^{-/-}$*, and *Braf^{V600E}/Lats1/2$^{-/-}$*, mice aged 8–12 weeks had an ~2 cm^2 shaved on the right flank using surgical clippers and sufficient 4-HT solution to wet the skin was applied once daily to the shaved area for 3 consecutive days. For *Braf^{V600E}* mice, a higher concentration of 4-HT was required; 4-HT was dissolved in dimethylsulfoxide (DMSO) to a concentration of 25 mg/ml, and topical administration was performed as above. For the depilation experiments using *Lats1/2$^{-/-}$* mice, a 2 cm^2 was shaved on both the left and right flank of each mouse, and 5 mg/ml 4-HT was topically applied to each square for 3 consecutive days as above on the right flank, as well as on an approximately 2 cm length of the tail for 3 consecutive days. Two days after the final application, chemical depilation was performed by application of Nair hair remover onto the right flank for 15 s, followed immediately by wiping with a damp tissue to prevent irritation. For systemic knockout experiments, mice were injected with 20 mg/ml tamoxifen (Sigma, T5648) dissolved in corn oil to induce deletion in all Tyrosinase expressing cells. 8–12-week-old mice were injected daily with 100 µl tamoxifen for 5 consecutive days. Tumor development was measured weekly using calipers.

Zebrafish studies. Zebrafish were handled in accordance with protocols approved by the University of Massachusetts Medical School IACUC (Protocol A-2171). Constructs *Pmitfa:EGFP:pA* and *Pmitfa:YAP-5SA:pA* were used in the miniCoopR assay as previously described[65]. Briefly, *mitfa(lf)* mutant animals were bred, and single-cell stage embryos were injected with 25 pg of a single construct and 25 pg of Tol2 transposase mRNA. Successful Tol2-mediated integration of the construct into the genome rescued the *mitfa(lf)* phenotype, enabling melanocyte development. Equal numbers of male and female zebrafish were used. Melanocyte rescue was scored at 4–5 days of development, and rescued animals were grown to adulthood and monitored weekly for the presence of melanomas.

Statistical analysis. All quantitative data are presented as mean ± SEM, unless otherwise indicated. The number of samples (n) represents the number of biologic replicates or animals in study, unless otherwise indicated. Prism 9 was used for all statistical analyses and for the creation of most graphs.

RNAi sequences. The siRNA's used in this study are as follows:
Non-targeting #1 (Control siRNA) (Dharmacon):
UGGUUUACAUGUCGACUAA
LATS1 ON-TARGETplus SMARTpool (Dharmacon):
GGUGAAGUCUGUCUAGCAA; UAGCAUGGAUUUCAGUAAU
GGUAGUUCGUCUAUAUUAU; GAAUGGUACUGGACAAACU
LATS2 ON-TARGETplus SMARTpool (Dharmacon):
GCACGCAUUUUACGAAUUC; ACACUCACCUCGCCCAAUA
AAUCAGAUAUUCCUUGUUG; GAAGUGAACCGGCAAAUGC
YAP1 ON-TARGETplus SMARTpool (Dharmacon)
GCACCUAUCACUCUCGAGA; UGAGAACAAUGACGACCAA
GGUCAGAGAUACUUCUUAA; CCACCAAGCUAGAUAAAGA
WWTR1 ON-TARGETplus SMARTpool (Dharmacon)
CCGCAGGGCUCAUGAGUAU; GGACAAACACCCAUGAACA
AGGAACAAACGUUGACUUA; CCAAAUCUCGUGAUGAAUC.

Reporting summary. Further information on research design is available in the Nature Research Reporting Summary linked to this article.

Data availability

TCGA and MSKCC datasets used in the study are publicly available and can be obtained from https://portal.gdc.cancer.gov. Gene set data used in the study are publicly available on the GEO repository: GSE61750, GSE154679. Sequencing data generated in this study are publicly available on an NCBI database, the Sequence Read Archive (SRA), accession code PRJNA835203. The authors declare that all other data supporting this study are either available within the article, supplementary figures, or available from the authors upon request. Source data are provided with this paper.

Received: 23 April 2021; Accepted: 15 June 2022;
Published online: 29 June 2022

References

1. SEER*Explorer, *National Program of Cancer Registries and Surveillance, Epidemiology, and End Results SEER*Stat Database: NPCR and SEER Incidence – U.S. Cancer Statistics Public Use Research Database, 2019 submission (2001–2017), United States Department of Health and Human Services, Centers for Disease Control and Prevention and National Cancer Institute*. www.cdc.gov/cancer/uscs/public-use (2020).
2. Cancer Genome Atlas, N. Genomic Classification of cutaneous melanoma. *Cell* **161**, 1681–1696 (2015).
3. Shain, A. H. & Bastian, B. C. From melanocytes to melanomas. *Nat. Rev. Cancer* **16**, 345–358 (2016).
4. Shain, A. H. et al. Genomic and transcriptomic analysis reveals incremental disruption of key signaling pathways during melanoma evolution. *Cancer Cell* **34**, 45–55.e4 (2018).
5. Dankort, D. et al. Braf(V600E) cooperates with Pten loss to induce metastatic melanoma. *Nat. Genet.* **41**, 544–552 (2009).
6. Dhomen, N. et al. Oncogenic Braf induces melanocyte senescence and melanoma in mice. *Cancer Cell* **15**, 294–303 (2009).
7. Damsky, W. et al. mTORC1 activation blocks BrafV600E-induced growth arrest but is insufficient for melanoma formation. *Cancer Cell* **27**, 41–56 (2015).
8. Goel, V. K. et al. Melanocytic nevus-like hyperplasia and melanoma in transgenic BRAFV600E mice. *Oncogene* **28**, 2289–2298 (2009).
9. Patton, E. E. et al. BRAF mutations are sufficient to promote nevi formation and cooperate with p53 in the genesis of melanoma. *Curr. Biol.* **15**, 249–254 (2005).
10. McNeal, A. S. et al. CDKN2B loss promotes progression from benign melanocytic nevus to melanoma. *Cancer Discov.* **5**, 1072–1085 (2015).
11. Pollock, P. M. et al. High frequency of BRAF mutations in nevi. *Nat. Genet.* **33**, 19–20 (2003).
12. Yeh, I., von Deimling, A. & Bastian, B. C. Clonal BRAF mutations in melanocytic nevi and initiating role of BRAF in melanocytic neoplasia. *J. Natl Cancer Inst.* **105**, 917–919 (2013).
13. Tsao, H. et al. The transformation rate of moles (melanocytic nevi) into cutaneous melanoma: a population-based estimate. *Arch. Dermatol.* **139**, 282–288 (2003).
14. Dovey, M., White, R. M. & Zon, L. I. Oncogenic NRAS cooperates with p53 loss to generate melanoma in zebrafish. *Zebrafish* **6**, 397–404 (2009).
15. Ackermann, J. et al. Metastasizing melanoma formation caused by expression of activated N-RasQ61K on an INK4a-deficient background. *Cancer Res.* **65**, 4005–4011 (2005).
16. Damsky, W. E. & Bosenberg, M. Melanocytic nevi and melanoma: unraveling a complex relationship. *Oncogene* **36**, 5771–5792 (2017).
17. Pampena, R. et al. A meta-analysis of nevus-associated melanoma: prevalence and practical implications. *J. Am. Acad. Dermatol.* **77**, 938–945.e4 (2017).
18. Michaloglou, C. et al. BRAFE600-associated senescence-like cell cycle arrest of human naevi. *Nature* **436**, 720–724 (2005).
19. Kuilman, T. et al. The essence of senescence. *Genes Dev.* **24**, 2463–2479 (2010).
20. Courtois-Cox, S., Jones, S. L. & Cichowski, K. Many roads lead to oncogene-induced senescence. *Oncogene* **27**, 2801–2809 (2008).
21. Di Micco, R. et al. Oncogene-induced senescence is a DNA damage response triggered by DNA hyper-replication. *Nature* **444**, 638–642 (2006).
22. Cotter, M. A. et al. Absence of senescence-associated beta-galactosidase activity in human melanocytic nevi in vivo. *J. Invest Dermatol.* **127**, 2469–2471 (2007).
23. Michaloglou, C. et al. Comment on "Absence of senescence-associated beta-galactosidase activity in human melanocytic nevi in vivo". *J. Investig. Dermatol.* **128**, 1582–1583 (2008).
24. Tran, S. L. et al. Absence of distinguishing senescence traits in human melanocytic nevi. *J. Investig. Dermatol.* **132**, 2226–2234 (2012).
25. Ruiz-Vega, R. et al. Dynamics of nevus development implicate cell cooperation in the growth arrest of transformed melanocytes. *eLife* **9**, e61026 (2020).
26. Moroishi, T. et al. A YAP/TAZ-induced feedback mechanism regulates Hippo pathway homeostasis. *Genes Dev.* **29**, 1271–1284 (2015).
27. Meng, Z., Moroishi, T. & Guan, K. L. Mechanisms of Hippo pathway regulation. *Genes Dev.* **30**, 1–17 (2016).
28. Zanconato, F. et al. Genome-wide association between YAP/TAZ/TEAD and AP-1 at enhancers drives oncogenic growth. *Nat. Cell Biol.* **17**, 1218–1227 (2015).
29. Koo, J. H. et al. Induction of AP-1 by YAP/TAZ contributes to cell proliferation and organ growth. *Genes Dev.* **34**, 72–86 (2020).
30. Nallet-Staub, F. et al. Pro-invasive activity of the Hippo pathway effectors YAP and TAZ in cutaneous melanoma. *J. Investig. Dermatol.* **134**, 123–132 (2014).
31. Zhang, X. et al. Somatic hypermutation of the YAP oncogene in a human cutaneous melanoma. *Mol. Cancer Res.* **17**, 1435–1449 (2019).

32. Zhang, X. et al. The Hippo pathway oncoprotein YAP promotes melanoma cell invasion and spontaneous metastasis. *Oncogene* **39**, 5267–5281 (2020).
33. Wajapeyee, N. et al. Oncogenic BRAF induces senescence and apoptosis through pathways mediated by the secreted protein IGFBP7. *Cell* **132**, 363–374 (2008).
34. Gupta, P. B. et al. The melanocyte differentiation program predisposes to metastasis after neoplastic transformation. *Nat. Genet.* **37**, 1047–1054 (2005).
35. Frost, H. R. Variance-adjusted Mahalanobis (VAM): a fast and accurate method for cell-specific gene set scoring. *Nucleic Acids Res.* **48**, e94 (2020).
36. Wang, Y. et al. Comprehensive molecular characterization of the hippo signaling pathway in cancer. *Cell Rep.* **25**, 1304–1317.e5 (2018).
37. Cordenonsi, M. et al. The Hippo transducer TAZ confers cancer stem cell-related traits on breast cancer cells. *Cell* **147**, 759–772 (2011).
38. Menzel, M. et al. In melanoma, Hippo signaling is affected by copy number alterations and YAP1 overexpression impairs patient survival. *Pigment Cell Melanoma Res.* **27**, 671–673 (2014).
39. Kastan, N. et al. Small-molecule inhibition of Lats kinases may promote Yap-dependent proliferation in postmitotic mammalian tissues. *Nat. Commun.* **12**, 3100 (2021).
40. Ganem, N. J. et al. Cytokinesis failure triggers hippo tumor suppressor pathway activation. *Cell* **158**, 833–848 (2014).
41. Liu, J. et al. Phosphorylation of Mps1 by BRAFV600E prevents Mps1 degradation and contributes to chromosome instability in melanoma. *Oncogene* **32**, 713–723 (2013).
42. Dikovskaya, D. et al. Mitotic stress is an integral part of the oncogene-induced senescence program that promotes multinucleation and cell cycle arrest. *Cell Rep.* **12**, 1483–1496 (2015).
43. Cui, Y. et al. Oncogenic B-Raf(V600E) induces spindle abnormalities, supernumerary centrosomes, and aneuploidy in human melanocytic cells. *Cancer Res.* **70**, 675–684 (2010).
44. Brito, D. A. & Rieder, C. L. Mitotic checkpoint slippage in humans occurs via cyclin B destruction in the presence of an active checkpoint. *Curr. Biol.* **16**, 1194–1200 (2006).
45. McNeal, A. S. et al. BRAF(V600E) induces reversible mitotic arrest in human melanocytes via microRNA-mediated suppression of AURKB. *eLife* **10**, e70385 (2021).
46. Klein, R. M. et al. B-RAF regulation of Rnd3 participates in actin cytoskeletal and focal adhesion organization. *Mol. Biol. Cell* **19**, 498–508 (2008).
47. Klein, R. M. & Aplin, A. E. Rnd3 regulation of the actin cytoskeleton promotes melanoma migration and invasive outgrowth in three dimensions. *Cancer Res.* **69**, 2224–2233 (2009).
48. Vial, E., Sahai, E. & Marshall, C. J. ERK-MAPK signaling coordinately regulates activity of Rac1 and RhoA for tumor cell motility. *Cancer Cell* **4**, 67–79 (2003).
49. Kim, M. H. et al. Actin remodeling confers BRAF inhibitor resistance to melanoma cells through YAP/TAZ activation. *EMBO J.* **35**, 462–478 (2016).
50. Misek, S. A. et al. Rho-mediated signaling promotes BRAF inhibitor resistance in de-differentiated melanoma cells. *Oncogene* **39**, 1466–1483 (2020).
51. Mercer, K. et al. Expression of endogenous oncogenic V600EB-raf induces proliferation and developmental defects in mice and transformation of primary fibroblasts. *Cancer Res.* **65**, 11493–11500 (2005).
52. Heallen, T. et al. Hippo pathway inhibits Wnt signaling to restrain cardiomyocyte proliferation and heart size. *Science* **332**, 458–461 (2011).
53. Snyder, A. et al. Genetic basis for clinical response to CTLA-4 blockade in melanoma. *N. Engl. J. Med.* **371**, 2189–2199 (2014).
54. Hooijkaas, A. I. et al. Targeting BRAFV600E in an inducible murine model of melanoma. *Am. J. Pathol.* **181**, 785–794 (2012).
55. Deken, M. A. et al. Dermal delivery of constructs encoding cre recombinase to induce skin tumors in Pten(LoxP/LoxP);Braf(CA/+) mice. *Int. J. Mol. Sci.* **17**, 2149 (2016).
56. Verfaillie, A. et al. Decoding the regulatory landscape of melanoma reveals TEADS as regulators of the invasive cell state. *Nat. Commun.* **6**, 6683 (2015).
57. Wouters, J. et al. Robust gene expression programs underlie recurrent cell states and phenotype switching in melanoma. *Nat. Cell Biol.* **22**, 986–998 (2020).
58. Moon, H. et al. Melanocyte stem cell activation and translocation initiate cutaneous melanoma in response to UV exposure. *Cell Stem Cell* **21**, 665–678.e6 (2017).
59. Kohler, C. et al. Mouse cutaneous melanoma induced by mutant BRaf arises from expansion and dedifferentiation of mature pigmented melanocytes. *Cell Stem Cell* **21**, 679–693 e6 (2017).
60. Tumaneng, K. et al. YAP mediates crosstalk between the Hippo and PI(3)K-TOR pathways by suppressing PTEN via miR-29. *Nat. Cell Biol.* **14**, 1322–1329 (2012).
61. Gan, W. et al. LATS suppresses mTORC1 activity to directly coordinate Hippo and mTORC1 pathways in growth control. *Nat. Cell Biol.* **22**, 246–256 (2020).
62. Hu, J. K. et al. An FAK-YAP-mTOR signaling axis regulates stem cell-based tissue renewal in mice. *Cell Stem Cell* **21**, 91–106.e6 (2017).
63. Aylon, Y. et al. A positive feedback loop between the p53 and Lats2 tumor suppressors prevents tetraploidization. *Genes Dev.* **20**, 2687–2700 (2006).
64. Viros, A. et al. Ultraviolet radiation accelerates BRAF-driven melanomagenesis by targeting TP53. *Nature* **511**, 478–482 (2014).
65. Ceol, C. J. et al. The histone methyltransferase SETDB1 is recurrently amplified in melanoma and accelerates its onset. *Nature* **471**, 513–517 (2011).
66. Li, Q. et al. Lats1/2 sustain intestinal stem cells and Wnt activation through TEAD-dependent and independent transcription. *Cell Stem Cell* **26**, 675–692 (2020).
67. Shain, A. H. et al. The genetic evolution of melanoma from precursor lesions. *N. Engl. J. Med.* **373**, 1926–1936 (2015).
68. Fox, J. C., Reed, J. A. & Shea, C. R. The recurrent nevus phenomenon: a history of challenge, controversy, and discovery. *Arch. Pathol. Lab Med.* **135**, 842–846 (2011).
69. King, R. et al. Recurrent nevus phenomenon: a clinicopathologic study of 357 cases and histologic comparison with melanoma with regression. *Mod. Pathol.* **22**, 611–617 (2009).
70. Lin, L. et al. The Hippo effector YAP promotes resistance to RAF- and MEK-targeted cancer therapies. *Nat. Genet.* **47**, 250–256 (2015).
71. Dutchak, K. et al. MOB3A bypasses BRAF and RAS oncogene-induced senescence by engaging the Hippo pathway. *Mol. Cancer Res.* **20**, 770–781 (2022).
72. Feng, X. et al. Hippo-independent activation of YAP by the GNAQ uveal melanoma oncogene through a trio-regulated rho GTPase signaling circuitry. *Cancer Cell* **25**, 831–845 (2014).
73. Li, H. et al. YAP/TAZ activation drives uveal melanoma initiation and progression. *Cell Rep.* **29**, 3200–3211.e4 (2019).
74. Yu, F. X. et al. Mutant Gq/11 promote uveal melanoma tumorigenesis by activating YAP. *Cancer Cell* **25**, 822–830 (2014).
75. Zack, T. I. et al. Pan-cancer patterns of somatic copy number alteration. *Nat. Genet.* **45**, 1134–1140 (2013).
76. Bielski, C. M. et al. Genome doubling shapes the evolution and prognosis of advanced cancers. *Nat. Genet.* **50**, 1189–1195 (2018).
77. Quinton, R. J. et al. Whole-genome doubling confers unique genetic vulnerabilities on tumour cells. *Nature* **590**, 492–497 (2021).
78. Vergara, I. A. et al. Evolution of late-stage metastatic melanoma is dominated by aneuploidy and whole genome doubling. *Nat. Commun.* **12**, 1434 (2021).
79. Kapoor, A. et al. Yap1 activation enables bypass of oncogenic Kras addiction in pancreatic cancer. *Cell* **158**, 185–197 (2014).
80. Fisher, M. L. et al. Inhibition of YAP function overcomes BRAF inhibitor resistance in melanoma cancer stem cells. *Oncotarget* **8**, 110257–110272 (2017).
81. Stuart, T. et al. Comprehensive integration of single-cell data. *Cell* **177**, 1888–1902.e21 (2019).

Acknowledgements

We would like to thank Jackie King and Ross King for their unwavering resolve to promote melanoma awareness and research, as well Qi Sun, Shuyang Chen, and the entire Ganem Lab for wisdom and advice. We would also like to thank April Deng, Karen Dresser, Constance Brinckerhoff, Robert Weinberg, and Arthur Lander for sharing cell lines, reagents, and/or assistance. The results published herein are partly based upon data generated by the TCGA Research Network: https://www.cancer.gov/tcga. We thank all the patients who donated specimens to both the TCGA and the MSKCC database and the Molecular Biology Core Facilites at the Dana-Farber Cancer Institue for their assistance with the copy-number analysis. M.A.V. is supported by a Ruth L. Kirchstein National Research Service Award (F30) from the NCI (1F30CA228388) and was previously supported by a training grant from the NIGMS (5T32GM008541). E.X. and S.M. were both supported by an award from the Boston University Undergraduate Research Opportunities Program. X.V. is supported by the NHLBI (R01HL124392) and the American Cancer Society - Ellison New England Research Scholar Grant (RSG-17-138-01-CSM). N.M.K. was supported by the NHLBI (F31HL146163). C.J.C. was supported by NIAMS (AR063850) and by the USA Department of Defense (W81XWH2010288). N.J.G. is a member of the Shamim and Ashraf Dahod Breast Cancer Research Laboratories and this work was supported in his lab by the NIGMS (GM117150), the Harry J. Lloyd Charitable Trust, the Jackie King Young Investigator Award from the Melanoma Research Alliance, and the Searle's Scholars Program. This work was also supported by a pilot grant from the ACS and the Boston University Clinical and Translational Science Institute Bioinformatics Group (1UL1TR001430).

Author contributions

M.A.V. and N.J.G. conceptualized the study, designed the in vitro experiments, and wrote the manuscript. M.A.V., N.K., X.V., and N.J.G. designed all in vivo studies. M.A.V. performed most of the cell biological assays, tissue staining, and imaging analysis. N.K. performed in vivo experiments, with the assistance of M.A.V. and K.K., and prepared all tissue samples. K.K., N.K., E.X., S.M., and A.T.L. assisted M.A.V. with the cell biological

and tissue assays. X.X. provided dermatopathology consult and tissue analysis. R.D. and C.C. performed zebrafish experiments. R.H. and J.D.C. completed the single-cell analysis and M.A.V. performed GSEA. L.H. and D.L. provided critical reagents.

Competing interests
The authors declare no competing interests.

Additional information
Supplementary information The online version contains supplementary material available at https://doi.org/10.1038/s41467-022-31399-w.

Correspondence and requests for materials should be addressed to Neil J. Ganem.

Peer review information *Nature Communications* thanks the anonymous reviewer(s) for their contribution to the peer review of this work. Peer reviewer reports are available.

Reprints and permission information is available at http://www.nature.com/reprints

Publisher's note Springer Nature remains neutral with regard to jurisdictional claims in published maps and institutional affiliations.

Open Access This article is licensed under a Creative Commons Attribution 4.0 International License, which permits use, sharing, adaptation, distribution and reproduction in any medium or format, as long as you give appropriate credit to the original author(s) and the source, provide a link to the Creative Commons license, and indicate if changes were made. The images or other third party material in this article are included in the article's Creative Commons license, unless indicated otherwise in a credit line to the material. If material is not included in the article's Creative Commons license and your intended use is not permitted by statutory regulation or exceeds the permitted use, you will need to obtain permission directly from the copyright holder. To view a copy of this license, visit http://creativecommons.org/licenses/by/4.0/.

© The Author(s) 2022

nature COMMUNICATIONS

ARTICLE

https://doi.org/10.1038/s41467-022-31899-9 OPEN

Oncogenic BRAF induces whole-genome doubling through suppression of cytokinesis

Revati Darp[1,2], Marc A. Vittoria[3], Neil J. Ganem[3] & Craig J. Ceol[1,2]✉

Melanomas and other solid tumors commonly have increased ploidy, with near-tetraploid karyotypes being most frequently observed. Such karyotypes have been shown to arise through whole-genome doubling events that occur during early stages of tumor progression. The generation of tetraploid cells via whole-genome doubling is proposed to allow nascent tumor cells the ability to sample various pro-tumorigenic genomic configurations while avoiding the negative consequences that chromosomal gains or losses have in diploid cells. Whereas a high prevalence of whole-genome doubling events has been established, the means by which whole-genome doubling arises is unclear. Here, we find that $BRAF^{V600E}$, the most common mutation in melanomas, can induce whole-genome doubling via cytokinesis failure in vitro and in a zebrafish melanoma model. Mechanistically, $BRAF^{V600E}$ causes decreased activation and localization of RhoA, a critical cytokinesis regulator. $BRAF^{V600E}$ activity during G1/S phases of the cell cycle is required to suppress cytokinesis. During G1/S, $BRAF^{V600E}$ activity causes inappropriate centriole amplification, which is linked in part to inhibition of RhoA and suppression of cytokinesis. Together these data suggest that common abnormalities of melanomas linked to tumorigenesis – amplified centrosomes and whole-genome doubling events – can be induced by oncogenic BRAF and other mutations that increase RAS/MAPK pathway activity.

[1] University of Massachusetts Chan Medical School, Program in Molecular Medicine, Worcester, MA, USA. [2] University of Massachusetts Chan Medical School, Department of Molecular, Cellular and Cancer Biology, Worcester, MA, USA. [3] Departments of Pharmacology and Experimental Therapeutics and Medicine, Division of Hematology and Oncology, Boston University School of Medicine, Boston, MA, USA. ✉email: Craig.Ceol@umassmed.edu

Increased ploidy is a common feature of solid tumors. The most frequently observed increased karyotypes approach tetraploidy, which led to the hypothesis that such 'near-tetraploid' tumors had undergone a whole-genome doubling (WGD) event during tumor progression and subsequently experienced a small net loss of chromosomes[1,2]. Recent bioinformatic analyses support this hypothesis, showing that WGD events are prevalent in a diverse set of solid tumors, and nearly 37% of all solid tumors measured, including 40% of melanomas, experienced at least one WGD event in their progression[3,4]. Based on these analyses, WGD frequently occurs early in tumor formation, and the presence of tetraploid cells in some pre-cancerous lesions, such as Barrett's esophagus and lesions of the cervix and kidney, suggests that WGD may even precede frank tumor formation in some tissues[5–8] Tetraploidy was also observed in hyperplastic lesions of the pancreas[9], in localized prostate cancer[10–12] and some colon adenomas[13,14], and for certain malignancies, such as oral tumors[15], tetraploidy is a strong predictor of malignant transformation. Additionally, in established cancers from many tissue types WGD is a predictor of poor clinical outcome[16].

Tetraploidy has been experimentally linked to tumorigenesis. Viral-induced cell fusion has been shown to enhance the transformation and tumor-forming capabilities of different cell types[17–20]. Additionally, in mouse mammary epithelial cells that were made tetraploid through treatment with the actin filament poison dihydrocytochalasin B, tetraploid cells were able to form tumors in mice whereas their isogenic diploid counterparts were not[21]. In support of a role for WGD in tumorigenesis, deep sequencing of tumor samples has shown WGD to be an early event in non-small cell lung cancer, medulloblastoma and other tumor types[1,2,22,23].

There are different and mutually inclusive ways in which tetraploidy could contribute to tumorigenesis. First, tetraploidy can enable cells to become tolerant to the negative consequences of chromosome gains, losses, gene deletions, and inactivating mutations[24–30]. Hence, tetraploidy is likely to allow tumor cells to withstand a higher incidence of mutations, thereby increasing the probability of adaptive changes. Second, tetraploid cells have an increased rate of chromosome missegregation[31–33], thus increasing the possibility that a developing tumorigenic clone will accumulate and tolerate the mutations needed for its progression to a malignant state[34]. Thirdly, proliferating tetraploid cells are genetically unstable and can facilitate tumor progression by giving rise to aneuploidy, a known hallmark of cancer[35].

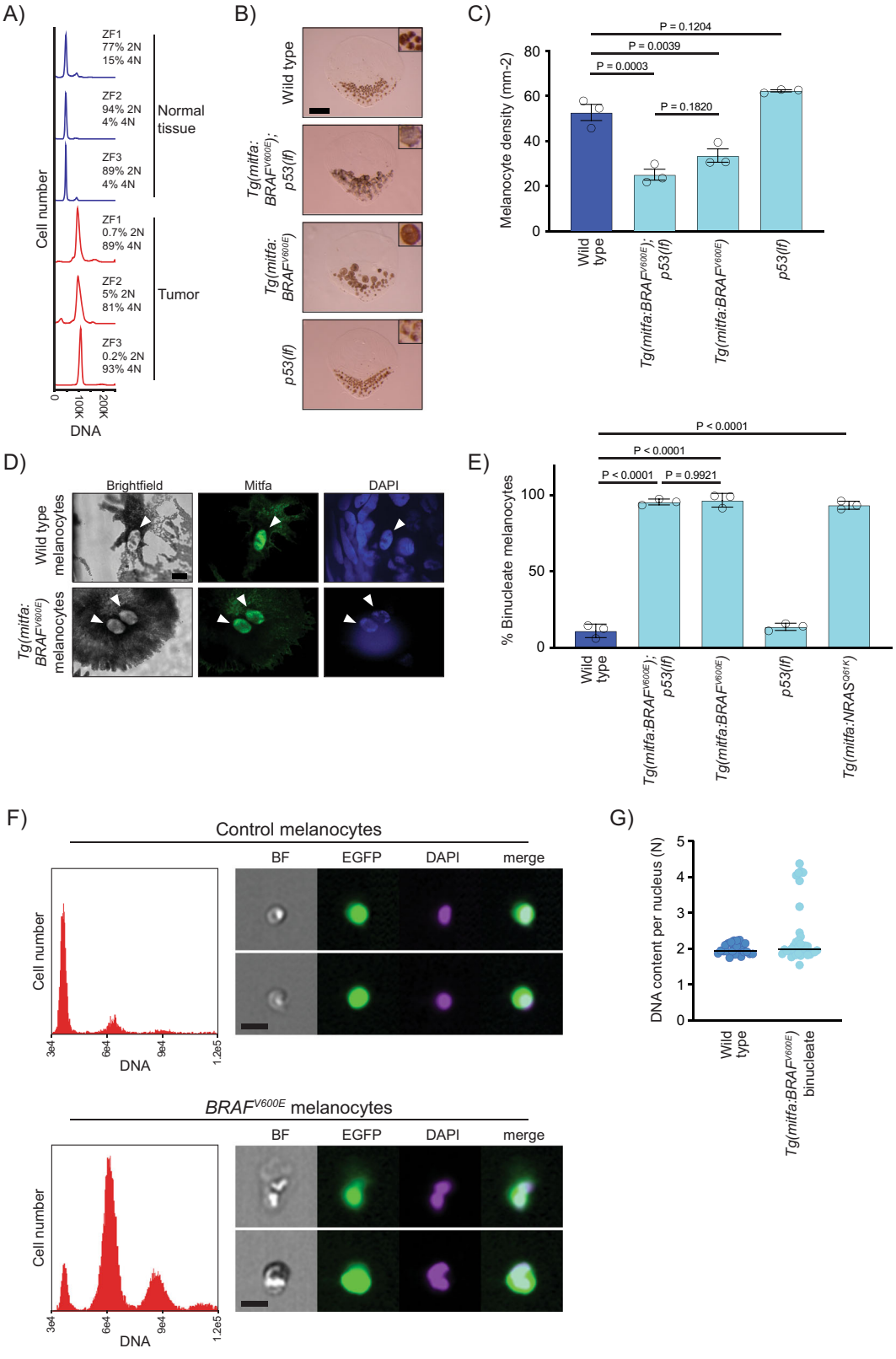
Melanomas are a tumor type in which WGD is prevalent[4]. Although molecular genetic analyses have provided great insights into the genes that are involved in melanoma, very little is known about the process by which melanocytes with these lesions become tumorigenic, and whether any mutations underlie WGD in tumors is unclear. We examined melanocytes in zebrafish strains that are predisposed to melanoma and discovered an abundance of binucleate, tetraploid melanocytes. Tetraploidy was caused by expression of $BRAF^{V600E}$, which increases RAS/MAPK-pathway activity and is commonly found in human melanomas. Using an in vitro model combined with live imaging, flow cytometry and immunofluorescence approaches, we found that $BRAF^{V600E}$ generated tetraploid cells via cytokinesis failure and reduced activity of the small GTPase RhoA, which is critical for cytokinesis[36]. We also show that $BRAF^{V600E}$ activity causes inappropriate centrosomal amplification, which is linked in part to the inhibition of RhoA and suppression of cytokinesis. Additionally, we show that zebrafish melanomas have a tetraploid karyotype and tumor-initiating cells in the zebrafish are tetraploid. These data collectively suggest that $BRAF^{V600E}$-induced WGD occurs and has a role in tumor formation.

Results

$BRAF^{V600E}$ causes melanocytes in zebrafish to be tetraploid and binucleate. In this and previous studies, we used a zebrafish model of melanoma which combined melanocyte-lineage expression of human $BRAF^{V600E}$ with an inactivating mutation in the endogenous zebrafish *p53* gene[37–39]. Animals of this genotype, *Tg(mitfa:*$BRAF^{V600E}$*); p53(lf)*, develop melanomas that have histopathological and molecular features similar to those of human melanomas. To determine if tumors arising in this model exhibited ploidies consistent with having undergone a WGD event, we harvested tumors from *Tg(mitfa:*$BRAF^{V600E}$*); p53(lf)* animals and quantified DNA content. The ploidy of these zebrafish melanomas was predominantly 4N and higher (Fig. 1A), indicating that WGD is likely a feature of this model. The analyzed tumors displayed a small fraction of 2N cells, which we speculate were admixed stromal cells.

To investigate when the WGD event could occur, we began by examining melanocytes from *Tg(mitfa:*$BRAF^{V600E}$*); p53(lf)* animals. We reasoned that closer analyses of epidermal melanocytes in the *Tg(mitfa:*$BRAF^{V600E}$*)* strains might reveal the basis of the observed tetraploidy and provide insight into early cellular events that occur in melanoma tumorigenesis. To this end we developed assays to quantify and determine cell biological characteristics of these melanocytes. To quantify dorsal epidermal melanocytes, we treated fish with epinephrine then plucked and fixed scales to which these melanocytes are attached. As the number of melanocytes per scale depends on the size of the scale, we obtained a normalized melanocyte density measurement. Melanomas arise from dorsal regions of these zebrafish, and we found that the scale-associated epidermal melanocytes in these dorsal regions were larger in size and fewer in number than those of wild-type zebrafish (Fig. 1B, C, Supplementary Fig. 1A). This was due to $BRAF^{V600E}$ expression, as *Tg(mitfa:*$BRAF^{V600E}$*)* melanocytes were also larger and fewer in number, whereas *p53(lf)* melanocytes were similar to those of wild-type zebrafish. Previously, injection of $BRAF^{V600E}$ had been shown to cause nevus-like proliferations of melanocytes in zebrafish[38], and we also showed nevus-like melanocyte proliferations can arise in the *Tg(mitfa:*$BRAF^{V600E}$*); p53(lf)* strain[37]. However, our current characterization of melanocytes in strains stably expressing the *Tg(mitfa:*$BRAF^{V600E}$*)* transgene indicates that, aside from a few melanocytes that clonally proliferate, $BRAF^{V600E}$ expression primarily results in a reduced number and increased size of melanocytes. Cell size increases can be caused by increased ploidy, which could be reflected in a larger nuclear size[40]. To determine if $BRAF^{V600E}$ expression caused nuclear enlargement, we stained for the melanocyte nuclear protein Mitfa. Most nuclei in large *Tg(mitfa:*$BRAF^{V600E}$*)* melanocytes were similar in size to those of wild-type melanocytes; however, melanocytes in *Tg(mitfa:*$BRAF^{V600E}$*)* contained two nuclei (Fig. 1D, E). Melanocytes from *Tg(mitfa:*$BRAF^{V600E}$*); p53(lf)* animals were similarly binucleate, whereas *p53(lf)* melanocytes had one nucleus (Fig. 1E, Supplementary Fig. 1B), indicating that the binuclearity is associated with $BRAF^{V600E}$ expression. Whereas binucleate dorsal epidermal melanocytes are rare in wild-type animals, binucleate stripe-associated dermal melanocytes are more commonly observed[41,42], suggesting that mechanisms that coordinate nuclear and cellular divisions may be particularly prone to regulation in zebrafish melanocytes.

To determine if the binuclearity we observed was uniquely associated with $BRAF^{V600E}$ or was caused by Ras/BRAF pathway overactivity in general, we stained scale-associated melanocytes expressing a common oncogenic variant of *NRAS*, mutations in which are present in about 28% of human melanomas[43]. Melanocytes from animals expressing an $NRAS^{Q61L}$ oncogene that is commonly found in human melanomas were also binucleate (Fig. 1E, Supplementary Fig. 1C)[44], and binucleation has also been



observed in zebrafish melanocytes that express an oncogenic variant of *HRAS*[45]. Together these data indicate that binucleate cells arise from overactivation of RAS/MAPK signaling.

To examine ploidy of *Tg(mitfa:BRAF^{V600E})* melanocytes, flow cytometry and DNA densitometry were performed. Zebrafish melanocytes retain melanin pigment, so an *mitfa:EGFP* transgene and *albino* mutation were introduced so that melanocytes could be reliably identified by GFP-positivity and characterized without melanin spectral interference. Flow cytometry showed that *Tg(mitfa:BRAF^{V600E})* melanocytes were predominantly tetraploid, with small fractions of diploid and octoploid cells observed (Fig. 1F). Flow cytometry also confirmed the binucleate nature of these cells (Supplementary Fig. 1D). DNA densitometry of fixed samples found that most nuclei in binucleate *Tg(mitfa:BRAF^{V600E})*

Fig. 1 *BRAF^{V600E}* causes melanocytes in zebrafish to be tetraploid. A DNA content of normal and tumor tissue from *Tg(mitfa:EGFP); Tg(mitfa:BRAF^{V600E}); p53(lf); alb(lf)* zebrafish. ZF1, ZF2, and ZF3 are three different animals. **B** Scales from wild-type, *Tg(mitfa:BRAF^{V600E});p53(lf), Tg(mitfa:BRAF^{V600E}) and p53(lf)* strains. Melanin pigment is dispersed throughout the cytoplasm of zebrafish melanocytes, revealing markedly different cell sizes. Scale bar = 250 μm, insets are at same scale as one another. **C** Quantification of melanocyte densities per scale of wild-type, *Tg(mitfa:BRAF^{V600E});p53(lf), Tg(mitfa:BRAF^{V600E}) and p53(lf)* strains. $N = 5$ for three animals of each genotype; the mean density of each animal is plotted. One-way ANOVA with Tukey's multiple comparisons test. Error bars represent mean ± SEM. **D** Images from brightfield (left), anti-Mitfa (middle) and DAPI (right) staining of a single wild-type (top) or *Tg(mitfa:BRAF^{V600E})* (bottom) epidermal melanocyte. Only the melanocyte nuclei stain positively for Mitfa. White arrowheads indicate nuclei within a single melanocyte. Scale bar = 5 μm. Representative cells quantified in **E** are shown. **E** Mean percent binucleate cells as determined by anti-Mitfa staining of pigmented melanocytes. $N = 3$ experiments examining in total wild type = 636, *Tg(mitfa:BRAF^{V600E});p53(lf)* = 458, *Tg(mitfa:BRAF^{V600E})* = 454, *p53(lf)* = 538, and *Tg(mitfa:NRAS^{Q61K})* = 122 melanocytes. One-way ANOVA with Tukey's multiple comparisons test. Error bars represent mean ± SEM. **F** Flow cytometry and DNA content analysis of control *Tg(mitfa:EGFP); alb(lf)* and *Tg(mitfa:EGFP); Tg(mitfa:BRAF^{V600E}); alb(lf)* melanocytes with brightfield, EGFP and DAPI images of single melanocytes. **G** DNA content analysis of wild-type and *Tg(mitfa:BRAF^{V600E})* melanocyte nuclei by confocal densitometry. $N = 25$ nuclei for wild type and $N = 35$ for *Tg(mitfa:BRAF^{V600E})*. Bars represent median.

melanocytes had a 2N DNA content (Fig. 1G). Therefore, expression of *BRAF^{V600E}* causes melanocytes in zebrafish to become tetraploid as a result of having two nuclei, each with a 2N DNA content.

BRAF^{V600E} binucleate, tetraploid cells arise via failure of cytokinesis. To determine how BRAF^{V600E} generates binucleate, tetraploid cells and to recapitulate the phenotype we observed in our zebrafish model, we developed an in vitro system suitable for mechanistic analyses. This system is based on a single-cell clone we created in which BRAF^{V600E} was inducibly expressed in RPE-1 FUCCI cells at a level similar to that of endogenous BRAF (Fig. 2A, B). RPE-1 cells were chosen for this analysis because they are non-transformed, hTERT-immortalized, and have a stable, diploid karyotype. We combined DNA content analysis with the fluorescent ubiquitin-based cell cycle indicator (FUCCI) reporter system to enable abnormal tetraploid cells in the G1 phase of the cell cycle (Cdt-mCherry-positive) to be distinguished from normal tetraploid cells in the G2 or M phases of the cell cycle (Geminin-GFP-positive)[46,47]. In these cells, synchronization was performed by serum starvation, then after serum addition and progression through mitosis *BRAF^{V600E}* was induced using doxycycline, and cells were synchronized again with a thymidine block. Following release from thymidine synchronization and progression through mitosis, G1 tetraploids were measured as Cdt-mCherry-positive cells with a 4N DNA content (Fig. 2C, Supplementary Fig. 2A). Expression of *BRAF^{V600E}* caused a nearly three-fold increase in the percentage of G1 tetraploid cells (Fig. 2D). These cells were CyclinD1-positive, confirming that they were in G1 and not G2 cells that had dysregulated Cdt-mCherry expression (Supplementary Fig. 2B). Expression of wild-type or kinase-dead *BRAF* showed no similar increase in G1 tetraploids (Fig. 2D). Using a single-cell clone in which *BRAF^{V600E}* was inducibly expressed in RPE-1 H2B-GFP cells, live-cell imaging was used to investigate whether the G1 tetraploids were binucleate and, if so, how they arose. Indeed, after *BRAF^{V600E}* induction and release from synchronization, binucleate cells were observed in the following G1 phase of the cell cycle (Fig. 2E, F). These cells arose through failure of cytokinesis characterized by the formation then regression of the cytokinetic cleavage furrow. Modest increases in other mitotic defects, including lagging chromosomes, chromosome bridges and micronuclei, were observed although none of these increases was statistically significant (Supplementary Fig. 2C–E). Mitotic duration was not affected, even in cells that had undergone cytokinesis failure (Supplementary Fig. 2F). Together these data indicate that oncogenic BRAF^{V600E} causes WGD and the formation of binucleate, tetraploid cells by impairment of cytokinesis rather than cell fusion or other means.

BRAF^{V600E} causes cytokinesis failure by reducing the localization and function of RhoA. To understand how BRAF^{V600E} inhibits cytokinesis, we investigated the localization and function of proteins that are involved in mitotic exit and the cytokinetic process. Polo-like kinase I (PLK1) helps to initiate cytokinesis[48], and it has been shown to interact with CRAF in G2/M[49]. We tested whether cytokinesis failure was dependent on PLK1 and found that an inhibitor of PLK1 did not affect BRAFV600E tetraploid formation (Supplementary Fig. 3A). MPS1/TTK1, a kinase which is activated by BRAFV600E and promotes activation of the mitotic spindle checkpoint[50], was not activated in response to BRAFV600E expression in RPE-1 cells and thus not likely involved in BRAFV600E-driven cytokinetic failure (Supplementary Fig. 3B). Other proteins that have been extensively characterized as being critical during cytokinesis, mainly in contractile ring and cleavage furrow formation, are RhoA, a member of the RhoGTPase family and its scaffold protein Anillin[36,51]. Following anaphase Anillin is required to maintain the assembly of cytokinetic furrow components at the equatorial cell cortex. In cells expressing *BRAF^{V600E}*, Anillin staining was greatly reduced (Fig. 3A, B). Anillin localization is regulated by RhoA[52], which activates and coordinates several downstream events in the cytokinetic process. RhoA is spatiotemporally activated and accumulates at the equatorial cell cortex in anaphase and during cytokinesis. This accumulation is both necessary and sufficient for cytokinesis to proceed[53]. Similar to Anillin, RhoA localization to the cell equator was reduced in *BRAF^{V600E}*-expressing cells (Fig. 3C, D). RhoA reduction in *BRAF^{V600E}*-expressing cells was dependent on increased MAPK signaling because treatment with the MEK inhibitor trametinib or ERK inhibitor SCH772984 restored RhoA localization (Fig. 3C, D). Since RhoA localization is promoted by its activation at the equatorial cell cortex[54], we quantified the levels of active, GTP-bound RhoA in *BRAF^{V600E}*-expressing cells. Levels of GTP-bound RhoA were reduced as a consequence of *BRAF^{V600E}* expression (Fig. 3E, F). *BRAF^{V600E}*-dependent reduction in GTP-bound RhoA has also been observed in immortalized melanocyte Mel-ST cells, indicating relevance to melanocyte biology[55]. If BRAF^{V600E} acts to reduce function of RhoA, then an increase in RhoA function would be predicted to suppress the effect of BRAF^{V600E} on the formation of binucleate, tetraploid cells. This occurred, as treatment of *BRAF^{V600E}*-expressing cells with RhoA activators LPA or S1P reduced the formation of tetraploid cells (Fig. 3G). Furthermore, expression of the *RHOA^{Q61L}* activated variant suppressed *BRAF^{V600E}*-induced tetraploidy (Fig. 3H). These data indicate that BRAF^{V600E} reduces the activity of RhoA and its downstream effector Anillin, which underlies the failure of cytokinesis and the formation of binucleate, tetraploid cells.

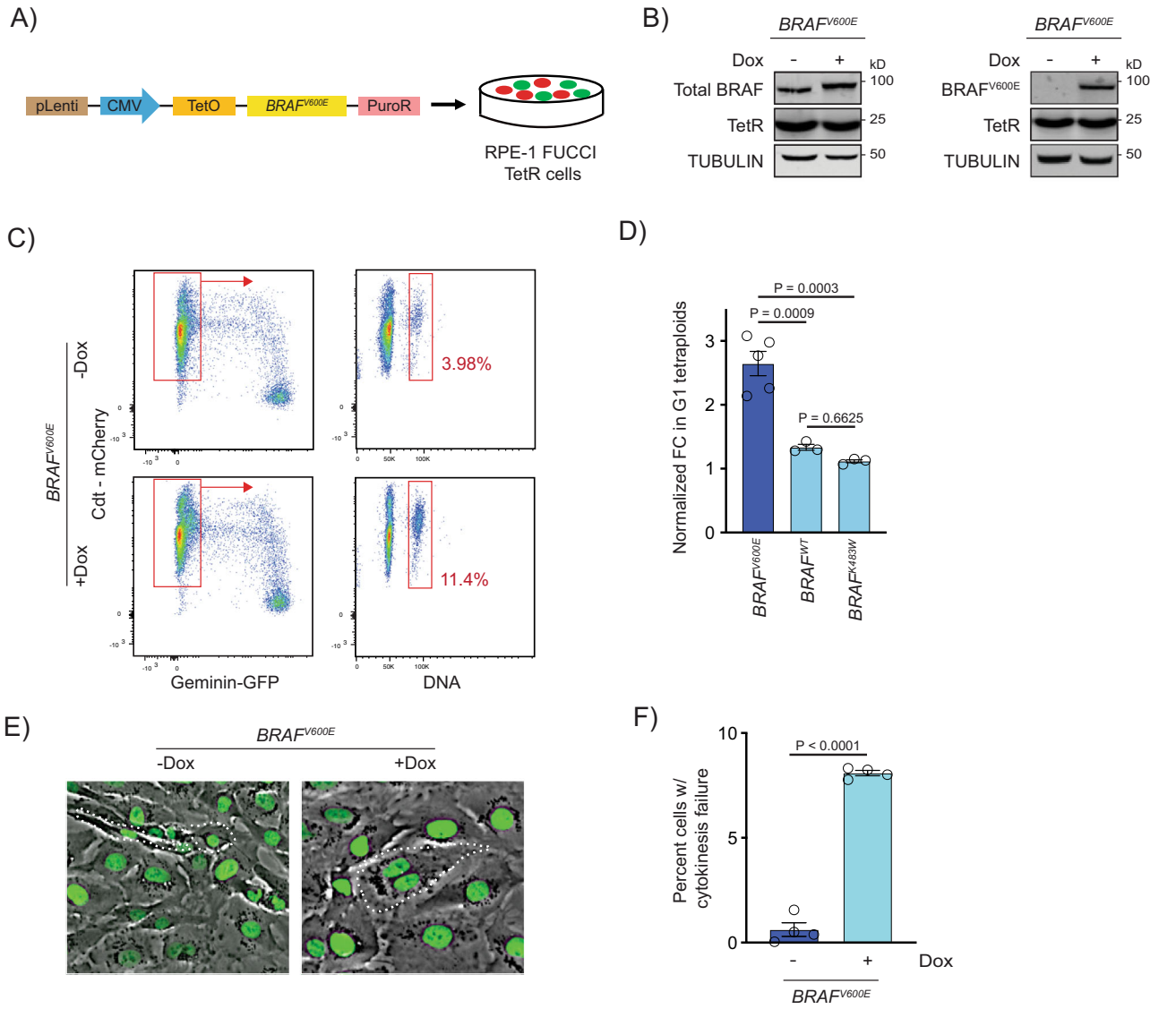
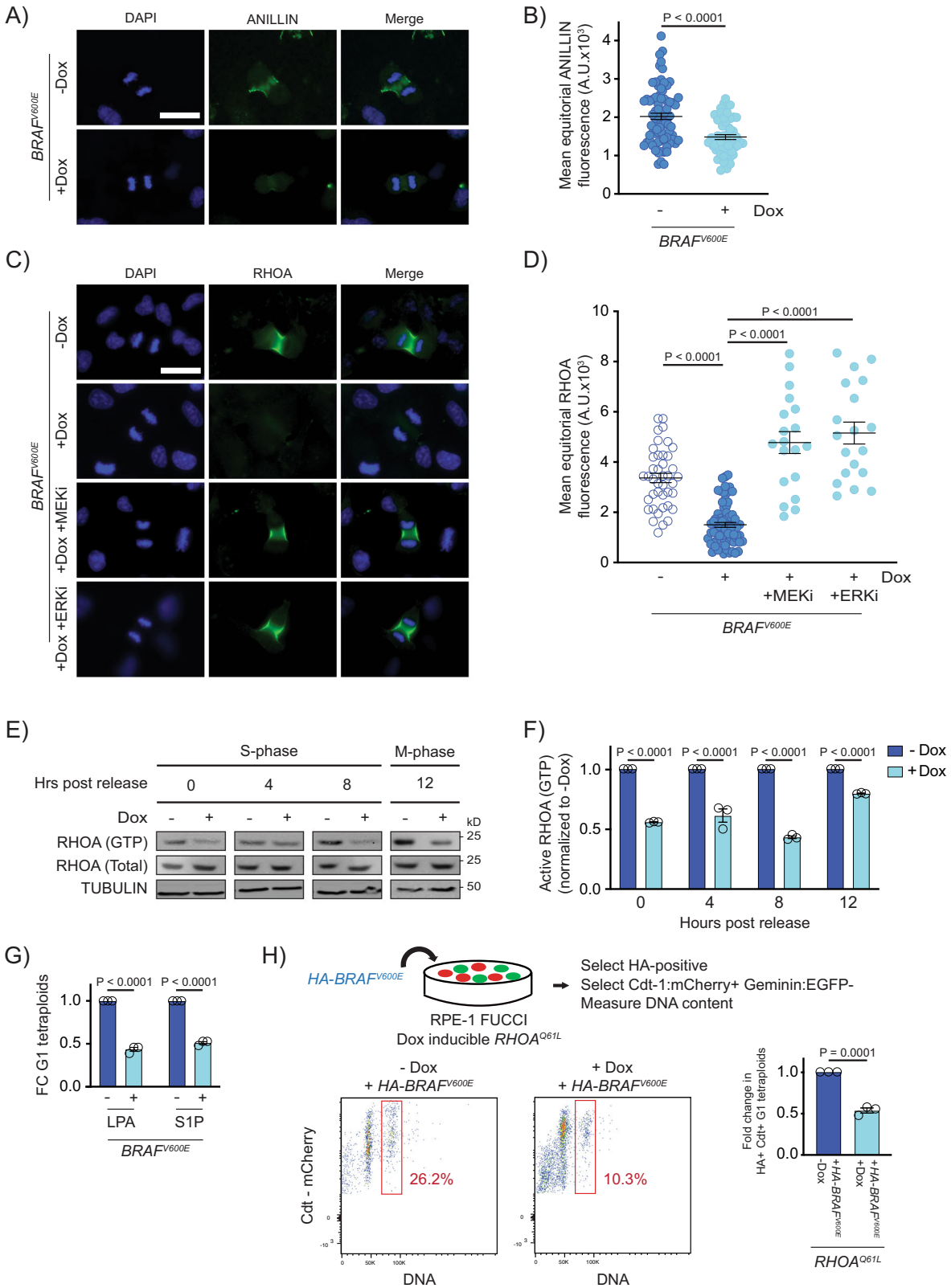


Fig. 2 *BRAF*^{V600E}-induced binucleate, tetraploid cells arise via cytokinesis failure. A Generation of *BRAF*^{V600E}-expressing RPE-1 FUCCI cell lines with a lentiviral-based doxycycline-inducible vector. **B** Western blot showing inducible expression of BRAF^{V600E} (+Dox) in RPE-1 FUCCI cells using a BRAF and BRAF^{V600E}-specific antibody. Expression of the Tet repressor protein is shown. TUBULIN was used as the loading control. A representative of three independent biological replicates is shown. **C** Flow cytometry plots of control (−Dox) and *BRAF*^{V600E}-expressing (+Dox) RPE-1 FUCCI cells. Tetraploid cells accumulating in G1 were quantified based on Cdt1-mCherry positivity and Hoechst incorporation. Percentages of G1 tetraploid cells in control and *BRAF*^{V600E}-expressing cultures are indicated. **D** Fold change (FC) in G1 tetraploids normalized to the control (−Dox) are shown for *BRAF*^{V600E}, *BRAF*^{WT} and *BRAF*^{K483W} (kinase-dead) -expressing RPE-1 FUCCI cell lines. $N = 5$ independent experiments for *BRAF*^{V600E}, $N = 3$ for *BRAF*^{WT} and $N = 3$ for *BRAF*^{K483W}. One-way ANOVA with Tukey's multiple comparisons test. Error bars represent mean ± SEM. **E** Merged phase contrast and GFP photomicrographs of H2B-GFP expressing control (−Dox) and *BRAF*^{V600E}-expressing (+Dox) RPE-1 cells that have recently undergone mitosis. White dotted lines indicate 2 cells with 1 nucleus each that have separated following a successful cytokinesis (−Dox) and 1 cell with 2 nuclei that has failed cytokinesis (+Dox). **F** Percentages of cells exhibiting cytokinesis failure in H2B-GFP RPE-1 control (−Dox) and *BRAF*^{V600E}-expressing (+Dox) cells. $N = 4$ independent experiments examining -Dox = 934 and +Dox = 568 cells. Unpaired Student's *t* test. Error bars represent mean ± SEM.

BRAF^{V600E} and MAPK pathway activity is required during late G1 and early S phases for generating tetraploids. BRAF^{V600E} acts in G1/S to promote cell cycle progression, yet some reports have suggested that MAPK activity is important during mitosis[56–58]. To determine when BRAF^{V600E} and MAPK signaling is required to generate tetraploids, we treated *BRAF*^{V600E}-expressing cells with the BRAF^{V600E} inhibitor vemurafenib, MEK inhibitor trametinib and ERK inhibitor SCH772984 at various points in the cell cycle and measured whether the inhibitors suppressed tetraploid formation (Fig. 4A). The ability of inhibitors to reduce downstream MAPK activity was confirmed by western blot of phosphorylated ERK (Supplementary Fig. 4A, B). Additionally, we also confirmed that treatment with inhibitors at the concentrations used did not cause cell cycle arrest and did not substantially impact growth kinetics, cell cycle progression or cell viability (Supplementary Fig. 4C–E). Treatment with inhibitors throughout the cell cycle suppressed formation of *BRAF*^{V600E}-induced tetraploids (Fig. 4A). By contrast, treatment during the S/G2/M phases had little effect on tetraploid formation. Treatment during G1 and specifically during late G1 and early S suppressed formation of tetraploids. This suppression occurred with each of the three inhibitors tested as well as the 'paradox-breaking' BRAF^{V600E} inhibitors PLX7904 and PLX8394 (Supplementary Fig. 4F), which inhibit BRAF^{V600E} while not simultaneously



activating downstream MAPK activity like vemurafenib can[59–61]. Thus, BRAF^{V600E}, and MAPK signaling in general, act during late G1 and early S phases to ultimately cause inhibition of RhoA and failure of cytokinesis.

Rac1 is activated by BRAF^{V600E} and contributes to RhoA downregulation. To understand how BRAF^{V600E} and MAPK signaling activity during G1/S could lead to downregulation of RhoA and failed cytokinesis, we considered regulators of cytokinesis that are active during G1 or S phases and whose dysregulation could impair cytokinesis. The small GTPase Rac1 is a negative regulator of cytokinesis that inhibits function of the contractile ring[53]. Rac1 is active throughout the cell cycle except during a small window in mitosis, with its nadir of activity during

Fig. 3 BRAF^{V600E} causes cytokinesis failure by reducing the localization and function of RhoA. A DAPI and anti-ANILLIN staining in control (−Dox) and *BRAF^{V600E}*-expressing (+Dox) anaphase RPE-1 cells. Images are maximum intensity projections of z-stacks. Scale bar = 7.5 μM. **B** Mean ANILLIN fluorescence intensity at the equator of control and *BRAF^{V600E}*-expressing anaphase RPE-1 cells. $N = 79$ cells for −Dox and $N = 53$ for +Dox. Unpaired Student's *t* test. Error bars represent mean ± SEM. **C** DAPI and anti-RHOA staining in -*BRAF^{V600E}* (−Dox) cells, *BRAF^{V600E}*-expressing (+Dox) cells, and *BRAF^{V600E}*-expressing (+Dox) RPE-1 cells treated with MEKi or ERKi. Drugs were added coincident with Dox administration. Images are maximum intensity projections of z-stacks (0.20 μM). Scale bar = 7.5 μM. **D** Mean RHOA fluorescence intensity at the equator of control RPE-1 cells, *BRAF^{V600E}*-expressing RPE-1 cells, and *BRAF^{V600E}*-expressing RPE-1 cells treated with MEKi or ERKi. $N = 41$ cells for −Dox, $N = 68$ for +Dox, $N = 19$ for +Dox +MEKi, and $N = 19$ for +Dox +ERKi. Brown-Forsythe and Welch one-way ANOVA with Dunnett's multiple comparisons test. Error bars represent mean ± SEM. **E** Western blot analysis of immunoprecipitated RHOA-GTP from control (−Dox) and *BRAF^{V600E}*-expressing (+Dox) RPE-1 cell lysates at different time points post thymidine release. Total RHOA protein and alpha tubulin were used as a controls. A representative of three independent biological replicates is shown. **F** Western blot quantification of immunoprecipitated RHOA-GTP levels from control (−Dox) and *BRAF^{V600E}*-expressing (+Dox) RPE-1 cell lysates at different time points post thymidine release. Samples were normalized to the −Dox condition. $N = 3$ independent experiments. Unpaired Student's *t* test. Error bars represent mean ± SEM. **G** Fold change (FC) in G1 tetraploid RPE-1 FUCCI cells following addition of RHOA activators. LPA (1 μM) and S1P (1 μM) were added coincident with Dox administration. Fold changes in G1 tetraploids relative to the control (+Dox no drug) are shown. $N = 3$ independent experiments. Unpaired Student's *t* test. Error bars represent mean ± SEM. **H** G1 tetraploid generation following expression of HA-tagged-BRAF^{V600E} in *RHOA^{Q61L}*-inducible cells. Experimental design (top): RPE-1 FUCCI cells with Dox inducible *RHOA^{Q61L}* were transiently transfected with an HA-tagged-BRAF^{V600E}-expressing construct and selected accordingly. G1 tetraploids were quantified (bottom left and middle) by gating HA-positive, Cdt-1:mCherry-positive cells with increased Hoechst incorporation. Fold change in G1 tetraploids (bottom right), normalized to control (−Dox) cells. $N = 3$ independent experiments. Unpaired Student's *t* test. Error bars represent mean ± SEM.

anaphase and early telophase[62]. Loss of Rac1 activity promotes cytokinesis[63], and overactivation of Rac1 impairs RhoA localization to the equatorial cell cortex[64] and causes cytokinesis failure leading to formation of binucleate cells[65]. To investigate whether BRAF^{V600E} affects Rac1 activity, we performed ELISA assays to detect active, GTP-bound Rac1 at various points following *BRAF^{V600E}* expression and release from synchronization. As compared to control cells, GTP-bound Rac1 levels in *BRAF^{V600E}*-expressing cells were higher upon release from synchronization and thereafter (Fig. 4B). To determine if higher Rac1 activity contributes to the *BRAF^{V600E}*-induced formation of binucleate cells, we treated cells with the Rac1 inhibitors NSC2366 and EHT1864 and measured G1 tetraploid formation in *BRAF^{V600E}*-expressing RPE-1 FUCCI cells. Treatment with either inhibitor suppressed the formation of tetraploid cells (Fig. 4C). Furthermore, treatment with either inhibitor led to the reestablishment of equatorial RhoA localization (Fig. 4D, E). Together these data indicate that BRAF^{V600E} acts through Rac1 to inhibit RhoA and cause failure of cytokinesis.

Supernumerary centrosomes are observed in *BRAF^{V600E}*-expressing cells. In assessing how Rac1 activity could be upregulated in *BRAF^{V600E}*-expressing cells, we discovered that mitotic spindles in *BRAF^{V600E}*-expressing cells showed structural organizations consistent with the presence of multiple, clustered centrosomes at the same spindle pole. Extra centrosomes increase microtubule nucleation, which in turn stimulates the activity of Rac1[66,67]. To determine whether extra centrosomes were present in *BRAF^{V600E}*-expressing cells, we performed quantification of centrosomes via gamma-tubulin staining in S phase cells. Here, we observed a significant increase in cells with more than 2 centrosomes in the *BRAF^{V600E}*-induced population (Supplementary Fig. 5A, B). Gamma-tubulin can stain fragments, derived from previously intact centrosomes, that can continue to nucleate microtubules[68]. To address this possible artifact and confirm the presence of supernumerary centrosomal components in *BRAF^{V600E}*-expressing cells, we stained for the centriolar marker Centrin-2 in mitotic cells (Fig. 5A). Supernumerary Centrin-2-positive centrioles (>4 centrioles per cell) were observed in 22% of *BRAF^{V600E}*-expressing cells, which is an eight-fold increase as compared to control cells (Fig. 5B). In some cases, unpaired, single centrioles, suggestive of centriole overduplication were observed (Supplementary Fig. 5C). To determine if supernumerary centrioles were able to accumulate pericentriolar material (PCM) and nucleate microtubules, we stained for the PCM marker Pericentrin and alpha-tubulin to visualize microtubules. Cells that had three or more foci of centrioles were assessed so PCM at a supernumerary centriole could be distinguished. We found that 91% of cells had Pericentrin at three or more foci. (Supplementary Fig. 5D). For alpha-tubulin staining, cells that had two or more foci of centrioles at a spindle pole were assessed so microtubules at a supernumerary centriole could be distinguished. We found that 79% of cells had microtubules emanating from two or more foci (Supplementary Fig. 5E). These data indicate that supernumerary centrioles arose as a consequence of BRAFV600E expression and many of these centrioles were competent to accumulate PCM and nucleate microtubules. Supernumerary centrioles were also present in *BRAF^{V600E}*-expressing human Mel-ST cultured melanocytes (Supplementary Fig. 6A, B) and *BRAF^{V600E}*-expressing zebrafish melanocytes (Fig. 5C, D, Supplementary Fig. 6C, D), supporting the relevance of observations in RPE-1 cells to melanocyte and melanoma biology. To determine whether supernumerary centrioles arose due to BRAF^{V600E}-dependent MAPK signaling activity, we treated *BRAF^{V600E}*-expressing cells with the MEK inhibitor trametinib and ERK inhibitor SCH772984. Both inhibitors suppressed the increase in centrioles (Fig. 5A, B), indicating that BRAF^{V600E}-dependent overactivation of MAPK signaling led to supernumerary centrioles.

Supernumerary centrioles contribute to RhoA downregulation and *BRAF^{V600E}*-induced WGD. Our findings indicated that BRAF^{V600E} caused RhoA downregulation and failure of cytokinesis as well as an increase in centrioles. We sought to determine whether the increase in centrioles contributed to RhoA downregulation and tetraploid cell formation. First, we examined if *BRAF^{V600E}*-expressing cells with extra centrioles had reduced RhoA localization as compared to *BRAF^{V600E}*-expressing cells with normal centrioles. *BRAF^{V600E}*-expressing cells with a normal number and arrangement of centrioles had reduced RhoA staining; however, *BRAF^{V600E}*-expressing cells with extra centrioles had an even greater reduction in RhoA localization (Fig. 6A, B). To establish that the reduced localization of RhoA in these cells was dependent on extra centrioles, we treated cells with centrinone, a PLK4 inhibitor that blocks centrosomal duplication[69]. Centrinone treatment suppressed the formation of extra centrioles in *BRAF^{V600E}*-expressing cells (Fig. 6C). The centrinone-treated *BRAF^{V600E}*-expressing cells had higher RhoA

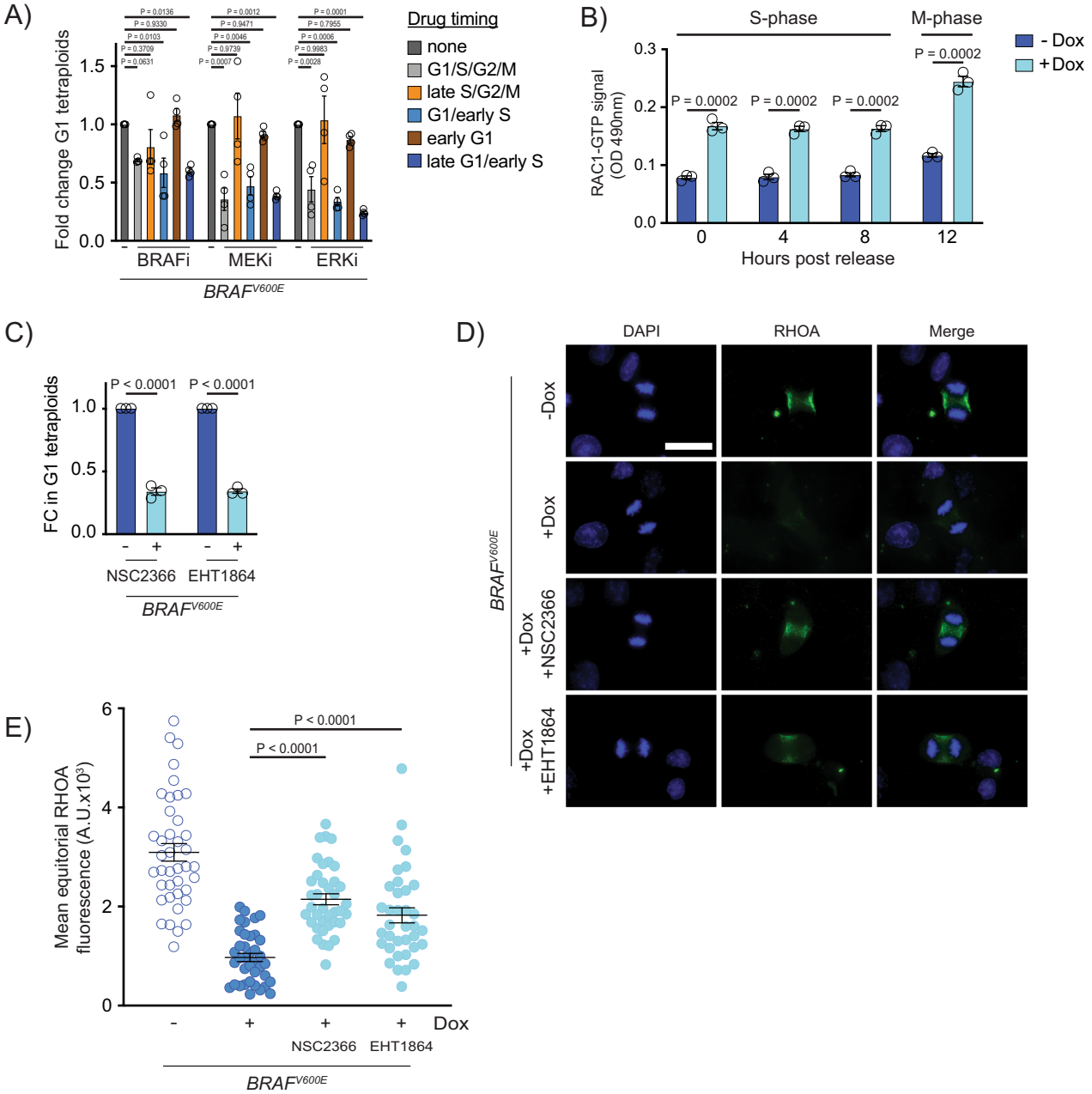


Fig. 4 BRAF^{V600E} acts during G1/S and activates RAC1 to downregulate RhoA and generate tetraploid cells. A Fold change in G1 RPE-1 FUCCI tetraploids following inhibitor treatment. Fold changes are expressed relative to control (+*BRAF*^{V600E}, no drug) samples. Inhibitors were added at indicated timepoints. $N = 4$ independent experiments. One-way ANOVA with Dunnett's multiple comparisons test. Error bars represent mean ± SEM. **B** ELISA-based quantification of RAC1-GTP levels in control (−Dox) and *BRAF*^{V600E}-expressing (+Dox) RPE-1 cells. Cells were measured at the indicated timepoints post thymidine release. RAC-1 GTP signal was measured using a colorimetric assay at 490 nM absorbance. $N = 3$ independent experiments. Unpaired Student's *t* test. Error bars represent mean ± SEM. **C** Fold change (FC) in G1 RPE-1 FUCCI tetraploids following addition of RAC1 inhibitors. NSC2366 and EHT1864 were added coincident with *BRAF*^{V600E} induction. Fold changes are expressed relative to control (+*BRAF*^{V600E}, no drug) cells. $N = 3$ independent experiments. Unpaired Student's *t* test. Error bars represent mean ± SEM. **D** DAPI and anti-RHOA staining in -*BRAF*^{V600E} (−Dox) cells, *BRAF*^{V600E}-expressing (+Dox) cells, and *BRAF*^{V600E}-expressing (+Dox) RPE-1 cells treated with NSC2366 or EHT1864. Drugs were added coincident with Dox administration. Images are maximum intensity projections of z-stacks (0.20 µM). Scale bar = 7.5 µM. **E** Mean RHOA fluorescence intensity at the equator of control RPE-1 cells, *BRAF*^{V600E}-expressing RPE-1 cells, and *BRAF*^{V600E}-expressing RPE-1 cells treated with NSC2366 or EHT1864. Fluorescence intensities (mean gray values) of the equator were measured by sum intensity projections of z-stacks. $N = 40$ cells for −Dox, $N = 38$ for +Dox, $N = 38$ for +Dox +NSC2366, and $N = 36$ for +Dox +EHT1864. Brown-Forsythe and Welch one-way ANOVA with Dunnett's multiple comparisons test. Error bars represent mean ± SEM.

equatorial localization as compared to control *BRAF*^{V600E}-expressing cells (Fig. 6D, E). This recovery of RhoA localization was evident not only when centrinone treatment was coincident with *BRAF*^{V600E} expression, but also when centrinone treatment was limited to late G1 and early S. Centrinone treatment also partially suppressed the *BRAF*^{V600E}-driven formation of tetraploid cells (Fig. 6F). Thus, suppression of supernumerary centrioles in *BRAF*^{V600E}-expressing cells recovered not only RhoA localization but also promoted cytokinesis. Taken together, these data indicate that the reduction of RhoA localization and

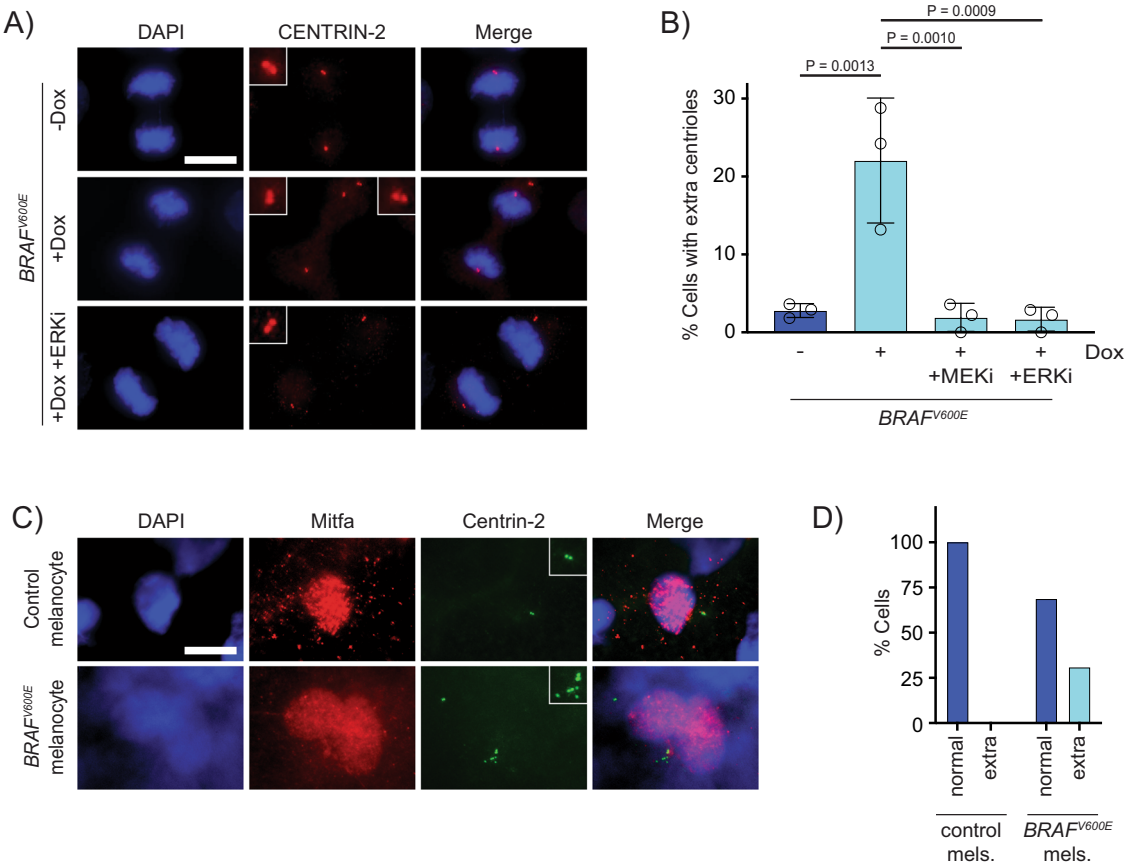


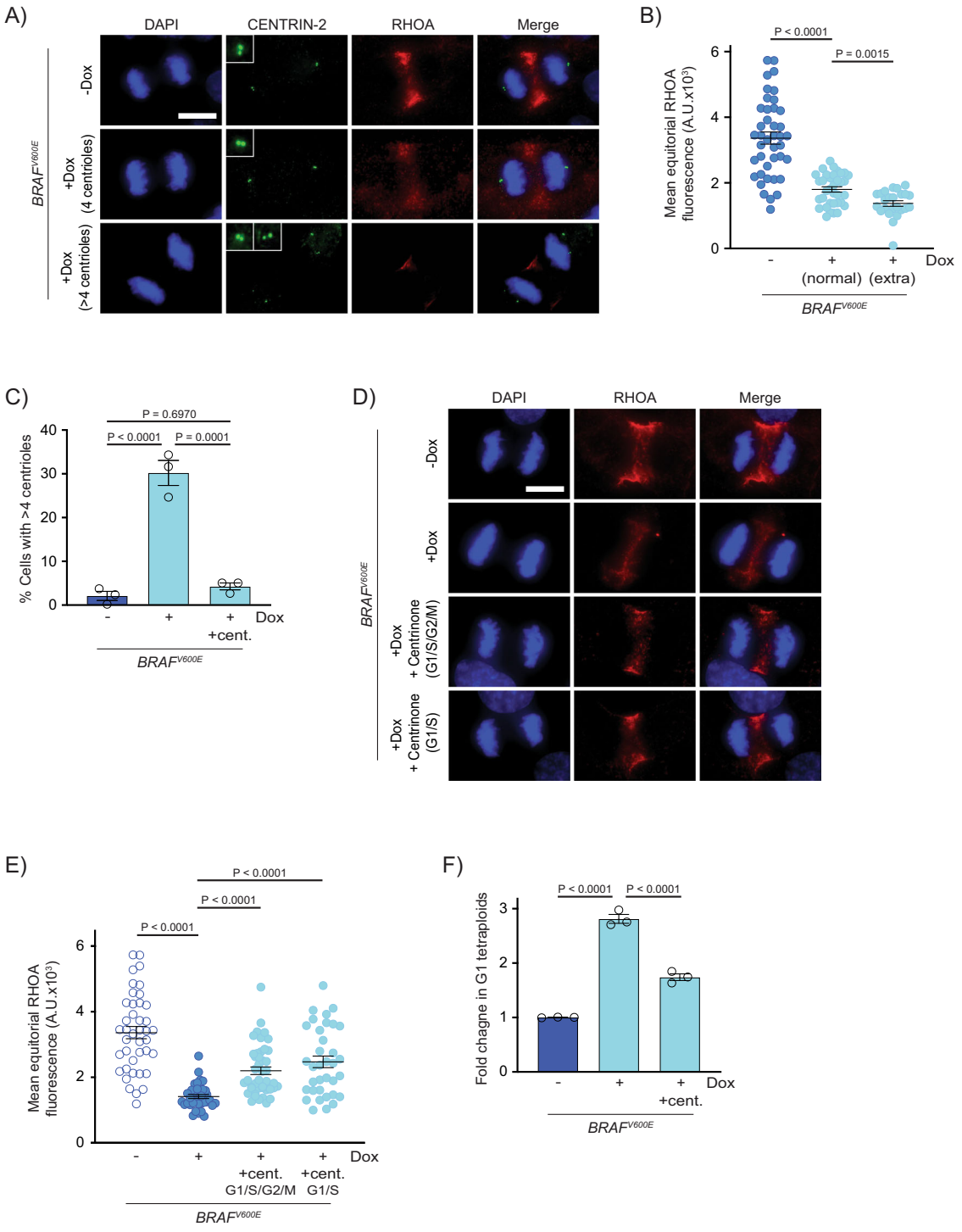
Fig. 5 Supernumerary centrioles are observed in *BRAF*^{V600E}-expressing cells. A DAPI and anti-CENTRIN-2 staining in control (−Dox) and *BRAF*^{V600E}-expressing (+Dox) anaphase RPE-1 cells. Insets show centrioles at one pole. Images are maximum intensity projections of z-stacks. Scale bar = 7.5 μM. **B** Percent cells with supernumerary (>4) centrioles in control RPE-1 cells, *BRAF*^{V600E}-expressing cells and *BRAF*^{V600E}-expressing cells treated with MEKi or ERKi. Quantification of RPE-1 cells in mitosis with supernumerary (>4) centrioles. Drugs were added coincident with Dox administration. $N = 3$ independent experiments examining −Dox = 131, +Dox = 169, +Dox +MEKi = 85, and +Dox +ERKi = 91 cells. One-way ANOVA with Tukey's multiple comparisons test. Error bars represent mean ± SEM. **C** DAPI, anti-Mitfa and anti-Centrin-2 staining of control *Tg(mitfa:EGFP); alb(lf)* and *Tg(mitfa:EGFP); Tg(mitfa:BRAF*^{V600E}*); alb(lf)* non-cycling zebrafish melanocytes. Scale bar = 7.5 μM. Insets show centrioles. **D** Percent cells with normal (2) and extra (>2) centrioles in control *Tg(mitfa:EGFP); alb(lf)* and *Tg(mitfa:EGFP); Tg(mitfa:BRAF*^{V600E}*); alb(lf)* zebrafish melanocytes. $N = 36$ melanocytes for *Tg(mitfa:EGFP); alb(lf)* and $N = 50$ for *Tg(mitfa:EGFP); Tg(mitfa:BRAF*^{V600E}*); alb(lf)*. Chi-square test $P = 0.000843$.

cytokinesis in *BRAF*^{V600E}-expressing cells is partially dependent on the *BRAF*^{V600E}-driven increase in centrioles. Because the suppression of supernumerary centrioles in *BRAF*^{V600E}-expressing cells did not fully restore RhoA localization and cytokinesis, a separate, centriole-independent mechanism driven by BRAF^{V600E} also reduces RhoA localization and cytokinesis.

p53 blocks cell cycle progression of *BRAF*^{V600E}-induced tetraploid cells. Our finding that BRAF^{V600E} can cause failure of cytokinesis and lead to tetraploidy suggests that this may underlie the genome doubling events that are evident in BRAF^{V600E}-mutated melanomas. However, for *BRAF*^{V600E}-expressing cells to contribute to tumor formation, they would likely have to overcome the G1 phase arrest that tetraploid cells experience[21,70]. This tetraploid arrest can be triggered by Hippo pathway activation, which itself is activated by supernumerary centrosome-dependent activation of Rac1[46]. Hippo pathway activation, in turn, activates p53, which has been shown to mediate arrest of tetraploid cells[70,71]. Additionally, inactivation of p53 is strongly correlated with WGD in clinical samples, supporting the possibility of a p53-dependent arrest in tumors[16].

To determine if *BRAF*^{V600E}-expressing tetraploid cells were arrested, we first examined *Tg(mitfa:BRAF*^{V600E}*)* as compared to *Tg(mitfa:BRAF*^{V600E}*); p53(lf)* zebrafish melanocytes. Strikingly, the nuclei of *Tg(mitfa:BRAF*^{V600E}*); p53(lf)* melanocytes were much larger than those of *Tg(mitfa:BRAF*^{V600E}*)* melanocytes (Fig. 7A, Supplementary Fig. 7A). Since DNA content is correlated with nuclear size[40,72], we determined if *Tg(mitfa:BRAF*^{V600E}*); p53(lf)* melanocyte nuclei had a higher DNA content than those of *Tg(mitfa:BRAF*^{V600E}*)* melanocytes. Using DNA densitometry we found that, whereas *Tg(mitfa:BRAF*^{V600E}*)* and *p53(lf)* nuclei were predominantly 2N, *Tg(mitfa:BRAF*^{V600E}*); p53(lf)* nuclei were mostly 4N (Fig. 7B). This suggests that *BRAF*^{V600E} expression causes an arrest of tetraploid cells that is dependent on p53. We also analyzed DNA content in zebrafish melanocytes by flow cytometry. GFP-positive melanocytes from *Tg(mitfa:EGFP); p53(lf); alb(lf)* animals were largely diploid as compared to melanocytes from *Tg(mitfa:EGFP); Tg(mitfa:BRAF*^{V600E}*); p53(lf); alb(lf)* animals, most of which had a higher than 4N DNA content (Supplementary Fig. 7B), consistent with results from the nuclear DNA content densitometry analysis. These data suggest that, at least one and sometimes additional rounds of DNA replication can occur in the same melanocyte. The ploidy defects are dependent on both *BRAF*^{V600E} expression and *p53* deficiency, mirroring the genetic synergism displayed by *Tg(mitfa:BRAF*^{V600E}*)* and *p53(lf)* in melanoma formation.

To more directly address a p53-dependent arrest, we used Crispr/Cas9-mediated genome editing to knock out P53 in our



BRAF^{V600E}-inducible RPE1-FUCCI cell clone. We isolated a clone in which both *P53* alleles were targeted and P53 protein expression abrogated (Supplementary Fig. 7C, D). These cells had DNA content profiles similar to P53 wild-type parental cells (Supplementary Fig. 7E, F). As compared to parental *BRAF*^{V600E}-inducible RPE1-FUCCI cells, *BRAF*^{V600E}-inducible *P53*$^{-/-}$ RPE-1 FUCCI cells had a lower fraction of G1 tetraploids following *BRAF*^{V600E} expression (Supplementary Fig. 7G, H), consistent with the notion that an arrest of G1 tetraploids was bypassed in *P53*$^{-/-}$ cells. Such a failure to arrest would be evidenced by the presence of Geminin-GFP-positive S/G2/M cells with a >4N DNA content. Such cells were present at a much higher fraction in *BRAF*^{V600E}-inducible *P53*$^{-/-}$ RPE-1 FUCCI cultures and were observed after Dox withdrawal in extended cultures (Supplementary Fig. 7I, J), suggesting that, once generated, tetraploid cells could continue to cycle in a *P53*$^{-/-}$ background. To more directly determine if a P53-dependent arrest prevents *BRAF*^{V600E}-expressing tetraploids from entering the cell cycle, we isolated G1 tetraploids after release from synchronization, cultured them for 24 h, then assessed cell cycle progression. As measured by Geminin-GFP expression, *BRAF*^{V600E}-expressing RPE1-FUCCI cells showed little to no progression (Fig. 7C, D). By contrast, nearly 15% of *BRAF*^{V600E}-expressing p53$^{-/-}$ RPE-1 FUCCI cells were Geminin-GFP-positive. The majority of these Geminin-

Fig. 6 Supernumerary centrioles contribute to RhoA downregulation and BRAF^{V600E}-induced tetraploidy. A DAPI, anti-CENTRIN-2 and anti-RHOA staining in control (−Dox) and *BRAF^{V600E}*-expressing (+Dox) anaphase RPE-1 cells. Insets show centrioles at one pole. Images are maximum intensity projections of z-stacks. Scale bar = 7.5 μM. **B** Mean RHOA fluorescence intensity at the equator of control RPE-1 anaphase cells ($n = 30$) and *BRAF^{V600E}*-expressing RPE-1 anaphase cells with normal (4) and supernumerary (>4) centrosomes. $N = 41$ cells for −Dox, $N = 35$ for +Dox with normal centrioles, and $N = 24$ for +Dox with supernumerary centrioles. Brown-Forsythe and Welch one-way ANOVA with Dunnett's multiple comparisons test. Error bars represent mean ± SEM. **C** Percent RPE-1 cells in mitosis with supernumerary (>4) centrioles in control RPE-1 cells, *BRAFV600E*-expressing RPE-1 cells and *BRAFV600E*-expressing RPE-1 cells treated with Centrinone. Centrinone was added coincident with Dox administration. $N = 3$ independent experiments examining −Dox = 119, +Dox = 124, +Dox +Centrinone = 122 cells. One-way ANOVA with Tukey's multiple comparisons test. Error bars represent mean ± SEM. **D** DAPI and anti-RHOA staining in -*BRAF^{V600E}* (−Dox) RPE-1 cells, *BRAF^{V600E}*-expressing (+Dox) RPE-1 cells, and *BRAF^{V600E}*-expressing (+Dox) RPE-1 cells treated with Centrinone. Centrinone was added coincident with Dox administration (G1/S/G2/M) or only during G1/S. Images are maximum intensity projections of z-stacks (0.20 μM). Scale bar = 7.5 μM. **E** Mean RHOA fluorescence intensity at the equator of control RPE-1 cells, *BRAF^{V600E}*-expressing RPE-1 cells, and *BRAF^{V600E}*-expressing RPE-1 cells treated with Centrinone coincident with Dox administration (G1/S/G2/M) or only during G1/S. $N = 41$ cells for −Dox, $N = 39$ for +Dox, $N = 44$ for +Dox +Centrinone in G1/S/G2/M, and $N = 35$ for +Dox +Centrinone in G1/S. Brown-Forsythe and Welch one-way ANOVA with Dunnett's multiple comparisons test. Error bars represent mean ± SEM. **F** Fold change in G1 tetraploids in control RPE-1 FUCCI cells (−Dox), *BRAF^{V600E}*-expressing RPE-1 FUCCI cells (+Dox) and *BRAF^{V600E}*-expressing RPE-1 FUCCI cells treated with Centrinone (+Dox +cent.). Fold changes are expressed relative to the control cells. $N = 3$ independent experiments. One-way ANOVA with Tukey's multiple comparisons test. Error bars represent mean ± SEM.

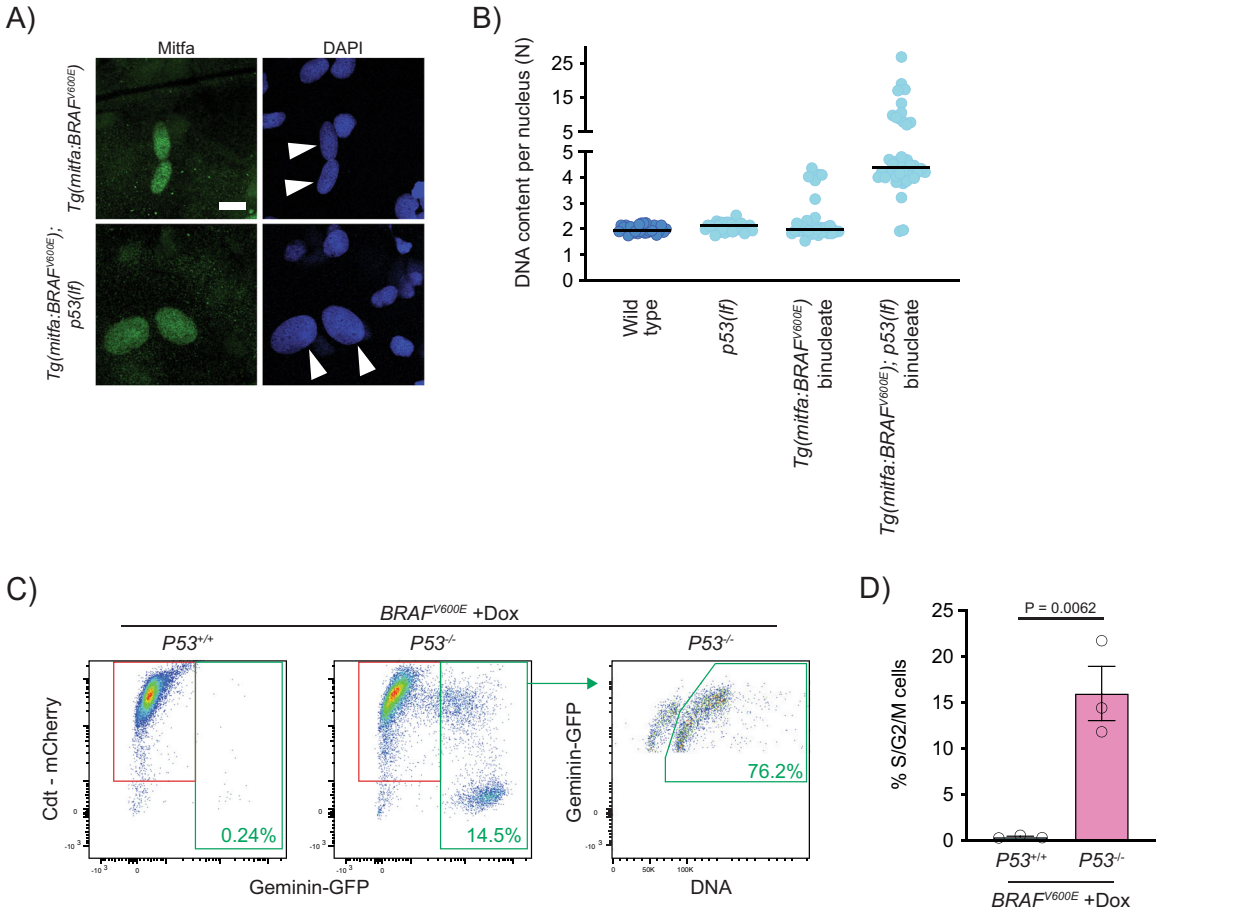
GFP-positive cells had DNA content reflective of progression into S/G2/M cell cycle phases (Fig. 7C). Together these data indicate that *BRAF^{V600E}*-induced tetraploid cells arrest in G1, and this arrest is alleviated by loss of P53. Our analysis of human tumor samples confirmed that loss of p53 pathway activity was strongly correlated with WGD, including in tumors that harbor BRAF mutations and other mutations that activate RAS/MAPK signaling (Supplementary Fig. 8).

Nascent tumor cells in *BRAF^{V600E}*-driven zebrafish melanomas are tetraploid and have higher ploidy. Our data indicate that BRAF^{V600E} can induce tetraploidy in melanocytes, and these melanocytes are prevented from progressing further by a p53-dependent block. Since *BRAF^{V600E}* and loss of *p53* cooperate to form melanomas, and because *BRAF^{V600E}* causes tetraploidy as seen in our in vivo and in vitro models, we were interested in understanding whether *BRAF^{V600E}*-generated tetraploid cells serve as intermediates in melanomagenesis in our zebrafish model, potentially as cells of origin. This would be consistent with findings in tumor types with frequent WGD, in which tumors that have undergone a WGD event are thought to have undergone that event early in tumor progression[3,73]. To determine if tetraploid cells are present in the earliest stages of tumor formation, we took advantage of the zebrafish model in which early melanomas can be identified because of their reactivation of the neural crest gene *crestin*[74]. Using a *Tg(mitfa:BRAF^{V600E}); p53(lf); Tg(crestin:EGFP)* strain that marks tumor initiating cells, we identified zebrafish with early tumors (<20 cells), dissected these tumors and performed flow cytometry to determine DNA content of *crestin:EGFP*-positive tumor cells. The *crestin:EGFP*-positive cells were mostly tetraploid, and several octoploid cells were also observed (Fig. 7E). Notably, none of the cells were diploid, indicating that cells were tetraploid very early in tumor formation and it is likely that the cell of origin was tetraploid. Furthermore, the octoploid nascent tumor cells were mostly mononucleate (Fig. 7E) and thus different from the octoploid, binucleate melanocytes present in *Tg(mitfa:BRAF^{V600E}); p53(lf)* strains. We speculate that these mononuclear, octoploid tumor cells arose from tetraploid cells of origin, and were cycling tetraploid cells in G2 and M phases. These data suggest that WGD can be present at the time of tumor initiation and potentially support tumor progression.

Discussion

Our results indicate that BRAF^{V600E}, and RAS/MAPK signaling in general, can cause the WGD that is a hallmark of melanomas and other tumor types. BRAF^{V600E} causes WGD by suppressing the activity of RhoA, leading to failure of cytokinesis. This suppression stems, in part, from supernumerary centrosomes that are formed as a result of BRAF^{V600E} activity. Supernumerary centrosomes are known to activate Rac1, and we found that Rac1 activity was necessary for BRAF^{V600E}-dependent WGD. Taken together, our data support a model in which BRAF^{V600E} causes the formation of supernumerary centrioles and centrosomes, leading to the activation of Rac1, which in turn causes inhibition of RhoA and failure of cytokinesis. The binucleate, tetraploid cells that result arrest in G0/G1 unless cells have an underlying mutation, in our models it is loss of P53, that abrogates the arrest and enables further cell cycle progression. Thus, in addition to stimulating cell cycle progression, suppressing cell death and providing other tumor-promoting activities, BRAF^{V600E} can cause WGD, which has been shown to support tumorigenesis and tumor progression.

A key component of this model is the formation of supernumerary centrosomes in *BRAF^{V600E}*-expressing cells. The requirement for BRAF^{V600E} activity in G1/S coincides with the timing of centrosomal duplication in most cell types. Furthermore, gamma-tubulin staining in *BRAF^{V600E}*-expressing cells showed an increase in centrosome numbers in cells that had only progressed into S and G2 phases after *BRAF^{V600E}* induction in G1. Together these observations suggest that the defect caused by BRAF^{V600E} is that of centrosomal overduplication. A similar phenotype has been observed upon *BRAF^{V600E}* overexpression in established melanoma cell lines, although such cells had a high background of underlying centrosomal abnormalities[75,76]. More recently, direct staining of melanoma samples suggests that supernumerary centrosomes in patient samples arise predominantly through overduplication[77]. The mechanism by which BRAF^{V600E} could cause overduplication is not clear, although the ability of centrinone to suppress *BRAF^{V600E}*-induced supernumerary centrioles indicates that this mechanism is PLK4-dependent. Our data also indicate that supernumerary centrioles accumulate pericentriolar material (PCM) and have microtubule organizing center (MTOC) activity once they are formed. This is surprising because, under normal circumstances, newly-formed centrioles need to traverse through mitosis to accumulate PCM and nucleate microtubules[78]. How precocious maturation of *BRAF^{V600E}*-induced supernumerary centrioles could occur is not entirely clear, although a combination of studies suggest premature centriole disengagement might be important. RAS/MAPK pathway activity, such as that induced by BRAFV600E, is a well-established cause of replication stress[79,80]. Recently, it has been



	Percent mononucleate	Percent binucleate	n
4N	76.9	23.1	173
8N	85.6	14.4	118

shown that replication stress causes premature centriole disengagement, leading to the formation of multipolar spindles that show microtubule nucleation on prematurely disengaged centrioles[81]. Premature centriole disengagement caused by disruption of *Cep57* and PCM components also leads to precocious maturation, suggesting that premature disengagement can generally enable precocious maturation and MTOC activity[82]. Thus, taken together, RAS/MAPK-induced replication stress caused by $BRAF^{V600E}$ expression could lead to premature centriole disengagement followed by precocious maturation and MTOC activity. As noted, the effect of supernumerary centrosomes only accounts for some of the RhoA reduction and cytokinesis failure upon $BRAF^{V600E}$ induction. Nonetheless, our findings together with the association of $BRAF^{V600E}$ with centrosomal amplification in

Fig. 7 Progression of p53-mutant BRAF^{V600E}-induced tetraploid cells. A Anti-Mitfa and DAPI staining of nuclei in *Tg(mitfa:BRAF^{V600E})* and *Tg(mitfa:BRAF^{V600E}); p53(lf)* melanocytes. Melanin pigment was bleached to more clearly visualize nuclear size. White arrowheads indicate two nuclei within a single melanocyte. Scale bar = 10 μm. **B** DNA content per nucleus as measured by confocal densitometry. Each data point represents a single nucleus. $N = 25$ nuclei for wild type, $N = 31$ for *p53(lf)*, $N = 35$ for binucleate *Tg(mitfa:BRAF^{V600E})*, and $N = 42$ for binucleate *Tg(mitfa:BRAF^{V600E});p53(lf)* cells. Bars represent median. **C** Flow cytometry plots of *BRAF^{V600E}*-expressing (+Dox) p53 wild-type (left) and p53 mutant (middle) tetraploid cells. Prior to analysis, RPE-1 FUCCI G1 tetraploid cells were isolated and plated for 24 h in the presence of nocodazole. Percentages of Geminin-GFP-positive cells in S/G2/M are indicated. Flow cytometry plot of *BRAF^{V600E}*-expressing (+Dox) p53 mutant S/G2/M cells (right). Percentage of ≥4 N S/G2/M cells is indicated. **D** Percent S/G2/M cells from flow cytometry analysis in (**C**). $N = 3$ independent experiments. Unpaired Student's *t* test. Error bars represent mean ± SEM. **E** Flow cytometry and DNA content analysis of normal tissue (left, top) and nascent melanomas (left, bottom) from *Tg(crestin:EGFP); Tg(mitfa:BRAF^{V600E}); p53(lf)* zebrafish. Brightfield, EGFP and DAPI images of single melanocytes are shown. Quantification of percent mononucleate and binucleate cells in the 4N and 8N peaks of nascent melanomas (right).

papillary thyroid, colorectal and other cancers suggests there may be a broad link between BRAF^{V600E}-induced supernumerary centrosomes and WGD[83,84].

Our findings begin to address the fate of cells that undergo WGD through cytokinesis failure. Zebrafish melanocytes and RPE-1 cells that have undergone cytokinesis failure arrest in G1 as binucleate tetraploid cells. However, in established zebrafish melanomas and late-stage human tumors that have previously experienced a WGD event, tumor cells go through the cell cycle, are predominantly mononuclear and do not indefinitely undergo cytokinesis failure. This raises the questions of how cells having just undergone a WGD event overcome the G1 block and, once they do, divide productively without creating giant, multinucleated cells. Newly-generated G1 binucleate tetraploid cells undergo a P53-dependent arrest, as evidenced by the progression into S phase of P53-mutant RPE-1 G1 tetraploids. The polyploid nature of *Tg(mitfa:BRAF^{V600E}); p53(lf)* melanocytes indicates that this arrest also occurs in the zebrafish model. However, these zebrafish melanocytes are found as binucleates with most nuclei appearing to have gone through a single S phase without any further mitosis. This suggests that additional blocks may exist to prevent such cells from progressing further into the cell cycle, and such blocks would have to be overcome during tumorigenesis. If such cells were to progress and continue cycling, then conditions would have to exist to prevent them from stalling tumor growth as multinucleated cells. One possible condition is that the penetrance of BRAF^{V600E}-induced cytokinesis failure is incomplete as in RPE-1 cells. Enough cytokinesis failure to enable WGD would be present, but not enough to prevent the amount of cell divisions required for tumor growth. Another possible condition is the attenuation of cytokinesis failure following a WGD event. RhoA activity has been shown to be upregulated in tumors[85–87], and this could be an adaptation that prevents pervasive cytokinesis failure that would be detrimental to tumor progression.

Our finding that nascent zebrafish melanoma cells were tetraploid or had higher ploidy supports the notion that BRAF^{V600E}-induced WGD can be present at the time of tumor initiation. In cancer types that have a high prevalence of WGD, such as melanoma, WGD in tumors frequently occurred early in tumor formation and might have been present at the time of tumor initiation and clonal outgrowth[3,73]. This raises the question of whether BRAF^{V600E}, which is present in ~80% of benign nevi[88,89], can cause WGD at the earliest stages of tumor formation and possibly in benign lesions. Although cells in common cutaneous nevi are primarily diploid[90,91], several observations suggest that cytokinesis failure and associated WGD can occur in these cells. Cultures of nevocytes have been shown to contain binucleated cells[92]. Furthermore, the presence of binucleate and multinucleated giant cells in nevi is not uncommon[93], and polyploid cells are observed at a low fraction in many nevus samples[94]. Together these observations suggest that some level of cytokinesis failure occurs in nevi and may be caused by BRAF^{V600E}. The prevalence of early WGD in melanomas as compared to its relative absence in nevi, at least its absence when nevi begin clonal outgrowth, suggests there is some advantage to WGD in tumor formation. The ability to sample various pro-tumorigenic genomic configurations may underlie the benefit of WGD[95] as would the ability of WGD to make haploid regions of a nascent tumor cell diploid and thus protect these regions from mutations incurred in essential genes[24]. Lastly, although the focus has been on WGD supporting tumor initiation, it is clear that many tumors analyzed bioinformatically, including the majority (~60%) of melanomas, show no evidence of having undergone WGD. However, this does not mean WGD is irrelevant in such tumors. Recent evidence suggests that WGD in melanomas can be late truncal and even occur privately in metastases[96,97]. Therefore, while WGD may not be necessary in all tumors for initiation, it nonetheless could play a role in disease progression. It is worth noting that the WGD observed in nevocytes, primary tumors and metastases overlaps with the presence of BRAF^{V600E} or other RAS/MAPK-activating mutations that could support WGD in such lesions.

Methods

Zebrafish strains and husbandry. Zebrafish were handled in accordance with protocols approved by the University of Massachusetts Medical School IACUC (A-2171). Strains were maintained at 28 °C as described by Westerfield[98]. AB was used as the wild-type strain. The following mutations were used: *p53(zdf1)*[99], *mitfa(w2)*[100], *alb(b4)*[101] and are designated throughout as "*lf*" for loss-of-function mutation. The integrated transgene *Tg(mitfa:BRAF^{V600E})* expresses oncogenic human *BRAF^{V600E}* under the control of the zebrafish pigment cell-specific *mitfa* promoter[38]. Equal numbers of male and female animals were used in experiments.

Cell line generation. RPE-1 FUCCI cells were grown in DMEM: F12 media containing 10% tetracycline-free FBS, 100 IU/ml penicillin, and 100 μg/ml streptomycin. Mel-ST cells were grown in DMEM media containing 5% tetracycline-free FBS, 100 IU/ml penicillin, and 100 μg/ml streptomycin. Cells were maintained at 37 °C with 5% CO_2 atmosphere. TetR was expressed in cells using pLenti CMV TetR Blast (Addgene #17492). Transduced cells were selected with 5 μg/ml blasticidin and bulk cells expressing the TetR protein were clonally isolated in 96-well plates using FACS (BD-Aria). *BRAF^{V600E}* and *BRAF^{WT}* were expressed in cells using Gateway-compatible lentiviral constructs (pLenti CMV/TO puro DEST, pLenti CMV/TO neo DEST; gifts from Eric Campeau and Paul Kaufman[102]). Lentivirus carrying *BRAF^{WT}* or *BRAF^{V600E}* construct was generated by transfection of HEK-293T cells, with appropriate packaging plasmids (pMD2.G and psPAX2) using lipofectamine 2000, according to the manufacturer's instructions. RPE-1 and Mel-ST cells were infected for 48 h with virus carrying a BRAF construct in the presence of 8 μg/ml polybrene, washed, and allowed to recover for 24 h before selection. Cells were selected with the appropriate antibiotic selection marker (5 μg/ml puromycin or 1 mg/ml neomycin) and clonally isolated in 96-well plates using FACS (BD-Aria). Doxycycline was used at 1 μg/ml to induce the expression of *BRAF*.

Synchronization and ploidy analysis. To turn on *BRAF^{V600E}* in a synchronized cell population, we serum starved RPE-1 FUCCI cells with 0.1% serum for 48 h. Serum-starved cells were released into media with 10% serum until they reached the next G1 (~33 h). *BRAF^{V600E}* was turned on using doxycycline, and cells were resynchronized at G1/S using thymidine (2.5 mM). Following thymidine washout cells were allowed to progress through the cell cycle, and ploidy was analyzed in next G1 (16 h after thymidine release) using Hoechst incorporation (2.5 μg/ml) in

hCdt1-mcherry expressing cells by flow cytometry, which was performed using a BD-LSR flow cytometer, acquired using BD FACS Diva software (v. 8.0.1) and analyzed using FlowJo software (v. 10.0). For immunofluorescence experiments of mitotic cells, cells were fixed at 12 h after thymidine release.

Live cell imaging. For live cell imaging, RPE-1 H2B-GFP-transfected cells were grown on glass-bottom 12-well tissue culture dishes (MatTek) and imaged on a Nikon TE2000E inverted microscope equipped with a cooled Hamamatsu Orca-ER CCD 11 camera and the Nikon Perfect Focus system. The microscope was enclosed within an incubation chamber that maintained an atmosphere of 37 °C and 3–5% humidified CO_2. GFP and phase-contrast images were captured at multiple locations every 5 min with either 20× or 40× Nikon Plan Fluor objectives. All captured images were analyzed using NIS-Elements software. For imaging, cells were synchronized with thymidine and imaged for 48 h after release. Each cell going through mitosis was observed and cytokinesis was scored by phase contrast imaging. To verify cytokinesis failure and to confirm that the nuclei stayed within one cell, cells were carefully traced for at least ten frames. To quantify mitotic duration, each frame beginning from the start of nuclear envelope breakdown to anaphase onset was counted.

Immunofluorescence and imaging. RPE-1 $BRAF^{V600E}$ cells were grown directly on collagen IV (Sigma) -coated coverslips, fixed in 3.7% formalin, permeabilized using 0.1% Triton X-100, and treated with 0.1% SDS. They were blocked in 1% BSA and then incubated with primary antibody diluted in blocking solution in a humidity chamber at 4 °C overnight, washed with 1X PBS, and incubated with secondary antibody. Cells were mounted using mounting media containing DAPI (Vector Laboratories). All secondary antibodies were Alexa Fluor conjugates (488, 555, and 647) (Thermofisher) used at a 1:500 dilution. All images were acquired on a Leica DM 600 inverted microscope at 100× magnification and analyzed using Leica LAS X software (v. 3.7.1.21655). Z stack images were taken at 0.20 µM each. For melanocyte binucleate counts and immunofluorescence staining, zebrafish adult dorsal scales were fixed using 4% paraformaldehyde for 2 h, washed with PBST (PBS + 0.1% Triton X) and water then blocked in 1%BSA/PBS for 30 min prior to primary antibody incubation. Affinity-purified anti-Mitfa antibodies were used at a 1:100 dilution for staining. All images were acquired on a Nikon Eclipse Ti A1R-A1 confocal microscope and analyzed using NIS-Elements software.

RhoA and Rac1 activation assays. RPE-FUCCI cells were synchronized as described above, and lysates were collected at 0, 4, 8, 12 h post release from thymidine. GTP-bound RhoA and Rac1 were immunoprecipitated from cells according to manufacturers' protocols (BK-036, BK-128, Cytoskeleton).

Western blotting and antibodies. Cells were lysed in ice-cold RIPA buffer containing a Complete protease inhibitor tablet (Roche). Protein concentration was measured using the Pierce BCA Protein Assay Kit (Life Technologies). Samples were run on 10% polyacrylamide gels, transferred, and developed using fluorophore-conjugated antibodies (LI-COR). Primary antibodies and dilutions used were: Total BRAF, 1:1000 (10146, Millipore); TetR, 1:1000 (631132, Takara); TUBULIN 1:1000 (2144S, Cell Signaling); $BRAF^{V600E}$ 1:1000 (E19290, Spring Bioscience); RHOA(GTP) 1:500 (ARH03, Cytoskeleton); Total RHOA, 1:500 (ARH05, Cytoskeleton), RAC1 1:500 (ARC03, Cytoskeleton); p-MPS1 T676 1:1000 (PA5-64614, Thermofisher); Total MPS1 (PA5-116969, Thermofisher); p-MEK 1:1000 (9154, Cell Signaling); Total MEK 1:1000 (8727, Cell Signaling); p-ERK 1:1000 (m8159, Sigma); Total ERK 1:1000 (4695, Cell Signaling); P53 1:1000 (sc-126, SCBT); GAPDH 1:5000 (AM4300, Thermofisher). Secondary antibodies and dilutions used were: IRDye 800CW Donkey anti-Rabbit 1:10,000 (LI-COR 926-32213); IRDye 680RD Goat anti-Mouse 1:10,000 (LI-COR 926-68070). Uncropped and unprocessed scans of western blots are provided in Source Data.

Cyclin D1 staining for flow cytometry. RPE-1 FUCCI cells were trypsinized, washed with 1XPBS and fixed in 2% PFA at RT for 15 min. Cells were then washed with PBS/1%FBS and permeabilized with 100% methanol (for CYCLIN D1). Cells were washed with PBS, incubated with Alexa Fluor 647-conjugated primary antibodies for 60 min at room temperature, washed and stained with 1:1000 DAPI for 15 min before flow cytometry (BD-LSR).

CRISPR cell line generation. Oligos targeting p53 were annealed and inserted into lentiCRISPR v2 (gift of Feng Zhang) as described previously[103,104] The lentiviral packaging plasmids pMD2.G (Addgene plasmid #12259) and psPAX2 (Addgene plasmid #12260) were used for transfection using lipofectamine. For lentiviral transduction, cells (300,000) were plated in a 6 well plate the day before transduction. Lentivirus was harvested and added to OptiMEM supplemented with 8 µg/mL polybrene. Media was changed 24 h after transduction to remove polybrene. Media supplemented with 5 µg/mL puromycin (Sigma Aldrich) or was changed 48 h after transduction to select lentiCRISPRv2 transduced cells. Following transduction with p53-targeting lentiCRISPRv2 containing lentivirus, antibiotic-resistant cells were selected then clonally isolated by FACS in 96-well plates. Clones were then assayed for indels via the surveyor assay (706020, IDT). Cells that showed indels were then cloned into the pGEM-T Easy vector (Promega), and colonies were picked using blue/white screening then sequenced. The p53 gRNA sequence was CCCCGGACGATATTGAACAA. Primers used for sequencing indels were as follows:

Forward – 5′ GTAAGGACAAGGGTTGGGCT 3′
Reverse – 5′ GAAGTCTCATGGAAGCCAGC 3′

Flow cytometry of zebrafish melanocytes, normal tissue and tumors. To isolate zebrafish melanocytes for flow cytometry, 4- to 6-month-old fish were treated for 5 min with the anesthetic tricaine methanesulfonate. Scales were plucked from the dorsal anterior region of fish and put in 0.9× PBS. Cells were dissociated using TH liberase (Roche) for 30 min by constant agitation at 37 °C. Cells were immediately fixed for 2 h in 4% paraformaldehyde. Following fixation, cells were washed and permeabilized 3× with 0.1% Triton X/PBS and immediately stained with DAPI (1:1000). Cells were then filtered through a 40 µM mesh filter and spun down at 2000rpm. Analysis for GFP+ and DAPI+ cells was performed on the Amnis Flowsight using IDEAS software (v. 6.0). For ploidy analysis of zebrafish tumors, melanomas from *Tg(mitfa:EGFP); (mitfa:$BRAF^{V600E}$); p53(lf);alb* animals were removed, homogenized in PBS, and stained and analyzed in the same manner as described above. For normal tissue analysis, the caudal peduncle and fin were dissected and homogenized.

Confocal densitometry. Zebrafish scales were obtained and stained with anti-Mitfa antibody and DAPI as described above. Melanin pigment interferes with quantitative UV-based imaging so scales were bleached prior to staining. Mitfa-positive melanocyte nuclei were identified, and Z stacks of the DAPI signal of these nuclei were obtained. The same distance between Z slices (0.37 µM) and pixel intensity lookup table were used for each nucleus measured. In analyzing each slice, nuclear boundaries were specified, and pixel intensity values within the nuclear area measured. Pixel intensities for all slices of one nucleus were summed to derive a raw DNA content. Ploidy was estimated using nearby Mitfa-negative nuclei as 2 N controls. Nuclei in the same binucleate cell are typically arranged as mirror-image pairs, and this orientation allowed us to identify nuclei of binucleate cells in the absence of melanin pigment.

Melanocyte density assay. Four- to six-month-old fish were treated for 5 min with the anesthetic tricaine methanesulfonate and epinephrine, which contracts melanosomes to the central cell body of melanocytes (Goodrich and Nichols, 1931), thereby resolving overlapping cells. Scales were plucked from the dorsal anterior region of fish from the scale rows adjacent to the dorsal midline row. Scales were immediately fixed for ≥30 min in 4% paraformaldehyde. After fixation, scales were flat-mounted and melanocytes counted. Area was estimated by multiplying maximal antero-posterior and left-right distances of the scale.

Data collection and statistical analysis. Microsoft Excel (v. 16.16.27) and Graphpad Prism (v. 8.0) were used for data collection. Significance calculations were performed on samples collected in a minimum of biological triplicate. *P* values from two-tailed Student's *t* tests or ANOVA were calculated for all comparisons of continuous variables. All further significance tests were performed in GraphPad Prism (v. 8.0). A P value < 0.05 was considered significant.

Drug treatments. Cells were synchronized as described with serum starvation and thymidine arrest. Treatment of cells with small molecule compounds was performed as follows: G1/S/G2/M—drug was added 33 h following serum addition and coincident with doxycycline; S/G2/M—drug was added following thymidine washout; G1/S—drug was added 39 h following serum addition and washed off 12 h later; G1—drug was added 33 h following serum addition and washed off 6 h later; early G1 – drug was added 33 h following serum addition and washed off 2 h later. Small molecule inhibitors used were—Vemurafenib, 1 µM (S1267, Selleck Chemicals), Trametinib 50 nM (S2673, Selleck Chemicals), SCH772984 50 nM (S1701, Selleck Chemicals), PLX7904 1 µM (S7964, Selleck Chemicals), PLX8394 1 µM (HY-18972, MCE), Centrinone 300 nM (5687, Tocris), NSC2366 5 µM (13196, Cayman Chem), EHT1864 5 µM (17258, Cayman Chem), LPA 1 µM (BML-LP100-0005, Enzo), S1P 1 µM (62570, Cayman Chem), Dihydrocytochalasin B 4 µM (D1641, Sigma).

Immunofluorescence, flow cytometry and antibodies. For RHOA staining, cells were fixed in 10% Trichloroacetic acid (TCA) (T6399, Sigma) on ice for 15 min, washed with PBS/30 nM glycine, then permeabilized with 0.2% Triton X/PBS/30 nM glycine for 10 min on a rocking platform. Cells were then washed with PBS/30 nM glycine, blocked with 3% BSA/PBS/0.01% Triton X-100 for 1 h at room temperature before staining with primary antibody in a humidity chamber at 4 °C overnight. For ANILLIN Staining, cells were fixed in ice cold methanol at −20 °C for 2 h. Cells were then washed with PBST (PBS/0.01% Triton X-100), permeabilized with 0.2% Triton X-100 in PBS for 10 min, washed with PBST and then incubated with primary antibody in a humidity chamber at 4 °C overnight. To quantify RHOA and ANILLIN staining, fluorescence intensities (mean gray values) of the equator were measured by sum intensity projections of z-stacks. For

CENTRIN-2 staining alone or other markers, cells were fixed in ice cold 100% methanol at −20 °C, permeabilized with 0.2% TritonX/PBS and blocked in 1%BSA/PBS before incubating with primary antibody (1:100) in a humidity chamber at 4 °C, overnight. Primary antibodies and dilutions used for immunofluorescence were: ANILLIN 1:100 (PA5-28645, Thermofisher); RHOA 1:75 (sc-418, SCBT); CENTRIN-2 1:100 (04-1624, Millipore); Mitfa[37] 1:100; γ-TUBULIN 1:500 (T6557, Sigma); α-TUBULIN DM1A 1:2000 (3873S, Cell Signaling); PERICENTRIN 1:100 (ab4448, Abcam). Antibodies and dilutions used for flow cytometry were: CYCLIN D1, 1:100 (NBP2-33138AF647, Novus Bio), Rabbit IgG Isotype control, 1:100 (3452S, Cell Signaling), HA tag, 1:100 (IC6875R, R&D systems), Mouse IgG1 Isotype control 1:100 (IC002R, R&D systems). Secondary antibodies and dilutions used for immunofluorescence and flow cytometry were: Alexa Fluor 555 goat anti-rabbit IgG 1:500 (A-21429, ThermoFisher); Alexa Fluor 488 goat anti-mouse IgG2a 1:500 (A-21137, ThermoFisher); Alexa Fluor 555 goat anti-mouse IgG1 1:500 (A-21121, ThermoFisher); Alexa Fluor 488 donkey anti-mouse IgG 1:500 (A-21202, ThermoFisher).

RhoA and Anillin intensity measurements. Fluorescence intensities were quantified using ImageJ as previously described[105]. Briefly, Z-stack images were loaded on ImageJ (v. 1.53a) and the sum intensity projection was obtained using the Z-stack function. RhoA and Anillin equatorial fluorescence intensities were obtained by measuring the intensity profile of the fluorescence signal along a line manually placed along the cell equator, parallel to the anaphase DNA position. The mean fluorescence intensity was obtained by averaging the two intensity values at each side of the furrow. The mean background signal was obtained by averaging the signal of three manually selected circular regions with a diameter of 50 pixels outside of the cell and the value was subtracted from the equatorial intensities.

Growth and apoptosis assays. To perform growth curves, 20,000 cells were plated in 12-well plates and appropriate samples were treated with inhibitors and doxycycline. Cells were counted every 24 h over 4 days using the hemocytometer. Cell death following inhibitor treatment was assessed by the caspase glow assay according to the manufacturer's instructions (G8090, Promega).

Whole-genome doubling analysis. Whole-genome doubling (WGD) data for each cohort were obtained for TCGA samples[106] and MSK-IMPACT samples[16], and mutation data were obtained from cBioPortal[107,108]. Associations of WGD with BRAF mutations as well as ANY RAS/MAPK pathway genes (BRAF, NRAS, KRAS, HRAS, NF1, MAP2K1, MAP3K13 and PTPN11) were analyzed. Associations of WGD with BRAF or ANY RAS/MAPK mutations together with TP53 or CDKN2A mutations and copy number losses were also analyzed, with the rationale that our data support a combination of RAS/MAPK activation plus TP53 pathway inactivation enable progression of cells that undergo WGD.

Reporting summary. Further information on research design is available in the Nature Research Reporting Summary linked to this article.

Data availability

All data generated or analyzed in this study are included in this published article and its Supplementary Information file. Source data are provided with this paper.

Received: 23 April 2021; Accepted: 7 July 2022;
Published online: 15 July 2022

References

1. Dewhurst, S. M. et al. Tolerance of whole-genome doubling propagates chromosomal instability and accelerates cancer genome evolution. *Cancer Discov.* **4**, 175–185 (2014).
2. Carter, S. L. et al. Absolute quantification of somatic DNA alterations in human cancer. *Nat. Biotechnol.* **30**, 413–421 (2012).
3. Zack, T. I. et al. Pan-cancer patterns of somatic copy number alteration. *Nat. Genet.* **45**, 1134–1140 (2013).
4. Quinton, R. J. et al. Whole-genome doubling confers unique genetic vulnerabilities on tumour cells. *Nature* **590**, 492–497 (2021).
5. Galipeau, P. C. et al. 17p (p53) allelic losses, 4N (G2/tetraploid) populations, and progression to aneuploidy in Barrett's esophagus. *Proc. Natl Acad. Sci. USA* **93**, 7081–7084 (1996).
6. Reid, B. J. et al. Barrett's esophagus: ordering the events that lead to cancer. *Eur. J. Cancer Prev.* **5**, 57–65 (1996).
7. Olaharski, A. J. et al. Tetraploidy and chromosomal instability are early events during cervical carcinogenesis. *Carcinogenesis* **27**, 337–343 (2006).
8. Shackney, S. E. et al. Origins and clinical implications of aneuploidy in early bladder cancer. *Cytometry* **22**, 307–316 (1995).
9. Tanaka, T., Mori, H., Takahashi, M. & Williams, G. M. DNA content of hyperplastic and neoplastic acinar cell lesions in rat and human pancreas. *J. Exp. Pathol.* **1**, 315–326 (1984).
10. Deitch, A. D., Miller, G. J. & deVere White, R. W. Significance of abnormal diploid DNA histograms in localized prostate cancer and adjacent benign prostatic tissue. *Cancer* **72**, 1692–1700 (1993).
11. Montgomery, B. T. et al. Stage B prostate adenocarcinoma. Flow cytometric nuclear DNA ploidy analysis. *Arch. Surg.* **125**, 327–331 (1990).
12. Pihan, G. A. et al. Centrosome defects can account for cellular and genetic changes that characterize prostate cancer progression. *Cancer Res.* **61**, 2212–2219 (2001).
13. Hamada, S., Itoh, R. & Fujita, S. DNA distribution pattern of the so-called severe dysplasias and small carcinomas of the colon and rectum and its possible significance in the tumor progression. *Cancer* **61**, 1555–1562 (1988).
14. Levine, D. S. et al. Distribution of aneuploid cell populations in ulcerative colitis with dysplasia or cancer. *Gastroenterology* **101**, 1198–1210 (1991).
15. Zaini, Z. M., McParland, H., Moller, H., Husband, K. & Odell, E. W. Predicting malignant progression in clinically high-risk lesions by DNA ploidy analysis and dysplasia grading. *Sci. Rep.* **8**, 15874 (2018).
16. Bielski, C. M. et al. Genome doubling shapes the evolution and prognosis of advanced cancers. *Nat. Genet.* **50**, 1189–1195 (2018).
17. Duelli, D. & Lazebnik, Y. Cell-to-cell fusion as a link between viruses and cancer. *Nat. Rev. Cancer* **7**, 968–976 (2007).
18. Duelli, D. M. et al. A virus causes cancer by inducing massive chromosomal instability through cell fusion. *Curr. Biol.* **17**, 431–437 (2007).
19. Gao, P. & Zheng, J. High-risk HPV E5-induced cell fusion: a critical initiating event in the early stage of HPV-associated cervical cancer. *Virol. J.* **7**, 238 (2010).
20. Hu, L. et al. Human papillomavirus 16 E5 induces bi-nucleated cell formation by cell-cell fusion. *Virology* **384**, 125–134 (2009).
21. Fujiwara, T. et al. Cytokinesis failure generating tetraploids promotes tumorigenesis in p53-null cells. *Nature* **437**, 1043–1047 (2005).
22. Jamal-Hanjani, M. et al. Tracking thE Evolution of Non-small-cell Lung Cancer. *N. Engl. J. Med.* **376**, 2109–2121 (2017).
23. Jones, D. T. et al. Dissecting the genomic complexity underlying medulloblastoma. *Nature* **488**, 100–105 (2012).
24. Lopez, S. et al. Interplay between whole-genome doubling and the accumulation of deleterious alterations in cancer evolution. *Nat. Genet.* **52**, 283–293 (2020).
25. Hwang, S. et al. Consequences of aneuploidy in human fibroblasts with trisomy 21. *Proc Natl Acad Sci USA* **118**. https://doi.org/10.1073/pnas.2014723118 (2021).
26. Sheltzer, J. M., Torres, E. M., Dunham, M. J. & Amon, A. Transcriptional consequences of aneuploidy. *Proc. Natl Acad. Sci. USA* **109**, 12644–12649 (2012).
27. Torres, E. M., Williams, B. R. & Amon, A. Aneuploidy: cells losing their balance. *Genetics* **179**, 737–746 (2008).
28. Davoli, T. et al. Cumulative haploinsufficiency and triplosensitivity drive aneuploidy patterns and shape the cancer genome. *Cell* **155**, 948–962 (2013).
29. Passerini, V. et al. The presence of extra chromosomes leads to genomic instability. *Nat. Commun.* **7**, 10754 (2016).
30. Thompson, D. A., Desai, M. M. & Murray, A. W. Ploidy controls the success of mutators and nature of mutations during budding yeast evolution. *Curr. Biol.* **16**, 1581–1590 (2006).
31. Mayer, V. W. & Aguilera, A. High levels of chromosome instability in polyploids of *Saccharomyces cerevisiae*. *Mutat. Res.* **231**, 177–186 (1990).
32. Storchova, Z. et al. Genome-wide genetic analysis of polyploidy in yeast. *Nature* **443**, 541–547 (2006).
33. Wangsa, D. et al. Induced chromosomal aneuploidy results in global and consistent deregulation of the transcriptome of cancer cells. *Neoplasia* **21**, 721–729 (2019).
34. Davoli, T. & de Lange, T. The causes and consequences of polyploidy in normal development and cancer. *Annu Rev. Cell Dev. Biol.* **27**, 585–610 (2011).
35. Pfau, S. J. & Amon, A. Chromosomal instability and aneuploidy in cancer: from yeast to man. *EMBO Rep.* **13**, 515–527 (2012).
36. Chircop, M. Rho GTPases as regulators of mitosis and cytokinesis in mammalian cells. *Small GTPases* **5**, https://doi.org/10.4161/sgtp.29770 (2014).
37. Ceol, C. J. et al. The histone methyltransferase SETDB1 is recurrently amplified in melanoma and accelerates its onset. *Nature* **471**, 513–517 (2011).
38. Patton, E. E. et al. BRAF mutations are sufficient to promote nevi formation and cooperate with p53 in the genesis of melanoma. *Curr. Biol.* **15**, 249–254 (2005).
39. Venkatesan, A. M. et al. Ligand-activated BMP signaling inhibits cell differentiation and death to promote melanoma. *J. Clin. Investig* **128**, 294–308 (2018).

40. Sher, N. et al. Fundamental differences in endoreplication in mammals and Drosophila revealed by analysis of endocycling and endomitotic cells. *Proc. Natl Acad. Sci. USA* **110**, 9368–9373 (2013).
41. Saunders, L. M. et al. Thyroid hormone regulates distinct paths to maturation in pigment cell lineages. *Elife* **8**. https://doi.org/10.7554/eLife.45181 (2019).
42. Usui, Y., Kondo, S. & Watanabe, M. Melanophore multinucleation pathways in zebrafish. *Dev. Growth Differ.* **60**, 454–459 (2018).
43. Cancer Genome Atlas, N. Genomic classification of cutaneous melanoma. *Cell* **161**, 1681–1696 (2015).
44. Dovey, M., White, R. M. & Zon, L. I. Oncogenic NRAS cooperates with p53 loss to generate melanoma in zebrafish. *Zebrafish* **6**, 397–404 (2009).
45. Santoriello, C. et al. Kita driven expression of oncogenic HRAS leads to early onset and highly penetrant melanoma in zebrafish. *PLoS ONE* **5**, e15170 (2010).
46. Ganem, N. J. et al. Cytokinesis failure triggers hippo tumor suppressor pathway activation. *Cell* **158**, 833–848 (2014).
47. Sakaue-Sawano, A. et al. Visualizing spatiotemporal dynamics of multicellular cell-cycle progression. *Cell* **132**, 487–498 (2008).
48. Archambault, V., Lepine, G. & Kachaner, D. Understanding the Polo Kinase machine. *Oncogene* **34**, 4799–4807 (2015).
49. Mielgo, A. et al. A MEK-independent role for CRAF in mitosis and tumor progression. *Nat. Med.* **17**, 1641–1645 (2011).
50. Cui, Y. & Guadagno, T. M. B-Raf(V600E) signaling deregulates the mitotic spindle checkpoint through stabilizing Mps1 levels in melanoma cells. *Oncogene* **27**, 3122–3133 (2008).
51. Piekny, A. J. & Glotzer, M. Anillin is a scaffold protein that links RhoA, actin, and myosin during cytokinesis. *Curr. Biol.* **18**, 30–36 (2008).
52. Prokopenko, S. N. et al. A putative exchange factor for Rho1 GTPase is required for initiation of cytokinesis in Drosophila. *Genes Dev.* **13**, 2301–2314 (1999).
53. Basant, A. & Glotzer, M. Spatiotemporal regulation of RhoA during cytokinesis. *Curr. Biol.* **28**, R570–R580 (2018).
54. Yuce, O., Piekny, A. & Glotzer, M. An ECT2-centralspindlin complex regulates the localization and function of RhoA. *J. Cell Biol.* **170**, 571–582 (2005).
55. Marc, A. et al. Inactivation of the Hippo tumor suppressor pathway promotes melanoma. *Nat. Commun.* **13**, https://doi.org/10.1038/s41467-022-31399-w (2022).
56. Liu, X., Yan, S., Zhou, T., Terada, Y. & Erikson, R. L. The MAP kinase pathway is required for entry into mitosis and cell survival. *Oncogene* **23**, 763–776 (2004).
57. Mulner-Lorillon, O., Chasse, H., Morales, J., Belle, R. & Cormier, P. MAPK/ERK activity is required for the successful progression of mitosis in sea urchin embryos. *Dev. Biol.* **421**, 194–203 (2017).
58. Wright, J. H. et al. Mitogen-activated protein kinase kinase activity is required for the G(2)/M transition of the cell cycle in mammalian fibroblasts. *Proc. Natl Acad. Sci. USA* **96**, 11335–11340 (1999).
59. Hatzivassiliou, G. et al. RAF inhibitors prime wild-type RAF to activate the MAPK pathway and enhance growth. *Nature* **464**, 431–435 (2010).
60. Poulikakos, P. I., Zhang, C., Bollag, G., Shokat, K. M. & Rosen, N. RAF inhibitors transactivate RAF dimers and ERK signalling in cells with wild-type BRAF. *Nature* **464**, 427–430 (2010).
61. Zhang, C. et al. RAF inhibitors that evade paradoxical MAPK pathway activation. *Nature* **526**, 583–586 (2015).
62. Yoshizaki, H. et al. Activity of Rho-family GTPases during cell division as visualized with FRET-based probes. *J. Cell Biol.* **162**, 223–232 (2003).
63. Canman, J. C. et al. Inhibition of Rac by the GAP activity of centralspindlin is essential for cytokinesis. *Science* **322**, 1543–1546 (2008).
64. Bastos, R. N., Penate, X., Bates, M., Hammond, D. & Barr, F. A. CYK4 inhibits Rac1-dependent PAK1 and ARHGEF7 effector pathways during cytokinesis. *J. Cell Biol.* **198**, 865–880 (2012).
65. Yoshizaki, H. et al. Cell type-specific regulation of RhoA activity during cytokinesis. *J. Biol. Chem.* **279**, 44756–44762 (2004).
66. Godinho, S. A. et al. Oncogene-like induction of cellular invasion from centrosome amplification. *Nature* **510**, 167–171 (2014).
67. Waterman-Storer, C. M., Worthylake, R. A., Liu, B. P., Burridge, K. & Salmon, E. D. Microtubule growth activates Rac1 to promote lamellipodial protrusion in fibroblasts. *Nat. Cell Biol.* **1**, 45–50 (1999).
68. Rusan, N. M. & Wadsworth, P. Centrosome fragments and microtubules are transported asymmetrically away from division plane in anaphase. *J. Cell Biol.* **168**, 21–28 (2005).
69. Wong, Y. L. et al. Cell biology. Reversible centriole depletion with an inhibitor of Polo-like kinase 4. *Science* **348**, 1155–1160 (2015).
70. Andreassen, P. R., Lohez, O. D., Lacroix, F. B. & Margolis, R. L. Tetraploid state induces p53-dependent arrest of nontransformed mammalian cells in G1. *Mol. Biol. Cell* **12**, 1315–1328 (2001).
71. Kuffer, C., Kuznetsova, A. Y. & Storchova, Z. Abnormal mitosis triggers p53-dependent cell cycle arrest in human tetraploid cells. *Chromosoma* **122**, 305–318 (2013).
72. Heijo, H. et al. DNA content contributes to nuclear size control in *Xenopus laevis*. *Mol. Biol. Cell* **31**, 2703–2717 (2020).
73. Jolly, C. & Loo, Van P. Timing somatic events in the evolution of cancer. *Genome Biol.* **19**, 95 (2018).
74. Kaufman, C. K. et al. A zebrafish melanoma model reveals emergence of neural crest identity during melanoma initiation. *Science* **351**, aad2197 (2016).
75. Liu, J. et al. Phosphorylation of Mps1 by BRAFV600E prevents Mps1 degradation and contributes to chromosome instability in melanoma. *Oncogene* **32**, 713–723 (2013).
76. Cui, Y., Borysova, M. K., Johnson, J. O. & Guadagno, T. M. Oncogenic B-Raf(V600E) induces spindle abnormalities, supernumerary centrosomes, and aneuploidy in human melanocytic cells. *Cancer Res.* **70**, 675–684 (2010).
77. Denu, R. A. et al. Centriole overduplication is the predominant mechanism leading to centrosome amplification in melanoma. *Mol. Cancer Res.* **16**, 517–527 (2018).
78. Nigg, E. A. & Holland, A. J. Once and only once: mechanisms of centriole duplication and their deregulation in disease. *Nat. Rev. Mol. Cell Biol.* **19**, 297–312 (2018).
79. Di Micco, R. et al. Oncogene-induced senescence is a DNA damage response triggered by DNA hyper-replication. *Nature* **444**, 638–642 (2006).
80. Grabocka, E., Commisso, C. & Bar-Sagi, D. Molecular pathways: targeting the dependence of mutant RAS cancers on the DNA damage response. *Clin. Cancer Res.* **21**, 1243–1247 (2015).
81. Wilhelm, T. et al. Mild replication stress causes chromosome mis-segregation via premature centriole disengagement. *Nat. Commun.* **10**, 3585 (2019).
82. Watanabe, K., Takao, D., Ito, K. K., Takahashi, M. & Kitagawa, D. The Cep57-pericentrin module organizes PCM expansion and centriole engagement. *Nat. Commun.* **10**, 931 (2019).
83. Zhang, Y. et al. Mps1 is associated with the BRAF(V600E) mutation and predicts poor outcome in patients with colorectal cancer. *Oncol. Lett.* **17**, 2809–2817 (2019).
84. Maric, I. et al. Centrosomal and mitotic abnormalities in cell lines derived from papillary thyroid cancer harboring specific gene alterations. *Mol. Cytogenet.* **4**, 26 (2011).
85. Fritz, G., Just, I. & Kaina, B. Rho GTPases are over-expressed in human tumors. *Int. J. Cancer* **81**, 682–687 (1999).
86. Kakiuchi, M. et al. Recurrent gain-of-function mutations of RHOA in diffuse-type gastric carcinoma. *Nat. Genet.* **46**, 583–587 (2014).
87. Jung, H., Yoon, S. R., Lim, J., Cho, H. J. & Lee, H. G. Dysregulation of rho GTPases in human cancers. *Cancers.* **1**. https://doi.org/10.3390/cancers12051179 (2020).
88. Pollock, P. M. et al. High frequency of BRAF mutations in nevi. *Nat. Genet.* **33**, 19–20 (2003).
89. Piris, A., Mihm, M. C. Jr & Hoang, M. P. BAP1 and BRAFV600E expression in benign and malignant melanocytic proliferations. *Hum. Pathol.* **46**, 239–245 (2015).
90. Winokur, T. S., Palazzo, J. P., Johnson, W. C. & Duray, P. H. Evaluation of DNA ploidy in dysplastic and Spitz nevi by flow cytometry. *J. Cutan. Pathol.* **17**, 342–347 (1990).
91. Newton, J. A., Camplejohn, R. S. & McGibbon, D. H. The flow cytometry of melanocytic skin lesions. *Br. J. Cancer* **58**, 606–609 (1988).
92. Gilchrest, B. A. et al. Characteristics of cultivated adult human nevocellular nevus cells. *J. Investig. Dermatol.* **87**, 102–107 (1986).
93. McKee, P. H. *Pathology of the Skin: with Clinical Correlations* (Mosby, 2005).
94. Skowronek, J. et al. DNA ploidy in malignant melanoma, skin cancer and pigmented nevi. *Neoplasma* **44**, 282–288 (1997).
95. Watkins, T. B. K. et al. Pervasive chromosomal instability and karyotype order in tumour evolution. *Nature* **587**, 126–132 (2020).
96. Birkeland, E. et al. Patterns of genomic evolution in advanced melanoma. *Nat. Commun.* **9**, 2665 (2018).
97. Vergara, I. A. et al. Evolution of late-stage metastatic melanoma is dominated by aneuploidy and whole genome doubling. *Nat. Commun.* **12**, 1434 (2021).
98. Westerfield, M. *The Zebrafish Book. A Guide for the Laboratory Use of the Zebrafish* (*Danio rerio*) (University of Oregon Press, 2000).
99. Berghmans, S. et al. tp53 mutant zebrafish develop malignant peripheral nerve sheath tumors. *Proc. Natl Acad. Sci. USA* **102**, 407–412 (2005).
100. Lister, J. A., Robertson, C. P., Lepage, T., Johnson, S. L. & Raible, D. W. nacre encodes a zebrafish microphthalmia-related protein that regulates neural-crest-derived pigment cell fate. *Development* **126**, 3757–3767 (1999).
101. Chakrabarti, S., Streisinger, G., Singer, F. & Walker, C. Frequency of gamma-ray induced specific locus and recessive lethal mutations in mature germ cells of the zebrafish, *Brachydanio rerio*. *Genetics* **103**, 109–123 (1983).
102. Campeau, E. et al. A versatile viral system for expression and depletion of proteins in mammalian cells. *PLoS ONE* **4**, e6529 (2009).
103. Sanjana, N. E., Shalem, O. & Zhang, F. Improved vectors and genome-wide libraries for CRISPR screening. *Nat. Methods* **11**, 783–784 (2014).
104. Shalem, O. et al. Genome-scale CRISPR-Cas9 knockout screening in human cells. *Science* **343**, 84–87 (2014).

105. Kotynkova, K., Su, K. C., West, S. C. & Petronczki, M. Plasma membrane association but not midzone recruitment of RhoGEF ECT2 is essential for cytokinesis. *Cell Rep.* **17**, 2672–2686 (2016).
106. Taylor, A. M. et al. Genomic and functional approaches to understanding cancer aneuploidy. *Cancer Cell* **33**, 676–689 e673 (2018).
107. Cerami, E. et al. The cBio cancer genomics portal: an open platform for exploring multidimensional cancer genomics data. *Cancer Discov.* **2**, 401–404 (2012).
108. Gao, J. et al. Integrative analysis of complex cancer genomics and clinical profiles using the cBioPortal. *Sci. Signal.* **6**, pl1 (2013).

Acknowledgements

We thank Kristyna Kotynkova for advice on RhoA and Anillin immunofluorescence staining; Paul Kaufman and Eric Campeau for the pLenti-CMV/TO neo/puro plasmids; Daryl Bosco for use of the Leica-DM inverted microscope; Desiree Baron for imaging and microscopy advice; Charles Kaufman for the *Tg(crestin:EGFP)* zebrafish strain; Melissa Guerin for help with fish genotyping; Patrick White, Ed Jaskolski and the staff at the UMMS Animal Medicine Department for fish care; Tammy Krumpoch and Susanne Pechhold at the UMMS Flow Cytometry Core for guidance and assistance in performing flow cytometry and FACS experiments. M.A.V. was supported by 1F30CA228388 and 5T32GM008541. N.J.G. was supported by GM117150, the Harry J. Lloyd Charitable Trust, and the Jackie King Young Investigator Award from the Melanoma Research Alliance. This research was supported by NIAMS of the National Institutes of Health under award number AR063850 and by the USA Department of Defense under award W81XWH2010288 to C.J.C.

Author contributions

R.D. and C.J.C. conceptualized the study, designed the in vitro experiments, and wrote the manuscript. R.D. and C.J.C. designed all the zebrafish experiments. R.D. and C.J.C. performed all the in vitro biological assays, immunofluorescence staining, flow cytometry and image analysis. M.A.V. and N.J.G. performed the live-cell imaging experiments and R.D. analyzed the data. N.J.G. provided critical reagents.

Competing interests

The authors declare no competing interests.

Additional information

Supplementary information The online version contains supplementary material available at https://doi.org/10.1038/s41467-022-31899-9.

Correspondence and requests for materials should be addressed to Craig J. Ceol.

Peer review information *Nature Communications* thanks the anonymous reviewer(s) for their contribution to the peer review of this work. Peer reviewer reports are available.

Reprints and permission information is available at http://www.nature.com/reprints

Publisher's note Springer Nature remains neutral with regard to jurisdictional claims in published maps and institutional affiliations.

Open Access This article is licensed under a Creative Commons Attribution 4.0 International License, which permits use, sharing, adaptation, distribution and reproduction in any medium or format, as long as you give appropriate credit to the original author(s) and the source, provide a link to the Creative Commons license, and indicate if changes were made. The images or other third party material in this article are included in the article's Creative Commons license, unless indicated otherwise in a credit line to the material. If material is not included in the article's Creative Commons license and your intended use is not permitted by statutory regulation or exceeds the permitted use, you will need to obtain permission directly from the copyright holder. To view a copy of this license, visit http://creativecommons.org/licenses/by/4.0/.

© The Author(s) 2022

Hallmarks of Skin Cancer Conference HoSC 2021
University of Heidelberg
Keynote Lecture

Targeting BMP signaling as anti-melanoma therapy

Craig J. Ceol

[1]Program in Molecular Medicine, Department of Molecular, Cell and Cancer Biology, University of Massachusetts Chan Medical School, Worcester, MA, USA

Despite major advances in melanoma therapies, a majority of patients with late-stage tumors will still die from their disease. These patients typically exhibit resistance to targeted and immunotherapies. To identify new disease genes whose targeting could complement existing therapies, we screened candidate oncogenes and tumor suppressors that were shortlisted using integrative comparative oncogenomics. One of the new melanoma genes identified was GDF6, a BMP ligand normally expressed in the neural crest but absent in most adult tissues, including melanocytes. GDF6 was present in nearly 80% of human melanomas, where it activates BMP signaling. Knockdown of GDF6 or inhibition of BMP signaling caused differentiation and death of melanoma cells. Developmental studies in zebrafish indicated that GDF6-driven BMP signaling normally suppresses melanocytic differentiation of neural crest cells. Together these studies show that ligand-dependent BMP signaling promotes melanoma initiation and maintenance, and this activity is a reiteration of the normal function of GDF6-driven BMP signaling during development. The dependence of melanomas on GDF6-driven BMP signaling presents an opportunity for therapeutic intervention, and we developed inhibitors to target this activity. In xenograft studies, anti-GDF6 therapy had potent anti-tumor effects, supporting the clinical application of anti-BMP therapy in melanoma treatment.